Developing talin-based shock absorbing materials

Jack Anfield Doolan

A thesis submitted to the University of Kent for the degree of Doctor of Philosophy in Biochemistry

School of Biosciences

University of Kent

2022

Declaration

No part of this thesis has been submitted in support of an application for any degree or other qualification of the University of Kent, or any other University or Institution of learning.

Covid-19 impact statement

During the Covid-19 pandemic, between the months of March 2020 and June 2020, the laboratories at the University of Kent were closed. Therefore, over this time period I had no access to either the chemistry or biology labs. At the time of this closure, I was attempting to synthesise the maleimide based crosslinkers and express and purify pGEL001 for talin shock absorbing material formation. As I was within the first year of my PhD, I had very little data at the time of the universities closure, and therefore could not utilise the time out of the lab for data analysis. Instead, I utilised this time to aid members of Jennifer Hiscock's group with the writing of the manuscript titled: 'Supramolecular self-associating amphiphiles (SSAs) as nanoscale enhancers of cisplatin anticancer activity', in addition to starting the review: 'Advancements in antimicrobial nanoscale materials and self-assembling systems.' However, whilst these opportunities were valuable for developing scientific writing skills and enhancing my publication record, I was unable to make progress in collecting data required for my thesis. Following the reopening of the laboratories in June 2020, we began to operate on a rota system due to capacity limits within the laboratory. As a result, over the months leading up to September 2020, I only had access to the biology lab approximately 2.5 days every two weeks until the lab capacity limits were increased. Alongside this time in the biology labs, I also had access to the chemistry lab in the mornings. Due to my limited access to the biology lab, progress on attempting to make the first talin shock absorbing material was severely impacted, with insufficient time to express and purify pGEL001 on a large enough scale for gelation trials. Instead, I utilised this time period to focus on the synthesis of the maleimide crosslinkers and potential future crosslinkers which are not included within this thesis. From September 2020, our lab moved into a four day per week rota system until December 2020, at which point the labs subsequently closed again until mid-January 2021. Upon returning to the labs in January 2021 we continued to operate on a four day per week rota system with intermittent disruptions until April 2021. In summary, although I was able to make progress in manuscript writing and drafting aspects of my PhD thesis during the lockdowns, the limited access to the biology laboratory had major implications on my ability to

progress this project for a large portion of the first year of my PhD. Overall, I lost out on approximately five months of research time. With these lost months, I would have further investigated the interesting results displayed by the talin shock absorbing materials, including the increased rigidity witnessed in the rheology experiments described in Section 4.4.2. Furthermore, I would have conducted light gas gun projectile experiments over a wider variety of velocities to define the upper performance limit of the material, with the added time enabling me to express and purify larger quantities of pGEL001.

Acknowledgements

Firstly, I would like to thank both of my supervisors, Professor Ben Goult and Professor Jennifer Hiscock for their guidance and support during this project. Over the course of my PhD I have been given many opportunities to pursue unique and exciting avenues of research that have greatly expanded my skill set and reinforced my passion for science. Furthermore, I am incredibly grateful for the extensive time each of you invested in developing my scientific writing. I could not have asked for better supervisors and I look forward to following the future research outputs from both of your labs.

Secondly, I would like to thank all of the Goult, Hiscock, Mulvihill and Geeves lab members both past and present for the helping me over the course of my PhD. Due to the interdisciplinary nature of this project, many of the experiments performed within this project fell outside of my skillset prior to starting this PhD. Without the valuable guidance and support from each and every one of the members within these labs I would not have been able to achieve the successes of this project. My time in each of these labs has been a pleasure, and I wish everyone the best moving forward. In particular I would like to thank Lorena for being a great post doc who was always willing to help out, and George for not only making the antimicrobial review possible, but also for going above and beyond to help me in all areas of my development as a scientist. I would also like to say a massive thank you to Luke Alesbrook for the SEM training and our collaborations on the light gas gun; Alex Jones for his training and support with the bioreactors; Gary Thompson for his continued training in NMR and aid with NMR experiments; Antoine Paris for his time helping me with the C-trap; and Kevin Howland for training me on the LCMS.

Finally, I would like to thank my family and friends who have been a great support network over this time period. In particular I would like to thank my wife for listening to me rant about science for the last three years, keeping me positive when things were going wrong in the lab and believing in me when I didn't. The successes of this PhD would not have been possible without everyone mentioned here, and I am very grateful for everyone I have had the pleasure of knowing during my time at Kent.

Publications

Doolan, J. A., Williams, G. T., Hilton, K. L. F., Chaudhari, R., Fossey, J. S., Goult, B. T. & Hiscock, J. R. (2022). Advancements in antimicrobial nanoscale materials and self-assembling systems*. Chemical Society Reviews*, 51, 8696-8755.

Dora, N. O., Blackburn, E., Boles, J. E., Williams, G. T., White, L. J., Turner, S. E. G., Horthersall, J. D., Askwith, T., Doolan, J. A., Mulvihill, D. P., Garrett, M. D. & Hiscock, J. R. (2021). Supramolecular self-associating amphiphiles (SSAs) as nanoscale enhancers of cisplatin anticancer activity. *RSC Advances*, 11, 14213-14217.

Doolan, J. A., Alesbrook, L., Baker, K., Brown, I., Williams, G. T., Hiscock, J. R. & Goult, B. T. Next generation protein-based materials capture and preserve projectiles from supersonic impacts. *BioRxiv*, 2022.

Patents

Patent application number: GB2216633.4 (08/11/22).

Manuscripts in preparation

Doolan, J. A., Jones, A., Hilton, K. L. F., Goult, B. T. & Hiscock, J. R. High-throughput characterisation of protein-based hydrogels using UV-vis and optical density measurements.

Abstract

Shock absorbing materials are essential for a range of applications. The military and police force require ballistic armour for the protection of their personnel, whilst the aerospace industry require materials that enable the capture, preservation and study of high velocity projectiles. However, the industry standard materials employed for these purposes each display several inherent limitations, including low durability and alteration of the projectiles structure following capture. Protein-based shock absorbing materials, specifically in the form of hydrogels, directly mitigate the limitations of the industry standard materials used for these purposes, with potential for high durability and endothermic mechanisms of energy dissipation. Despite these promising attributes, research to date conducted on protein-based shock absorbing hydrogels has solely focused on biomedical applications. Here, the mechanosensory protein talin was selected as a protein monomer unit for the development of talin-based shock absorbing materials (TSAMs). Talin can undergo repeated force induced unfolding/refolding cycles, dissipating energy in the process through the endothermic mechanism of protein unfolding. Therefore, talin presents as the perfect monomer unit for the development of a shock absorbing hydrogel. Following extensive investigation into the formation and characterisation of the resulting TSAM, experiments were conducted to elucidate TSAMs performance as a high velocity projectile capture and preservation material. When subjected to impacts of 1.5 km/s, the TSAMs were shown to successfully capture and preserve basalt projectiles and aluminium shrapnel, revealing an industrial application for the material outside of the biomedical sector. Due to the inherent attributes of TSAMs incurred from the talin monomer unit, this material presents many advantages over the aerogel materials employed as the industry standard for these experiments. With additional preliminary studies into the scalability and tunability of the TSAMs conducted within this project, this work defined a novel application for protein-based shock absorbing hydrogels with great commercial potential.

Table of contents

List of figures

List of tables

Abbreviations

G'	Storage modulus
γ_o	Shear strain
°C	Degrees Celsius
[Ru(bpy)3]2+	Tris(2,2'-bipyridyl)ruthenium(II)
2M9	Minimal media
Å	Ångström
bp, kbp	Base-pairs, kilobase-pairs
BSA	Bovine serum albumin
BTEA	Blast tank exit aperture
C-terminal	Carboxy terminal
CAB	Sodium cacodylate buffer
CD	Circular dichroism
CDK1	Cyclin-dependent kinase-1
C_p	Concentration of protein
D_2O	Deuterated water
Da, kDa	Dalton, kilodalton
DCM	Dichloromethane
DMF	Dimethyl formamide
DMSO	Dimethyl sulfoxide
DNA	Deoxyribonucleic acid
DTT	Dithiothreitol
E. coli	*Escherichia coli*
G	Shear modulus
G"	Loss modulus
G*	Complex modulus
GFP	Green fluorescent protein
His-tag	6x polyhistadine tag
HPLC	High performance liquid chromatography
HSQC	Heteronuclear single-quantum coherence

IAEDANS	5-((((2-iodoacetyl)amino)ethyl)amino) naphthalene-1-sulphonic acid
Ig	Immunoglobulin-like
IPTG	Isopropyl β-D-1-thiogalactopyranoside
K	Kelvin
Kank	Kidney ankyrin repeat-containing protein
kJ	kilojoules
kPa	kilopascal
LB	Lysogeny broth
LCMS	Liquid chromatography mass spectrometry
LVER	Linear viscoelastic region
m, nm, μm	Metres, nanometres, micrometres
MGC	Minimum gelation concentration
MOPS	(3-(N-morpholino)propanesulfonic acid)
M_R	Molecular weight
mwco	Molecular weight cut-off
N-terminal	Amino terminal
N_2	Nitrogen
N_A	Avogadro's constant
NMR	Nuclear magnetic resonance
OD	Optical density
PBST	Phosphate buffered saline, Tween 20
PCR	Polymerase chain reaction
PDB	Protein Data Bank
PIP2	Phosphatidylinositol bisphosphate
pN	Piconewton
pO_2	Dissolved oxygen probe
ppm	Parts per million
PVDF	Polyvinylidene difluoride
PVP	Polyvinylpyrrolidone
R1-13	Rod domain 1-13

RIAM	Rap1-GTP-interacting adaptor molecule
rpm	Rotations per minute
SDS-PAGE	Sodium dodecyl sulphate poly-acrylamide Gel electrophoresis
SEC	Size exclusion chromatography
t	Time
TB	Terrific broth
TBST	Tris-buffered saline, Tween 20
TCEP	Tris(2-carboxyethyl)phosphine Hydrochloride
TEV	Tobacco etch virus
TFA	Trifluoroacetic acid
TIP-1	Tax-interacting protein-1
T_m	Melting temperature
TSAM	Talin shock absorbing material
UV	Ultraviolet
VD1-5	Vinculin domain 1-5
VNp	Vesicle nucleating peptide
δ	Phase angle
τ	Shear stress
ω	Frequency

Chapter 1: Introduction

1.1 Shock absorbing materials

1.1.1 What are shock absorbing materials?

Shock absorbing materials are utilised in a wide array of applications, many of which are common place in our everyday lives (Spiteri, 2019). Rubber soles contained within shoes or oil pistons within cars absorb shock utilising viscoelasticity, whilst car bumpers and bike helmets absorb shock through destructive modifications of the materials structure (Frenzel *et al*., 2016). Mechanical shock refers to the sudden change in velocity and acceleration of an object induced by impacts, earthquakes and other phenomena (Qian *et al*., 2015). When a sudden change in velocity and acceleration occurs, the kinetic energy of the object in question must be absorbed and dissipated; for instance, a projectile of 161.2 g travelling at 1550 m/s contains 193.6 kJ of kinetic energy (Lynch, 1999). When stopped upon impact, the entirety of the projectile kinetic energy is transferred to the impacted material. Therefore, shock absorbing materials are those capable of efficient energy absorption, commonly exploiting viscoelasticity or destructive modifications to achieve this feat (Frenzel *et al*., 2016). When subjected to shock, materials must contend with the physical phenomenon of elastic propagation, shock propagation, wave propagation, fracture, fragmentation, preformation and spallation, all caused by the transferred energy, exemplifying the extreme conditions shock absorbing materials can be exposed to (Qiao *et al*., 2008). Important considerations for materials intended for shock absorbing applications are the lifetime, durability, weight, yield point and mechanism of energy absorption/dissipation. Adding to the complexity of material design, several of these properties are linked; for instance, materials employing destructive mechanisms of energy dissipation may only be used once before needing replacement, consequently displaying inherently low durability. Therefore, both the mechanism of energy dissipation and the properties required for the downstream application, such as weight and durability, should be considered in tandem at the design stage due to their interlinked relationship.

1.1.2 Mechanisms of shock absorption

The two major mechanisms of energy dissipation utilised in shock absorbing materials are that of viscoelasticity (Shedbale and Muley, 2017) (Figure 1.1) and destructive modifications (Zhang *et al*., 2020a) (Figure 1.2). Viscoelastic mechanisms are commonly employed in applications requiring dampening of vibrations, such as in buildings exposed to strong wind effects or located in earthquake prone regions (Figure 1.1), as well as automobiles (Shedbale and Muley, 2017). Unaddressed vibrational energy can result in structural failure, leading to costly repairs and even severe safety hazards. Viscoelastic materials are those that possess both viscous and elastic behaviour, utilising properties such as disentanglement of hydrogel fibres for energy dissipation. Unlike a purely elastic or purely viscous material, viscoelastic materials store a fraction of the energy through elastic deformation and dissipate the remainder through viscous flow via conversion to thermal energy (Tanzi *et al*., 2019). Viscoelastic materials present the distinct benefit of durability, capable of undergoing repeated cycles of shock without compromise of the energy dissipation mechanism. However, the primary drawback with viscoelastic systems is the time-dependency of the materials performance, with energy dissipation highly dictated by the timescale of loading and unloading (Frenzel *et al*., 2016); materials loaded at a faster rate will experience a higher peak stress (Yang, 2018) and are therefore less suited to high speed impacts.

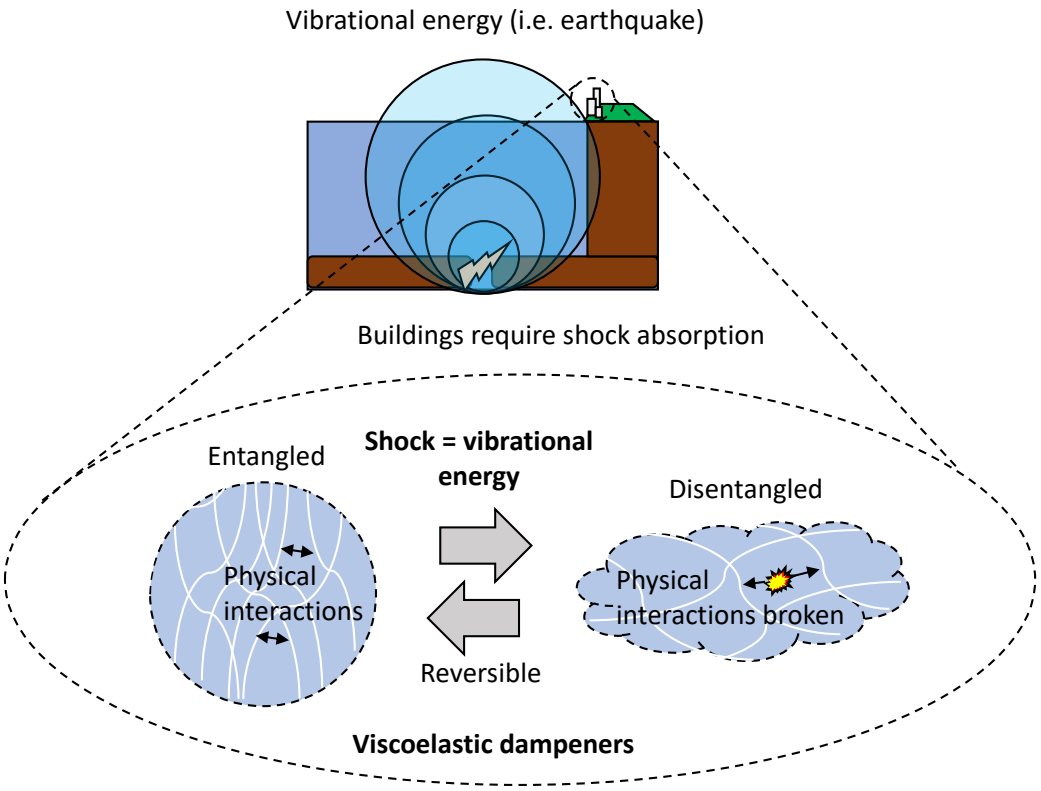

Figure 1.1: An example of a viscoelastic energy dissipating material. When exposed to shock, viscoelastic dampeners employed for earthquake shock absorption can exploit fibre disentailment to dissipate the energy.

Destructive-based mechanisms of energy dissipation are commonly employed for high energy impact purposes. Here, the shock absorbing material dissipates kinetic energy through the compromise of its own internal structure, resulting in an often irreversibly damaged material. One such example is body armour, commonly used by military and civilian forces to protect the wearer against penetration from projectiles, such as bullets or shrapnel (Park *et al*., 2012). Frequently, this armour consists of a multi-layered system, commonly a ceramic face backed by a fibre-reinforced composite (Fejdys *et al*., 2021), shown in Figure 1.2a. The multi-layered design enables the hard brittle ceramic to destroy the projectile tip, distributing the kinetic energy over the backing, in turn reflecting the tensile wave and acting to capture the shattered ceramic (Reis *et al*., 2021). Despite the effective penetration blocking of these armour systems, a remainder of the kinetic energy is still distributed to the wearer, possibly resulting in behind armour blunt trauma (Wen *et al*., 2015). Furthermore, during impacts this form of armour is irreversibly damaged,

compromising its structural integrity for further use. Therefore these armour systems present low durability. Another example material employing destructive modifications are the impact materials utilised within the aerospace sector, illustrated in Figure 1.2. Here, shock absorbing materials are used for the unique task of capturing and preserving space debris, space dust and micrometeoroids (Kearsley, 2017). These captured projectiles are then returned to earth and further studied, enhancing our understanding of the local environments of aerospace equipment, including that of the international space station (Woignier *et al*., 2013). Data from these experiments facilitate aerospace equipment design, improving the safety of astronauts and the longevity of costly aerospace equipment. Silica aerogels are the current industry standard materials for projectile capture and preservation, achieving energy dissipation through conversion of projectile kinetic energy into both mechanical and thermal energy (Jones *et al*., 2013). However, the resulting temperature elevation that occurs upon impact, further enhanced by the remarkable insulating properties of aerogel (Alwin and Shajan, 2020), can cause the aerogel structure to melt (Jones *et al*., 2013). Furthermore, these elevated temperatures may compromise the structure of the captured projectiles, altering their chemical composition (Jones *et al*., 2013, Bheekhun *et al*., 2013). The experienced thermal and mechanical energy results in chemical bond breakage within the aerogels, rendering the material irreversibly damaged post-impact.

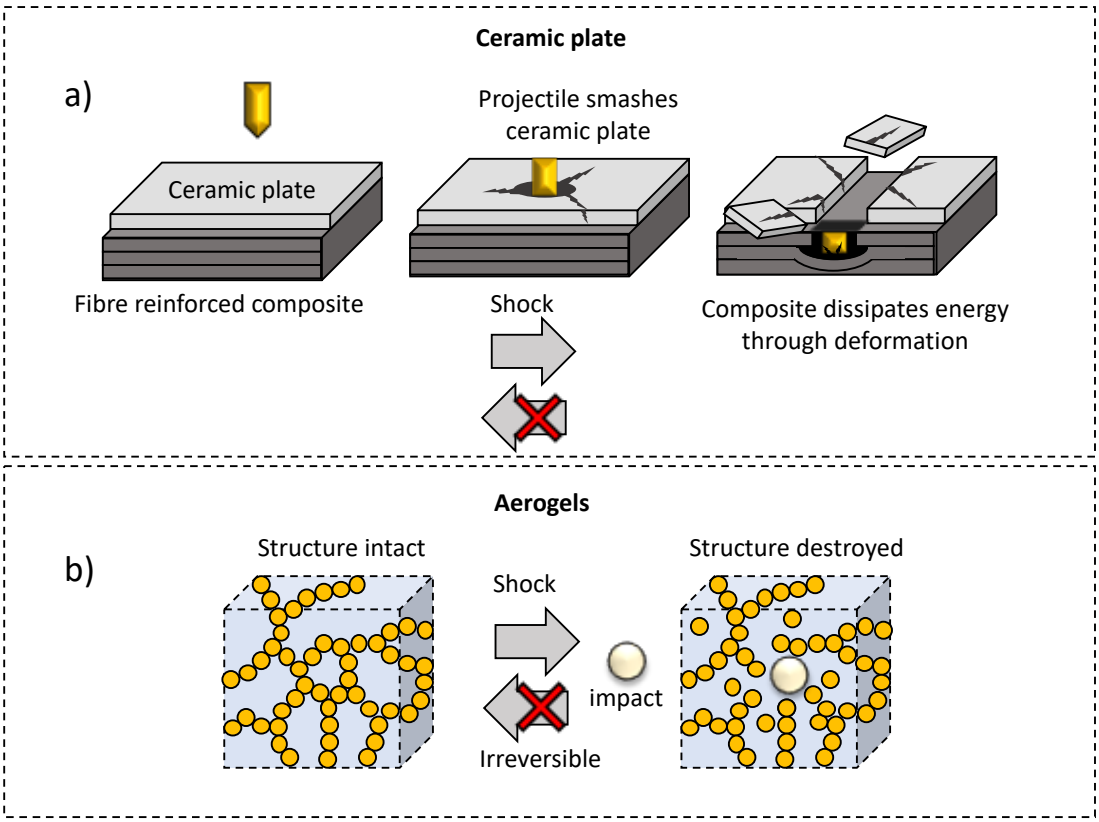

Figure 1.2: Shock absorbing materials exploiting destructive mechanisms of energy dissipation. a) Ceramic plates dissipate energy through a multi-layered system which becomes irreversibly damaged upon shock. b) Aerogels dissipate energy through destruction of its internal structure, rendering the material irreversibly damaged upon shock.

It is apparent from the discussed examples, a shock absorbing material presenting the durability, reusability and light weight of viscoelastic systems, with the non-time dependant and stronger energy dissipation mechanism of deformable materials could result in a next generation shock absorbing material capable of outperforming many of the industry standards. Over the last decade multiple new avenues have been exploited to develop next generation shock absorbing materials, possible through advancements in technology and manufacturing processes (Lin *et al*., 2019). A lightweight 3D polymer micro lattice material was developed by Frenzel *et al*. (Frenzel *et al*., 2016) with tailored buckling elements, producing a self-recoverable shock absorbing material. Thevamaran and co-workers produced aramid nanofiber reinforced low density multiwalled carbon nanotube films that presented efficient energy dissipation and mitigation of localised fracture during supersonic microprojectile impacts of 400 m/s-1000 m/s (Cai *et al*., 2021). Each of these systems

focused on improving shock absorption whilst reducing the weight of the material, a vital consideration for impact applications such as armour and aerospace materials. Investigations such as these demonstrate the potential for great advances in shock absorbing technology by investigating and optimising novel materials, facilitated by our ever improving technologies. One such area rife with unique shock absorbing materials is nature, with many organisms employing innovative systems to dissipate energy, facilitating their survival.

1.1.3 Shock absorbing materials inspired by nature

Whilst most shock absorbing materials employed for industrialised purposes revolve around synthetic compounds and inorganic materials, several notable materials inspired by nature lend themselves towards a range of applications. Nacre, a material found in the shells of mollusks, presents a toughness many times higher than that expected from its 95% brittle ceramic composition (Raphel *et al.,* 2019). The observed toughness results from the organised structure of nacre, consisting of aragonite plates contained within a protein matrix, illustrated in Figure 1.3. When exposed to impacts, the aragonite plates slide away from each other, dissipating energy during their displacement (Figure 1.3a). This energy dissipation was shown to occur through multiple mechanisms, including the formation of dovetail joints between the plates (Barthelat *et al.*, 2007), breakage of mineral bridges between overlapping plates and intra granular cracks forming, enabled by the protein matrix (Zhang *et al*., 2016). Although bioinspired materials of nacre are not in widespread use due to the current technological limitations in manufacturing structures of this kind, work by Yin *et al*. employed a nacre-like structure to create a toughened glass (Yin et al., 2019). This was achieved by producing borosilicate glass sheets that can slide past each other when bonded with ethylene-vinyl acetate. The resulting five-layered glass composite displayed high levels of impact resistance, high stiffness, surface hardness, deformability and transparency. Furthermore, the manufacturing methodologies of laser engraving and lamination fabrication employed were inexpensive and amenable to large scale-production methods. Therefore, with further research, materials of this kind may find their way into everyday applications.

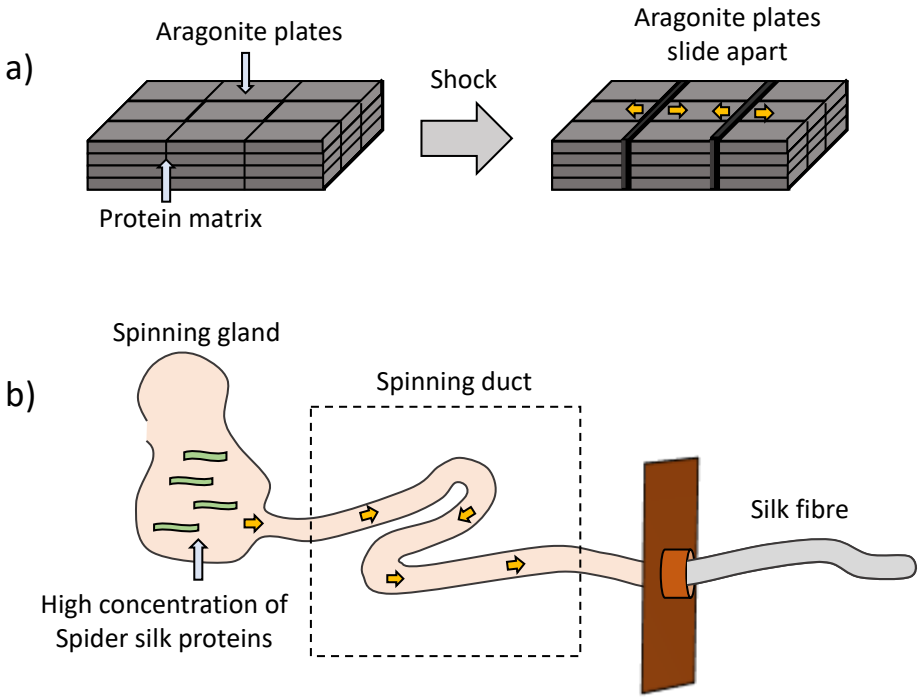

Figure 1.3: Shock absorbing materials inspired by nature. a) Nacre's structure dissipating energy when exposed to shock via sliding of its aragonite plates. b) The process of forming spider silk fibres in the spinning gland and spinning duct of spiders.

Some of the most popular bioinspired materials seek to capture the remarkable properties of spider silk. Spider silk presents toughness three to four times higher than that of Kevlar, high extensibility matching that of rubber (30% elongation) in addition to biocompatibility (Kiseleva *et al.*, 2020). Spider silk fibres consist of proteins presenting large quantities of nonpolar and hydrophobic amino acids including glycine and alanine, with repetitive sequences of 10-50 amino acids often accounting for 90% of the proteins sequence (Romer and Scheibel, 2008). These proteins are secreted from the spinning glands of spiders where they exist intrinsically unfolded and at extremely high concentrations, which then assemble during their passage through the spinning duct, rendering the silk fibres water insoluble (Displayed in Figure 1.3b). The resulting spider silk fibres present mechanical properties superior to that of silkworm silk, synthetic mimetics such as Kevlar and nylon, in addition to a more rounded strength vs elasticity profile than that of carbon fibre (Romer and Scheibel, 2008). Thus, natural spider silk is superior

to any of its synthetic counterparts. However, due to the complexities of spider farming, including the cannibalistic nature of the species, large scale application of spider silk is not currently possible (Romer and Scheibel, 2008). Therefore, current research has turned to recombinant spider silk protein expression and artificial spinning, hoping to produce fibres closer to that of spider silk than currently achievable through synthetic mimetics. Despite these efforts, to date all materials produced via these methods still present mechanical properties much lower than that of naturally obtained spider silk. Thus, synthetic biomimetics and the less impressive silkworm silk are currently utilised for most industrial applications requiring these forms of shock absorbing material, with Kevlar employed as body armour (Nair *et al*., 2020) and nylon as high strength rope (Huntley and Ieee, 2016).

Together, these examples of materials inspired by nature show the range of future industrial applications possible for both bioinspired materials and protein-based materials themselves.

1.2 Protein-based materials

1.2.1 Protein-based material types

Protein-based materials have been present within society for millennia. Common examples include that of silk, wool and leather (Abascal and Regan, 2018). With increasing technological breakthroughs, the development of materials more efficiently encapsulating the desired properties of the integrated proteins has become possible. Specifically, advances in genetic engineering and recombinant protein expression (Desai and Lee, 2015), in addition to computational technologies (Ljubetic *et al*., 2017) facilitating the design of proteins and material development techniques including electrospinning (Xue *et al*., 2019) have escalated advancements in protein-based material development. For example, the unique extensibility of elastin was successfully incorporated into vascular grafts via electrospinning, mimicking the mechanical properties of mammalian arteritis (Wise *et al*., 2011). A host of proteins that display highly specialised properties desired in materials exist within nature; elastin and resilin display high levels of extensibility, silk fibroins

present high tensile strength and toughness (Hu *et al*., 2012), detection of light is possible with rhodopsin (Rosenbaum *et al*., 2009) and transfer of chemical energy into work is achieved with myosin and actin (Spudich, 2001). Together, materials integrating these proteins present great potential to solve many technological, medical and scientific problems currently faced by society (Huang *et al*., 2016). Utilising proteins displaying these properties over synthetically constructed counterparts results in a range of benefits. Proteins generally exhibit lower toxicity, better biodegradability, biocompatibility and flexibility than their synthetic equivalents (Teng *et al*., 2015) (Shen *et al*., 2017). Importantly, these benefits are balanced against the issues of proteolytic degradation especially if employed *in vivo* (Stie *et al*., 2022), as well as common protein handling considerations such as temperature (Lapidus, 2017) and organic solvents (Pace *et al*., 2004) effect on folding/stability. Furthermore, high concentrations of protein are often required for material formation, limiting the quantity of material that can be produced (Huerta-Lopez and Alegre-Cebollada, 2021).

Protein-based materials can be generated in a range of material types, each suited to specific downstream purposes (Shen *et al*., 2021). Films and coatings display great use as biodegradable food packaging (Chen *et al*., 2019); micro-fibres and yarns developed from spinning processes can be further incorporated into larger materials or tissue scaffolds (Magaz *et al*., 2018); whilst hydrogels formed for protein-based materials are suited to a variety of applications, tailorable on size, shape and underlying structure (Davari *et al*., 2022). Although each material type displays inherent benefits, hydrogels present the most versatile system, enabling preservation of protein folding through the water content pertained within the hydrogel (Huerta-Lopez and Alegre-Cebollada, 2021) in addition to potential accessibility of the proteins to secondary swelled in molecules.

1.2.2 Hydrogels

In the simplest terms, a hydrogel is a polymer network extensively swollen with water (Ahmed, 2015). Hydrogel formation is achieved via extensive crosslinking of monomers to form polymeric networks, resulting in a solution-to-gel transition

occurring at the minimum gelation concentration (MGC). These hydrogels are capable of absorbing and retaining large volumes of water due to the hydrophilic nature of the polymeric networks surface groups (Chai *et al.*, 2017). In recent years, interest in hydrogel research has increased due to the vast array of potential applications, including use as biosensors, diagnostic devices and wound dressings, to name a few (Davari *et al.*, 2022). These applications are possible due to the multiplicity of benefits associated with hydrogels, specifically that of their high water content, flexibility, tailorability and softness (Calo and Khutoryanskiy, 2015). The mechanism of monomer crosslinking can be divided into two categories: physical and chemical, each with distinct advantages and disadvantages.

1.2.2.1 Chemically crosslinked hydrogels

Chemically crosslinked hydrogels are those in which the polymeric network is formed through the covalent linkage of individual monomeric units, forming 'permanent' hydrogels (Hoffman, 2002) (Figure 1.4). Example methods exploited for chemical crosslinking include: chain growth polymerisation (Lee *et al.*, 2016), step growth polymerisation (Lee *et al.*, 2016) and irradiation polymerisation, employing high energy ionizing radiation (Maitra and Shukla, 2014).

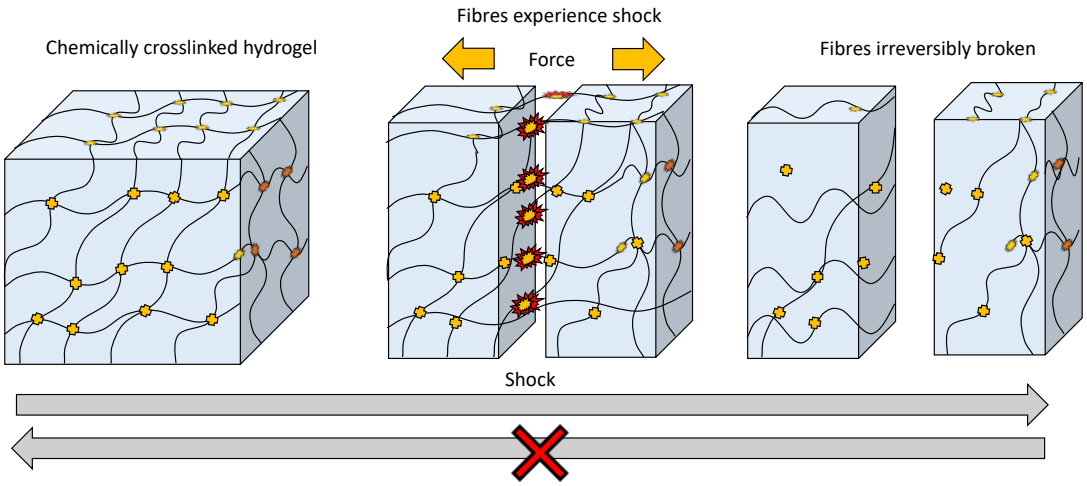

Figure 1.4: Chemically crosslinked hydrogels. When exposed to force, the hydrogel fibres will snap, irreversibly breaking.

Chain growth polymerisation via free radical polymerisation is most commonly achieved with monomers containing carbon-carbon double bonds, and occurs through three steps: initiation, propagation and termination. Firstly, an active radical

centre is produced on the initiator species (produced via homolytic dissociation of weak bonds or redox reactions), followed by the propagation of active sites through the carbon-carbon double bonds forming polymer chains. This sequence terminates with the propagating radicals reacting by combination of two radical species or through disproportionation (Kirtania *et al*., 2021). Chain growth polymerisation is regarded as versatile due to its ability to produce hydrogels with a variety of structures, and is frequently employed to produce natural hydrogels for bioapplications (Varghese *et al*., 2020). However, due to the fast propagation, a very heterogeneous network structure is formed, with little control over the crosslink functionality or number of crosslinked arms per monomer (Ranganathan, 2018). The need for often harmful chemicals for initiation also presents a problem when the resulting material is required for therapeutic use. Step-growth polymerisation can be used in place of chain-growth polymerisation, allowing for more control over the polymerisation sites and therefore a more homogenous hydrogel (Ranganathan, 2018). This form of polymerisation occurs through reactions between two functional groups present on the monomers and crosslinkers, acting via addition or condensation, which results in the final high molecular weight polymer. One such example is the Michael addition polymerisation that occurs between maleimides and sulfhydryl groups (Mejia *et al*., 2021). In particular, Michael addition of maleimides offer a distinct advantage with protein-based crosslinking due to the rarity of cysteines present within many protein structures, therefore enabling site specific introduction of cysteines and minimal requirement for wild-type mutations (Kim *et al*., 2008). One commonly associated issue with step-wise polymerisation is the need to add reactive crosslinking groups, often toxic in nature. This is particularly detrimental for hydrogels with intended therapeutic uses, and requires extensive washing to remove unreacted crosslinkers . Finally, irradiation polymerisation occurs through exposure of monomer units to high energy radiation, such as gamma or electron beams, generating reactive species across the monomer units. These react together, forming crosslinked networks (Saini, 2017). This methodology offers the benefits of controlled frequency of crosslinking and pore size by varying the irradiation dose, whilst also removing the need to add toxic chemicals (Saini, 2017).

However, as with chain growth polymerisation, less control over the polymerisation sites is incurred compared to that of the step growth polymerisation method.

1.2.2.2 Physically crosslinked hydrogels

Physically crosslinked hydrogels are those in which the polymeric network forms through the self-assembly of monomer units (Ranganathan, 2018). In place of covalent linkages, the hydrogel networks form via secondary molecular interactions including hydrogen bonding, hydrophobic interactions, and electrostatic interactions (Akhtar *et al*., 2016) all of which are summed up in Figure 1.5. Within physically crosslinked hydrogels, all crosslinks are reversible and can therefore be returned to the original solution state.

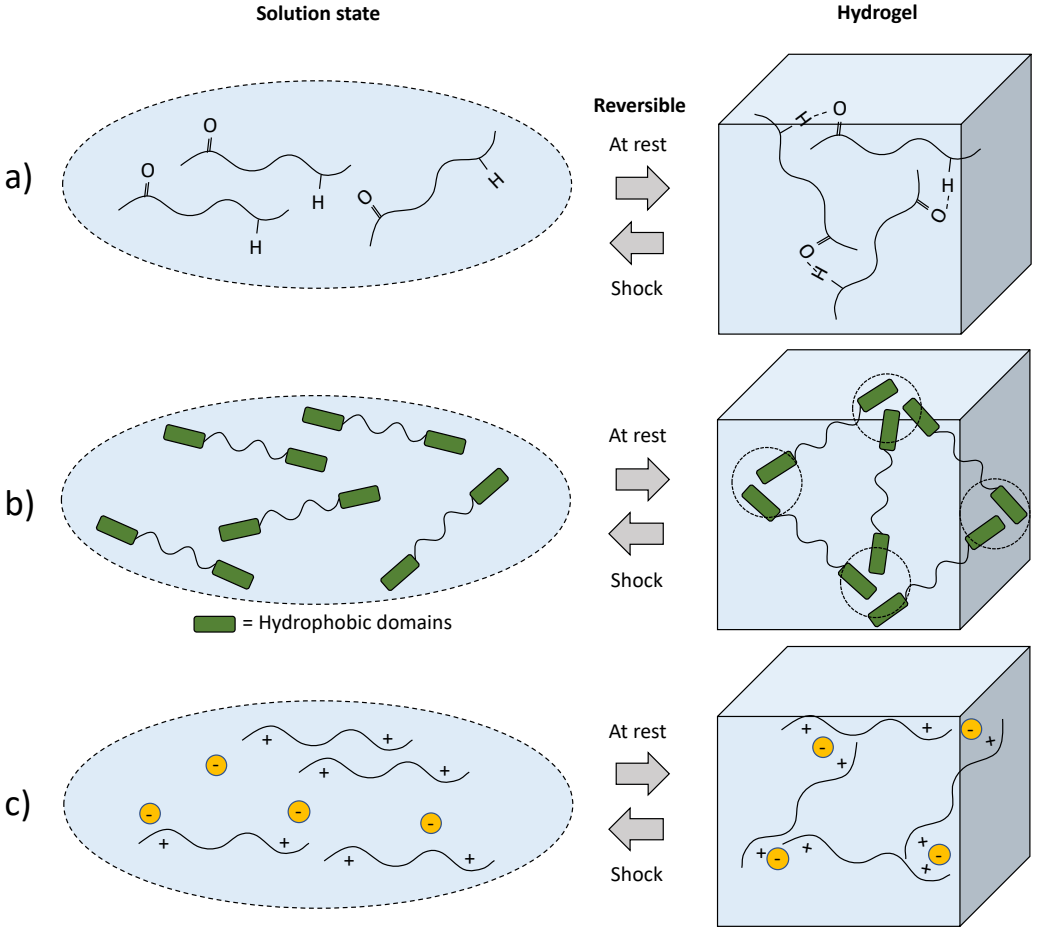

Figure 1.5: Physically cross-linked hydrogels all display properties of reversibility. When at rest the monomers will form a hydrogel. When exposed to shock, the physical crosslinks will break, and can revert back to individual monomer species. a) Hydrogels formed from hydrogen bonding of the monomer units. b) Hydrogel formed through hydrophobic interactions. c) Hydrogel formed through electrostatic interactions.

Utilising hydrogen bonding for crosslinking (Figure 1.5a) instils high strength bonds, reversibility, low toxicity and sacrificial destruction for effective energy dissipation within the hydrogel (Yu *et al*., 2022). However, these benefits are balanced against the reduced stability and crosslinking efficiency that can occur as a result of disturbances of the bonds from the aqueous environment (Long *et al*., 2018). Hydrophobic interactions (Figure 1.5b), introduced through incorporation of hydrophobic sequences within hydrophilic polymer chains, boast enhanced mechanical properties of the resulting hydrogel compared to their chemically crosslinked counterparts, specifically that of toughness resulting from efficient energy dissipation (Tuncaboylu *et al*., 2011). However, increased hydrophobic content of monomer units also reduces solubility in aqueous solutions, an important consideration when high concentrations of monomer units are required for hydrogel assembly (Tuncaboylu *et al*., 2011). Electrostatic interactions (Figure 1.5c) offer many of the same benefits as the other non-covalent crosslinking methodologies, enhancing the overall mechanical properties of the hydrogels (Criado-Gonzalez *et al*., 2020) and instilling potential self-healable and triggerable properties (Talebian *et al*., 2019). Furthermore, electrostatic crosslinks remove the solubility difficulties associated with hydrophobic interaction-based crosslinkers when working within aqueous solutions (Seo *et al*., 2018). Offsetting these benefits, careful consideration into the solution pH is of paramount importance when employing electrostatic crosslinks, whilst the number of electrostatic interactions will have profound implications on the strength of the resulting crosslinks (Seo *et al*., 2018). Therefore, larger crosslinkers may be required to enhance the overall number of electrostatic interactions to increase the crosslink strength. Formation of hydrogels via physical crosslinking is of great interest due to the alleviation of the addition of toxic crosslinking reagents and increased homogeneity of the resulting material (Parhi, 2017). Additional properties of self-healing and tuneability of mechanical properties can also be instilled within the hydrogel design (Liu and Hsu, 2018).

1.2.2.3 Crosslinking considerations for protein hydrogels

To ensure optimal performance of the hydrogel in its desired application, careful consideration of the crosslinking technique is vital. Physically crosslinked hydrogels

result in many desirable properties for biomedical applications. Removal of potential toxic crosslinkers, self-healing properties, enhanced mechanical properties and triggered release of therapeutic reagents are all benefits achievable by employing physical crosslinking (Yu *et al*., 2022) (Talebian *et al*., 2019). As a consequence, when seeking downstream biomedical applications, physically crosslinked hydrogels would likely provide an optimal combination of material properties. Oppositely to physical crosslinking, chemical crosslinking produces strong covalent linkages between the monomers, and as a consequence generally results in a hydrogel with poor mechanical properties. This is due to the lack of energy dissipation occurring when strain is applied to the material, causing the crosslinkers themselves to experience high forces, resulting in crosslinker breakage (Wang and Heilshorn, 2015). However, when looking to capture the energy dissipating mechanism inherent to a protein, chemical crosslinking's strong covalent bonds become vital to developing a hydrogel that effectively captures the proteins energy dissipating mechanism of action. Specifically, chemical crosslinking allows force transduction onto the protein monomer itself (Wu *et al*., 2018), as opposed to physically crosslinked systems which may break apart before strain builds within the hydrogel fibres and, by extension, the proteins. Thus, researchers investigating shock absorbing hydrogels seeking to employ the naturally present energy dissipating mechanisms of proteins most commonly turn to chemical crosslinkers. Unless aimed for use *in vivo*, potentially toxic crosslinkers present limited issues, therefore most of the limitations incurred within chemically linked hydrogels do not impact their use for non-biomedical shock absorbing applications.

1.2.3 Current protein-based energy dissipating hydrogels

Within nature many proteins have adapted to handle physiological forces. Specific examples include: titin, formed of many immunoglobulin-like (Ig) domains, acting as a molecular spring in the sarcomeres of muscle cells (Freundt and Linke, 2019); elastin, a highly crosslinked connective tissue protein found in cardiovascular, pulmonary and other tissues, enabling resilience to repeated physical deformations whilst maintaining tensile ability (Wang *et al*., 2021a); resilin, a structural protein found in insect exoskeletons, similar to elastin in its abundance of natural crosslinks

and presents high resilience (Balu *et al*., 2021) (Chen *et al*., 2013); and talin, a mechanosensory protein found within adhesions (Goult *et al*., 2018). Each of these proteins has undergone extensive optimisation through evolutionary processes, producing molecules with complexity far beyond our current synthetic capabilities (Alberts 2002). Therefore, in recent years, increasing effort has been focused to encapsulate such folded proteins into functional materials. Some examples of this work are described herein, and are summarised in Figure 1.6.

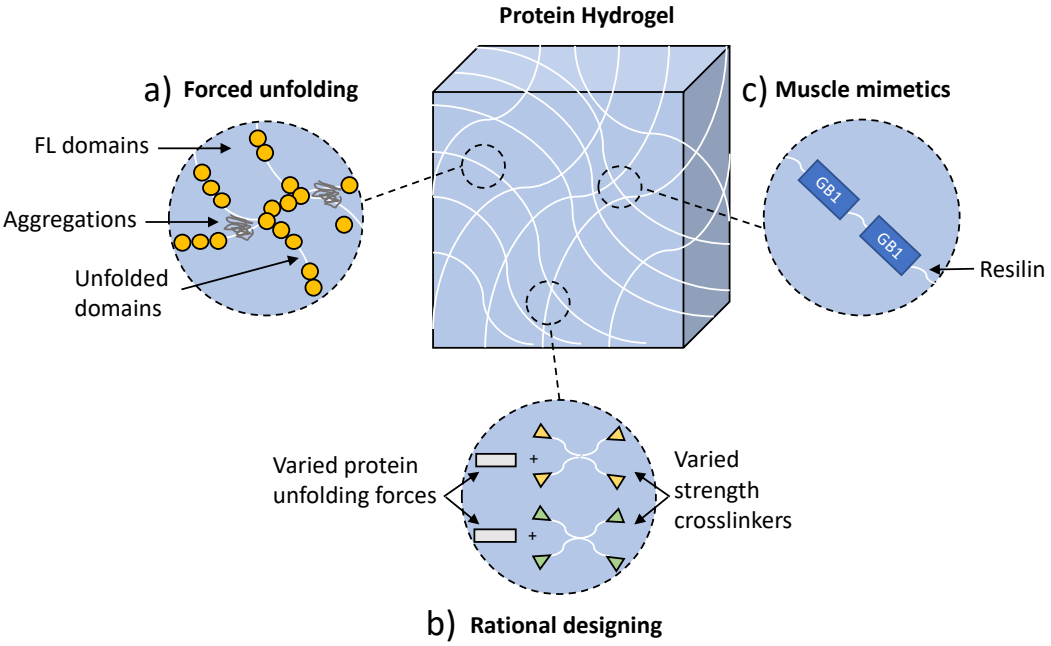

Figure 1.6: Overview of current protein hydrogels developed. a) Fang *et al*. hydrogel utilising forced unfolding of mechanically liable proteins. b) Wu *et al.* investigation of the rational designing of protein-based hydrogels. c) Lv *et al.* muscle mimetic hydrogel.

Fang *et al*. (Fang *et al*., 2013) looked to address previous theoretical estimations from Doi that suggested during hydrogel deformations of up to 100-200 pN, force experienced by protein domains could be as low as a few pN (Doi, 1995). To overcome this issue Fang *et al*. employed an extremely mechanically labile protein as the monomer unit for the hydrogel, ensuring forced unfolding occurred at low strains. Such an occurrence would instil effective energy dissipation, enabling the formation of a highly elastic and tough protein hydrogel. The authors reasoned a material exhibiting these properties had the potential to expand the scope of

hydrogel applications in tissue engineering. A *de novo*-designed protein containing eight ferredoxin-like folded domains was engineered and photochemically crosslinked to produce the hydrogel, illustrated in Figure 1.7.

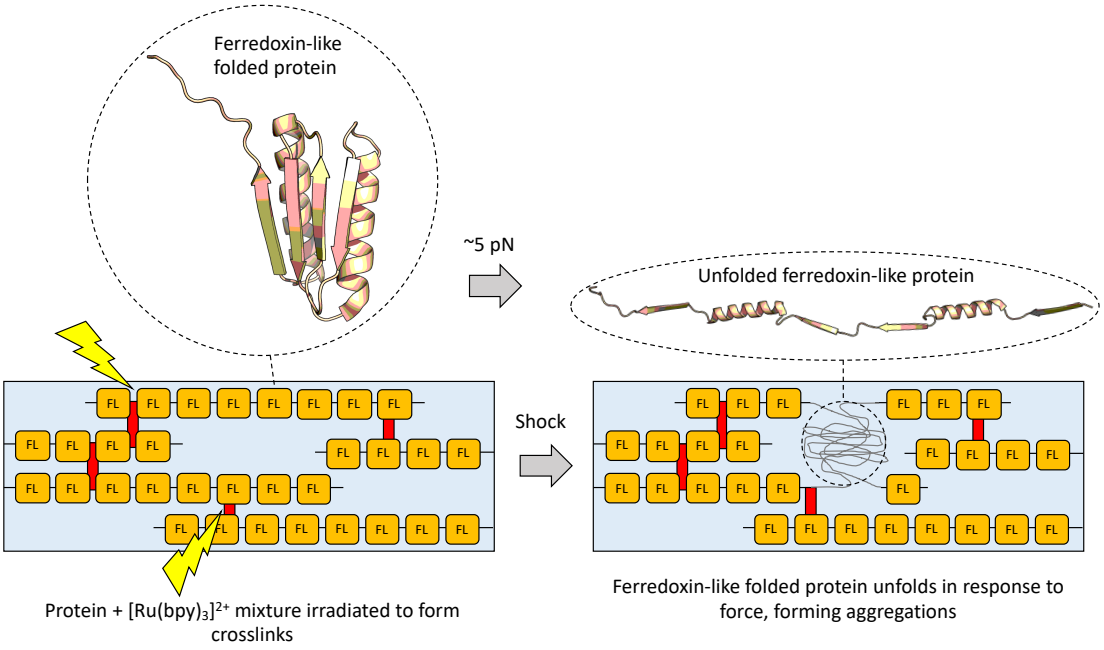

Figure 1.7: Hydrogels formed by Fang *et al* utilising photochemical crosslinking of ferredoxin-like folded domains. (Fang *et al*., 2013)**.** When exposed to forces above 5 pN, the ferredoxin-like folded protein unfolds, dissipating energy in the processes. Protein structures made in PyMOL, Protein Databank (PDB): 2KL8 (Koga et al., 2012).

Ferredoxin-like folded protein domains were chosen due to optical tweezer experiments establishing a low unfolding force of 5 pN (Fang *et al*., 2013), while the chemical crosslinking method of Tris(2,2'-bipyridyl)ruthenium(II) ($[Ru(bpy)_3]^{2+}$) catalysed dityrosine adduct formation was chosen due to its proven success in previous hydrogel formations (Elvin *et al*., 2009) (Elvin *et al*., 2010). Cysteine shotgun experiments utilising the fluorescent dye 5-((((2-iodoacetyl)amino)ethyl)amino) naphthalene-1-sulphonic acid (IAEDANS) confirmed the presence of unfolded domains following swelling; when unfolded, a cysteine introduced at the buried methionine 23 site becomes accessible to the dye, measurable by fluorescence at 490 nm. Material characterisation experiments revealed extension of >5 fold, whilst stress-strain experiments revealed remarkable hysteresis between stretching and relaxation cycles, indicating significant energy dissipation. Furthermore, indications of aggregations forming between unfolded domains was found, producing further

crosslinks (Figure 1.7), likely contributing towards the energy dissipation characteristics observed. Although no downstream application was tested, the authors reasoned the data obtained showed that, through the combination of *de novo* protein design, single molecule measurements and considered biomaterial construction, unique materials could be produced for applications in the biomedical and tissue engineering sector.

Also addressing the theoretical findings of Doi regarding the forces experienced by hydrogel domains (Doi, 1995), Wu *et al*. investigated the rational designing of protein hydrogels to enable predictable mechanical properties (Wu *et al*., 2018). Here, Wu *et al*. determined the predictability of the macroscale hydrogel properties, such as Young's modulus, when varying both protein unfolding force and crosslinker breakage force, with the building blocks of the hydrogel displayed in Figure 1.8.

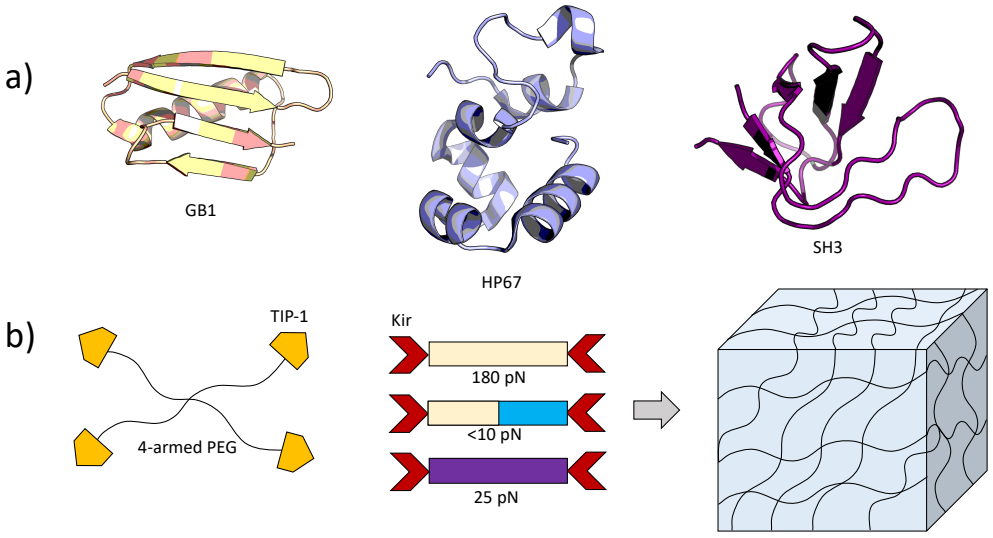

Figure 1.8: The protein building blocks and crosslinker employed in the investigation conducted by Wu *et al*. (Wu *et al*., 2018). a) The three proteins, GB1 (PDB: 3GB1) (Kuszewski *et al.*, 1999), HP67 (PDB: 2RJY) (Meng and McKnight, 2008) and SH3 (PDB: 1PRL) (Feng *et al*., 1994) were used to make the protein blocks shown in b) with a range of unfolding forces. b) The crosslinker consisted of 4-armed polyethylene glycol with the Tax-interacting protein-1 (TIP-1) peptide at each terminal. The TIP-1 peptide could form a chemical crosslink with the Kir peptide attached to both terminals of the protein monomer blocks, resulting in a hydrogel.

Combining single-molecule force microscopy, protein engineering and theoretical calculations, it was demonstrated that the mechanical hierarchy of the crosslinker and the protein monomer unit incorporated within the hydrogel could accurately

predict the mechanical properties of the resulting material. Specifically: the failure stress of hydrogels was correlated with the mechanical stability of the chosen crosslinker, where chemically crosslinked hydrogels demonstrated a higher failure stress than physically crosslinked hydrogels; the hydrogels elasticity and Young's modulus were found to be dependent on the distance between the crosslinker points, determined by the folded vs unfolded state of the protein; and finally the hydrogels toughness was determined by the mechanical hierarchy of the crosslinker and protein monomer, requiring crosslinkers with sufficiently strong bonds to allow force transduction onto the protein monomer unit. Importantly, within this investigation the results suggested, with sufficiently strong crosslinkers, the protein building blocks within the hydrogel could experience forces up to several hundred pN at a strain of 200%. Corroborating the work by Fang *et al.* it was also found swelling of the hydrogel was sufficient to produce forces of several pN, suggesting mechanically labile proteins can unfold from swelling alone. Within the scope of this investigation a host of valuable information required for protein hydrogel design was obtained, however no industrial application was tested.

In an attempt to create a biomaterial mimicking the mechanical properties of muscles, Lv *et al*. engineered artificial elastomeric proteins based on the protein titin (Lv *et al*., 2010). The GB1 domains mimicking the Ig domains found within titin, were combined with the consensus repeat of resilin and photochemically crosslinked utilising the $[Ru(bpy)_3]^{2+}$ tyrosine crosslinking strategy, shown in Figure 1.9.

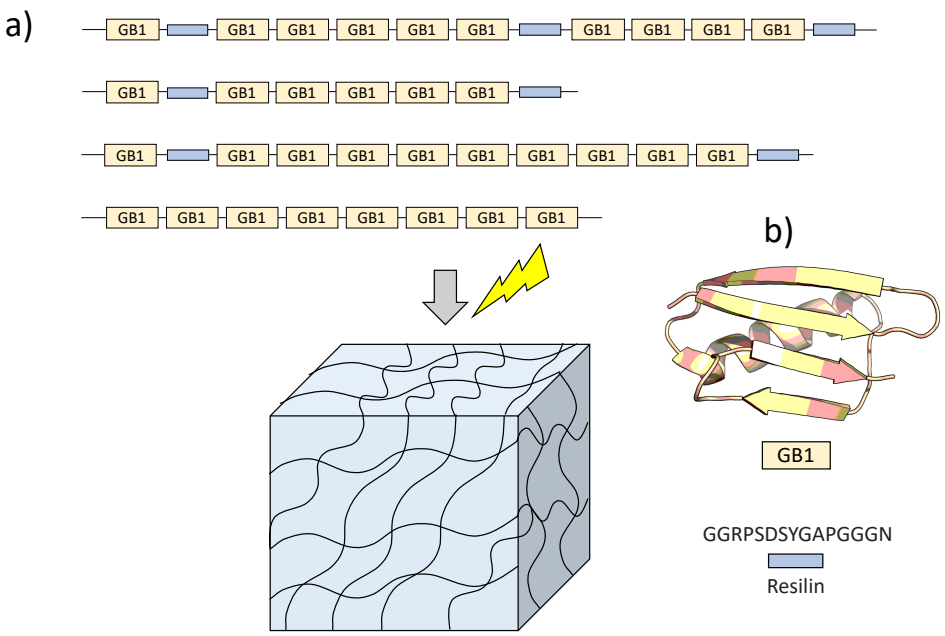

Figure 1.9: Muscle mimetic material developed by Lv *et al*. (Lv *et al*., 2010). a) The elastomeric protein monomers were developed using a combination of GB1 domains (titin Ig domain mimetics) and a consensus repeat of resilin, resulting in a hydrogel upon photochemical crosslinking. b) The PyMOL generated structure of GB1 (PDB: 3GB1) (Kuszewski *et al.*, 1999) and the amino acid sequence of the resilin repeat.

Atomic force microscopy was employed to characterise the mechanical properties of the resulting artificial proteins on the single molecule level, with the unfolding force of 180 pN measured closely resembling that of titin. Hydrogels were produced at concentrations >150 mg/mL of lyophilised protein and presented as transparent. Stress-strain experiments conducted on the hydrogels revealed strains of 135% before breakage, with Young's modulus values of 50-70 kPa. Furthermore, high resilience (ability to deform reversibly without loss of energy (Gosline *et al*., 2002)) was seen in the hydrogels at low strains, whilst at high strains hysteresis was observed suggesting energy dissipation. The authors noted the energy dissipating behaviour observed matched that of myofibrils or myocytes (Helmes *et al*., 1999) (Linke *et al*., 1994), suggesting the hydrogel was acting similar to muscles as a shock-absorbing material. Overall the GB1-resilin hydrogel revealed itself as a promising muscle mimetic material, presenting potential as a scaffold and matrix for artificial muscle.

From the research discussed, alongside further examples (Gao *et al*., 2016, Xiang *et al*., 2020, Haas *et al*., 2022), two key points are apparent; firstly it is possible to produce hydrogels incorporating the energy dissipating mechanisms of protein unfolding; secondly, most applications investigated for these materials focus on the biomedical sector. The focus on biomedical research for protein hydrogels is not surprising due to the distinct biodegradability and biocompatibility benefits often exhibited by protein-based materials. However, with the high levels of complexity observed within shock absorbing proteins, future work should seek to expand the use of protein-based materials into other applications. As discussed within Section 1.1.2, materials displaying as lightweight and durable, whilst also capable of dissipating large quantities of energy could present as next generation materials capable of outperforming the current industry standard materials for applications within the aerospace and armour sectors. Protein hydrogels present all three of these attributes, and may therefore demonstrate great commercial promise within these sectors.

1.3 Talin

1.3.1 Structure

Talin is a large, ~270 kilodalton (kDa) cytosolic protein, consisting of an amino terminal (N-terminal) FERM domain connected via an unstructured linker to the carboxyl terminal (C-terminal) thirteen helical rod domains, terminating in a dimerization domain, displayed in Figure 1.10 (Goult *et al*., 2018). Two isoforms of talin exist, talin1 and talin2, each displaying almost identical sequence lengths (talin1: 2541 aa, talin2: 2540 aa) and identical domain structure (Gough and Goult, 2018). Due to the identical domain structures, the structural aspects described herein apply to both isoforms.

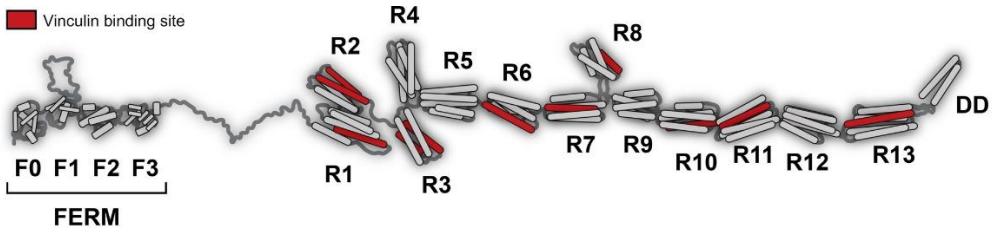

Figure 1.10: Structure of talin with the cryptic vinculin binding sites contained within the rod domains shown in red. Figure taken from Gough and Goult (Gough and Goult, 2018).

The N-terminal FERM domain of ~50 kDa contains four globular segments, termed F0-F3, labelled in Figure 1.10. FERM domains have demonstrated importance in processes of cell adhesion, motility, proliferation and differentiation as well as the facilitation of a multitude of protein-protein and protein-lipid interactions (Elliott *et al*., 2010). Through studies conducted on the ezrin, radixin and moesin (ERM) family of proteins, a consensus FERM domain defined by three segments (F1-F3) in a globular cloverleaf arrangement was established (Pearson *et al*., 2000). In contrast to these consensus FERM domains, the talin FERM domain contains a 30 residue unstructured loop within the F1 segment, as well as presenting an additional segment termed F0 (Goult *et al*., 2010, Elliott *et al*., 2010). Furthermore, an investigation conducted by Elliott *et al*. revealed talin's FERM domain to adopt a non-canonical open/linear structure as opposed to the consensus globular cloverleaf arrangement. Following this work, Zhang *et al*. later revealed a cloverleaf conformation of the talin FERM domain occurring when extended to include the presence of the C-terminal poly-lysine motif (Zhang *et al.*, 2020b). Utilising this new information, Wen *et al*. (Wen *et al*., 2022) proposed a model whereby the talin head can adopt different conformations, imparted through the flexibility of the F1-F2 linker, in response to cellular signals to maximise affinity for binding partners. Talin's FERM domain is responsible for a range of interactions, some of which are discussed in section 1.3.2. Talin's C-terminal region, consisting of thirteen helical rod domains shown in Figure 1.9, is connected to the FERM domain via an 82 amino acid unstructured linker (Bate *et al*., 2012). Here, the C-terminal region extends over 2000 residues, forming 62 α-helices arranged in thirteen four/five α-helical bundles (Goult

et al., 2013b) (Figure 1.10). Within this region two distinct sectors are revealed; a linear sector consisting of five consecutive five α-helix bundles (R9-R13) and a compact sector resulting from the mixture of four-helix (R2-R4, R8) and five-helix (R1, R5-R7) bundles. Importantly, the five helix bundles observed within talin are not common in nature, with the additional N-terminal helix packing against helices 3 and 4 of the bundle resulting in N- and C-terminals located on opposite poles of the protein (Gough and Goult, 2018). This conformation provides an optimal structure for the formation of a linear rod-like chain, in addition to increasing the thermal and mechanical stability of the domains themselves when compared to their four-helix bundle counterparts. The extreme C-terminal dimerization domain connected to R13 is defined as helix 62, and is capable of forming an anti-parallel dimer with the helix 62 of a nearby talin. Although theoretical predictions suggest talin1 and talin2 should be capable of forming heterodimers due to the high level of conservation between helix 62 on each isoform, currently only homodimers have been observed (Gough and Goult, 2018). Through the production of dimers, talin can form an autoinhibited confirmation in the cytosol, wrapping around itself to form a double doughnut with the FERM domains buried within the structure (Goult *et al*., 2013a).

1.3.2 Function

The talin1 isoform displays ubiquitous expression, most abundant in the heart, whilst the talin2 isoform is most abundant in the brain and the heart, with lower levels found elsewhere (skeletal muscle, lungs etc.) (Monkley *et al*., 2000). Each of the isoforms display no known compensation mechanism, with the knockout of one isoform resulting in no increase in the other (Das *et al*., 2014). When discovered almost four decades ago, talin was found to be enriched at cell adhesion sites (Burridge and Connell, 1983). Specifically, these adhesion sites refer to the connections between cells and the extracellular matrix. Importantly, these adhesions are required to resist numerous mechanical challenges including shear forces (cell layer movement) and pulling forces (muscle contraction) (Klapholz and Brown, 2017). Further investigation revealed adhesion sites to consist of four main components; an extracellular matrix ligand, integrin, talin and actin (Liu *et al*., 2015), displayed in

Figure 1.11. Together, these four components define the core of integrin adhesion complexes, including focal adhesions, focal complexes, fibrillar adhesions, invadopodia and hemiadherens (Klapholz and Brown, 2017). These structures play pivotal roles in cell migration (Tang, 2018), bone remodelling (Chastney *et al*., 2021), cancer progression (Augoff *et al*., 2020) among a host of other significant cellular processes.

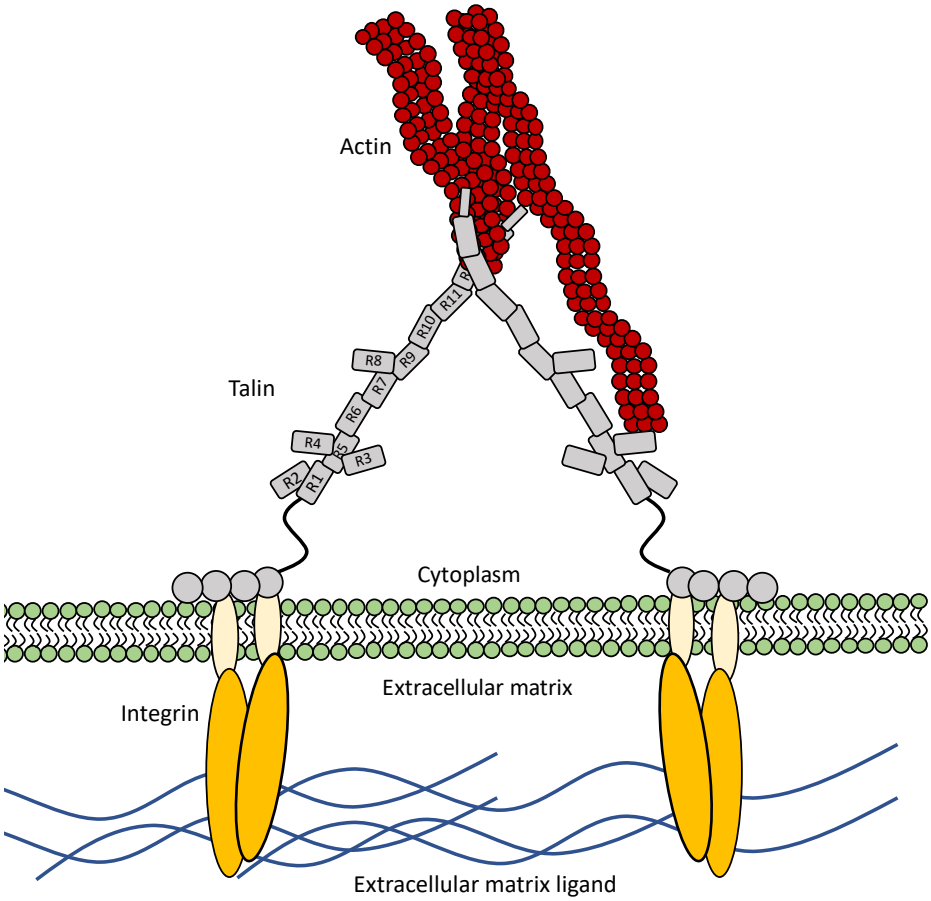

Figure 1.11: The core of integrin adhesion complexes. Actin, talin, integrins and extracellular matrix ligands are shown interacting within the cellular environment.

Here, talin can bind the cytoplasmic tail of the β-integrin subunit via two binding sites, one in the folded F3 domain and one in the R11-R12 domains (Gingras *et al*., 2009), and bind F-actin via three binding sites, one in the F2-F3 domains, one at R4-R8 and one at the R13-dimerisation domain site (Hemmings *et al*., 1996) (Owen *et al*., 2022). Through the actomyosin generated force experienced by talin upon its connection to the extracellular matrix via integrins, talin plays a central role in

mechanotransduction within cells, providing force dependent interactions with a range of binding partners.

1.3.3 Mechanotransduction

To achieve its role in mechanotransduction and mechanosensing, talin employs the thirteen four/five α-helix bundles. Each of the thirteen bundles, when exposed to force, is capable of acting as a mechanochemical switch. Here, the force transduced through the molecule causes breakage of the intermolecular bonds between the bundled α-helices, extending each rod domain into a linear α-helix chain or, with enough force, an extended polypeptide sequence, shown in Figure 1.12. The resulting protein unfolding is an endothermic process, dissipating energy through the breakage of the intermolecular bonds (Schon *et al*., 2017) (Fang *et al*., 2013).

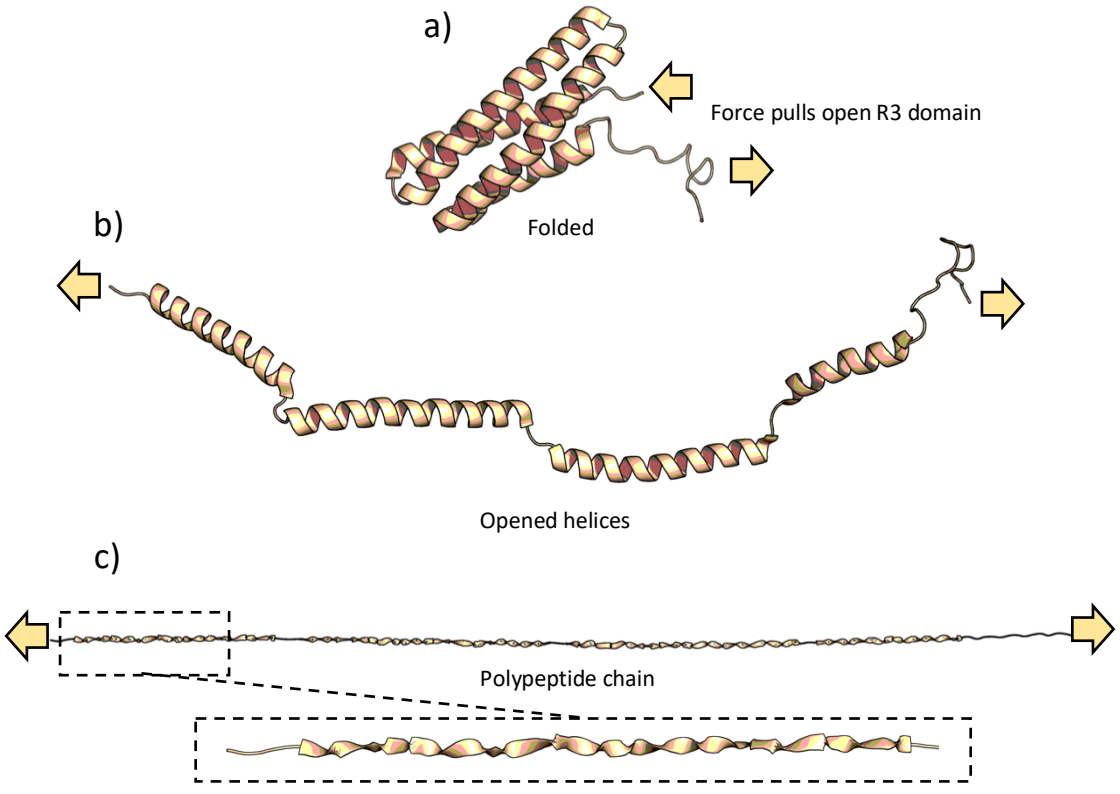

Figure 1.12: Talin R3 domains response to force. a) Below 5 pN R3 remains in folded state as helical bundle. b) When exposed to >5 pN force R3 unfolds first into opened helices. c) When force >25 pN R3 fully unfolds into a polypeptide chain. Images produced in PyMOL using PDB: 2L7A (Goult *et al.*, 2013b).

Extensive characterisation of the unfolding and refolding kinetics of the domains in talin1 was previously performed by Goult, Yan and Schwartz (Goult *et al*., 2018) using high-precision magnetic tweezers (Yao *et al*., 2014). Here, it was found R3 unfolded at the lowest force of ~5 pN due to the presence of a destabilising cluster of threonine residues buried within its hydrophobic core (Goult *et al*., 2013b). Additionally, R3 was shown to present rapid equilibrium in unfolding and refolding, therefore capable of responding rapidly to variations in force. All thirteen rod domains were found to exhibit fully reversible unfolding when forces experienced by the molecule were dropped to <3 pN (Yao *et al.*, 2016). Each of the thirteen domains was also found to exhibit their own characteristic unfolding force between 5-25 pN. When stretched over the physiological relevant extension range, talin was shown to be capable of buffering the force experienced within the force transmission pathway to below 10 pN. Many of the thirteen domains also display cryptic binding sites, allowing for the conversion of mechanical forces into biological signals. One such example is that of the R3 domain, capable of binding the single helix binding site of Rap1-GTP-interacting adaptor molecule (RIAM) only when folded. When unfolded (Figure 1.12b), its two cryptic vinculin binding sites are revealed (Figure 1.10), allowing vinculin binding whilst abolishing RIAM binding (Gough and Goult, 2018) (Goult *et al.*, 2013b). A similar phenomenon is seen across the entirety of the thirteen rod domains, with a total of 11 cryptic vinculin binding sites (Figure 1.10). Talin also presents binding sites for RIAM, phosphatidylinositol bisphosphate (PIP2) (Song *et al*., 2012), cyclin-dependent kinase-1 (CDK1) (Gough *et al*., 2021), paxillin (Atherton *et al*., 2020) and Kidney ankyrin repeat-containing protein-1 (KANK1) (Bouchet *et al*., 2016) when in the folded state. Therefore, the recruitment of binding partners and the subsequent activation of a downstream signalling pathway are dependent on the tension experienced by talin, directly resulting from the environment of the cell. *In vivo* measurements of talin revealed a length between 90-250 nm normally present (Margadant *et al*., 2011), compared to the 50-60 nm measured *in vitro* (Goult *et al*., 2013b), therefore suggesting talin generally presents at least several unfolded domains in its physiological state, exemplifying its common role in mechanotransduction.

1.4 Vinculin

1.4.1 Structure

Vinculin is a 116 kDa multidomain protein consisting of a seven-helical bundle head domain connected to a five-helical bundle tail domain via a proline rich linker (Borgon *et al*., 2004) (Boujemaa-Paterski *et al*., 2020). The structure is split into five distinct vinculin domains (VD), VD1, VD2, VD3, VD4 which make up the head domain, and VD5 defined as the tail domain (Wang *et al*., 2021b). Vinculin's structure is shown in figure 1.13, with each domain labelled. Both VD1 and VD2 have previously been shown to demonstrate large changes in conformation following binding events with talin (VD1) and through dynamic flexibility witnessed in the full length crystal structure (VD2). Furthermore, indications of the vinculin protein as a whole displaying global and dynamic changes in structure upon activation have also been witnessed (Borgon *et al*., 2004). Vinculin is autoinhibited through the interactions of VD1 and VD4 with the tail domain, VD5, masking its binding sites for talin, α-catenin, F-actin and paxillin (Borgon *et al*., 2004).

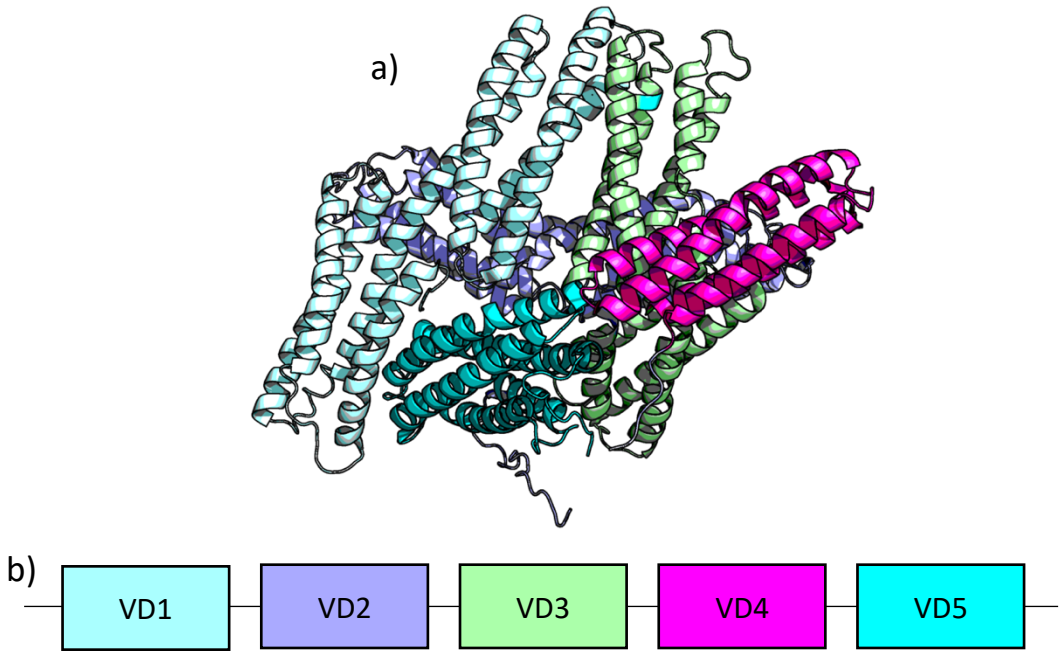

Figure 1.13: Full length vinculin structure. The colours of the rod domains shown within the PyMOL generated image of vinculin in a) (PDB: 1TR2) (Borgon *et al*., 2004) correspond to the domains of the same colour shown in b).

1.4.2 Function

Similar to talin, vinculin is an important component of adhesions. Here, vinculin interacts with a multitude of proteins involved in the mechanotransduction pathway formed between the extracellular matrix and the cell. Specifically, α-catenin and talin bind at the VD1 domain, whilst F-actin and paxillin bind at the tail domain. Through these interactions vinculin provides an important role in stabilising connections within the integrin adhesion complex (Gingras *et al*., 2005), therefore presenting a central role in cell adhesion, maturation and turn over (Wang *et al*., 2021b). The interaction between talin and vinculin occurs at vinculin binding sites, defined by the hydrophobic surface of a single talin amphiphilic helix buried within the hydrophobic core of the rod domains (Papagrigoriou *et al*., 2004). Thus, binding of vinculin to talin can only occur upon unfolding of the rod domains, which in turn liberates VD1 from its autoinhibition via recruitment to the exposed vinculin binding site (Wang et al., 2021b). A total of 11 vinculin binding sites have been elucidated within the talin rod (Gingras *et al*., 2005). Yao *et al*. performed a detailed investigation on the force dependant interactions of VD1 binding to the five vinculin binding sites contained within the talin rod domains R1-R3 (Yao *et al*., 2014). Here, it was found VD1 binding was biphasic, inhibited when forces were maintained below 5 pN and when forces exceeded 25 pN. Each of these forces correspond to important structural states of the R1-R3 domains; specifically at 5 pN R1-R3 remains folded, therefore exposing no vinculin binding sites, whilst at 25 pN, R1-R3 undergoes a helix to coil transition, forming an extended polypeptide chain. Furthermore, within this study it was observed VD1 binding to the talin domains inhibited re-folding upon release of force. Thus, VD1 can provide a valuable tool in manipulating the state of talin, locking the rod domains in an unfolded state.

1.5 Project aims and objectives

Established from the literature discussed in Section 1.1, a material presenting durability, high levels of energy dissipation and a low weight would present as a strong candidate for a next generation shock absorbing material. Such a material could be capable of outperforming the current industry standard materials used for

armour and aerospace projectile capture, presenting great commercial promise. The chemically crosslinked protein-based hydrogels discussed in Section 1.2.3 were each shown to display all three of these properties, revealing protein-based hydrogels as great candidates for next generation shock absorbing materials. However, despite these promising attributes, protein-based hydrogels have almost exclusively been investigated for biomedical applications to date.

This investigation seeks to incorporate the adhesion protein talin into a functional material and probe its performance for non-biomedical shock absorbing applications. Talin contains domains with unfolding forces between 5-25 pN and can therefore act similarly to Fang *et al.*'s mechanically labile protein monomer, in addition to the stronger GB1 domains employed by Lv *et al*. Talin has been shown to repeatedly undergo force induced unfolding and refolding cycles, revealing the perfect protein for a durable energy dissipating material. By incorporating talin into a functional hydrogel material and testing its performance as a shock absorber in a non-biomedical application, this research will reveal a novel application for protein-based materials and elucidate potential future industrial applications. Furthermore, talin's mechanotransduction role within cells provides a host of binding proteins that can be exploited as tools to manipulate the folding state of the talin domains.

Aim 1: Produce the first iteration of a talin shock absorbing material (TSAM)

Objectives:

- Design a recombinant protein incorporating the R1-R3 domains of talin to produce a protein-monomer with a range of unfolding forces. This will address the work from Doi *et al*, Fang *et al*. and Lv *et al*. in Section 1.2.3 who together showed how the unfolding force in combination with the crosslinker strength are important to capturing the proteins energy dissipating mechanism of action.
- Characterise the recombinant protein to ensure the wild-type R1-R3 folding is retained.

- Synthesise maleimide-based crosslinkers to enable the formation of chemically crosslinked hydrogels via step-growth polymerisation, discerned as the best crosslinking option for this system within Section 1.2.2.
- Characterise the relevant physiochemical properties and functionality of the synthesised crosslinkers to determine the limits of their use before being tested on the recombinant protein.
- Develop a streamlined gelation protocol for the formation of the TSAMs
- Evaluate the potential shock-absorbing capacity of the newly formed TSAM to determine suitability for progression onto aim 2.

Aim 2: Characterise the TSAMs structure, properties and determine its shock absorbing performance:

Objectives:

- Characterise the underlying structure of the TSAM and confirm the recombinant protein monomers incorporation into hydrogel fibres.
- Confirm the energy dissipating mechanism of the talin R1-R3 domains within the recombinant protein monomer is retained when integrated into the TSAM hydrogel.
- Determine the TSAMs performance as a shock absorbing material during supersonic impacts to establish a commercial application for the material.

Aim 3: Progress the TSAMs towards industrial applications and begin work on tuning TSAMs shock absorbing performance:

Objectives:

- Investigate three gene expression technologies to determine the optimal expression method, producing the highest yield of protein.
- Establish a single molecule methodology for characterising the unfolding force of recombinant protein monomers, facilitating future TSAM design and development.

- Produce two new iterations of the protein monomer used for TSAM formation. Investigate the tunability of the macroscale properties of TSAMs based on the unfolding forces of the talin domains incorporated into the protein monomer.

Chapter 2: Materials & methods

2.1 Materials

2.1.1. Buffers and media

All buffers and media described in Table 2.1 were prepared using Milli-Q ultrapure water. Adjustments in pH were performed with hydrochloric acid or sodium hydroxide. All reagents were purchased from ThermoFisher Scientific, Melford, Promega or Sigma-Aldrich unless otherwise stated.

Table 2.1: list of buffers and media used

Buffer	Components	pH
10x TAE buffer	400 mM tris-acetate, 10 mM EDTA	8.3
5x sample buffer	18.75 mM Tris-HCl, 2% SDS, 5% β- mercaptoethanol, 0.005% bromophenol blue, 12% glycerol	6.8
Blocking solution	Phosphate buffered saline, 5% skimmed milk powder	-
C-trap™ binding buffer	20 mM $NaH_2PO_4.2H_2O$, 500 mM NaCl, 20 mM imidazole	7.4
C-trap™ elution buffer	20 mM $NaH_2PO_4.2H_2O$, 500 mM NaCl, 500 mM imidazole	7.4
Ellman's reagent buffer	0.1 M $NaH_2PO_4.2H_2O$, 1 mM EDTA	8.0
LCMS solvent A	0.05% trifluroacetic acid (TFA), HPLC grade water	-
LCMS solvent B	80% acetonitrile, 0.045% TFA, HPLC grade water	-
Lysogeny broth (LB)	10 g/L tryptone, 10 g/L NaCl, 5 g/L yeast extract	7.2
Minimal media (2M9) solution A	12.5 g/L $Na_2HPO_4.2H_2O$, 7.5 g/L KH_2PO_4	7.2
Minimal media (2M9) solution B	4.0 g/L glucose, 10.0 ml/L BME Vitamins (100x), 2.0 ml/L $MgSO_4$ (1M), 0.1 ml/L $CaCl_2$ (1M), 1.0 g/L (^{15}N (>98% ^{15}N)) NH_4Cl	-
Nickel buffer A	20 mM tris, 500 mM NaCl, 20 mM imidazole	8.0
Nickel buffer B	20 mM tris, 500 mM NaCl, 500 mM imidazole	8.0
NMR buffer	20 mM phosphate (NaH_2PO_4, Na_2HPO_4), 50 mM NaCl, 2 mM dithiothreitol (DTT)	6.5

Phosphate buffer	50 mM $NaH_2PO_4.2H_2O$, 20 mM NaCl	7.4
Phosphate buffered saline	100 mM Na_2HPO_4, 18 mM KH_2PO_4, 137 mM NaCl, 27 mM KCl	7.4
Phosphate buffered saline, Tween20 (PBST)	Phosphate buffered saline, 5% skimmed milk powder, 0.1% tween-20	-
Q buffer A	20 mM tris, 50 mM NaCl	8.0
Q buffer B	20 mM tris, 1 M NaCl	8.0
Running buffer	50 mM 3-(N-morpholino)propanesulfonic acid (MOPS), 50 mM Tris, 0.1% SDS, 1 mM EDTA	7.7
Size exclusion chromatography buffer	20 mM tris, 150 mM NaCl, 2 mM DTT	8.0
SM6	5.2 g/L NH_4SO_4, 3.83 g/L NaH_2PO_4 3.83 g/L, 4.03 g/L KCl, 1.04 g/L $MgSO_4.7H_2O$, 4.16 g/L citric acid, 0.5 g/L $CaCl_2.2H_2O$, 95 mL/L glycerol, 10 mL 10x SM6 elements	6.8
Terrific broth (TB) solution B	2.31 g/L KH_2PO_4, 12.54 g/L K_2HPO_4	-
Terrific broth (TB) solution A	12 g/L tryptone, 24 g/L yeast extract, 4 mL/L glycerol	7.2
Transfer buffer	For 250 mL: 50 mL 5x commercial transfer buffer, 50 mL methanol, 150 mL milli-Q ultrapure water	-
Tris-buffered saline, Tween20 (TBST)	20 mM Tris, 500 mM NaCl, 0.1% BSA and 0.5% Tween 20	-

2.2 Chemical synthesis

2.2.1 General Experimental methods

Unless otherwise stated all reagents used for synthetic schemes were purchased from commercial sources and used without further purification. A positive pressure of N_2 was supplied during all chemical syntheses. Nuclear magnetic resonance (NMR) spectra for the crosslinkers were obtained on a Bruker AV2 400 MHz spectrometer. The data was processed using Top Spin. NMR chemical shift values are reported in parts per million (ppm) and calibrated to the centre of the residual solvent peak set (s = singlet, br = broad, d = doublet, t = triplet, q = quartet, m = multiplet).

2.2.2 Crosslinker 1 synthesis:

Crosslinker **1** was synthesised as described by Eloh *et al.* (Eloh *et al*., 2016) with minor modifications. Maleic anhydride (1.00 g, 10.00 mmol) was dissolved in dichloromethane (DCM) (15 mL). *N*-butylamine (1.00 mL, 1.00 mmol) was added and the mixture was stirred at room temperature for 1 hour. The solvent was removed under reduced pressure, and the resulting white powder was re-dissolved in acetic anhydride (6 mL). To this solution, sodium acetate (0.50 g, 6.10 mmol) was added, and the mixture was heated at 80°C under reflux for 2 hours. The solution was diluted with distilled water (50 mL) and washed with diethyl ether (3 x 50 mL). The organic layer was collected and further washed with 0.1 M hydrochloric acid (1 x 50 mL) and 0.1 M sodium hydroxide (1 x 50 mL). The organic layer was dried over anhydrous sodium sulphate, filtered, and concentrated *in vacuo* to give the crude product as a colourless liquid. The *N*-butylmaleimide was further purified using silica chromatography, 85:15 (Ethyl acetate:hexane), producing a yellow oil with a yield of 11% (0.17g, 11.00 mM). ^{1}H NMR (400 MHz, 298 K, DMSO-d_6): δ: 7.01 (s, 2H), 3.38 (t, J = 7.1 Hz, 2H), 1.46 (m, 2H), 1.21 (m, 2H), 0.86 (t, J = 7.4 Hz, 3H). This is consistent with previously reported values.

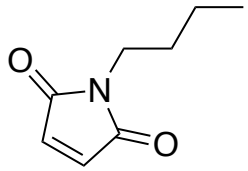

1

Figure 2.1: Chemical structure of crosslinker 1.

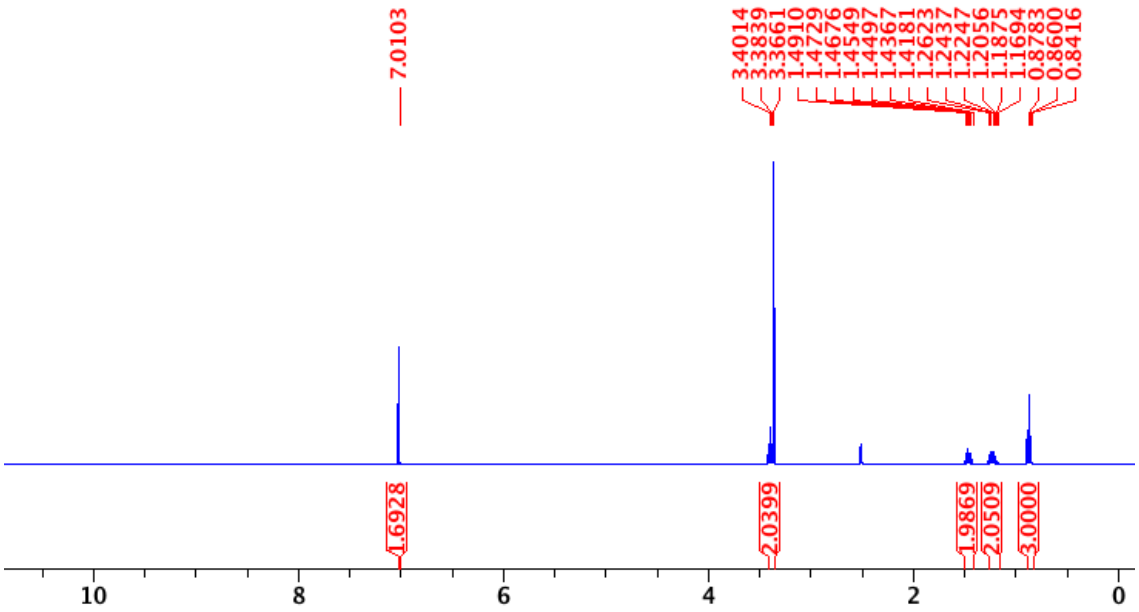

Figure 2.2: ^{1}H NMR spectra of crosslinker 1 in DMSO-d_6 conducted at 298.15 K.

2.2.3 Crosslinker 2 synthesis:

Crosslinker **2** was synthesised as described by Franke and Pingoud (Franke and Pingoud, 1999) with minor modifications. A solution of (0.86 g, 8.80 mmol) of maleic anhydride in 48 mL of ethyl acetate was prepared and cooled to 0°C. Once at 0°C the solution was added dropwise to a stirring solution of (0.35 g, 4.00 mmol) 1,4-diaminobutane in 16 mL of ethyl acetate at 0°C. A white precipitate formed immediately on addition of each drop. The mixture was stirred for a further hour at 0°C. The precipitate was collected via vacuum filtration and washed with ice cold diethyl ether. The precipitate was then added to a solution of (1.60 g, 19.50 mmol) of sodium acetate and 8 mL of acetic anhydride, and the mixture heated under reflux for 3 hours at 80°C. The resulting reaction mixture was poured into 12 mL of water cooled to 0°C and stirred for 2 hours. The crude product was isolated as a brown precipitate by suction filtration with a yield of 17%. No further purification was performed due to the crosslinkers poor solubility. ^{1}H NMR (400 MHz, 298 K, DMSO-d_6): δ: 6.99 (s, 4H), 3.38 (m, 4H), 1.44 (m, 4H). This is consistent with previously reported values.

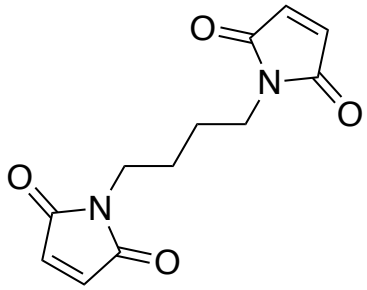

2

Figure 2.3: Chemical structure of crosslinker 2.

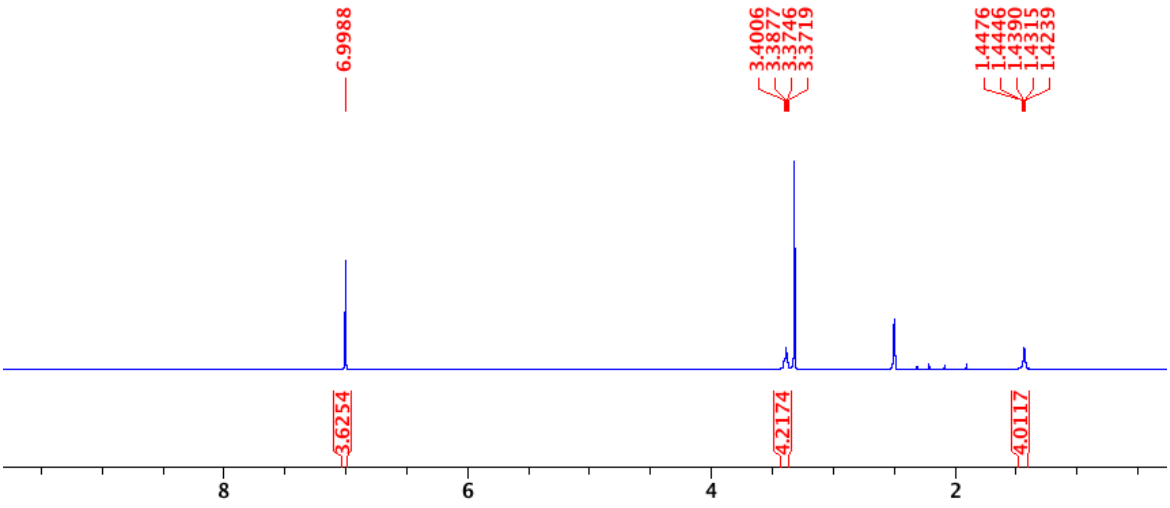

Figure 2.4: ^{1}H NMR spectra of crosslinker 2 in DMSO-d_6 conducted at 298.15 K.

2.2.4 Crosslinker 3 synthesis:

Crosslinker **3** was synthesised as described by Hanlon *et al*. (Hanlon *et al*., 2017) with minor modifications. A solution of maleic anhydride (0.59 g, 6.00 mmol) in anhydrous dimethyl formamide (DMF) (2.43 mL) was prepared under inert atmosphere and cooled to 0°C. Separately, a solution of tris(2-aminoethyl)amine (0.29 mL) in dry DMF (2.04 mL) was prepared under inert atmosphere, and added dropwise to the maleic anhydride solution at 0°C over 30 minutes. The solution was stirred for a further 30 minutes at 0°C. A solution of sodium acetate (0.048 g, 0.60 mmol) in acetic anhydride (0.60 mL) was added to the reaction mixture at room temperature and stirred

overnight at 50°C. The reaction mixture was concentrated using rotary evaporation, resuspended in DCM (50 mL) and washed with saturated brine (6 x 50 mL). The organic layer was collected, concentrated using rotary evaporation, resuspended in DCM (50 mL) and further washed with saturated sodium bicarbonate solution (6 x 50 mL). The organic layer was collected and concentrated using rotary evaporation to obtain the crude product. The crude product was purified using silica chromatography, 85:15 (Ethyl acetate:hexane). The resulting pure yellow crystalline product was dried under vacuum overnight with a yield of 9% (0.21 g, 0.54 mM). ^{1}H NMR (400 MHz, 298 K, DMSO-d_6): δ: 6.98 (s, 6H), 3.38 (t, J = 6.6 Hz, 6H), 2.60 (t, J = 6.6 Hz, 6H). This is consistent with previously reported values.

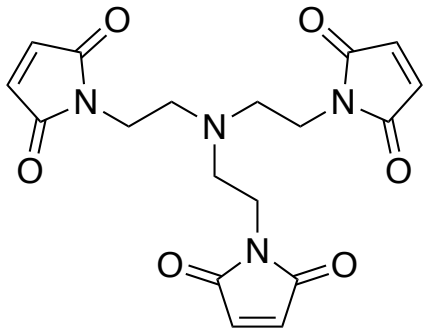

3

Figure 2.5: Chemical structure of crosslinker 3.

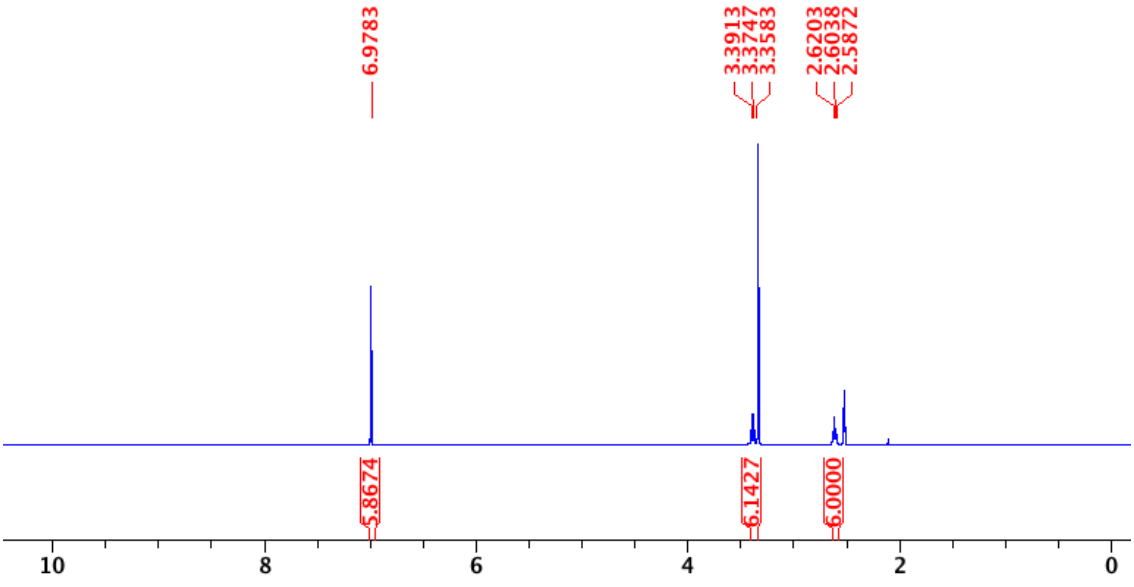

Figure 2.6: ^{1}H NMR spectra of crosslinker 3 in DMSO-d_6 conducted at 298.15 K.

2.3. Chemical crosslinker physiochemical characterisation

2.3.1 Solubility assays using ultraviolet (UV) measurements

Solubility assays used the inherent UV absorbance of maleimide groups at 299 nm to determine the solubility of each crosslinker over a range of concentrations. All crosslinker stock solutions were solubilised in 100% dimethyl sulfoxide (DMSO). Due to the potential for high concentrations of DMSO to impact protein folding, all additions of crosslinkers to aqueous solutions were calculated to produce a final 4% DMSO solution. For each crosslinker, the stock solution required to result in a 1:1 ratio of maleimide to cysteine at a final 4% DMSO solution in 200 mg/mL of pGEL001 was prepared in triplicate. All stock solutions were prepared within 0.5 hours of the first UV measurement. From each crosslinkers triplicate stock solution for 200 mg/mL pGEL001, dilutions were prepared to create triplicate stock solutions required for a 1:1 maleimide to cysteine ratio in pGEL001 solutions of 160, 120, 80 and 40 mg/mL. This resulted in three independently produced stock solutions for each crosslinker at each concentration, allowing for sample preparation errors to present within the obtained dataset. The spectrophotometer (Varian) was blanked with a 4% DMSO phosphate buffer solution before optical density at 299 nm (OD_{299}) measurements on the crosslinkers were conducted. Immediately before UV measurements were conducted, 40 μL of the desired crosslinker stock solution was added dropwise into 1 mL of phosphate buffer in a 1 mL quartz cuvette. Following the complete addition of the crosslinker to the phosphate buffer solution, the cuvette was placed in the spectrophotometer and the OD_{299} measured using the Cary WinUV simple reads software. This process was then repeated on the two remaining stock solutions of the same concentration. The triplicate of OD_{299} readings for each concentration of crosslinker were then averaged and plotted against the respective pGEL001 concentration, with the standard deviation plotted as error bars. This process was repeated for all three stock solutions at each concentration of 80, 120, 160 and 200 mg/mL for crosslinkers **1**, **2** and **3**.

2.3.2 Hydrolysis assays using UV measurements

Hydrolysis assays were adapted from the solubility assays described in Section 2.3.1. Crosslinker solutions were prepared in 100% DMSO and solubilised immediately before addition to the aqueous solution. Additions of the crosslinkers were calculated to result in a final 4% DMSO solution. The lowest concentration of each crosslinker tested In the solubility assays was used in the hydrolysis assays to ensure 1) the highest level of solubility and 2) initial OD_{299} readings were below 1.0. The spectrophotometer (Varian) was blanked with a 4% DMSO phosphate buffer solution. Immediately before UV measurements, 40 μL of the crosslinker stock solution was added dropwise to 1 mL of phosphate buffer in a 1 mL quartz cuvette. This was then placed into the spectrophotometer for ten hours, with the absorbance measured every minute, averaged across a 10 second window using the Cary WinUV Kinetics programme. This process was repeated for each crosslinker. The resulting OD_{299} measurements over the ten hour period were plotted against time for each crosslinker.

2.3.3 NMR-based hydrolysis assay

The stock solution of crosslinker **3** used within this study was prepared as described in the UV hydrolysis assay covered in Section 2.3.2, this time using deuterated DMSO as the solvent. Immediately prior to being placed in the NMR spectrometer (600 MHz Bruker AVANCE III spectrometer equipped with a QCI-P cryoprobe), the crosslinker **3** stock solution was added dropwise to 500 μL of phosphate buffer in deuterated water (D_2O) contained in a microcentrifuge tube. This was quickly transferred into a 5 mm NMR tube and placed into the NMR spectrometer. Locking onto the D_2O solution, tuning, shimming, and determination of the 90° pulse width was subsequently performed, followed by measuring of the 1D proton spectra. Using IconNMR automation software (Bruker), a 1D proton spectra was set to be measured every 20 minutes over a 10 hour period. The resulting 1D proton spectra were Fourier transformed, with required processing applied to all spectra equally using TopSpin software (Bruker). The resulting 1D proton spectra were incorporated into a stack plot to allow visualisation of hydrolysis over time.

2.3.4 Liquid chromatography mass spectrometry (LCMS)

LCMS was employed to determine the ability of each crosslinker to react completely with large biomolecules to form mono-, di- and tri-substituted species for crosslinker **1**-**3** respectively. For this purpose, a KANK1 KN ∆60-68 peptide was used as the biomolecule, with an amino acid sequence of: PYFVETPYGYQLDLDFLKYVDDIQKGNTIKPSVP-C. This peptide was part of previous extensive binding studies within the Goult laboratory, specifically designed to have a C-terminal cysteine to allow for maleimide coupled fluorescent dye labelling in fluorescent polarisation experiments. Therefore due to its well-known solubility properties and terminal cysteine, this peptide presented a perfect biomolecule for testing maleimide coupling with crosslinkers **1**-**3**. The crosslinker stock solutions were solubilised in 100% DMSO. The KANK1 KN ∆60-68 peptide was prepared at a concentration of 100 μM In phosphate buffer and reduced with 5 mM Tris(2-carboxyethyl)phosphine hydrochloride (TCEP). Following a 10 minute reduction period, the respective crosslinker was added to the peptide solution to produce a 10:1 ratio of cysteine to maleimide, with a final solution containing 4% DMSO. A total volume of 5 μL of the peptide-crosslinker solution was loaded into the LCMS for analysis. The LCMS experiments were performed on an Agilent high performance liquid chromatography (HPLC) system connected to a Bruker micrOTOF-Q mass spectrum instrument. All samples were run using LCMS solvent A and LCMS solvent B with a Phenomenex Aeris™ 3.6 μm WIDEPORE XB-C18 LC column. Spectra were analysed using Bruker's Compass Data Analysis software.

2.3.5 Ellman's reagent assays

All Ellman's reagent (ThermoFisher Scientific) assays used within this project were adapted from the protocols described in the manufacturers provided manuals. Ellman's reagent solution was prepared by resuspending 4 mg of Ellman's reagent in 1 mL of Ellman's reaction buffer as per the ThermoFisher Scientific user manual. A volume of 25 μL of Ellman's reagent solution, 1.25 mL of Ellman's reaction buffer and 125 μL of the unknown solution for testing were added into a 1 mL cuvette. This

mixture was then allowed to react for 15 minutes, followed by measuring of the absorbance at 412 nm on the spectrophotometer (Varian) using the simple reads software (Cary WinUV). For the TCEP removal experiments using PD-10 columns described in Section 3.4.3 a standard curve using TCEP concentrations between 0.0-1.5 mM was recorded and plotted. For the assay used to determine the reactivity of crosslinker **3** to TCEP discussed in Section 3.4.1, the unknown mixture was prepared by allowing crosslinker **3** to react with TCEP at a 1:1 maleimide to TCEP ratio for one hour in phosphate buffer at 25°C. Suitable controls consisting of the same concentration of TCEP or crosslinker **3** alone in phosphate buffer following 1 hour incubation at 25°C were also measured. All blanks were performed using either phosphate buffer or 4% DMSO containing phosphate buffer for the TCEP removal experiment and crosslinker **3** reactivity experiment respectively.

2.4 Molecular Biology

All solutions used for molecular biology purposes were sterilised via autoclaving (Prestige Medical) or via filter sterilisation using 0.2 μm filters (Sartorius).

2.4.1 Plasmid constructs

The recombinant proteins found in Table 2.2 are explained in further detail, including relevant design considerations and mutations, within Chapters 3-5.

Table 2.2: List of recombinant protein constructs used.

Protein	Species	Vector	Domains	Source
pGEL001	Mouse	pET151 TOPO	R1-R3	GeneArt, Invitrogen
pGEL002	Mouse	pET151 TOPO	R9-R9-R9	GeneArt, Invitrogen
pGEL003	Mouse	pET151 TOPO	R3-R3-R3	GeneArt, Invitrogen
GFP-VD1	Mouse	pET151 TOPO	VD1	GeneArt, Invitrogen
GFP	-	pET151 TOPO	-	Goult stock
R1-R3	Mouse	pET151 TOPO	R1-R3	Goult stock
R1	Mouse	pET151 TOPO	R1	GeneArt, Invitrogen
Mutated R1	Mouse	pET151 TOPO	R1	GeneArt, Invitrogen
R2	Mouse	pET151 TOPO	R2	Goult stock
Mutated R2	Mouse	pET151 TOPO	R2	GeneArt, Invitrogen
VNp6-pGEL001	Mouse	pSRFDuet-1	R1-R3	Sub-cloned
VNp15-pGEL001	Mouse	pSRFDuet-1	R1-R3	Sub-cloned

2.4.2 Oligonucleotides

Oligonucleotides in Table 2.3 were used to isolate the pGEL001 protein from pGEL001 pET151 TOPO plasmid and allow for subcloning to create the VNp6-pGEL001 and VNp15-pGEL001 pSRFDuet-1 plasmids.

Table 2.3: List of oligonucleotides used.

Protein	Restriction site	Direction	Sequence
VNp6-pGEL001 and VNp15-pGEL001	Bgl2	Forward	GCGGCGGTGGGAGTTGTCCTAGGTA
	Avr2	Reverse	TACCTAGGACAACTCCCACCGCCGC

2.4.3 Polymerase chain reaction (PCR)

PCR was employed to produce the VNp6-pGEL001 and VNp15-pGEL001 pSRFDuet-1 plasmids. This was conducted to isolate the pGEL001 protein whilst also adding Avr2 and Bgl2 restriction sites for subsequent sub-cloning. The PCR reaction mixture used is shown in Table 2.4. All dilutions were performed with sterilised Milli-Q ultrapure water.

Table 2.4: General PCR reaction mixture.

Component	Volume
Template deoxyribonucleic acid (DNA)	2 μL of 1/10 (~30-50 ng)
Forward oligonucleotide	1 μL of 1/10 (0.2 μM)
Reverse oligonucleotide	1 μL of 1/10 (0.2 μM)
dNTPs	1 μL (10 μM)
High fidelity Polymerase	0.5 μL (~1 unit)
10x reaction buffer	5 μL
Milli-Q-water	40.5 μL

Following preparation of the PCR reaction mixtures in sapphire 0.2 mL PCR tubes (Greiner Bio-One), the tubes were placed into a PRIME thermal cycler (Techme) and run using the programme shown in Table 2.5.

Table 2.5: PCR programme used for DNA amplification.

Stage	Time	Temperature °C	Cycles
Initial denaturation	2 minutes	95	1
Denaturation	0.5 minutes	95	30
Annealing	1 minute	55	
Extension	1.5 minutes	68	
Final extension	1.5 minutes	68	1
Final hold	-	4	1

Following completion of the PCR programme, a sample of the resulting DNA was analysed using agarose gel electrophoresis to confirm successful isolation and amplification of the insert.

2.4.4 Agarose gel electrophoresis

Agarose gel electrophoresis was employed throughout the sub-cloning process to confirm successful isolation, digestion or insertion of DNA fragments and vectors. Here, 0.75 g of agarose was dissolved in 75 mL of 0.5x TAE buffer and heated until fully dissolved. The mixture was poured into a gel tank mould, followed by addition of 50 μL of ethidium bromide and insertion of the relevant size comb to produce suitable well volumes. After the agarose gel had set, it was placed into the gel tank (Mupid® One) and covered with 0.5x TAE buffer. DNA samples were loaded and the resulting gel was run at 100 V until suitable DNA separation had occurred. DNA ladder (New England BioLabs) was used to determine DNA fragment size. DNA extraction or PCR purification was performed using a gel extraction kit (QIAGEN) according to the manufacturer's instructions. Measurements of the resulting DNA concentrations were performed by determining absorbance at 260 nm using a nanophotometer® N50 (IMPLEN).

2.4.5 Restriction enzyme digest and ligation

Restriction enzyme digests were performed on the DNA fragment and vector separately. In addition, due to the incompatibility of the restriction enzymes used, each digestion was performed separately. The reaction mixtures used are shown in Table 2.6. The reaction mixture was incubated at 37°C for 1-3 hours depending on the restriction enzyme employed. Following completion and confirmation of the digestion using agarose gel electrophoresis, the digestion mixture was purified from the agarose gel using a gel extraction kit (QIAGEN).

Table 2.6: Restriction digest reaction mixture.

Component	Volume
DNA	10 μL (~0.5-2 μg)
Restriction enzyme	2 μL (~10-20 units)
10x reaction buffer	10 μL
Milli-Q-water	48 μL

Ligation of the resulting gel extracted DNA samples was conducted overnight at 4°C using the reaction mixture shown in Table 2.7. Here, a 1:3 ratio of insert to vector was used.

Table 2.7: Ligation reaction mixture.

Component	Volume
Vector	1 μL (100-200 ng)
Insert	3 μL (100-300 ng)
T4 DNA ligase	1 μL (0.1-1.0 units)
T4 DNA ligase buffer	1 μL
Milli-Q-water	5 μL

2.4.6 Preparation of competent *Escherichia coli* (*E. coli*) cells

Competent *E. coli* cells were generated using the calcium chloride methodology. DH10-β or BL21(DE3) *E.coli* cells were streaked onto an LB agar plate containing no antibiotic and incubated overnight at 37°C. The following morning a single colony was selected and used to inoculate 40 mL of LB in a 500 mL non-baffled flask. This culture was incubated at 37°C, 200 rotations per minute (rpm) until an OD_{600} of 0.3 was reached. Once the desired OD_{600} value had been reached, the culture was incubated at 4°C for 10 minutes. The culture was then centrifuged at 3,000 rpm for 10 minutes at 4°C. The supernatant was discarded and the pellet resuspended in 20 mL of 0.1 M $CaCl_2$ cooled to 4°C, and the resulting solution incubated at 4°C for 20 minutes. Following the elapsed incubation time, the culture was centrifuged at 3,000

rpm for 10 minutes at 4°C. The resultant supernatant was discarded and the pellet resuspended in a 2 mL solution of 0.1 M $CaCl_2$ and 15% glycerol, aliquoted and frozen in liquid nitrogen for storage at -80°C.

2.4.7 DNA transformations

DNA required for molecular biology applications was transformed into DH10-β *E. coli* cells, whilst DNA ready for recombinant protein expression was transformed into either BL21 (DE3) or BL21 (DE3) pLysS *E. coli* cells. Transformations were conducted by pipetting 2 μL of DNA into 40 μL of cells and incubating at 4°C for 30 minutes. Following this time, the cells were heat shocked at 42°C for 70 seconds to promote uptake of the DNA. The cells were then incubated at 4°C for a further 5 minutes, before 350 μL of LB was added. This mixture was then incubated at 37°C for 1 hour. Following the 1 hour incubation, the cells were plated onto LB agar plates containing the relevant antibiotic for selection pressure. Specifically, ampicillin for the pET151 TOPO plasmid constructs and chloramphenicol for the pSRFDuet-1 plasmid constructs. The resulting plates were incubated overnight at 37°C to allow bacterial colony growth.

2.4.8 DNA validation

Following transformation of DNA into DH10-β *E. coli* cells and overnight incubation at 37°C, a single colony was picked and placed into 5 mL of LB with the relevant antibiotic in a 50 mL falcon tube to produce an overnight culture. The overnight culture was incubated at 37°C in a shaking incubator at 200 rpm. DNA was subsequently extracted from the overnight using a QIAprep miniprep kit (QIAGEN) as per the manufacturer's instructions. The DNA sequence was confirmed through Sanger sequencing (Eurofins Genomics).

2.5 Protein expression

All expression media was sterilised in autoclaves prior to use. The ampicillin, chloramphenicol and Isopropyl β-D-1-thiogalactopyranoside (IPTG) were sterilised

using 0.2 μm syringe filters (Sartorius). Additionally, any reagent added to the cultures within any expression method were sterilised with 0.2 μm filters.

2.5.1 Sodium dodecyl sulphate poly-acrylamide gel electrophoresis (SDS-PAGE)

SDS-PAGE was employed to analyse the molecular weight and purity of proteins at various stages of both expression and purification procedures. The 10% acrylamide/BIS separating and 4% acrylamide/BIS stacking gel components were prepared according to Novex® gel casting instructions (ThermoFisher Scientific) and cast within 1 mm Novex® gel cassettes (ThermoFisher Scientific). The gels were stored at 4°C until ready for use. Samples were prepared by addition of 5x sample buffer, followed by incubation at 95°C for 2 minutes. The gels were run at 200 V, 400 mA until separation of the protein bands had been achieved. Pre-stained protein ladder was loaded to allow for molecular weight determination of proteins within the loaded samples. Coomassie blue stain and destain solutions were used to visualise the proteins within the gels.

Yields of protein from cultures were determined using ImageJ analysis software (Schneider *et al.*, 2012). Here standard samples of bovine serum albumin (BSA) were run on the same gel as unknown concentration samples to produce intensity values that corresponded to known protein concentrations. The intensity of the unknown concentration bands could then be compared to the intensities of the known concentrations of the BSA standard sample bands to quantitate an approximate yield via the differences in the quantitated intensity between the samples.

2.5.2 Starter cultures

For all shake flask based bacterial expression methods discussed herein, an overnight culture was produced to inoculate cultures used for protein expression. This process first consisted of a DNA transformation into BL21 (DE3) or BL21 (DE3) pLysS *E. coli* cells as explained in Section 2.4.7. The following day a single colony was picked from the transformation plate and used to inoculate 10 mL of LB containing the relevant antibiotic. This culture was then incubated at 37°C overnight in a shaking incubator

at 200 rpm. The resulting overnight culture was used the following morning to inoculate cultures for expression trials or large scale expression methods. For several constructs a cryo-stock was produced consisting of 600 μL of overnight culture and 600 μL of sterilised 50% glycerol solution and stored at -80°C. This cryo-stock could be used in place of bacterial colonies to produce overnight cultures when necessary.

2.5.3 Expression trials

When working with a new construct for the first time, expression trials were conducted to confirm and optimise the recombinant protein expression. These trials were performed by inoculating 10 mL LB cultures in falcon tubes containing the relevant antibiotic, with a volume of overnight culture (produced as per Section 2.5.2) that resulted in an OD_{600} of 0.05. The inoculated cultures were then grown at 37°C in a shaking incubator at 200 rpm until an OD_{600} between 0.6-0.8 was reached (measured using a spectrophotometer (Varian)). At this time a pre-induction sample was taken, followed by induction of the cultures using a range of IPTG concentrations (200-1000 μM) and a range of subsequent growth temperatures (18-37°C). Samples of 100 μL were then taken at time points, commonly at 1 hour, 3 hours and overnight, with the OD_{600} measured and the sample centrifuged at 13,000 rpm for 5 minutes. The resulting pellet was resuspended in a volume of nickel buffer A calculated to result in 100 μL per 1 OD_{600} unit. The samples were diluted with 5x sample buffer and run using SDS-PAGE at 200 V, 400 mA for 30-40 minutes depending on the recombinant proteins size. Following Coomassie staining of the gel, direct comparisons between the pre- and post-induction time point samples were drawn, confirming expression of the protein. Additionally, using ImageJ analysis software, intensities of the bands could be calculated allowing for determination of the conditions that resulted in the highest yield of protein.

2.5.4 Unlabelled protein expression and harvesting

Due to the large quantities of protein required for this project multiple expression systems were investigated to optimise yields. Comparisons of the results obtained

from the three methodologies for unlabelled protein expression can be found in Section 5.2. The methodology for each tested expression system is outlined herein.

2.5.4.1 Traditional Shake flask expression

Traditional shake flask expression utilises overnights prepared as described in Section 2.5.2. Here, 750 mL of LB containing the relevant antibiotic was autoclaved in 2.0 L baffled flasks. Each 750 mL culture was inoculated with a volume of overnight that resulted in an OD_{600} of 0.05. following inoculation, the cultures were grown at 37°C, 200 rpm until an OD_{600} of 0.6-0.8 was reached. Induction was then performed, most often with 1 mM of sterilised IPTG (concentration determined from expression trials). Following induction, the cultures were then incubated at either 37°C for three hours or 18°C overnight at 200 rpm. For all pGEL constructs 18°C overnight was used as the incubation condition. After the pre-determined incubation time had elapsed, the cultures were harvested using a Beckman Coulter Avanti centrifuge by centrifugation at 6,000 rpm for 10 minutes at 4°C. The pellets were immediately resuspended in nickel buffer A, using 25 mL per pellet obtained from 1.5 mL of harvested culture. If protein degradation was found to occur from previous expression attempts, a single protease inhibitor tablet was also added to the resuspended pellet. The resuspended pellets were then stored in 50 mL falcon tubes and frozen at -20°C until ready for purification.

2.5.4.2 VNp expression system

To investigate optimisation of pGEL001 yields, a patent protected expression system developed within the Mulvihill laboratory was employed (Patent application number: GB2118435.3) (Eastwood *et al*., 2022). The mechanisms by which this system work are described in Section 5.2.1. Overnight cultures were prepared as described in section 2.5.2 using TB media in place of LB media. For small scale expression, 25 mL of TB media was autoclaved in 500 mL non-baffled flasks and inoculated with 250 μL of overnight. For large scale expression, 150 mL of TB media was autoclaved in 2.0 L flasks and inoculated with 1.5 mL of overnight. From this point onwards, both small scale and large cultures were treated identically. Immediately following inoculation the flasks were incubated at 37°C at 200 rpm until an OD_{600} of 0.8 was reached, at

which point IPTG was added at a final concentration of 20 μg/mL. The cultures where subsequently incubated overnight at 37°C, 200 rpm. During culture growth both pre- and post-induction samples were collected. Specifically, 100 μL of sample was collected with the OD_{600} measured. The samples were then centrifuged at 13,000 rpm for 5 minutes. The resulting pellet was resuspended in a volume of nickel buffer A calculated to result in 100 μL per 1 OD_{600} unit, whilst the remaining supernatant was taken to test for exported proteins. The samples were diluted with 5x sample buffer and run using SDS-PAGE as described in section 2.5.1. Harvesting of the culture was performed by centrifuging the culture at 4,000 rpm for 5 minutes in a Beckman Coulter Avanti centrifuge. The media sample containing the exported protein in vesicles was isolated from the pellet. The media was then stored at 4°C until ready for purification.

2.5.4.3 Bioreactor expression

The use of three fed-batch Multifors (Infors) 1.0 L bioreactor systems was also investigated to optimise pGEL001 yields. Information regarding the resulting yields as well as a discussion of the benefits and drawbacks of this system can be found in Section 5.2.2. The 5-day process required for bioreactor growth is described below.

Day 1: an overnight culture was prepared as described in section 2.5.2, using TB media in place of LB media.

Day 2: 500 mL of SM6 media was introduced into the clean bioreactor vessels and autoclaved. Following autoclaving, the bioreactors were set up ready for inoculation. This process was performed as follows: Firstly, the bioreactors were connected to their consoles, with the temperature sensor, condenser (attached to gas lines) and air filter tube all connected to the vessel. The air flow was set to 0.5 mL/min and the temperature to 30°C. A shot of the relevant antibiotic was added to the media to reduce chances of contamination. Following these steps the pH probe was calibrated and inserted into the vessel. The acid (25% sulfuric acid), base (25% ammonia) antifoam (Polypropylene glycol) and glycerol (80% w/w) pumps were then primed,

and the motor connected. The pO_2 (dissolved oxygen) probe calibration was performed, followed by setting of the stirrer to 500 min^{-1}. Alongside this process an overday culture was prepared by adding 100 μL of overnight to 10 mL of TB media containing the relevant antibiotics, which was then incubated for 6 hours at 30°C, 250 rpm. Following the 6 hour incubation period, 1 mL of the overday culture was added to 200 mL of SM6 media containing the relevant antibiotics in a 1 L baffled flask, and incubated at 37°C, 250 rpm overnight.

Day 3: the pH (set to pH 7) and antifoam controls were turned on, another shot of the relevant antibiotic was added, the batch was started on the console and the SM6 media within the bioreactor vessels was inoculated using 60 mL of the overnight culture prepared on day 2. The pO_2 was then set to 40% on the total flow setting with the minimum-maximum rpm set to 900-1600 rpm and total flow to 1.5-2.0 L/min.

Day 4: when both the stirrer and airflow were maxed out, the temperature was dropped to 25°C. Induction of the culture was performed when the OD_{600} value of 18 was reached using 4.5 mL of 4.31 g/L IPTG, at which point 4 mL of 1M $MgSO_4.7H_2O$ was also injected into the culture and the glycerol feed was started.

Day 5: in the morning another shot of the relevant antibiotic was added to the culture, in addition to 2.5 mL of 232.8 g/L $NaH_2PO_4.2H_2O$. When samples of the culture taken every 3 hours began to reveal a plateau of growth, normally reached at an OD_{600} 120-160 at the end of day 5, the batch was stopped and the culture harvested. Harvesting was performed by centrifuging the culture at 6,000 rpm for 15 minutes, with the media removed. This process was repeated on the same batch of media until it appeared translucent. Resuspension of the pellet was performed using nickel buffer A, using 10 mL of buffer per 1 g of pellet. The resuspended pellet was then stored at -20°C until ready for purification.

2.5.5 Isotopically labelled protein expression for NMR

For Isotopically labelled protein expression, starter cultures were prepared as described in Section 2.5.2. The following morning, 9 mL of starter culture was used to inoculate four flasks containing 750 mL of sterile LB with 100 μg/μL ampicillin in 2 L baffled flasks. The cultures were then incubated at 37°C and agitated at 200 rpm until an OD_{600} of 0.6-0.8 was reached. At this stage the media was centrifuged at 4,000 rpm for 10 minutes at 4°C, ensuring sterile conditions were maintained. The pellets were washed and combined together in 200 mL of sterile 2M9 minimal media containing 100 μg/μL ampicillin and centrifuged again at 4,000 rpm for 10 minutes at 4°C. The resulting pellets were gently resuspended in 750 mL of 2M9 minimal media (with the appropriate isotopically labelled source) containing 100 μg/μL ampicillin and incubated at 37°C, 200 rpm for one hour. Immediately upon completion of the one hour incubation period, 1 mM sterile IPTG was added to the culture and placed at 20°C, 200 rpm overnight. The following day the culture was harvested by centrifugation at 6,000 rpm for 10 minutes at 4°C. The resulting pellets were resuspended in a total of 25 mL of nickel buffer A.

2.6 Protein purification

2.6.1 Cell lysis

On the day of purification, protein pellets suspended in 25 mL of nickel buffer A were removed from storage at -20°C and thawed. Following complete thawing, the pellets were stored on ice. Cell lysis was performed using a Soniprep 150 sonicator (MSE) at 50% amplitude using cycles of 20 seconds on followed by 40 seconds off. The entire sonication was performed with the samples kept on ice. After lysis of the cells, cell debris were removed through centrifugation at 20,000 rpm for 40 minutes at 4°C. Here, the supernatant containing soluble proteins was removed and filtered with a 0.45 μm syringe filter (Sartorius) for purification. Samples were taken of both the pellet containing cell debris and insoluble proteins as well as the supernatant for analysis using SDS-PAGE as described in Section 2.5.1.

2.6.2 Affinity-tag chromatography purification

All 6x polyhistadine tag (His-tag) containing proteins were purified using affinity-tag chromatography. Two methods were employed for this purpose, namely; immobilised nickel ion affinity chromatography, or nickel resin batch purification. Both methods are outlined within this section. Purification with these methods was achieved through the efficient and specific capture of the His-tag of proteins via Ni^{2+} ions contained within the HisTrap HP column and nickel resin, due to the 6x polyhistidine region forming high affinity complexes with the Ni^{2+} ions.

2.6.2.1 Immobilised nickel ion affinity chromatography

Following the cell lysis procedure described in Section 2.6.1, immobilised nickel ion affinity chromatography was performed using a HisTrap HP column (Cytiva) connected to an AKTA start system (GE healthcare) controlled with Unicorn™ software. Here, the HisTrap HP column was equilibrated with nickel buffer A ready for application of the supernatant. Loading of the filtered supernatant was conducted at a constant flow rate of 2 mL/min. Following complete loading of the supernatant and washing with nickel buffer A to remove unbound protein, a gradient elution was performed using increasing percentages of nickel buffer B. The high concentration of imidazole within the nickel buffer B competes with the His-tag of the protein for complexation with the Ni^{2+} of the HisTrap HP column, leading to elution of the His-tagged protein. The resulting elution profile was monitored using UV measurements at 280 nm, revealing the presence of proteins containing aromatic residues such as tryptophan and tyrosine. Elution's corresponding to peaks in the UV readings were subsequently prepared for SDS-PAGE analysis to determine the molecular weight and purity of the protein as described in section 2.5.1.

2.6.2.2 Nickel resin batch purification

The supernatant obtained from the cell lysis procedure described in section 2.6.1 was applied to a suitable volume of washed HisPur™ Ni-NTA resin (ThermoFisher Scientific). The resultant mixture was left to agitate at 4°C for one hour. Following this time period, the mixture was centrifuged at 3,000 rpm for 3 minutes at 4°C to

pellet the nickel resin. The supernatant was subsequently removed and discarded, with the nickel resin washed in 20 mL of nickel buffer A. The mixture was once again centrifuged at 3,000 rpm for 3 minutes at 4°C, and washed in 20 mL of nickel buffer A. This washing procedure was repeated to result in a total of five washes of the nickel beads. Upon completion of the final wash, the nickel resin was isolated in a gravity flow column and the bound proteins eluted using nickel buffer B. Samples were taken at various stages of the process, including the fractions collected from the elution, and prepared for SDS-PAGE analysis as described in section 2.5.1.

2.6.3 Buffer exchange and TEV cleavage

Following completion of the affinity-tag chromatography purification and SDS-PAGE analysis, the fractions containing the protein of interest were combined for buffer exchange. The combined fractions were inserted into the relevant molecular weight cut-off (mwco) dialysis membrane and when removal of the His-tag was required for future experimentation, tobacco etch virus (TEV) protease was also added to the solution. The membrane was then dialysed in the respective buffer required for the next step of purification or desired experiment. Dialysis was conducted at 4°C overnight. Following the final buffer exchange proteins were flash frozen in liquid nitrogen and stored at -20°C or stored as a solution at 4°C.

2.6.4 Ion exchange chromatography

Ion exchange chromatography separates proteins based on their charge, and was utilised within this project to separate TEV and the cleaved His-tag from the cleaved protein, or as an additional purification step. Ion exchange chromatography was performed using HiTrap Q HP (Cytiva) or HiTrap S HP columns (Cytiva) connected to an AKTA start system (GE healthcare) controlled with Unicorn™ software. Selection of the anion exchange column (HiTrap Q HP) or cation exchange column (HiTrap S HP) was determined through calculation of the proteins theoretical isoelectric point using ExPASy's protein parameters tool, protparam. The required column was equilibrated in Q or S buffer A. The proteins for ion exchange chromatography were buffer exchanged as per Section 2.6.3 into Q or S buffer A and filtered using a 0.45

μm syringe filter (Sartorius) immediately prior to loading onto the column. Loading of the proteins was conducted at a constant flow rate of 2.5 mL/min. Following completion of loading, washing of the column was conducted using Q or S buffer A to remove unbound protein. A salt gradient was subsequently performed, using increasing percentages of Q or S buffer B to elute the bound proteins from the column. Here, the increasing concentration of salt competes with the protein for the charged resin within the column, leading to the protein eventually eluting above a certain salt concentration. The resulting elution profile was monitored using UV measurements at 280 nm. Fractions collected from the elution corresponding to peaks in the UV readings were subsequently prepared for SDS-PAGE analysis to determine the molecular weight and purity of the protein as described in section 2.5.1. Finally buffer exchange was performed as described in section 2.6.3 into the buffer required for future experiments. Following buffer exchange, the protein concentration was measured, and proteins were either frozen in liquid nitrogen and stored at -20°C or stored as a solution at 4°C until ready for use.

2.6.5 Size exclusion chromatography (SEC)

SEC separates protein by size due to the differential interaction of the varied size proteins with pores contained in the column. Specifically, large proteins do not enter pores within the columns matrix and therefore elute off the column first, whilst smaller proteins diffuse into the pores causing their flow to be retarded and therefore elute slower. SEC experiments for protein purification purposes were performed using a 16/60 Sephacryl S-300 column connected to an AKTA explorer system controlled with Unicorn™ software. Following buffer exchange into phosphate buffer, described in Section 2.6.3, proteins were loaded onto the column (pre-equilibrated in phosphate buffer) at a constant flow rate of 1 mL/min. Fractions of 1 mL were subsequently collected form the column, with protein presence monitored using UV measurements at 280 nm. Fractions corresponding to peaks in the UV readings were subsequently prepared for SDS-PAGE analysis to determine the molecular weight and purity of the protein as described in section 2.5.1. Fractions containing the protein of interest were combined and stored until ready for use.

2.6.6 Protein concentration measurements

Protein concentrations were determined using a nanophotometer® N50 (IMPLEN). Measurements were performed at 280 nm using molecular weight and extinction coefficients calculated with the ExPASy protparam tool.

2.6.7. Western blots

All western blots used the N-terminal anti-His peroxidase mouse monoclonal antibody (Sigma). Samples of interest were first run using SDS-PAGE as described in Section 2.5.1, with the resulting non-Coomassie stained gel and polyvinylidene difluoride (PVDF) membrane (Bio-Rad) washed in methanol and soaked in transfer buffer. A semi dry transfer (Bio-Rad) was performed at 15 V, 400 mA for 20 minutes. Following the successful transfer of the protein onto the PVDF membrane, the membrane was blocked in blocking buffer at 25°C for one hour. After the blocking time had elapsed, the anti-His antibody as a 1/1000 dilution in 10 mL phosphate buffered saline with 5% skimmed milk powder was applied to the membrane and incubated at 4°C overnight. The next morning, the PVDF membrane was washed 2x with PBST and 1x with phosphate buffered saline. Immediately before imaging, the membrane was dried of any excess phosphate buffered saline and a mixture of 50% Luminol and 50% peroxidase (Bio-Rad) was applied to the front of the membrane. The membrane was then imaged using a Gel Doc machine with the exposure time optimised to obtain the clearest protein bands.

2.7 Biochemical and biophysical characterisation

2.7.1 Circular Dichroism (CD)

CD was utilised to determine the secondary structure of proteins and allow comparisons in stability between wild-type and mutated constructs. These experiments exploit the differential absorbance of left- and right-handed circularly polarised light displayed by the chiral amino acids within the protein structure. Within proteins, the different secondary structure conformations induce changes in the optical transitions of the chromophores of the amides in the polypeptide

backbone due to their alignment in arrays, resulting in differing exciton interactions (Greenfield, 2006). Therefore, different secondary structure elements produce characteristic spectra, enabling structural features to be determined from far-UV measurements. All CD experiments were performed on the JASCO J-175 spectropolarimeter using a 1 mm pathlength quartz cuvette (Starna Scientific). Far UV-spectra were obtained between 200-260 nm with an average of 4 scans at 100 nm/min, 0.5 nm step resolution, 1.0 second response and 0.5 nm bandwidth. Following far-UV measurements to determine secondary structure of the protein, spectral scans were performed to determine its thermal stability, through calculation of the melting temperature (T_m) when measured at a fixed wavelength. For these spectral scans CD bandwidth was set to 222 nm. Measurements were taken between 20-90°C with 20 second step resolution, 4 seconds of response and 1.0 nm bandwidth. Samples were prepared between 20-50 μM in 400 μL of phosphate buffer for all CD experiments. Resulting spectra were processed using OriginPro software.

2.7.2 Protein NMR

NMR was employed to determine precise structural changes occurring from mutations introduced into the primary structure of the protein. Here, NMR-active nuclei are placed in a strong magnetic field, causing the nuclei to align with the field in the Z-axis. Radio-frequency pulses are subsequently applied to the sample, knocking the nuclei 90° into the xy plane perpendicular to the magnetic field, allowing the nuclei to resonate at their specific resonant frequency, followed by eventual relaxation back into the Z-plane. The resulting free induction decay from this process is collected by radio receivers and the resulting frequency domain is extracted through Fourier transformation, producing NMR spectra for each measured nuclei. When labelled with ^{15}N, 2D heteronuclear single-quantum coherence (HSQC) experiments can correlate the chemical shifts of protons to their directly attached ^{15}N for each amino acid (with the exception of proline) within the protein (Storaska and Neubig, 2013). These HSQC experiments produce a spectral

map with each peaks position determined through both its amino acid structure and its position within the folded protein due to the differences in chemical environment.

Protein NMR experiments were conducted at 298 K using a Bruker AVANCE III spectrometer equipped with a QCI-P cryoprobe. The ^{15}N-labelled protein was measured at 150 μM in NMR buffer. Spectra were processed with TopSpin and CcpNmr Analysis 2.5.2. Initially, 1D proton experiments were conducted to assess suitable signal to noise and solvent suppression. Following this, 2D HSQC experiments were performed due to the protein presenting as under 20 kDa, therefore producing suitably sharp decoupled HSQC peaks. For each of these experiments, locking, tuning, shimming and determination of the 90° pulse width were performed before acquisition of the spectra was conducted.

2.7.3 SEC binding assays

Binding of green fluorescence protein (GFP)-VD1 to pGEL001 was probed using SEC. Here, the increased size of the complex resulting from binding between the two proteins could be deduced via its faster passage through the column compared to the smaller individual proteins. Therefore, confirmation of protein binding was possible through determining the presence of increased molecular weight species. These experiments were performed using a Superdex 200 size-exclusion column (GE Healthcare) connected to an AKTA pure system controlled with Unicorn™ software. All experiments were performed in SEC buffer, and loaded using 100 μL volumes at a constant flow rate of 1 mL/min. Fractions of 1 mL were collected from the column, with protein presence monitored using UV measurements at 280 nm. Elution's corresponding to peaks in the UV readings were subsequently prepared for SDS-PAGE analysis to confirm the molecular weight of each species. Firstly, each protein at 150 μM was loaded onto the column separately to establish the elution profile for the protein in the absence of a complex. Following the individual runs, GFP-VD1 and pGEL001 were mixed at 1:1 (150 μM:150 μM) and 3:1 (450 μM:150 μM) ratios and incubated at 25°C for one hour. Immediately upon completion of the incubation

time, the protein mixture was loaded onto the column to monitor existence of protein complexes.

2.7.4 C-trap™

The C-trap™ apparatus combines high resolution optical tweezers with fluorescence microscopy to allow for dynamic single-molecule measurements. Through the use of focused light to trap tethered beads, single molecule unfolding events can be monitored, including resulting changes in force and extension. Before application on the C-trap™ apparatus, the protein of interest requires labelling and tethering. Following these steps, the protein can be loaded into the flow cell ready for measurements. The two key procedural elements are described below.

2.7.4.1 Labelling and tethering of the protein

Protein labelling and tethering was conducted using the protein labelling and tethering kit (cysteine) obtained from Lumicks as per the manufacturers instructions. Firstly, 40 μL of the protein of interest at 20 μM in C-trap™ phosphate buffer was reduced using 0.5 mM TCEP for 10 minutes. Following the reduction period, 40 μL of the maleimide-modified oligo solution was added dropwise, and incubated at 25°C for 2 hours. After the two hour period had elapsed, the solution was buffer exchanged into C-trap™ binding buffer using 10 kDa mwco centrifugal concentrators. The protein was then purified using the His SpinTrap™ (GE Healthcare) according to the manufacturer's instructions and eluted using C-trap™ elution buffer. Confirmation of the protein of interests presence in the eluted sample was conducted using SDS-PAGE described in section 2.5.1. The eluted sample was buffer exchanged into Q buffer A using a 10 kDa mwco centrifugal concentrator and diluted to give a DNA concentration of 20 ng/μL, measured using a nanophotometer® N50 (IMPLEN). The protein was frozen in liquid nitrogen and stored at -80°C.

Anti-digoxigenin-coated bead preparation: On the day of C-trap™ measurements, an aliquot of labelled protein was thawed, with 1 μL of the protein solution added to 4 μL of DNA handles. The mixture was incubated for 10 minutes at 25°C. Following

this time, 1 μL of the protein-DNA handle mixture was added to 15 μL of Q buffer A. In a separate tube, 4 μL of the diluted protein-DNA handle mixture was then added to 5 μL of anti-digoxigenin coated beads, mixed and incubated for 5 minutes at 25°C. Following this time, 500 μL of Q buffer A was added to the mixture.

Streptavidin-coated bead preparation: On the day of C-trap™ measurements, 2 μL of streptavidin-coated beads were added to 500 μL of Q buffer A.

2.7.4.2 C-trap™ measurements

Anti-digoxigenin-coated beads prepared as per Section 2.7.4.1 were injected into microfluidic channel 1, Q-buffer A was injected into microfluidic channel 2 and streptavidin coated beads prepared as per Section 2.7.4.1 were injected into microfluidic channel 3. All channels were opened and a pressure of 0.3-0.5 bar was applied. A bead of each type was captured and moved into channel 2, with the flow then switched off and a template for each bead defined on the brightfield camera window. The captured anti-digoxigenin-coated bead was subsequently referred to as bead 1 and the streptavidin coated bead as bead 2. Bead 1 was then moved within 5-10 μm of bead 2 and trap calibrations were performed ready for measurements to take place. Following the calibrations, the two beads were aligned on the horizontal plane at a distance of 3-5 μm. The piezo distance was selected, the theoretical worm-like chain model chosen, and the total contour length of the DNA handles entered at 1.06 kbp or 0.35 μm. The piezo tracking window was turned on and bead 1 was moved within 1 μm of bead 2. Following this step, the speed of trap 1 was locked at 0.1 μm/s. Capturing of tethers was subsequently performed by moving bead 1 as close to bead 2 as possible and then monitoring the force response following movement of bead 1 away from bead 2. New beads were captured whenever snapping was witnessed.

2.8 TSAM formation and characterisation

2.8.1 Minimum gelation concentration (MGC) trials

MGC trials were performed to determine the concentration required for TSAM formation. Here, a 30:1 ratio of TCEP:cysteine was added dropwise to a solution of pGEL001 in phosphate buffer. After one hour, the pGEL001 solution was run through PD-10 desalting columns (Cytiva) and the flow through was subsequently re-applied to desalting columns for a second run through, ensuring high percentage TCEP removal. Immediately following the desalting step, the pGEL001 solution was concentrated to the desired concentration using 30 kDa mwco concentrators (ThermoFisher Scientific). Three repeats at each pGEL001 concentration of 40, 80, 160 and 200 mg/mL were tested during minimum gelation trials, measured using a nanophotometer® N50 (IMPLEN). Immediately after the desired concentration of pGEL001 had been reached, the respective crosslinker was added slowly at a 1:1 maleimide:cysteine ratio that resulted in a final 4% DMSO solution. Samples were left to set at 4°C overnight.

2.8.2 TSAM formation

All TSAMs formed throughout this project were conducted using the protocol described in section 2.8.1. The concentration of 200 mg/mL, determined through the minimum gelation trial, was employed as the concentration used to produce all TSAMs.

2.8.3 Determining gel fibre formation with plate reader assay

The pGEL001 samples measured within the plate reader assay were produced as described in section 2.8.1. Specifically, 100 μL of each pGEL001 concentration was added into a single well on a 96 well clear plate (Greiner Bio-One). The crosslinker was directly added to these solutions when contained within the plate and stored at 4°C overnight for the TSAMs to set. OD readings were performed using a CLARIOstar microplate reader (BMG LABTECH) with MARS data analysis software. Spectral scanning experiments were conducted first, measuring the OD across each well between 300-1000 nm. Following this, well scans were performed, whereby each

well was split into 166 segments and an OD value at the determined wavelength (chosen from the spectral scans) was recorded for each.

2.8.4 Transmission electron microscopy on immunogold-labelled TSAMs

Transmission electron microscopy was utilised to determine the presence of His-tag containing proteins within the TSAM material via immunogold staining. Here, 2 µl of TSAM was applied to carbon/formvar 400 mesh gold grids (Agar Scientific) and allowed to settle for 5 minutes. The sample was then fixed in 2% formaldehyde and 0.5% glutaraldehyde in 100 mM sodium cacodylate buffer pH 7.2 (CAB) for 15 minutes at room temperature. Samples were washed 2x 5 minutes in CAB and 2x 5 minutes in TBST. Grids were blocked in 2% BSA in TBST for 30 minutes and then moved into a 20 µl drop of anti His-Tag primary antibody (Sigma) diluted 1:100. Grids were washed 6x 2 minutes in drops of TBST before incubation in Goat anti-mouse IgG conjugated to 5 nm gold (British Biocell International) diluted 1:50 for 30 minutes. Grids were washed for 6x 2 minutes in TBST and 6x 2 minutes in distilled water. Negative controls were performed as above but primary antibody was replaced with TBST. Samples were then air dried and negative stained in 2% aqueous uranyl acetate. Samples were viewed in a Jeol 1230 Transmission electron microscope at 80 kV and images were recorded on a Gatan One View 16 MP digital camera.

2.8.5 Scanning electron microscopy

Scanning electron microscopy was utilised to determine the structure and elemental composition of the TSAMs. Before imaging, the TSAMs were dehydrated to form a xerogel and placed on a carbon tab mounted onto an aluminium stub. Imaging was achieved using a Hitachi S-3400N scanning electron microscope with energy dispersive X-ray analysis and analysed using Oxford instruments AZtec software. Imaging was conducted at 20 V on back scatter electron or secondary electron modes.

2.8.6 Rheology

Rheological measurements were performed on TSAMs to determine several important material properties, explained in Section 4.4.2. All rheology experiments were performed on an Anton Parr modular compact rheometer (MCR302). All measurements were performed at 298 K using a PP20 parallel plate. Oscillatory amplitude experiments maintained a frequency of 10 rad s^{-1} and were performed with an amplitude of oscillation range of 0.01-100%. A two minute rest time was set between each amplitude sweep, with a total of five sweeps performed on each TSAM. For the GFP-VD1, GFP and buffer swelled experiments, the TSAM was left in the respective solution at 2 mg/mL overnight before rheological measurements were performed. Oscillatory frequency sweep experiments were conducted at a constant shear strain of 1 % with an increasing frequency from 0.1–100 rad s^{-1} at 298 K. A two minute rest time was set between each amplitude sweep, with a total of five sweeps performed on each TSAM.

2.8.7 Fluorescence microscopy

GFP-VD1 and GFP treated samples of TSAM from the rheology experiments were visualised using an Olympus IX71 microscope employing a 1.6x magnification Optovar in combination with a PlanApo 100x OTIRFM-SP 1.49 NA lens mounted on a PIFOC z-axis focus drive (Physik Instrumente, Karlsruhe, Germany), and illuminated using LED light sources (Cairn Research Ltd, Faversham, UK) with DC/ET350/50x excitation, ET Quad Sedat dichroic, and DC/457/50m emission filters (Chroma, Bellows Falls, VT). Samples were visualised using a QuantEM (Photometrics) EMCCD camera, and the system was controlled with Metamorph software (Molecular Devices). Each 3D-maximum projection of volume data was calculated from 31 z-plane images and the best 6 were chosen, each 0.2 µm apart, and analysed using MetaMorph software.

2.8.8 Light gas gun experiments

To probe the shock absorbing performance of TSAMs, a light gas gun was employed. This apparatus is traditionally utilised for physics experiments investigating high velocity impacts, such as the formation of impact craters by meteoroids.

Compression of light gasses such as helium and nitrogen are used to accelerate projectiles up to speeds of 7 km/s (Burchell *et al.*, 1999, Hibbert *et al.*, 2017). To achieve compression of the gasses, gunpowder is used to force a piston to compress the light gas within a small diameter barrel, which when reaches a desired pressure causes the destruction of a calibrated burst disc. Upon destruction of the disc the projectile of choice is accelerated down a second barrel towards the target, with the final velocity of the projectile at the point of impact measured. The experiments used within this study utilised basalt particles of 20-70 μm in diameter, loaded into a sabot as a buck shot for the projectile. The sabot is a small vessel shown in Figure 2.7a with an opening to allow the loading of the projectiles. The sabot allows the grouping of projectiles to be accelerated down the barrel as a single unit and accurately hit the target, while the sabot itself separates into fragments that avoid impacting the target. The impact experiments were carried out using the Light Gas Gun facility at the University of Kent, Canterbury. Figure 2.7 summaries the light gas gun experimental set-up.

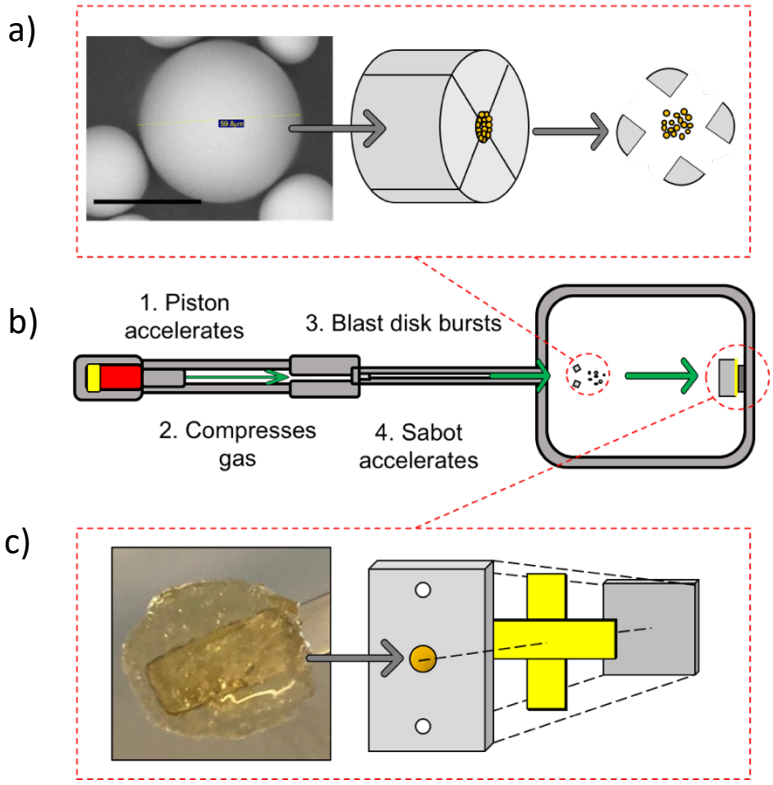

Figure 2.7: Light gas gun experiment schematic. a) Scanning electron microscopy image (Scale bar = 60 µm) of a basalt particle used as the projectile and representation of how the basalt particles were loaded into a sabot and their release during the shot. b) Diagram of the light gas gun apparatus with the labels of the key stages after the shot was triggered. c) Image of a TSAM and how it was prepared as the target for the experiments in Section 4.5.2. The TSAM was loaded into a target plate constructed of steel (Blast tank exit aperture, stainless 304), with tape used to seal the back of the hole, followed by an aluminium back plate (Al 5083).

During the light gas gun experiments a 500 µL TSAM target was set in a blast tank exit aperture (BTEA) with a circular, 8 mm diameter aperture, sealed with tape, and an aluminium (5083) back plate placed behind. Multiple 20-70 µm basalt particles were loaded into a single sabot utilising the "buckshot" method and were fired at roughly 1.5 km/s, with the speeds recorded via the BTEA - Muzzle laser method as described by Burchell *et al.* (Burchell *et al*., 1999). The target was removed prior to the air flushing procedure to reduce gun contamination on the TSAM. The combination of the BTEA and target mounted into a single device, allowed for minimal spreading of the buckshot projectile, increasing the chance of direct impact onto the TSAM, and maximized the BTEA-muzzle separation.

Chapter 3: Design and development of TSAM

3.1 Overview

This chapter focuses on the design strategy and subsequent investigation into the formation of the first iteration of a TSAM material. When designing this material several important considerations informed the design strategy. Firstly, to date the majority of protein-based materials produced involve lyophilisation of the protein and reconstitution at the required gelation concentration (Fang *et al*., 2013, Wu *et al*., 2018). This process exposes the protein to stresses including denaturation (Bhatnagar *et al*., 2007), pH shifts (Anchordoquy and Carpenter, 1996) and loss of hydrogen bonds resulting in intra- and inter-molecular interactions that differ to those in its previous solution state (Roughton *et al*., 2013). Therefore, we opted for a gelation strategy maintaining the protein in the solution state throughout the entire process, minimising the chances of altering wild-type protein folding. Secondly, with the downstream goal of producing a material amenable to upscale manufacturing processes and real-world applications, the materials within TSAM needed to be cheap and easy to manufacture. Therefore all crosslinkers, synthetic strategies and purification procedures were chosen with this consideration in mind.

3.2 Engineering and characterising the recombinant protein pGEL001

For the first iteration of a TSAM material, the primary focus was to develop a product that successfully captured the endothermic energy dissipating mechanisms of talin, discussed in Section 1.3.3. With this goal in mind, talin domains R1, R2 and R3 were selected for incorporation into the protein monomer. The three domains, R1-R3, have previously been shown to express and purify well, with their mechanical response extensively characterised, discussed in Section 1.3.3. The R1-R3 domains unfold at 20, 15 and 5 pN respectively (Yao *et al*., 2016), providing a stepwise unfolding with respect to force. Incorporating domains with a range of unfolding forces as the protein monomer into a hydrogel directly addresses the issue of theoretical predictions by Doi (Doi, 1995) who calculated the force experienced by an individual molecule within a hydrogel fibre to be in the range of a few pN. Here,

the unfolding force of R3 at 5 pN would ensure unfolding occurred even at these low forces, while the R1 and R2 domains resist immediate unfolding should forces higher than a few pN be experienced by the protein monomers. Following selection of the protein domains, the crosslinking strategy was considered, with the Michael addition reaction of maleimides to sulfhydryl groups of cysteines chosen. This mechanism was selected from those discussed in Section 1.2.2 due to the fast reaction kinetics and simple protein modifications required to introduce sulfhydryl groups into the protein monomer at specific locations. To enable tethering of the protein monomers via its two terminals, cysteines were introduced at both the N- and C-terminus, while all cysteines within the R1-R3 domains were mutated to serine. Cysteine to serine mutations were chosen due to the similarity between the bond lengths and angles between these residues, presenting as almost isostructural amino acids (Catalano *et al*., 2021). A long flexible linker region was introduced between the R1-R3 domains and the terminal cysteines, ensuring accessibility of the cysteines sulfhydryl group to the chosen crosslinkers, without incidence of steric hinderance occurring. This newly engineered talin construct was called pGEL001 as the first in a series of talin monomers. The AlphaFold predicted structure of pGEL001 is displayed in Figure 3.1a, with the design segments summarised in Figure 3.1b.

a)

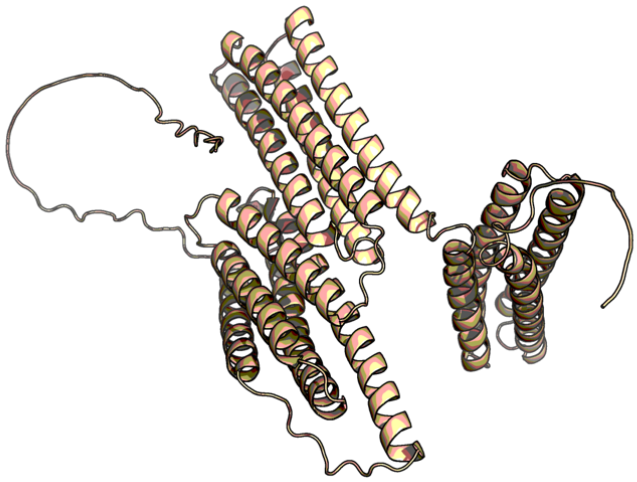

b)

Figure 3.1: Structure of pGEL001. a) AlphaFold predicted structure of pGEL001 produced with PyMOL. b) Graphical representation of the pGEL001 structure, showing each segment of the recombinant protein.

3.2.1 Developing an optimal purification procedure for pGEL001

Successful formation of a pGEL001 hydrogel would likely require vast quantities of protein. Therefore, optimisation of the protein purification procedure required to achieve adequate purity of pGEL001 in the highest yields possible was paramount. To enable purification of pGEL001, a His-tag was incorporated onto the N-terminus of the protein, with a TEV cleavage site placed between the His-tag and the cysteine for removal of the His-tag following purification (Figure 3.1b).

Following successful expression of pGEL001, affinity-tag purification was performed. Here, purification utilising a HisTrap HP column (Cytiva) connected to an AKTA start system was compared to the batch method using HisPur™ Ni-NTA resin. The resulting SDS-PAGE gels of the eluted protein fractions are shown in Figure 3.2. Using ImageJ image analysis software, the average purity of the elution's combined for further use was calculated. For the HisTrap HP column (Figure 3.2a), the average purity was calculated at 76%, whilst the batch methods (Figure 3.2b) average purity was calculated at 47%. From these results it was clear the HisTrap HP column achieved a

significantly higher purity and was chosen as the affinity-tag purification method moving forward. Further optimisations of the HisTrap HP column-based purifications revealed purities up to 95% when pGEL001 was loaded at sufficient yields to achieve saturation of the column. Therefore, all pGEL001 purifications were performed at concentrations close to or above the saturation limit of the column.

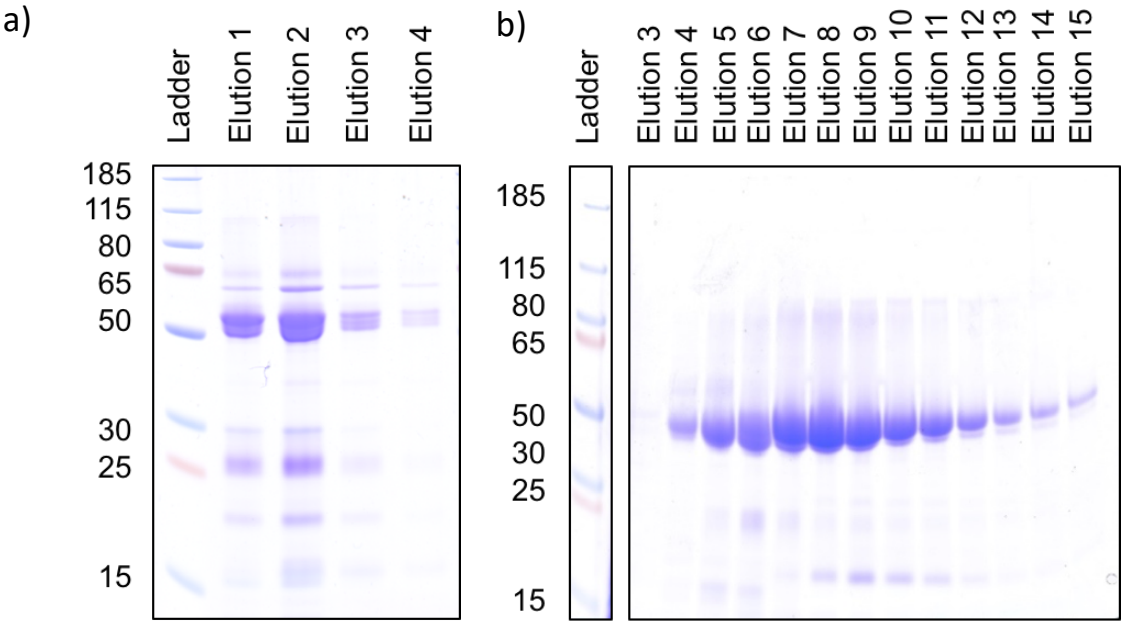

Figure 3.2: SDS-PAGE gels of pGEL001 affinity-tag purification. a) Elution's 1-4 following batch method His-tag purification using HisPur Ni-NTA resin. Average purity calculated at 47% using ImageJ software. b) Elution's 3-15 following His-tag purification utilising a HisTrap HP column (Cytiva) connected to an AKTA start system. Average purity calculated at 76% using ImageJ software.

A second purification step was subsequently investigated for circumstances where affinity-tag purification resulted in purities below 90%. Here, two approaches were evaluated, 1) anion exchange chromatography utilising a HiTrap HP Q column connected to an AKTA start system and 2) SEC using a 16/60 Sephacryl S-300 column connected to an AKTA Pure system. To ensure a valid comparison could be drawn between the two samples, protein from the same combined purification were used for both methods (76% purity). The resulting SDS-PAGE gels of the eluted protein fractions are shown in Figure 3.3. ImageJ image analysis software was utilised to calculate the average purity of the elution's combined for further use. Purification with SEC (Figure 3.3a) resulted in a calculated purity of 89%, whilst the average purity

from anion exchange chromatography (Figure 3.3b) was determined at 85%. Due to the similarity in purity levels achieved between the two techniques, ion exchange chromatography was selected due to its shorter run time and larger loading volume. These two factors were important when considering scaling up of material development based off the equipment available in the laboratory.

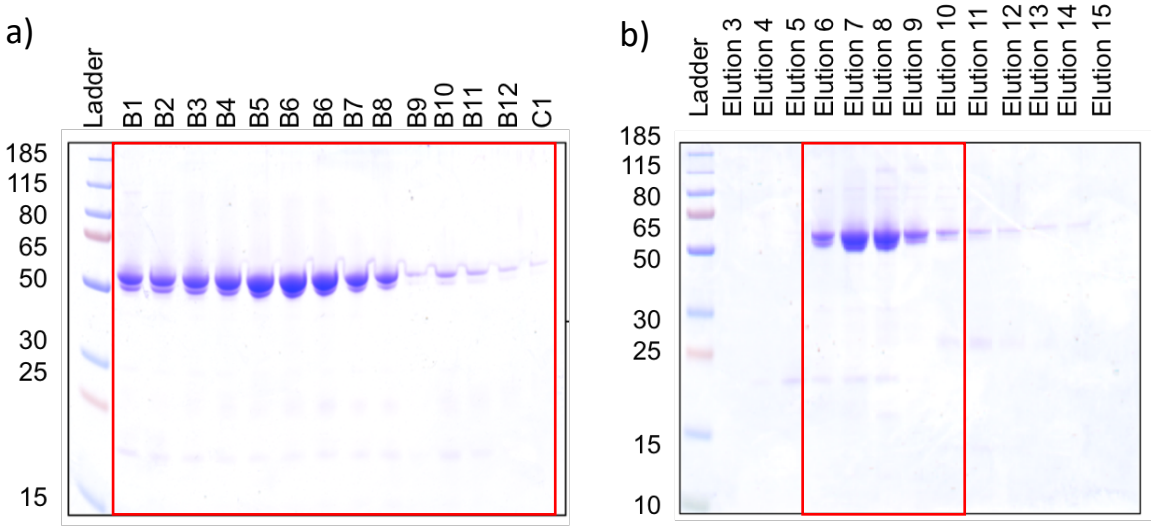

Figure 3.3: SDS-PAGE gels of SEC and ion exchange chromatography-based purification. Red boxes indicate fractions used in calculation. a) Elution's B1-C1 following SEC using 16/60 Sephacryl S-300 column connected to an AKTA Pure. Average purity calculated at 89% using ImageJ software. b) Elution's 3-15 following ion exchange chromatography utilising a HiTrap HP Q column (Cytiva) connected to an AKTA start system. Average purity calculated at 85% using ImageJ software.

3.2.2 Characterising effects of cysteine to serine mutations on R1-R3 folding

To determine structural changes that resulted from the mutations introduced within the R1-R3 domains of the pGEL001 construct, both CD and ^{1}H-^{15}N HSQC NMR experiments were employed. Specifically, one cysteine to serine mutation was introduced into R1 (C575S) (Figure 3.4a), four cysteine to serine mutations in R2 (C709S, C719S, C732S, C750S) (Figure 3.4b) and no mutations were introduced into R3. As the single cysteine in R1 was located on the outside of the helix, we predicted very few structural changes would result from mutating this residue to a serine. Contrarily, the cysteine residues within R2 appeared to be in close proximity as pairs, potentially indicating the presence of disulphide bonds. However, using PyMOL, the distances between the cysteine residues within the two pairs was measured at 5.3 Å and 9.4 Å (Figure 3.4b), generally considered outside the distance limit of 3.0 Å for

disulphide bonding, therefore suggesting disulphide bonding was unlikely to be occurring. Due to four mutations being introduced within the R2 domain, in addition to the small potential of disulphide bonds being present, we predicted a change in stability could have occurred within this domain.

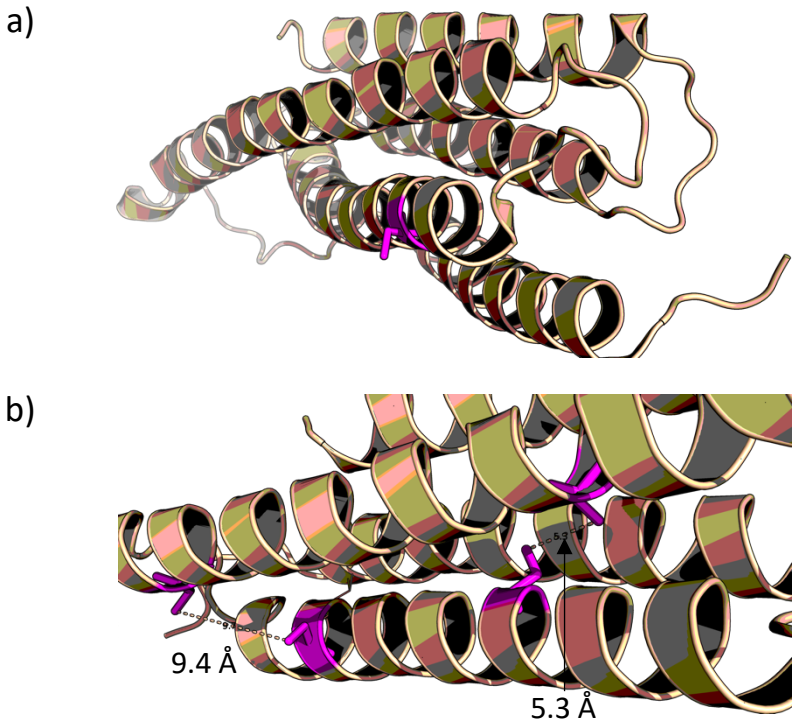

Figure 3.4: PyMOL generated figures of R1 and R2 (PDB: 1SJ8) (Papagrigoriou *et al.*, 2004) with locations of cysteines highlighted in magenta. a) Wild-type R1 with the location of cystine displayed in magenta in stick format. b) Wild-type R2 with the location of the cysteines displayed in magenta in stick format. The distances between the neighbouring cysteine residues is displayed in Å.

First, CD was performed on the full length pGEL001 and wild-type R1-R3 to confirm retention of alpha helical folding and determine differences in stability between the two constructs. The resulting UV scans measured at 20°C and 90 °C and the melting curve measured at 222 nm are shown in Figure 3.5. The UV-scan (Figure 3.5a) of both pGEL001 and R1-R3 displayed traces consistent with alpha helical folding, observed as the characteristic trace with two minima at 205 nm and 222 nm. Therefore, alpha helical folding was confirmed within both pGEL001 and R1-R3. Furthermore, the melting curve (Figure 3.5b) of both pGEL001 and wild-type R1-R3 revealed only a slight change in T_M of 3.2°C, suggesting little change in overall stability, with the

mutant being slightly more stable than the wild-type. Overall, it appeared only a small change had occurred to the structure of pGEL001 compared to wild-type R1-R3.

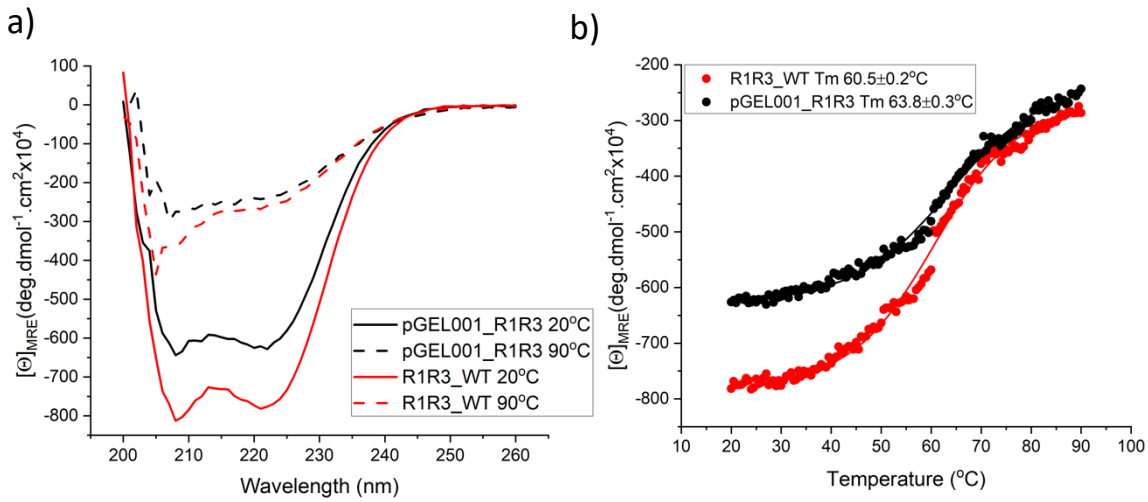

Figure 3.5: CD traces of pGEL001 and R1-R3. a) UV scan of pGEL001 and R1-R3 both display alpha helical folding at 20°C, with folding abolished at 90°C. b) Melting curves taken at 222 nm show small changes in T_m between pGEL001 and R1-R3.

Due to the long flexible linkers and cysteines introduced into the terminals of pGEL001 compared to the wild-type R1-R3, the individual mutated domains encapsulated within the pGEL001 monomer were isolated to allow direct structural comparisons resulting only from the cysteine to serine mutations. These isolated domains are herein referred to as mutated R1 and mutated R2. To determine structural changes occurring in the mutated R1 compared to wild-type R1, a ^{1}H-^{15}N HSQC NMR experiment was performed (Figure 3.6). A ^{15}N-labelled mutated R1 was expressed and purified, with the resulting HSQC spectra measured at 298 K. Assignments from wild-type R1 (BMRB file 17555) (Banno *et al*., 2012) were overlaid onto the HSQC of mutated R1 using CCPN analysis 2.5.2 to observe shifts resulting from the cysteine to serine mutation, shown in Figure 3.6. As seen in Figure 3.6 almost all wild-type R1 assignments directly overlaid onto the mutated R1 HSQC spectra, confirming no significant change to the protein folding had occurred. The only residues displaying significant shifts were 483G, 561T and the mutated residue C575S (Figure 3.6b), each highlighted in the PyMOL structure in Figure 3.7. When visualised in Figure 3.7, the residues showing shifts were all located near the mutated

residue, showing any structural changes were isolated to the local region of the mutation in the mutated R1.

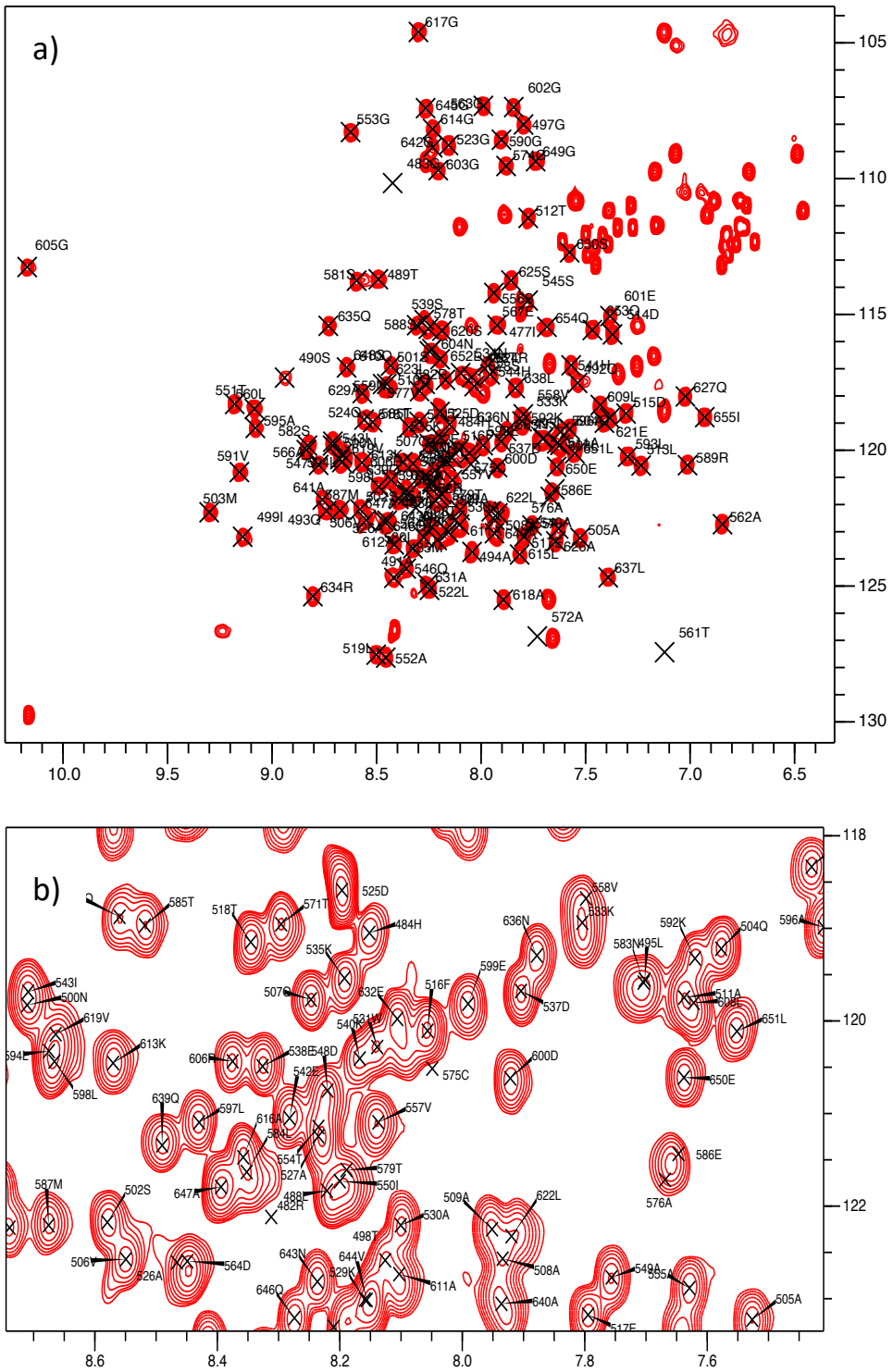

Figure 3.6: HSQC spectra of ^{15}N-labelled mutated R1 with wild-type R1 assignments overlaid. a) Minimal change to the structure occurred from the single mutation in the mutated R1 with almost all wild-type R1 peak assignments overlaying onto the mutated R1 peaks. b) HSQC centred on the region where the wild-type R1 cysteine assignment is positioned.

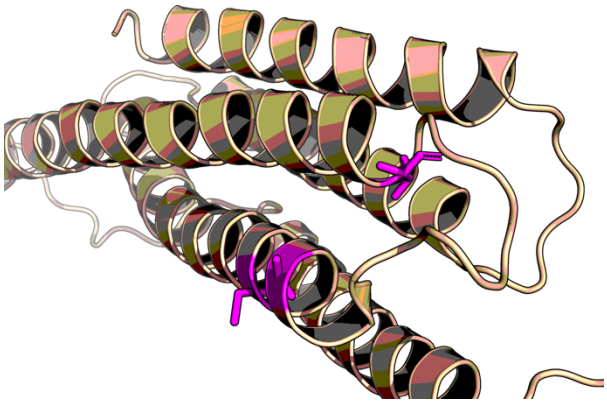

Figure 3.7: Wild-type R1 structure (PDB: 1SJ8) (Papagrigoriou *et al*., 2004) with residues displaying significant shifts compared to mutated R1 from HSQC experiment. Residues displaying shifts are shown in magenta as sticks. Image produced in PyMOL.

To investigate the folding changes occurring in mutated R2, attempts at growing ^{15}N-labelled mutated R2 were performed to conduct a ^{1}H-^{15}N HSQC NMR experiment. However, no expression of mutated R2 could be achieved using either the condensation method or growth directly from minimal media. Instead, small yields of mutated R2 were achieved when grown in LB, allowing CD UV-scan and melting curve experiments to be conducted. The same experiments were also performed on wild-type R2 allowing direct comparisons to be drawn. The resulting UV-scan and melting curves of both mutated R2 and wild-type R2 are shown in Figure 3.8. Here, both mutated R2 and wild-type R2 presented UV-scan (Figure 3.8a) traces characteristic of alpha helical folding at 20°C, however at 90°C mutated R2 displayed complete loss of structure, whilst wild-type R2 appeared to retain some structure, indicating a change in stability between the two proteins. This result was validated via the melting curves measured at 222 nm (Figure 3.8b), in which mutated R2 presented a T_m of 63.9°C, displaying a decrease in T_m of 5.8°C compared to the wild-type R2 with a T_m of 69.7°C, revealing some effects on the stability of the mutated R2 domain had occurred as a consequence of the four mutations. Despite this change in stability of the mutated R2, as stated alpha helical folding was still present, with the mutated R1 displaying almost no change in structure and R3 containing no mutations.

Together, combining the results of the isolated domains with the CD data on whole pGEL001 and R1-R3, pGEL001 was confirmed to be suitable for progression as the protein monomer for hydrogel formation.

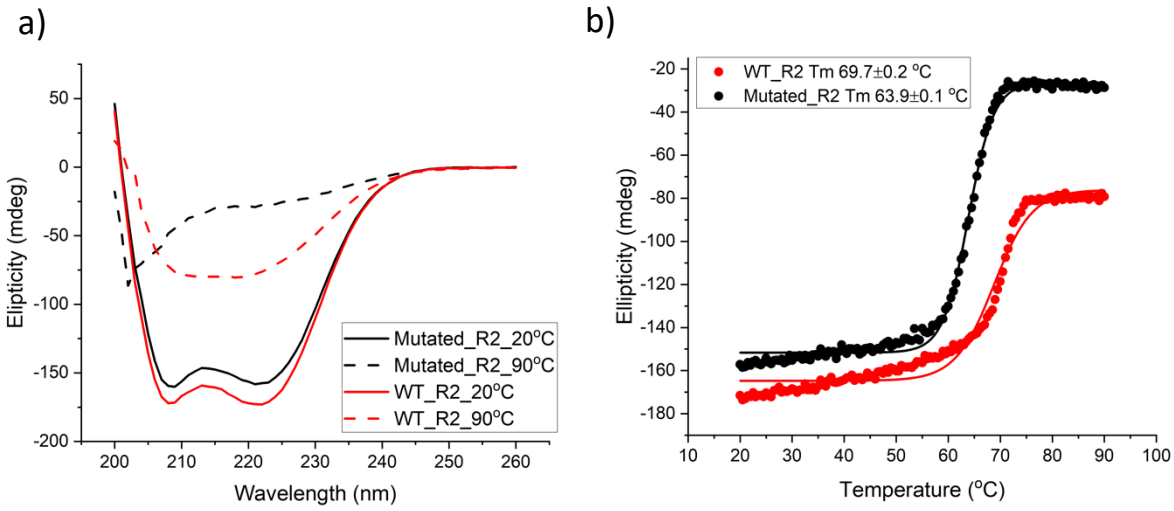

Figure 3.8: CD traces of mutated R2 and wild-type R2. a) UV scan of mutated R2 and wild-type R2. Both proteins contain alpha helical folding at 20°C, with alpha helical folding abolished in the mutated R2 at 90°C and largely removed in wild-type R2. b) Melting curves taken at 222 nm show a 5.8°C change in T_m between the mutated R2 and wild-type R2.

3.2.3 pGEL001 forms complexes with GFP-VD1

The protein vinculin plays a key role in focal adhesion formation, displaying a force dependent interaction with talin (Yao *et al.*, 2014). This interaction occurs through VD1 associating with vinculin binding sites on the talin rod domains (Discussed further in Section 1.4). These vinculin binding sites are defined by hydrophobic residues buried within the helices of the rod domains of talin, unavailable for interaction when talin exists in its folded state (Roberts and Critchley, 2009). Upon unfolding of the talin domains, these hydrophobic residues are exposed, allowing VD1 to interact and bind. VD1 is held in an autoinhibited state in full-length vinculin via the vinculin tail domain (Cohen *et al.*, 2005). When isolated from this autoinhibited structure, VD1 is capable of inducing unfolding of the rod domains of talin and binding, removing the requirement of force to unfold these rod domains (Goult et al., 2013b). Binding of VD1 to the talin rod domains locks these domains in the unfolded state, unable to refold unless forced into the extended polypeptide

confirmation (Yao *et al*., 2014). Previous work has shown the wild-type R1-R3 domains can bind five VD1 molecules (Goult et al., 2013b).

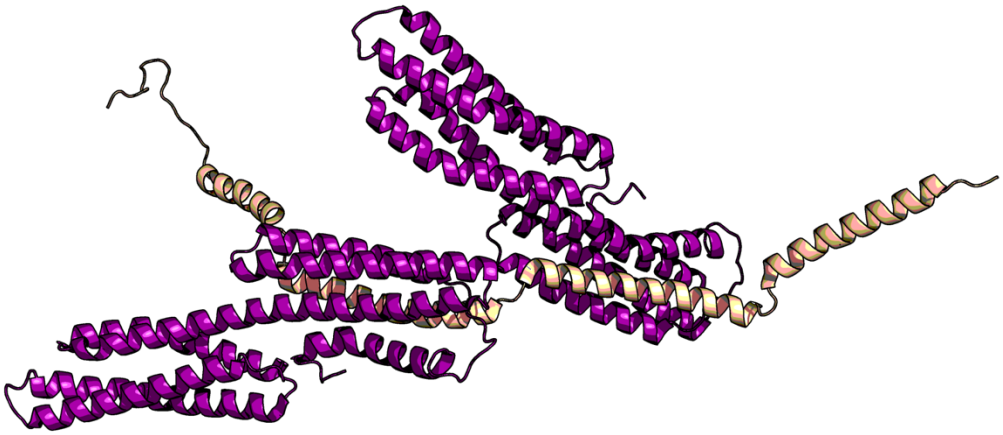

Figure 3.9: Two molecules of VD1 (purple) (PDB: 1U6H) (Fillingham *et al*., 2005) forming a complex with the opened helices structure of the R3 domain of pGEL001 (gold) (PDB: 2L7A) (Goult et al., 2013b). Produced in PyMOL.

To confirm VD1 binding was retained in pGEL001, important for validating the integrity of the talin monomers and for future experiments, SEC of pGEL001 in complex with GFP-VD1 was performed. SEC separates out proteins based on size, due to the differences in the interactions of the proteins with the pores in the column (Hong *et al*., 2012). Therefore, larger proteins elute off the column first due to their exclusion from the pores, whilst smaller proteins enter the pores and elute sequentially based on their size. When a complex forms between two proteins, the size of the complex is larger than either of the proteins existing individually, therefore complex formation can be confirmed through this change in size. An illustration of VD1 binding to the opened helices conformation of pGEL001 is displayed in Figure 3.9.

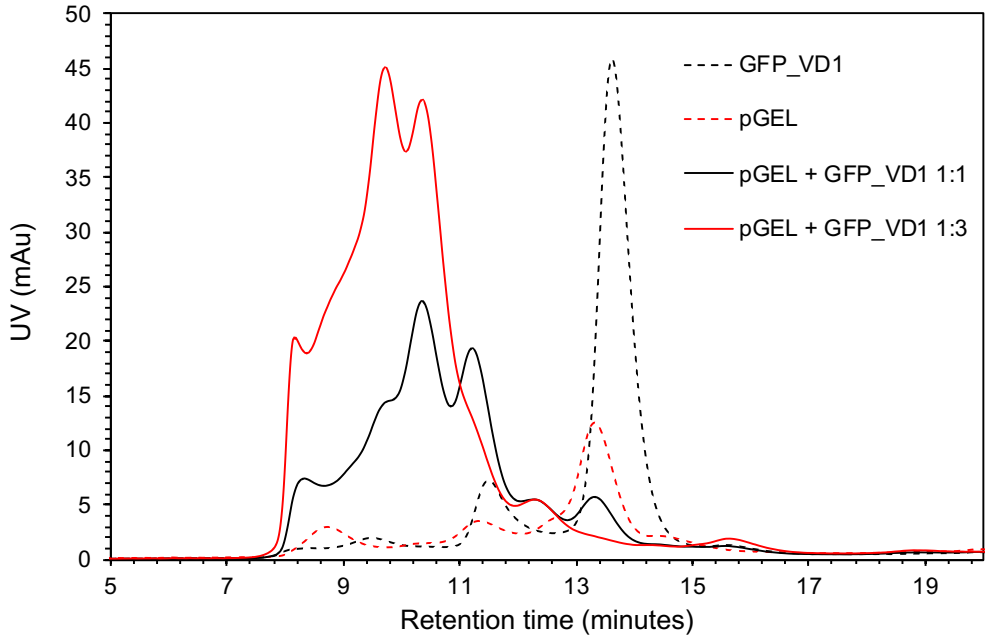

Figure 3.10: Confirming GFP-VD1 and pGEL001 complex formation with SEC. Black dotted line = GFP-VD1 (150 μM). Red dotted line = pGEL001 (150 μM). Black solid line = 1:1 GFP-VD1 to pGEL001 (150 μM:150 μM). Red solid line = 3:1 GFP-VD1 to pGEL (450 μM: 150 μM).

The SEC results are displayed in Figure 3.10. When pGEL001 (150 μM) was injected onto the SEC column, the majority eluted as a single peak corresponding to the monomer. Small dimer and trimer peaks were also observed, likely due to disulphide bonding between pGEL001 proteins. The same pattern was observed for GFP-VD1 (150 μM) when eluted off the SEC column, existing mostly as a monomer, with small dimer and trimer peaks also observed. When GFP-VD1 was incubated with pGEL001 at a 1:1 (150 μM: 150 μM) ratio for 1 hour at 25°C prior to injection onto the column, the peaks corresponding to the monomer for both pGEL001 and GFP-VD1 almost entirely disappeared, with a new broad peak containing multiple heads appearing at an earlier elution, corresponding to a larger protein size. Due to this peak not existing in either of the protein traces when run as isolated samples, combined with vastly reduced monomer peak intensity, it was concluded this broad peak corresponded to a complex formed between pGEL001 and GFP-VD1. The same result was obtained from GFP-VD1 incubated with pGEL001 at a 3:1 (450 μM: 150 μM) ratio, this time presenting a higher intensity broad peak corresponding to the complex, suggesting complete saturation of pGEL001 with GFP-VD1 did not occur at the lower 1:1 ratio. Saturation would not have been expected at the lower ratio of 1:1 as five GFP-VD1

molecules can bind a single wild-type R1-R3 protein, therefore a 1:1 ratio would not provide enough GFP-VD1 to occupy all vinculin binding sites in pGEL001. Therefore, the SEC data confirmed pGEL001 retained binding with VD1, able to bind multiple GFP-VD1 proteins, supported by the broad peak and increased intensity of the peak at the higher ratio of GFP-VD1 to pGEL001.

3.3 Synthesis and characterisation of TSAM crosslinkers

In order to crosslink the pGEL001 monomers to achieve hydrogel formation, three crosslinkers were synthesised. Although disulphide bonding between the terminal cysteines alone could result in a hydrogel formation, gelation would require long periods of time, and no tailorability of the resultant network structure would be possible. Therefore, synthesised crosslinkers were chosen to speed up the gelation process and allow more control over the network structure formed. The three crosslinkers chemical structure are shown in Figure 3.11. Crosslinker **1** was developed as a control capping agent, ensuring addition of a single maleimide containing molecule to the solution of pGEL001 was not responsible for the formation of any resulting hydrogel network. Crosslinker **2** was designed capable of forming di-substituted species, crosslinking two pGEL001 monomers together. Crosslinker **3** was designed capable of forming tri-substituted species, crosslinking three pGEL001 monomers together, forming a three-armed network structure. The resulting NMR characterisation can be found in Section 2.2.

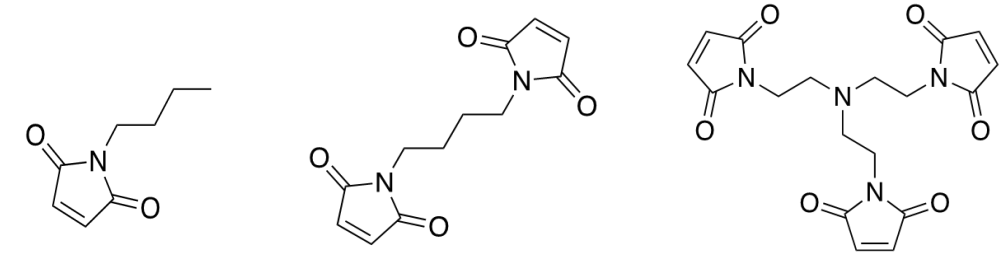

Figure 3.11: Chemical structures of crosslinkers 1-3.

3.3.1 Investigating the solubility of the crosslinkers in phosphate buffer

Before attempting crosslinking of pGEL001, each of the crosslinkers solubility in phosphate buffer (pH 7.4) was investigated. Maleimide groups absorb light in the region of 299 nm (Kirchhof *et al*., 2015), allowing for approximate quantifications of solubility based off of the Beer Lambert law. The Beer Lambert law states that absorption is linearly dependent on concentration (Mayerhofer and Popp, 2019). Therefore, if the crosslinkers remain soluble at higher concentrations a linear trend in the measured absorbance at 299 nm should be observed with increasing maleimide concentration. In this experiment the concentrations of each crosslinker required for a 1:1 maleimide:cysteine ratio at five protein concentrations were tested: 40, 80, 120, 160 and 200 mg/mL, covering the range of protein concentrations desired for testing in MGC trials. The results are displayed In Figure 3.12, and are plotted as the absorbance at 299 nm against the respective protein concentration that equates to 1:1 maleimide:cysteine at the concentration of crosslinker added.

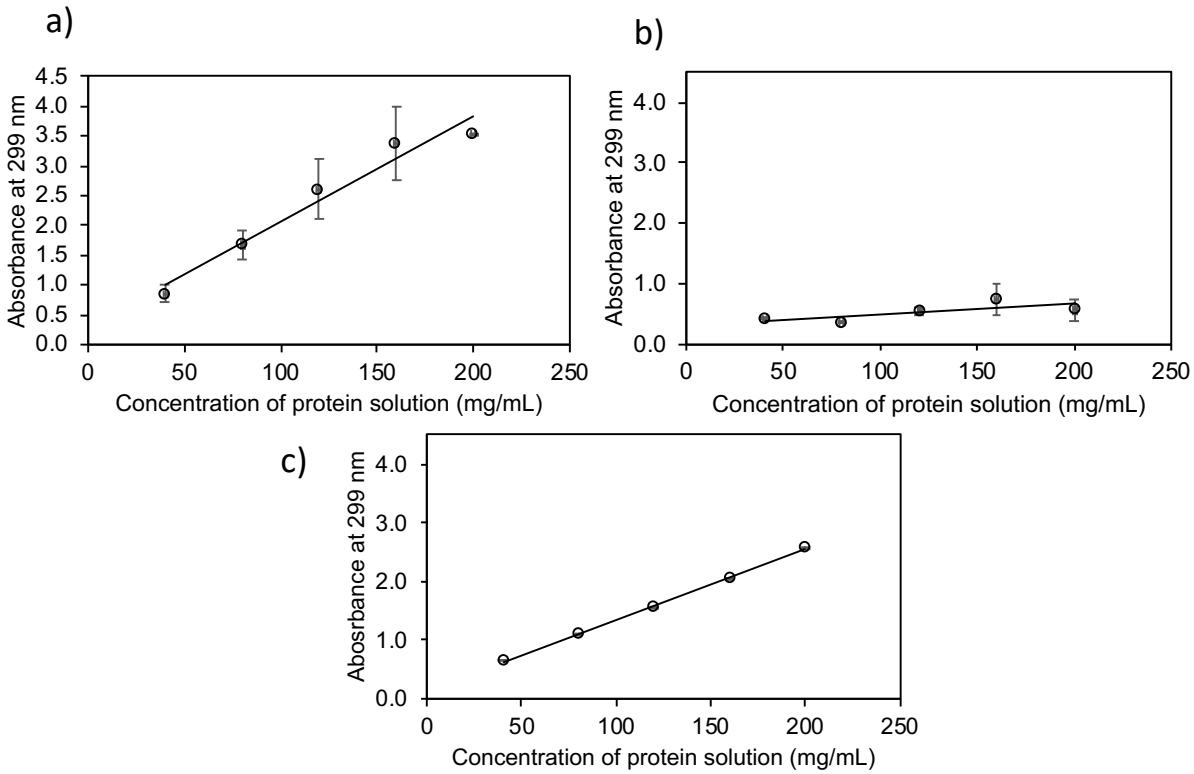

Figure 3.12: Solubility trials for crosslinkers 1-3. (n=3, error bars = standard deviation). The resulting absorbances obtained when the crosslinker was added to phosphate buffer (pH 7.4) at the concentration required for 1:1 maleimide:cysteine at the protein concentration plotted on the x-axis are shown for a) Crosslinker **1**. b) Crosslinker **2**. c) Crosslinker **3**.

The results in Figure 3.12a showed with increasing concentrations of crosslinker **1** a linear trend of absorbance at 299 nm was obtained. These data suggested that crosslinker **1** remained soluble up to the concentration required for a 200 mg/mL solution of protein. Crosslinker **2**, shown in Fig. 12b, presented very little change in absorbance with increasing concentrations. This pattern, in addition to the large deviation in absorbances seen compared to crosslinkers **1** and **3**, whereby the same concentration of maleimide groups were present at each measured point, suggested crosslinker **2** did not present high solubility even at the lowest tested concentration. Crosslinker **3**, shown in Fig 12c, presented a linear trend with increasing concentrations similar to crosslinker **1**. This suggested crosslinker **3** was suitable for additions up to the concentration required for a 200 mg/mL pGEL001 solution. Together these results revealed crosslinkers **1** and **3** were likely to remain soluble for minimum gelation trials up to 200 mg/mL, whilst crosslinker **2** presented low solubility even at the lowest tested concentration likely to result in no hydrogel formation.

3.3.2 Investigating the hydrolysis of the crosslinkers in phosphate buffer

When dissolved in an aqueous solution, maleimide groups are susceptible to hydrolysis resulting in ring opening (Matsui and Aida, 1978). If completion of the Michael addition reaction between the thiol present within the targeted cysteine group and the carbon-carbon double bond of the maleimide has occurred, hydrolysis mediated ring opening does not affect the crosslink. However, if hydrolysis occurs before completion of the crosslink, the maleimide group no longer presents reactivity towards thiols. Therefore, when all maleimide groups are hydrolysed no more crosslinking can occur. Thus, determining the time frame for complete hydrolysis of the maleimide groups within the crosslinkers allowed for the maximum reaction endpoint for the crosslinking of protein solutions be elucidated. To conduct this experiment, a similar methodology was utilised to that of the solubility investigations, harnessing the absorbance of maleimide groups at 299 nm.

Furthermore, the results from crosslinker **3** were also validated with an NMR time course study. These results are summarised in Figure 3.13.

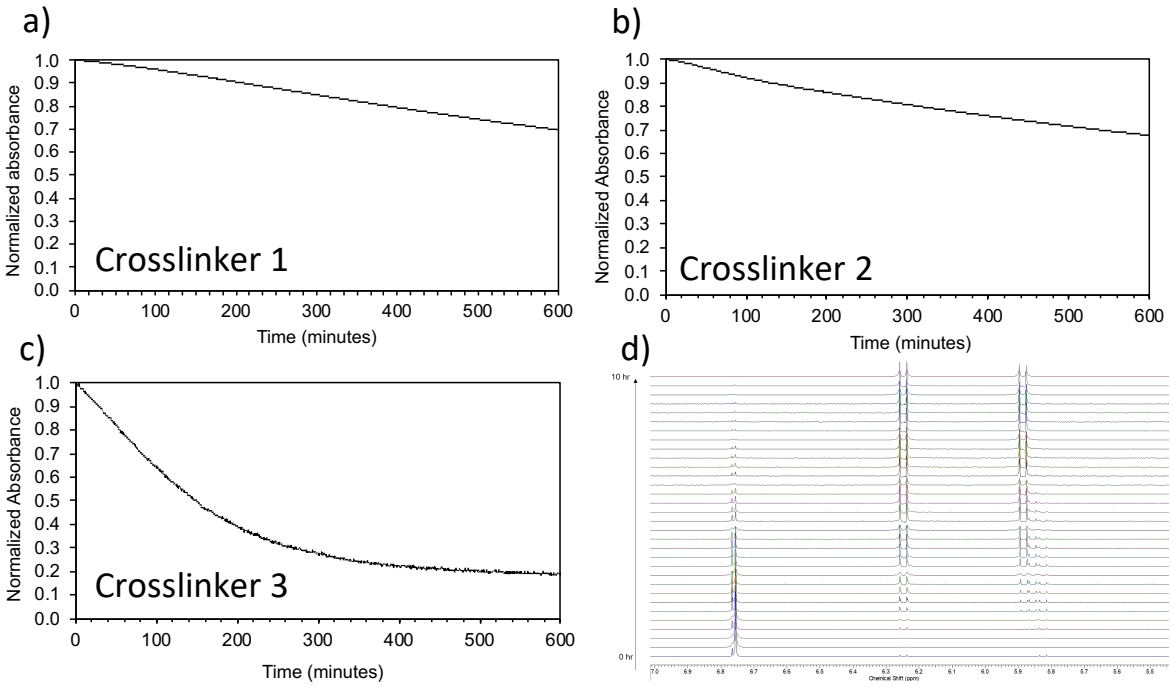

Figure 3.13: Hydrolysis trials for crosslinkers 1-3. a) The resulting normalised absorbance at 299 nm obtained when the crosslinker was added to phosphate buffer (pH 7.4) at a concentration of 40 mg/mL, measured every 10 seconds for 10 hours at 25°C. a) Crosslinker **1**. b) Crosslinker **2**. c) Crosslinker **3**. d) Stacked ^{1}H NMR spectra of crosslinker **3** in phosphate buffer measured every 20 minutes for 10 hours.

For crosslinker **1** (Figure 3.13a) the absorbance was found to decrease by 30% across the entire 10-hour study, confirming a significant concentration of maleimide groups remain available for crosslinking even after 10-hour exposure to phosphate buffer. Crosslinker **2** (Figure 3.13b) presented a similar trend to crosslinker **1**, once again showing a decrease in absorbance of 30% across the 10-hour experiment. However, crosslinker **3** (Figure 3.13c) displayed a significantly higher percentage decrease in absorbance over the 10-hour experiment. Specifically at hour 10, an 80% decrease in absorbance was observed, revealing few maleimide groups available for crosslinking after 10-hour exposure to phosphate buffer. To validate this result, a ^{1}H NMR spectra of crosslinker **3** was measured every 20 minutes over the course of a 10-hour period. The resulting stacked traces are shown in Figure 3.13d. Here, it was shown the peak corresponding to the two protons of the carbon-carbon double bond in the

maleimide that experiences hydrolysis almost entirely disappeared by the 10-hour time point. Furthermore, peaks corresponding to the hydrolysed maleimide increased in intensity proportionally with the decrease in the non-hydrolysed peak, confirming hydrolysis was responsible for this phenomenon. Therefore, the NMR experiment corroborated the absorbance results of crosslinker **3**, confirming over the 10-hour period almost all maleimides were hydrolysed. Work by Szijj *et al*. revealed a similar differential hydrolysis of varied maleimide compounds (Szijj *et al.*, 2018). From these results it was determined overnight incubation of the crosslinker with the relevant protein solution was optimal to allow maximal crosslinking time.

3.3.3 Confirming functionality of maleimide groups with LCMS

After determining the physiochemical characteristics of the synthesised crosslinkers to inform the crosslinking procedure for the future MGC trials, it was necessary to confirm reactivity of the functional groups of the synthesised crosslinkers. Moreover, ensuring these small molecule crosslinkers could bind to multiple large biomacromolecules uninhibited by steric hindrance was vital. For this purpose, a 4067.01 g/mol peptide of 95% purity, termed KANK1 d60-68 was employed (Figure 3.14a), containing a single N-terminal cysteine available for binding to the crosslinkers. Here, any complexes formed could be separated using liquid chromatography, with the resultant molecular masses measured with MS. The resulting MS traces are shown in Figure 3.14a-d. The LCMS experiments confirmed all three crosslinkers contained fully functional maleimide groups, capable of crosslinking one, two and three KANK1 peptides for crosslinkers **1**-**3** respectively (Figure 3.14b-d). Due to the 95% purity of the Kank1 peptide and limitations of the instruments resolution, the molecular weight was found to fluctuate by around 0.06 g/mol, explaining for the slight deviations in molecular weight of the crosslinkers when 4067.01 g/mol was utilised as the peptide mass in the calculation. To determine the complex present within each MS trace, the value of the tallest peak was taken, the mass of a proton subtracted, and the resulting value multiplied by the charge labelled above the peak (i.e. 3+ in Figure 3.14a). The known mass of the KANK1 peptide and the crosslinkers was then used to determine the existing complex by calculating the combination of each constituent required to achieve the value.

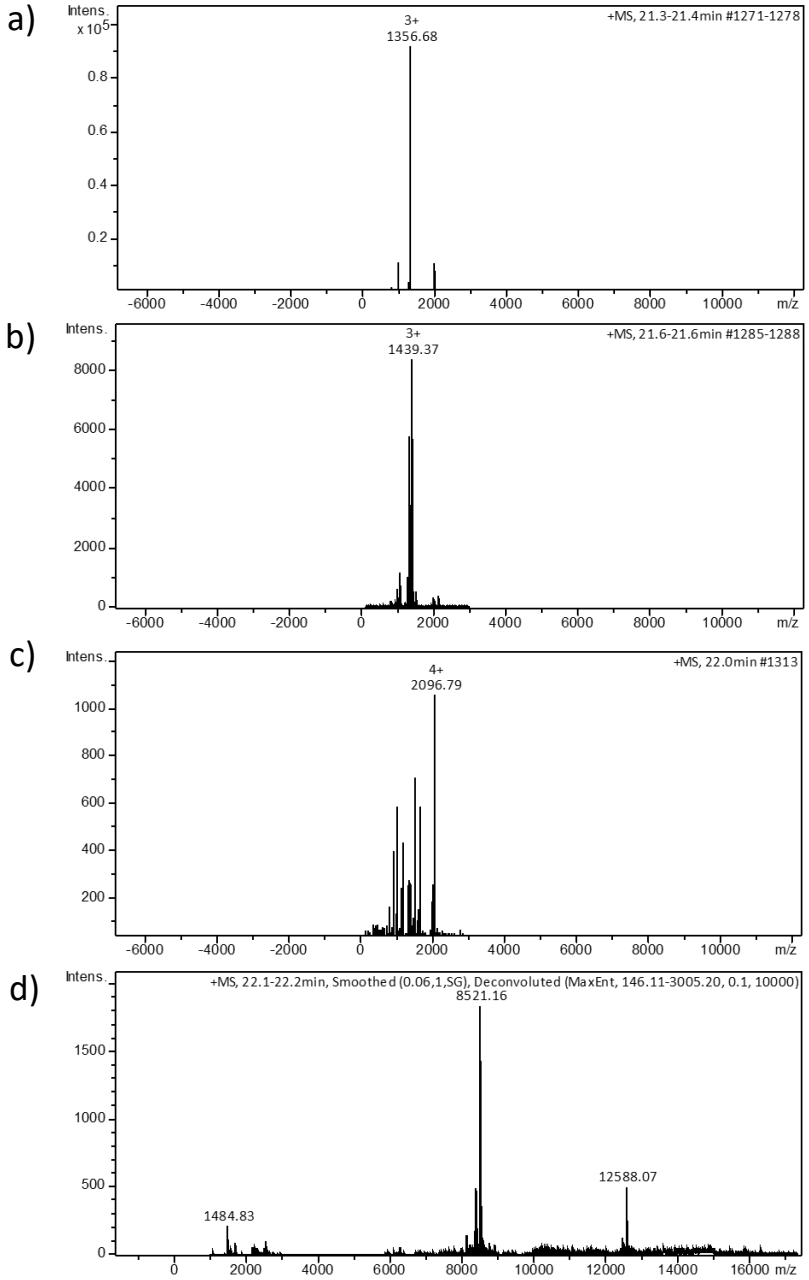

Figure 3.14: LCMS characterisation of crosslinkers 1, 2 and 3. a) KANK1 peptide (0.10 mM, 4067.01 g/mol) used for crosslinking characterisation. b) Crosslinker **1** (1.00 mM, 153.08 g/mol) bound to single KANK1 peptide (0.10 mM) confirming all maleimide groups capable of binding biological macromolecules. c) Crosslinker **2** (1.00 mM, 248.08 g/mol) bound to two KANK1 peptides (1.00 mM) confirming all maleimide groups capable of binding biological macromolecules d) Crosslinker **3** (1.00 mM, 386.12 g/mol) bound to three KANK1 peptides (1.00 mM) confirming all maleimide groups capable of binding biological macromolecules

3.4 Optimising the crosslinking protocol for MGC trial

During the protein and crosslinker characterisation experiments several issues likely to impact hydrogel formation with the crosslinking strategy chosen were elucidated.

The discovery of these issues and subsequent addressal are outlined within this section.

3.4.1 LCMS revealed maleimides react with TCEP

When investigating the ability of crosslinkers **1**-**3** to form substituted species with the KANK1 peptide, LCMS revealed a small molecule of ~250 g/mol also reacted with the crosslinkers. Multiple species containing combinations of the ~250 g/mol molecule were found, with two examples displayed in Figure 3.15a-b. These complexes were observed in all three crosslinker-peptide samples, suggesting the molecule was either present in the synthesised peptide or was added to the reaction mixtures during the experiment (I.e., reducing agent or buffer component). TCEP has previously been found to react with maleimides (Kantner and Watts, 2016), a reducing agent added to this reaction to ensure reduced thiols were present in KANK1 for crosslinking. TCEP matched the molecular weight of the ~250 g/mol contaminant found forming substituted species with the crosslinkers, presenting the only reasonable explanation for these observed complexes. To confirm TCEP as the culprit, a test was performed utilising Ellman's reagent (Figure 3.15c-d). Here, Ellman's reagent (DTNB) was used to determine the concentration of unreacted TCEP present through TCEPs reduction of DTNB to NTB producing TCEP oxide (Han and Han, 1994). NTB absorbs in the region of 412 nm, allowing for its production to be measured, also forming a yellow solution.

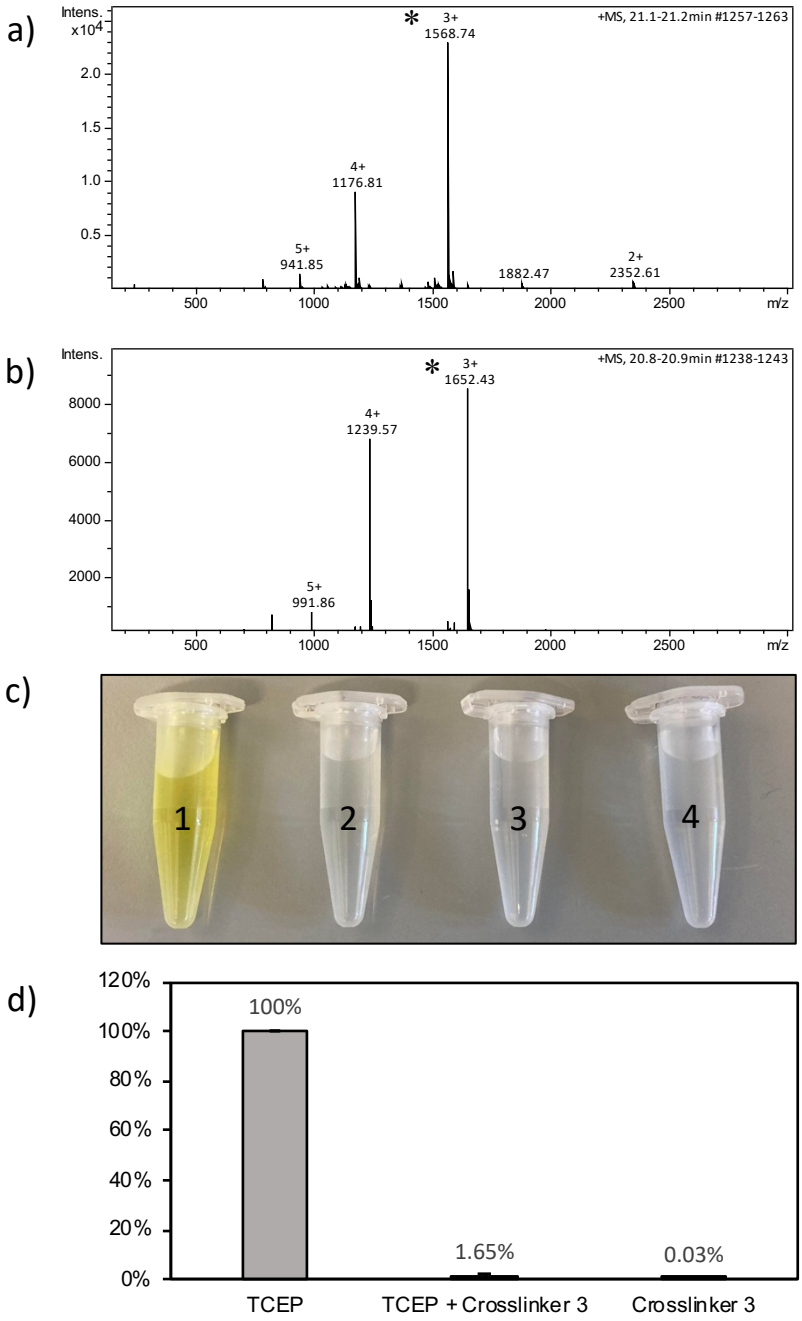

Figure 3.15: TCEP reacting with crosslinkers. a) LCMS spectra of crosslinker **3** bound to one KANK1 peptide and one molecule of TCEP, peak indicated with *. b) LCMS spectra of crosslinker **3** bound to one KANK1 peptide and two molecules of TCEP, peak indicated with *. c) Ellman's reagent was used to quantify crosslinker **3**s reactivity with TCEP. 1 = TCEP (1mM) in phosphate buffer pH 7.4 after 1 hour. 2 = Crosslinker **3** (1 mM) and TCEP (1 mM) in phosphate buffer pH 7.4 after 1 hour. 3 = Crosslinker **3** (1 mM) in phosphate buffer pH 7.4 after 1 hour. 4 = phosphate buffer pH 7.4 control after 1 hour. d) Quantification of % TCEP remaining calculated from absorbance at 412 nm. The TCEP in phosphate buffer pH 7.4 after 1 hour was set to 100% TCEP remaining for these calculations. (n=3, error bars = standard deviation).

Firstly a 1 mM solution of TCEP in phosphate buffer (pH 7.4) was incubated at room temperature for one hour and reacted with Ellman's reagent, revealing a colour change from clear to yellow (Figure 3.15c1), with the absorbance at 412 nm measured and calibrated as 100 % remaining TCEP. When the same 1 mM solution of TCEP in phosphate buffer was incubated with 1 mM of crosslinker **3** (Figure 3.15c2) and measured with Ellman's reagent, the absorbance was found to decrease by 98.35 % on average (n=3) (Figure 3.15d). This result confirmed TCEP and crosslinker **3** could undergo a crosslinking reaction, with the reaction reaching a high percentage completion within one hour. A Control of crosslinker **3** in phosphate buffer (pH 7.4) alone (Figure 3.15c3) was used to ensure no reactivity of crosslinker **3** with Ellman's reagent (n=3) (Figure 3.15d). Together these results confirmed TCEP reacted with maleimides under the conditions utilised for pGEL001 crosslinking, therefore TCEP needed removing from the reaction prior to addition of the crosslinker moving forward.

3.4.2 pGEL001 disulphide bonds with itself to form higher order species

During the purification optimisation procedure for pGEL001, UV-traces corresponding to the elutions that contained pGEL001 presented as a broad peak, with multiple peaks contained within. One explanation for this observation was disulphide bonding occurring between pGEL001 monomers, forming dimer, trimer and multimer species. Additionally, anti-His western blot analysis of purified pGEL001 revealed a band corresponding to the size of a pGEL001 dimer to contain His-tagged protein (Figure 3.16a). To confirm this hypothesis, pGEL001 samples following purification were run using SDS-PAGE in both non-reducing and reducing conditions. The results from this experiment are shown In Figure 3.16b. The reducing agents chosen for this test were dithiothreitol (DTT) and TCEP, with increasing concentrations of each reducing agent tested to determine the concentration required for complete reduction of pGEL001 over a one-hour period.

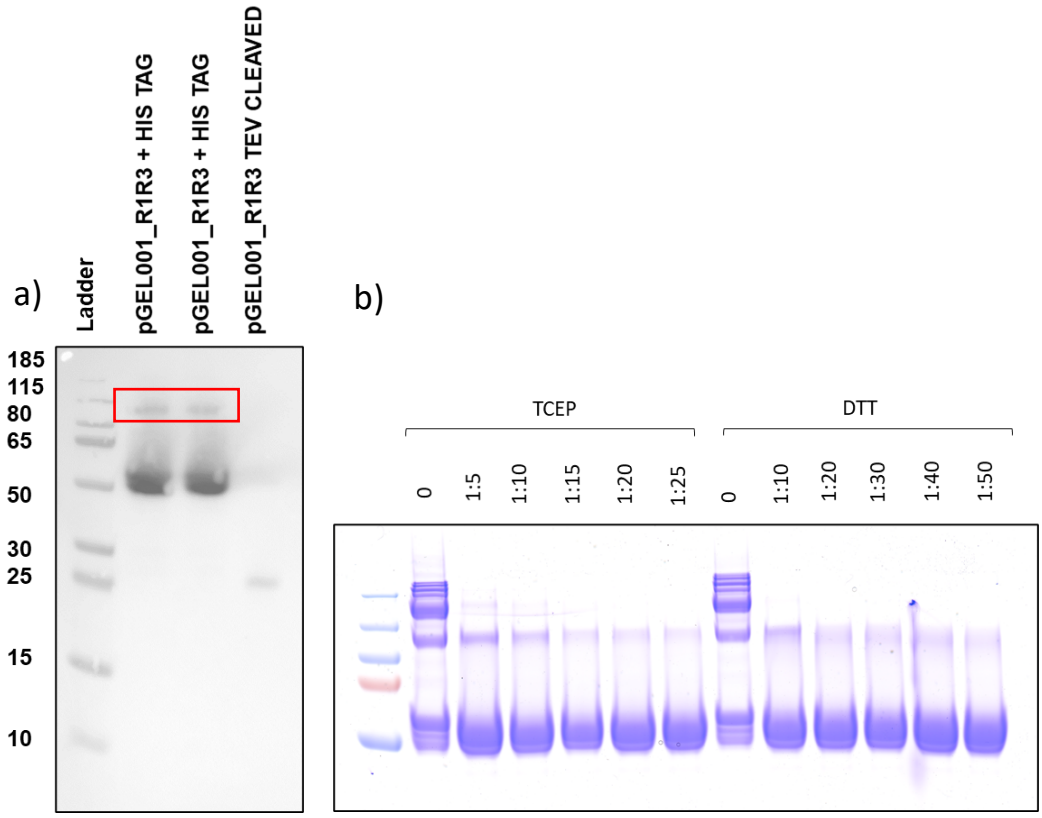

Figure 3.16: pGEL001 forming higher order species through disulphide bonding. a) An anti-His western blot of pGEL001 following purification, revealing a band corresponding to the molecular weight of a pGEL001 dimer highlighted with a red box. b) Wells labelled 0 were loaded with pGEL001 in sample buffer containing no BME. Wells not labelled 0 refer to the ratio of thiol to reducing agent, with these samples also loaded in sample buffer containing no BME. Samples were taken following one-hour incubation at 25°C.

Results from the SDS-PAGE (Figure 3.16b) revealed in non-reducing conditions pGEL001 existed predominantly as a monomer, with addition dimer, trimer and multimeric species present. When either TCEP or DTT was added, these larger species were removed, confirming pGEL001 disulphide bonds with itself. Therefore, due to the crosslinkers requiring reduced cysteines for the maleimide group to bind to the thiol, a reducing agent would be required before crosslinking could take place. As it was previously determined TCEP reacts with the maleimide based crosslinkers (3.4.1), the minimum concentration of these reducing agents required for complete pGEL001 reduction was determined. Here, it was found 1:15 cysteine to TCEP and 1:30 cysteine to DTT were necessary to achieve maximum reduction.

Following determination of the minimum concentration of reducing agent required, experiments were conducted to elucidate the effect of each reducing agent on the formation of higher order pGEL001 species following addition of crosslinker **3**. Here, crosslinker **3** was added to a reduced solution of pGEL001 using either DTT or TCEP at the minimum ratios determined. DTT was investigated here due to the presence of two sulfhydryl groups within its structure. Therefore, DTT could theoretically react with two maleimide groups, allowing for continued production of a network structure when bound to crosslinker **3**. Contrarily, TCEP can only bind a single maleimide, therefore any TCEP forming a complex with crosslinker **3** would terminate the network formation at that site. Samples of pGEL001 following addition of 1:1, 1:2 and 1:3 ratios of cysteine to maleimide group equivalents from crosslinker **3** were run using SDS-PAGE following a one-hour reaction period. Additionally, the effects of a second addition of crosslinker **3** at the same ratio was conducted immediately following the one-hour period and subsequently left for a second one-hour reaction period. These results are shown in Figure 3.17.

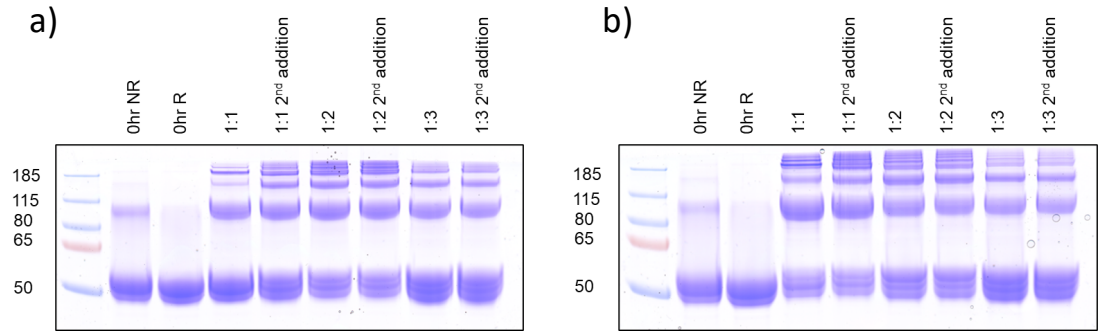

Figure 3.17: Formation of higher order pGEL001 species reduced with either TCEP or DTT following addition of crosslinker 3 over a range of concentrations. (NR = non-reduced, R = reduced). a) Formation of higher order species when pGEL001 was reduced with 30:1 DTT:cysteine and various ratios of pGEL001:crosslinker **3** were added. b) Formation of higher order species when pGEL001 was reduced with 30:1 TCEP:cysteine and various ratios of pGEL001:crosslinker **3** were added.

The results obtained, displayed in Figure 3.17a-b, revealed more pGEL001 was incorporated into higher order species in the TCEP reduced pGEL001 sample than the DTT reduced sample. When looking at the DTT reduced sample in Figure 3.17a, the 1:2 addition of crosslinker **3** yielded the best change from monomer to higher order

species of pGEL001. This result was also validated by the increase in higher order species observed from the second 1:1 addition of crosslinker **3** also seen in Figure 3.17a, confirming that 1:2 is the optimal ratio of cysteine to maleimide for higher order species formation in the DTT condition. Opposingly, for the TCEP reduced pGEL001 (Figure 3.17b), a 1:1 maleimide to cysteine ratio was found to be optimal in the conversion of monomer to higher order species with little change observed following a second addition of 1:1. Overall, the best condition in the TCEP sample revealed increased formation of higher order species compared to the best condition in the DTT reduced pGEL001. Therefore, TCEP was chosen as the reducing agent for all subsequent gelation formation trials.

3.4.3 Removal of TCEP following a one-hour reduction period from pGEL001 solutions

The final procedural element requiring addressal before progression to material formation experiments was determination of the optimal TCEP removal method. As previously stated, any TCEP that reacts with the maleimide groups of the crosslinkers would result in capping of the network. At a 15:1 ratio of TCEP to cysteine (minimum ratio determined for complete reduction of pGEL001), 15-fold more TCEP would be present in the reaction mixture than pGEL001 cysteines following reduction, likely resulting in the majority of maleimide groups becoming occupied by TCEP instead of the pGEL001 cysteine groups. TCEP occupation of maleimide groups would result in a vastly reduced network formation. Therefore, removal of the maximum concentration of TCEP possible from the reaction mixture following reduction was required to ensure formation of a hydrogel. As disulphide bonding is likely to begin upon removal of TCEP, the removal process needed to be fast with minimal increases in volume occurring (as the solution would require subsequent concentration). Desalting columns, specifically PD-10 (Cytiva) columns, were chosen for this purpose balancing speed of removal with minimised pGEL001 volume increases. To quantify the percentage TCEP removed by these columns, Ellman's reagent was employed. Firstly, a standard curve was produced using 0.0-1.5 mM TCEP, with the absorbance at each concentration measured. These absorbances were plotted against the respective TCEP concentration, shown in Figure 3.18. The linear portion of this graph was used for TCEP concentration calculations in the resulting experiments. Following

construction of the standard curve, 100 mM TCEP solution was applied to a PD-10 column, with a sample of the resulting elution taken to quantify the TCEP concentration remaining. This experiment was performed in triplicate, with the average values and standard deviation quoted. Here, after one application through the PD-10 column the resulting elution, when added to Ellman's reagent, produced an absorbance at 412 nm of 2.16 (standard deviation = 0.01). As this absorbance fell outside of the linear portion of the standard curve an exact concentration could not be calculated. However, the concentration required to produce this absorbance value had to be >1.5 mM. The elution was then applied to a second PD-10 column with the same procedure repeated. The resulting average absorbance of the elution from the second PD-10 column was determined to be 1.05 (standard deviation = 0.27). As this value fell within the linear region of the standard curve, the resulting TCEP concentration of 0.56 mM was calculated. Therefore, 99.44% of TCEP was removed after two applications of the solution through PD-10 columns. Applying this calculated percentage removal to the 15:1 ratio of TCEP:cysteine required for pGEL001 reduction, the ratio following application through two PD-10 columns would become 0.69:1. Although at this ratio 69% of maleimide sites could become occupied by TCEP, following application through these PD-10 columns, concentration of pGEL001 to 40, 80, 160 and 200 mg/mL would be conducted.

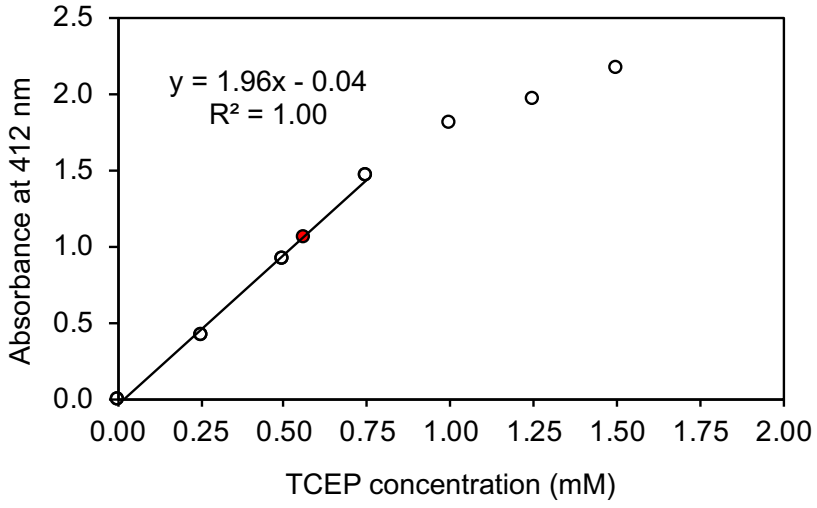

Figure 3.18: Standard curve of TCEP concentrations when added to Ellman's reagent. The absorbance of the elution from the second PD-10 column is plotted in red.

From previous experimentation, it was determined that the maximum concentration of pGEL001 that can be reduced with a 15:1 ratio of TCEP to cysteine was 12 mg/mL. This concentration was selected to reduce the risk of pGEL001 or TCEP aggregating out of solution. Following application to two sequential PD-10 columns this 12 mg/mL pGEL001 solution would be diluted to ~0.5x the initial concentration, equal to 6 mg/mL. To reach the first concentration of 40 mg/mL, the volume would decrease by ~3-fold, leading to 87.5% of the remaining TCEP removed by concentration in 30 KDa mwco concentrators. Thus at the lowest tested concentration of 40 mg/mL for minimum gelation trials, the ratio of TCEP to cysteine would equal ~0.086:1, at 80 mg/mL would equal ~0.043:1, at 140 mg/mL would equal ~0.011:1, and at 200 mg/mL would equal ~0.005:1. Therefore with this procedure by 140 mg/mL a maximum of 1% of maleimide groups could be occupied by TCEP.

3.5 Formation of TSAMs from pGEL001

Utilising all the information obtained from the previously described experiments, a complete method was designed to allow for optimal crosslinking of pGEL001 monomers in MGC trials. MGC trials started by concentrating pGEL001 in phosphate buffer (pH 7.4) to 12 mg/mL. To this solution, TCEP was added dropwise from a 0.244 M stock (found to result in no aggregation of protein) resulting in a final 15:1 TCEP to cysteine ratio. The pGEL001 solution was then left to reduce at room temperature for one hour. Following this time period, the solution was applied to the first round of PD-10 columns, with the elution immediately applied to a second round of PD-10 columns. At this point the solution was split into 30 kDa mwco centrifugal concentrators and concentrated to 40, 80, 160 and 200 mg/mL. Upon achieving the desired concentrations, the respective crosslinker was added to achieve a 1:1 maleimide to cysteine ratio and left at 4°C overnight for gelation to occur.

3.5.1 MGC trial of pGEL001

Due to the small volumes (100 μL) used in these trials, the typical inversion method for determining the MGC was not suitable, therefore gelation was determined through attempted pipetting of the solution. Complete gelation was defined as the

concentration at which the entire solution was unable to be drawn into the pipette. The results from this experiment are summarised in Table 3.1.

Table 3.1: The results from MGC trials on crosslinkers 1-3. (n=3). Yes = gel present, No = no gel present, Partial = gel was formed but liquid was still present, - = condition not tested.

	DMSO	Crosslinker 1	Crosslinker 2	Crosslinker 3
200 mg/mL	No	No	No	Yes
190 mg/mL	-	-	-	Partial
180 mg/mL	-	-	-	No
160 mg/mL	No	No	No	No
80 mg/mL	No	No	No	No
40 mg/mL	No	No	No	No

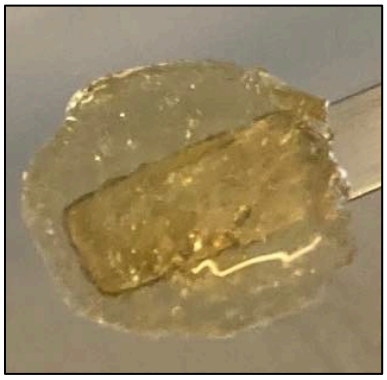

Figure 3.19: Image of a TSAM obtained from addition of crosslinker 3 to 200 mg/mL pGEL001.

As shown in Table 3.1 no gelation was observed at any of the tested concentrations following addition of 4% DMSO or crosslinker **1** to pGEL001. This was expected due to neither of these conditions containing a compound capable of forming crosslinks between pGEL001 monomers, with these results demonstrating that neither the presence of DMSO or maleimide groups alone were capable of inducing gelation. Crosslinker **2** also presented no gelation. During previous solubility investigations crosslinker **2** revealed low levels of solubility even at the lowest concentrations required for achieving 1:1 maleimide to cysteine ratios for the 40 mg/mL pGEL001 solution. Therefore it was likely that insufficient concentrations of crosslinker **2** were

dissolving into the solution to allow for extensive crosslinking of the pGEL001 monomers to take place. Crosslinker **3** induced no gelation up to 160 mg/mL, however at 200 mg/ml complete gelation was observed (Figure 3.19). This was confirmed through an inability to pipette the solution, with further examination revealing a highly extensible material when attempting to remove the hydrogel from its mould. To determine a more exact MGC, 180 mg/mL and 190 mg/mL pGEL001 solutions were also tested, with 180 mg/mL displaying no gelation and 190 mg/mL displaying partial gelation.

3.5.2 Theoretical calculation of maximum energy dissipation by TSAMs.

As the concentration of pGEL001 required to form the TSAM was determined at 200 mg/mL, in addition to the unfolding forces of each monomer and lengths of both the folded and unfolded domains previously elucidated, a calculation could be performed to estimate the theoretical maximum energy dissipation achievable by the material.

Firstly, the number of pGEL001 molecules in the TSAM is calculated using the equation 3.1.

$$(Equation\ 3.1)\ N_{pGEL001} = \frac{C_P \left(\frac{mg}{mL}\right) x\ N_A \left(\frac{Da}{g}\right) x\ 10^{-12} \left(\frac{mL}{\mu M}\right)}{M_R\ (Da)}$$

In equation 3.1, $N_{pGEL001}$ is the number of pGEL001 monomers in the gel, C_P is the concentration of protein in the material, N_A is Avogadro's number (6.02 x 10^{23} Da/g) and M_R is the proteins molecular weight. When these values are entered into equation 3.1, we get equation 3.2.

$$(Equation\ 3.2)\ N_{pGEL001} \left(\frac{Proteins}{\mu M^3}\right) = \frac{200 \left(\frac{mg}{mL}\right) x\ 6.02\ x\ 10^{23} \left(\frac{Da}{g}\right) x\ 10^{-12} \left(\frac{mL}{\mu M}\right)}{51851.44\ (Da)}$$

The solution to equation 3.2 gives equation 3.3.

$$(Equation\ 3.3)\ N_{pGEL001} = 2.32\ x\ 10^{9}\ \frac{proteins}{\mu M^{3}}$$

Next, the energy each pGEL001 molecule can dissipate during an unfolding event is calculated using equation 3.4.

$$(Equation\ 3.4)\ Work\ done\ (J) = force\ (N)\ x\ Distance\ moved\ (m)$$

Previous single molecule work (Yao *et al*., 2016) calculated the unfolding force of each rod domain of talin. R1, R2 and R3 unfolding forces were determined at 20, 15 and 5 pN respectively. Furthermore, taking measurements of folded (5 nm) and unfolded (12 nm) helices from (Barnett and Goult, 2022) the distance moved during an unfolding event for each domain can be calculated. These were estimated at 55 nm for R1 (5 helix bundle) and 43 nm for R2 and R3 (4 helix bundles). Therefore, making the assumption that the mutated forms of these rod domains within pGEL001 retain the same unfolding forces an estimate of work done can be calculated in equations 3.5-3.7.

$$(Equation\ 3.5)\ R1{:}\ 20\ x\ 10^{-12}\ (N)\ x\ 55\ x\ 10^{-9}\ (m) = 1.8\ x\ 10^{-18}\ J$$
$$(Equation\ 3.6)\ R2{:}\ 15\ x\ 10^{-12}\ (N)\ x\ 43\ x\ 10^{-9}\ (m) = 6.45\ x\ 10^{-19}\ J$$
$$(Equation\ 3.7)\ R3{:}\ 5\ x\ 10^{-12}\ (N)\ x\ 43\ x\ 10^{-9}\ (m) = 2.15\ x\ 10^{-19}\ J$$

As one pGEL001 monomer contains all three of these domains, the total energy one molecule can dissipate, $pGEL001\ E_{diss}$, is equal to the sum of each rod domains work done, giving equation 3.8.

$$(Equation\ 3.8)\ pGEL001\ E_{diss} = R1\ (J) + R2\ (J) + R3\ (J)$$

Entering the values from equations 3.5-3.7 into equation 3.8 gives the total energy dissipation of one molecule of pGEL001 shown in equation 3.9.

$$(Equation\ 3.9)\ 1.8\ x\ 10^{-18}(J) + 6.45\ x\ 10^{-19}(J) + 2.15\ x\ 10^{-19}(J) = 2.66\ x\ 10^{-18}\ (J)$$

Combining the calculated number of molecules of pGEL001 from equation 3.3 and the calculated pGEL001 energy dissipation from equation 3.9, the maximum energy absorption can be calculated per unit volume of TSAM using equation 3.10.

$$(Equation\ 3.10)\ TSAM\ E_{diss}(J) = V\ (\mu M^3)\ x\ N_{pGEL001}\ \left(\frac{proteins}{\mu M^3}\right) x\ pGEL001\ E_{diss}\ (J)$$

In equation 3.10, V is the volume of TSAM. Applying the values obtained in equations 3.3 and 3.9 to a TSAM volume of 1 L (assuming the density of the material is approximately the same as water) gives equation 3.11.

$$(Equation\ 3.11)$$

$$1\ x\ 10^{15}\ (\mu M^3)\ x\ 1.0\ \left(\frac{g}{mol}\right) x\ 2.32\ x\ 10^{9}\ \left(\frac{proteins}{\mu M^3}\right) x\ 2.66\ x\ 10^{-18}\ (J)$$

$$= 6.17\ x\ 10^{6}\ \frac{J}{kg} = 6.17\ \frac{MJ}{kg}$$

Therefore, 1 kg of TSAM could theoretically dissipate 6.17 MJ of energy when impacted if all the rod domains within the pGEL001 molecules in the TSAM unfold, shown in equation 3.10. This theoretical value exceeds that of Kevlar's experimentally obtained value, and a carbon nanotube based material tested in supersonic impact experiments (Cai *et al*., 2021). Therefore, TSAM materials offer great potential as a shock absorbing material.

3.6 Discussion

In this chapter, extensive investigation into the development of the first iteration of a TSAM material was conducted. The key characteristics of the elements required for formation of the TSAM were elucidated, informing the resulting protocol used for MGC trials.

Initially, the design of the recombinant protein, pGEL001 was discussed. This included the important design elements required to engineer the protein to be successfully incorporated into a TSAM material, with the optimum purification method subsequently determined. Following this, the resulting changes in structure to the R1 and R2 domains as a consequence of cysteine to serine mutations were investigated with NMR and CD. Here it was determined the R1 structure in pGEL001 was almost entirely retained, with only a few shifts observed in the ^{1}H-^{15}N HSQC spectra compared to the wild-type R1 spectra. The resulting structural changes in R2 were investigated using CD due to expression issues in the media required for NMR experimentation; with CD revealing a change in stability marked by a 5.8°C decrease in T_m of the mutated R2 compared to the wild-type. Despite this, due to R2 still presenting alpha helical folding (therefore able to unfold when exposed to force), with its reduced stability potentially occurring due to its inability to pack against the side of R1 when expressed in isolation, pGEL001 was determined to be viable for a prototype TSAM monomer. Furthermore, pGEL001 was shown to present overall enhanced stability compared to wild-type R1-R3. Following the successful synthesis of crosslinkers **1**-**3**, the solubility and hydrolysis profile of these compounds was determined. These parameters were important to inform the selection of protein concentrations for the MGC trial and obtain an estimate of the time course of the gelation reaction. Here it was confirmed the desired concentrations of 40-200 mg/mL pGEL001 could be used for MGC trials based on the solubility of crosslinkers **1** and **3**, while crosslinker **2** was likely to be insoluble at all tested concentrations. Furthermore, near complete hydrolysis was determined to occur following 10-hour exposure of crosslinker **3** to phosphate buffer (pH 7.4), indicating incubation of crosslinker and pGEL001 overnight to be suitable for the gelation period. Although

this hydrolysis experiment was conducted at 25°C, the incubation of the gelation mixture was performed at 4°C to ensure protein folding was retained. Therefore, this hydrolysis period was used as an indication of hydrolysis time, likely to be slower at 4°C, hence why overnight incubation was selected. Finally, LCMS confirmed the synthesised crosslinkers to be capable of crosslinking the respective number of large biomolecules expected.

The remainder of the chapter probed key issues requiring addressal to ensure efficient crosslinking of pGEL001 via the maleimide based compounds. Specifically, TCEPs reaction with maleimides was identified through LCMS and confirmed with a series of Ellman's reagent assays. Due to the efficient reactivity of TCEP with maleimides, it was determined TCEP required removal from the pGEL001 solution prior to addition of the crosslinker, to ensure capping of the crosslinkers did not occur. Therefore, the minimum concentration of TCEP capable of complete reduction of pGEL001 was found, with experimentation using the alternate reducing agent DTT confirming TCEP as the optimal reagent for this purpose. An assay utilising Ellman's reagent confirmed desalting columns to achieve the required level of TCEP removal, with subsequent calculations performed to determine the approximate levels of TCEP remaining at each concentration of pGEL001 following concentration of the protein. A MGC trial was subsequently conducted, producing the first iteration of a TSAM using crosslinker **3** In a 200 mg/mL solution of pGEL001. Finally, calculations were performed to reveal the maximum energy dissipation achievable from the resultant TSAM, indicating potential energy dissipation similar to that of Kevlar and carbon nanotube-based materials, both of which are employed as defence materials against high velocity impacts.

Overall, the first aim identified in Section 1.5 was achieved within this chapter. Specifically, the first iteration of a TSAM was produced, and key aspects within the process optimised. Building on these results, TSAMs properties and shock-absorbing performance will be probed in Chapter 4, allowing the second key aim from Section 1.5 to be addressed. The established pipeline discussed within this chapter will also

be utilised to produce further talin monomers for TSAM development, which will be investigated within Chapter 5.

Chapter 4: Characterisation and performance testing of TSAMs

4.1 Overview

This chapter focuses on the characterisation of the material properties of TSAMs. The primary goal of this project was to capture the energy dissipating mechanism of talin rod domain unfolding within a functional material, and was therefore a key question addressed. Furthermore, investigation into whether pGEL001s energy dissipating mechanism, when integrated into a material, translated into an effective shock absorber was conducted. Currently, almost all protein-based hydrogels developed have been solely applied to biomedical applications (Kan and Joshi, 2019). Here, we investigated TSAMs for a non-biomedical application as a proof of principle for TSAMs in alternative sectors. Specifically, supersonic impact experiments were performed utilising a light gas gun. To apply industrial relevance to this study, direct comparisons were drawn to the industry standard material, silica aerogels, currently employed for these supersonic impact studies (Malakooti *et al*., 2022).

4.2 Investigating the internal structure of TSAMs

Following the successful formation of a TSAM in the MGC trial, investigations into the underpinning structure of the hydrogels were performed. Transmission electron microscopy and scanning electron microscopy were employed for this purpose, allowing for both nanometre and micrometre scale elucidation of the network formation of crosslinked pGEL001 monomers.

4.2.1 Investigating the internal structure of TSAMs on the nanometre scale with transmission electron microscopy

Immunogold labelling coupled with transmission electron microscopy imaging is a valuable technique for determining the location of tagged proteins within a sample (Jones, 2016) (Rostamabadi *et al*., 2020). These methods were exploited here to determine the underlying structure of crosslinked pGEL001 monomers in TSAMs, aiming to confirm the presence of the expected lattice structure shown in Figure 4.1a. Gold particle conjugated anti-mouse antibodies localised to pGEL001 due to

their interactions with the mouse anti-His labelled pGEL001 monomers contain within the TSAM. Transmission electron microscopy reveals the position of the gold beads due to the inability of electrons from the generated electron beam to pass through the gold, whilst additional uranyl acetate staining of the TSAM allows for simultaneous mapping of its structure through the differential transmissibility of electrons by the TSAM components resulting from the different degrees of staining (Graham and Orenstein, 2007).

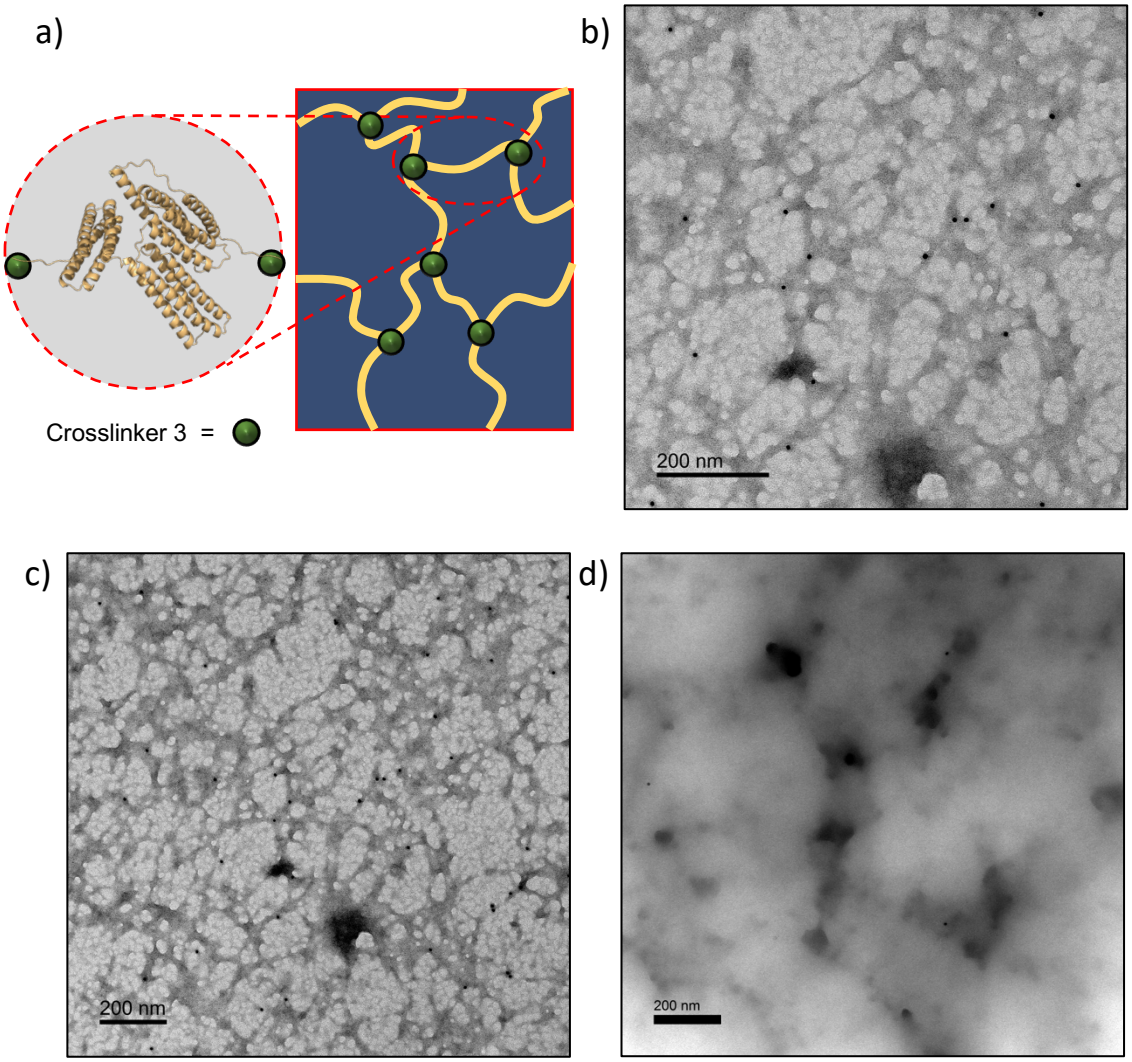

Figure 4.1: Immunogold stained TSAM imaged with transmission electron microscopy. a) Predicted structure of the TSAM network formed from pGEL001 and crosslinker **3** on the nanometre scale. b)-c) Transmission electron microscopy image of immunogold stained TSAM. d) Immunogold stained TEV cleaved TSAM control showing minimal gold bead labelling. Each black dot corresponds to a 5 nm gold bead bound to a pGEL001 monomer via its His-tag.

The resultant transmission electron microscopy images of the immunogold stained TSAM revealed a lattice structure shown in Figure 4.1b-c. The 5 nm gold beads were localised to the lattice structure, observed as black dots, confirming the presence of pGEL001. Therefore, it was confirmed on the nanometre scale, pGEL001 monomers linked to form the predicted network-like structure expected from the crosslinking system (Figure 4.1a). The control sample (Figure 4.1d), consisting of TEV cleaved pGEL001 (200 mg/mL) with crosslinker **3**, revealed a vastly reduced level of bound gold particles (>5-fold decrease in gold beads in Figure 4.1d compared to 1b-c). TEV cleavage of pGEL001 removes the His-tag from the protein, and in this instance due to the decreased staining of the control, confirmed the specificity of the gold beads for pGEL001s His-tag. It is important to note, only His-tags orientated towards the surface were available for labelling with gold beads. Therefore, only a small percentage of gold beads can bind compared to the number of His-tagged proteins present in the sample.

4.2.2 Investigating the internal structure of TSAMs on the micrometre scale with scanning electron microscopy

Scanning electron microscopy is a widely employed analytical method for characterising the internal structure of hydrogels (Gombert *et al*., 2020). In this technique a beam of electrons is scanned across the material with the backscattered or secondary electrons emitted detected (Omidi *et al*., 2017). These detected electrons are then used to construct an image of the material. Scanning electron microscopy imaging of a TSAM was conducted to elucidate the internal structure of TSAMs on the micrometre scale. Due to the high vacuum required for scanning electron microscopy imaging, the TSAM sample was dehydrated, forming a xerogel (a hydrogel following evaporative drying) to avoid desiccation in the sample chamber. Additionally, energy-dispersive X-ray analysis was performed on the sample. Energy-dispersive X-ray analysis utilises the incident beam of electrons in the scanning electron microscope to excite atoms within the sample. When these atoms return to the ground state, X-rays are emitted, with the wavelengths of the emitted X-rays unique to each element, allowing mapping of the elements contained within the sample of interest (Telegdi *et al*., 2018). Here, energy-dispersive X-ray analysis

was conducted on a TSAM to confirm the presence of pGEL001, by monitoring the presence and location of sulphur and carbon, two elements that were unique to pGEL001 in the sample mixture.

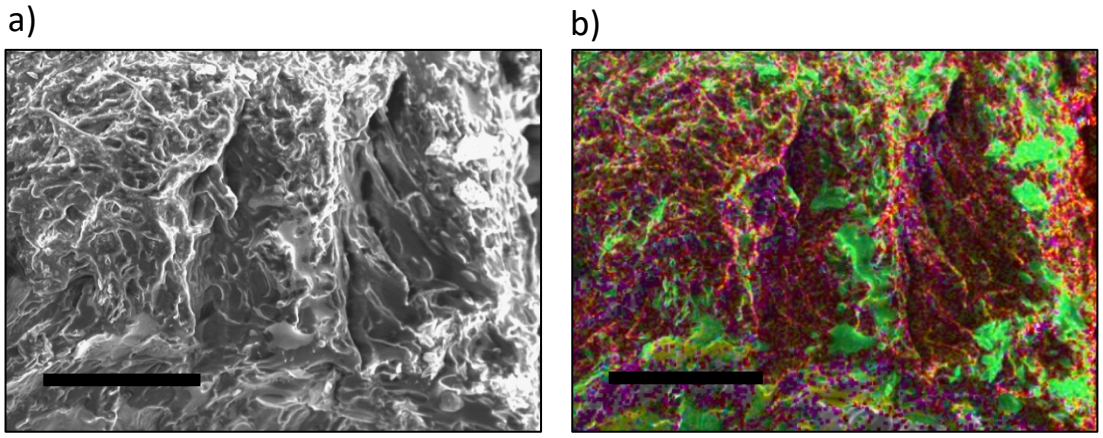

Figure 4.2: Scanning electron microscopy and energy-dispersive X-ray images of a TSAM xerogel. (Scale bar = 50 μm). a) Scanning electron microscopy image of a TSAM xerogel. b) Energy dispersive X-ray map of the same area of the TSAM in image. a) sulphur = yellow, carbon = red, oxygen = green, sodium = teal, phosphorus = purple.

Scanning electron microscopy images revealed fibrous structures contained within the TSAM xerogel (Figure 4.2a). The fibres presented widths of ~2 μm, with pores displaying diameters of ~10 μm. Energy dispersive X-ray analysis mapping shown in Figure 4.2b revealed the fibres to contain both carbon and sulphur atoms. As previously stated, within the TSAM material pGEL001 was the only component containing sulphur atoms, while both pGEL001 and crosslinker **3** were the only components to contain carbon. Thus, energy dispersive X-ray analysis confirmed the fibrous structures to contain pGEL001 monomers.

4.3 Developing a novel plate-reader methodology for quantifying gel fibre formation in TSAMs

When investigating hydrogel formation, effective characterisation of the hydrogel is important, particularly the determination of the MGC and detection of fibrous structure formation (Karoyo and Wilson, 2017). Many of the methodologies available for these purposes require large sample sizes and/or non aqueous states. These demands are particularly challenging to conform with when looking at protein

hydrogels due to the often large protein concentrations required for gelation (Wu *et al*., 2018) and need for aqueous conditions to retain protein folding (Gadzala *et al*., 2019). The TSAMs produced here exemplify these issues, with the MGC determined at 200 mg/mL, and the unique protein folding/unfolding mechanism of pGEL001 being the central interest of this material. Thus, there is a clear need for new methodologies achieving effective characterisation whilst addressing the aforementioned shortcomings. Previously a high throughput methodology for monitoring supramolecular gelation processes through plate reader measurements was proposed (White *et al*., 2020). In this section, I describe the development of a high throughput plate reader methodology adapted for monitoring protein-based hydrogel formation, demonstrated on TSAMs.

4.3.1 Wavelength scans to monitor OD changes resulting from crosslinker addition

Initially, UV-vis readings were performed to study the effect of the addition of either DMSO (vehicle) or crosslinkers **1** and **3** (in DMSO) to both buffer (Phosphate buffer pH 7.4) (Figure 4.3) and cysteine (Figure 4.3) containing solutions. The same experiment was subsequently performed on a selection of pGEL001 (Figure 4.3) solutions ranging from 40 mg/mL to 200 mg/mL. Here, measurements of the solutions OD following incident light wavelengths between 300-1000 nm were collected. For solutions of buffer, large increases in OD between 300-400 nm were observed from the addition of both crosslinker **1** (Figure 4.3a) and **3** (Figure 4.3d) compared to addition of the DMSO control, with the magnitude of the increase in OD correlating with crosslinker **1** and **3** concentration. This occurred due to maleimides absorbance at ~300 nm, with the high OD values obtained confirming the presence of unreacted maleimides in the solution. Between 400-1000 nm no increase in OD was observed from the addition of crosslinker **1** compared to DMSO, whilst crosslinker **3** presented an increase in OD across the full range of wavelengths, with the magnitude of the increase in OD decreasing with wavelength. Solutions of cysteine also presented an increase in OD between 300-400 nm upon addition of both crosslinker **1** (Figure 4.3b) and **3** (Figure 4.3e) compared to DMSO. However, the magnitude of the increase in OD from crosslinker **1** and **3** compared to DMSO was significantly lower than in the same region in the buffer solution conditions. This

reduction in OD between the buffer and cysteine conditions confirmed that a population of the crosslinkers maleimides underwent the desired Michael addition reaction with the cysteine molecules, therefore reducing the quantity of maleimides that absorb in the region of 300-400 nm. No increase in OD from the addition of crosslinker **1** compared to DMSO was observed between 400-1000 nm in the cysteine solution, whilst crosslinker **3** once again presented an increased OD across the full range of wavelengths, with this increase diminishing with wavelength. For the pGEL001 solution, a large OD between 300-400 nm was recorded for the DMSO control, crosslinker **1** (Figure 4.3c) and **3** containing pGEL001 solutions (Figure 4.3f). This occurred due to pGEL001s absorption in the region of 280 nm by tryptophan and tyrosine amino acids within its structure (Hazra *et al*., 2014). For the remainder of the wavelengths between 400-1000 nm, an increase in OD was observed from the addition of both crosslinkers **1** and **3** compared to the DMSO control. When looking specifically at the gelled sample of 200 mg/mL pGEL001 with crosslinker **3**, no obvious changes in the OD compared to the non-gelled pGEL0001 solutions was observed. The lack of an observable deviation in OD increase compared to the non-gelled samples was likely due to the translucent nature of the TSAMs, minimising the OD changes resulting from its new state.

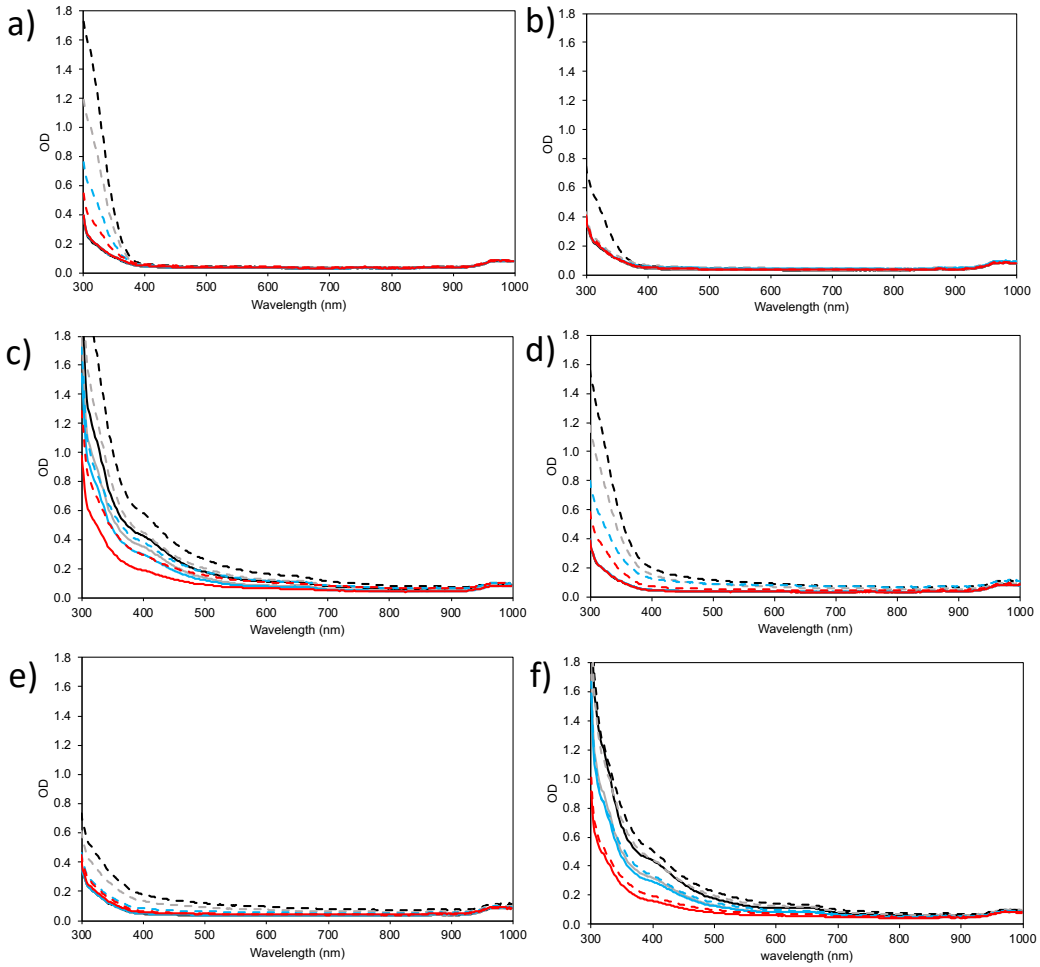

Figure 4.3: UV-vis wavelength scans. (n=3)**.** a) Buffer control (solid line) and buffer after addition of crosslinker **1** (dashed line). b) Cysteine control (solid line) and cysteine after addition of crosslinker **1** (dashed line). c) Protein control (solid line) and protein after addition of crosslinker **1** (dashed line). d) Buffer control (solid line) and buffer after addition of crosslinker **3** (dashed line). e) Cysteine control (solid line) and cysteine after addition of crosslinker **3** (dashed line). f) Protein control (solid line) and protein after addition of crosslinker **3** (dashed line). For all graphs the crosslinker added was equivalent to the pGEL001 solution of, red = 40 mg/mL, blue = 80 mg/mL, grey = 160 mg/mL, black = 200 mg/mL.

To probe further into the underlying OD changes that occurred due to gel fibre formation, a specific wavelength was selected for further OD readings. This allowed for more detailed analysis of the resultant OD values of the samples. Readings at OD_{520} were selected to avoid the residual high absorbance that occurred in the region below 400 nm from both pGEL001 and the crosslinkers, whilst keeping within a

wavelength where OD readings still remained above 0.1 to maintain accurate readings.

4.3.2 Spectral scanning of the wells revealed gel fibre formation caused a deviation from the predicted OD_{520} readings

Spectral scanning experiments measuring the OD_{520} were conducted on the same samples used in Section 4.3.1. Each well was split into 177 segments and an OD_{520} measurement recorded for each. The resulting experimental output is shown in figure 4.4, with a colour coded spectrum applied, with 0.01 OD_{520} coded to display as white, and 0.5 OD_{520} coded to display as black. Between these OD_{520} values a gradient was created, allowing visualization of the changes in OD_{520} across the wells in the different tested conditions. Corroborating the wavelength scan results, little change in OD_{520} was observed when comparing buffer or cysteine solutions added with either DMSO or crosslinker **1**. Additionally, the buffer and cysteine containing solutions presented similar OD_{520} readings at all tested concentrations regardless of DMSO or crosslinker **1** presence. The pGEL001 solutions revealed a slight increase in OD_{520} with increasing concentrations of protein, while little change in OD_{520} was observed between the DMSO and crosslinker **1** conditions at the same respective pGEL001 concentration. Thus crosslinker **1** appeared to have no observable effect on the OD_{520} of the three tested solutions. Contrastingly, crosslinker **3** induced an increase in OD_{520} compared to the DMSO treated sample at the comparable concentration for all three of the solutions; buffer, cysteine and pGEL001.

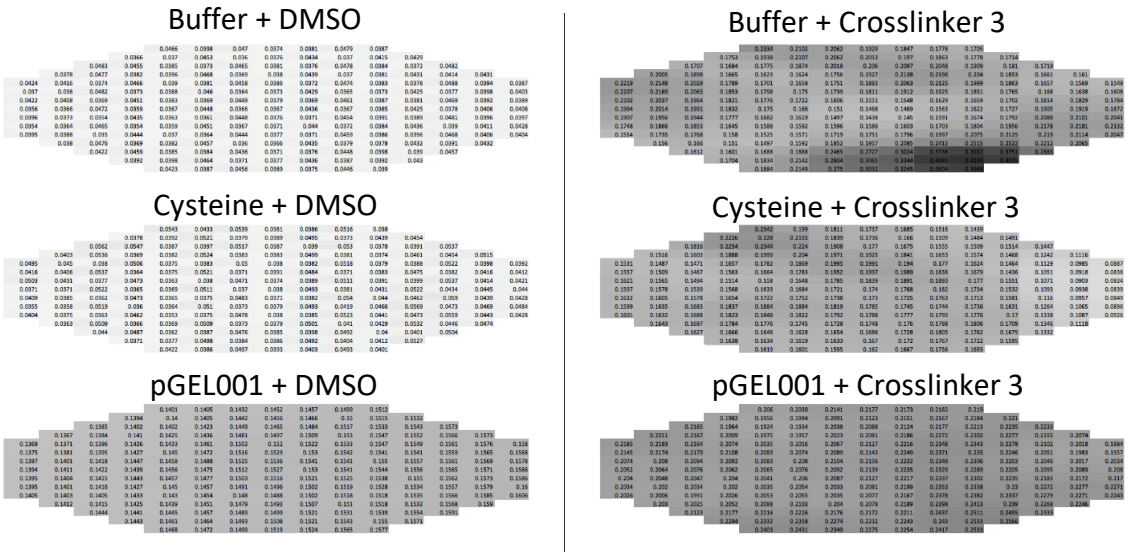

Figure 4.4: The output data from spectral scans displaying the 177 OD_{520} readings per well. Each reading is colour coded with white set to 0.01 and black set to 0.5.

To quantitate the observations revealed from the well scan images in Figure 4.4, an average OD_{520} reading across the entire well was determined for the buffer, cysteine and pGEL001 solutions added with DMSO, crosslinker **1** or **3** at all tested concentrations. Most of the wells presented high levels of uniformity across all 177 segments, validating the use of an average OD_{520}. Following calculation of the average OD_{520} reading for each sample, the OD_{520} of crosslinker **1** and **3** containing solutions were normalised by their respective DMSO control solution. This enabled the OD_{520} contribution from the crosslinkers only to be determined under each condition (buffer, cysteine and pGEL001) at each concentration. For simplicity all solution concentrations (buffer and cysteine) are referenced against the protein concentrations 40, 80, 160 or 200 mg/mL, whereby the same concentration of crosslinker **1** or **3** was added to the respective solution (buffer, cysteine or pGEL001) labelled as 40 mg/mL, 80 mg/mL etc. These results are displayed in Figure 4.5a-b and Table 4.1. Here, crosslinker **1** caused no increase in OD_{520} when added to cysteine or buffer solutions (Figure 4.5a). Conversely, when added to pGEL001, crosslinker **1** caused a slight increase in OD_{520} of 0.02-0.05, with no significant changes in OD_{520} between the range of concentrations of crosslinker **1** tested (Figure 4.5a). Crosslinker **3** produced a linear increase in OD_{520} with increasing concentrations for all three solutions of buffer, cysteine and pGEL001 (Figure 4.5b). Importantly it was observed

that in the gelled sample (pGEL001 at 200 mg/mL), the average OD_{520} value calculated deviated from the linear trend obtained in the buffer and cysteine solutions, in addition to the trend established at the three lower concentrations of pGEL001 that did not form hydrogels (Figure 4.5b). Therefore, it appeared gelation of pGEL001 caused a reduction in the expected OD_{520} contribution from crosslinker **3**.

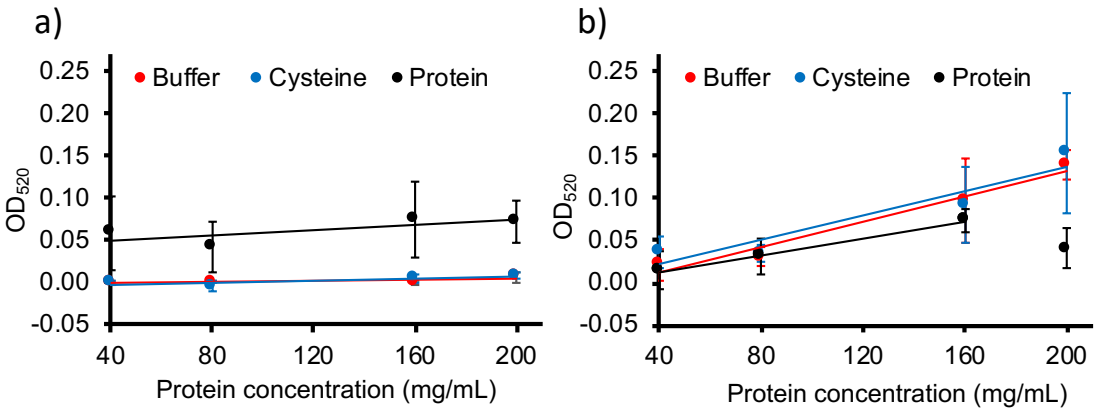

Figure 4.5: The average OD_{520} reading of each concentration of crosslinker in solution, normalised by the solution control, giving a value of OD_{520} that represents the effect of the addition of crosslinker to the solution. (n=3, error bars = standard deviation). a) Crosslinker **1**, b) Crosslinker **3**.

Table 4.1: Normalised OD_{520} values of the crosslinkers from each solution. The buffer and cysteine results displayed are shown as the relative protein concentration that had the same concentration of crosslinker added. G = gelled sample. (n=3).

	Crosslinker 1			Crosslinker 3		
Concentration (mg/mL)	Normalised by buffer	Normalised by cysteine	Normalised by protein	Normalized by buffer	Normalised by cysteine	Normalised by protein
200	0.01	0.01	0.07	0.14	0.15	0.04 (G)
160	0.00	0.01	0.07	0.10	0.09	0.07
80	0.00	0.00	0.04	0.03	0.03	0.03
40	0.00	0.00	0.06	0.02	0.04	0.01

The drop in OD_{520} reading that resulted from crosslinker **3** induced gelation (Figure 4.5b) could be further visualised through calculation of the predicted OD_{520} for the pGEL001 solutions upon addition of crosslinkers. This was calculated by adding the normalised OD_{520} contributions of crosslinkers **1** and **3**, determined from the buffer and cysteine conditions, to the OD_{520} reading of the respective pGEL001 DMSO control solution. The results from these calculations are displayed in Figure 4.6a-b and Table 4.2. For crosslinker **1**, the predicted values obtained from the normalised

cysteine conditions matched the actual OD_{520} values obtained from the pGEL001 solutions. Although the predicted values from the buffer normalised calculations for crosslinker **1** did not perfectly match the actual pGEL001 obtained results, the pattern of increasing OD_{520} with concentration still aligned with the pattern observed in the pGEL001 OD_{520} values. For crosslinker **3**, the predicted OD_{520} values based off the normalised crosslinker **3** OD_{520} readings from both the buffer and cysteine conditions were closely matched. When compared to the actual obtained OD_{520} readings for pGEL001, the non-gelled concentrations of 40, 80 and 160 mg/mL closely matched the predicted values from buffer and cysteine conditions. However, for the gelled sample of 200 mg/mL, the actual pGEL001 value deviated by ~0.1 OD_{520} from both the buffer and cysteine predicted values, with the largest deviation between the actual and predicted value for cysteine or buffer at the tested non-gelled conditions falling at 0.02 OD_{520}. Thus, it was apparent that formation of the hydrogel reduced the OD_{520} increase normally induced by crosslinker **3**. Therefore, this methodology successfully identified the formation of hydrogel fibres in the translucent TSAMs by establishing simple patterns in OD_{520} measurements, whilst using small volumes (100 μL) and maintaining pGEL001 in its hydrated state.

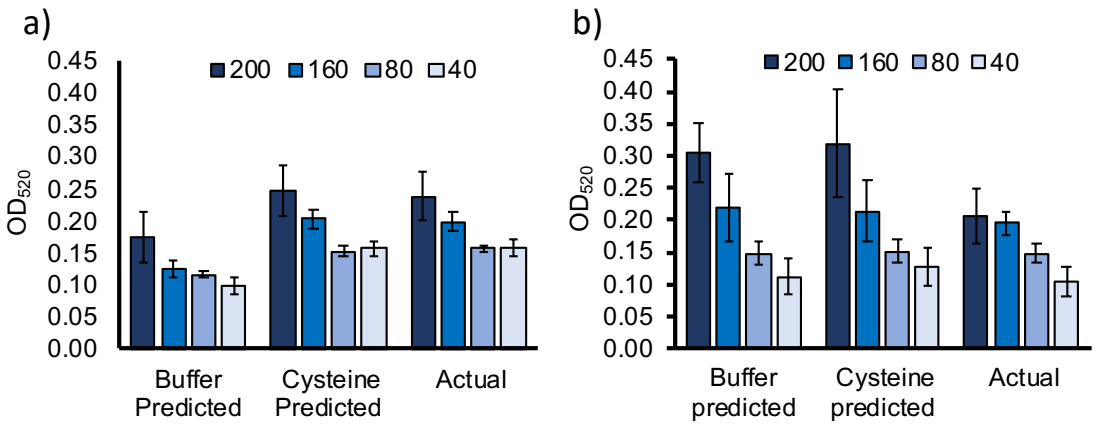

Figure 4.6: Predicted OD_{520} readings for the protein solution at each concentration calculated using the buffer controls or the cysteine controls. (n=3, error bars = standard deviation). a) Crosslinker **1**, b) Crosslinker **3**.

Table 4.2: Values for the predicted OD_{520} readings of pGEL001 following addition of crosslinker. (n=3)

	Crosslinker 1			Crosslinker 3		
Concentration (mg/mL)	Buffer Predicted	Cysteine Predicted	Actual	Buffer Predicted	Cysteine Predicted	Actual
200	0.17	0.25	0.24	0.31	0.32	0.21 (G)
160	0.12	0.21	0.20	0.22	0.21	0.20
80	0.11	0.15	0.16	0.15	0.15	0.15
40	0.10	0.16	0.16	0.11	0.13	0.10

4.4 Confirming TSAMs successfully incorporated the energy dissipating mechanism of talin rod domain unfolding

Following the investigation on TSAMs underlying structure, determining the retention of pGEL001s talin-dependent unfolding/refolding energy dissipating mechanism when integrated into hydrogel fibres became the principle focus. Many methods are available for monitoring protein unfolding in the solution state, namely; high resolution optical tweezers (Jiao *et al*., 2017), quantified real time thermocycling (Biggar *et al*., 2012), CD (Biggar *et al*., 2012) and NMR (Waudby *et al*., 2013) to name a few. However, when incorporated into the solid state (i.e. within hydrogel fibres) few techniques are available, each requiring complex methodologies and specialised equipment. Specifically solid state NMR can be employed (Xiao *et al*., 2019), whilst Fourier transform infrared spectroscopy can yield information on protein structure in the solid state through analysis of the amide 1 peak (Manning, 2005). However, neither of these methodologies allow measurements in real time under dynamic conditions. To elucidate the retention of protein unfolding in TSAMs in response to force, a series of rheological and fluorescent microscopy investigations were performed.

4.4.1 Material properties of TSAMs

Before investigation into the specific viscoelastic properties of TSAMs, several observations on its material properties were elucidated. Initial handling of the material revealed high levels of extensibility. A small sample of TSAM (100 μL) was stretched over 3-fold its original length (Figure 4.7a-b) returning to its original shape following removal of force. This extensibility characteristic was indicative of the expected properties resulting from pGEL001 folding/refolding within TSAM in

response to force. Furthermore, TSAMs presented as highly adhesive materials (Figure 4.7c). When attempting to remove TSAMs from plastic or metal based surfaces, high levels of adhesion were observed, an important property for applications including wound dressing, tissue adhesives and surgical sticky bandages (Xu *et al*., 2018). TSAMs also displayed mouldability, retaining its cylindrical shape for several days when removed from its mould (Figure 4.7d). Mouldability is an important material property required for structural components, lending TSAMs to a wide variety of applications.

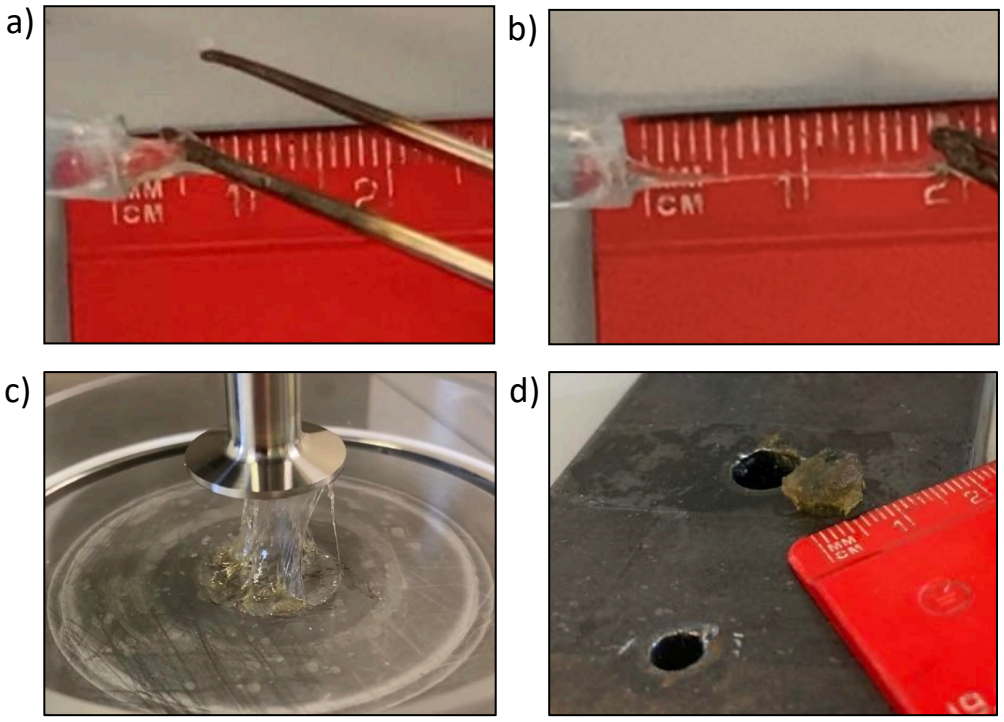

Figure 4.7: Characteristics of TSAMs. a) TSAM before being stretched. b) TSAM after being stretched to >3-fold its original length. c) Adhesion of TSAM to metal plates. d) A TSAM remaining in a cylindrical shape following removal from cylindrical mould.

4.4.2 Rheological characterisation of TSAMs revealed pGEL001 unfolding in response to shear strain

Rheology is a widely employed technique for characterising material properties. Specifically, rheology is the science of material deformation (Wilson, 2018). Multiple rheological measurement attachments exist, each tailored towards specific material types to enable the optimum set up for the sample of interest. Here, a parallel plate set up was applied, whereby the top plate (available in a range of diameters)

oscillates in a sinusoidal form, applying a shear strain to the material sitting on the bottom plate. The materials resultant exhibited sinusoidal shear stress is measured, with the delay between the applied shear strain and exhibited shear stress, termed the phase angle, indicating the viscoelasticity of the material (Carvalho and Kumar, 2022). These terms are summarised in Equations 4.1 and 4.2.

$$(Equation\ 4.1)\ \tau(t) = \gamma_o[G'\ sin(\omega t) + G"\ cos(\omega t)]$$

$$(Equation\ 4.2)\ \delta = tan - 1(\frac{G"}{G'})$$

In Equation 4.1, τ is shear stress, t is time, γ_o is shear strain, G' is the storage modulus, ω is frequency, G" is the loss modulus and in equation 4.2 δ is the phase angle. G' gives information on the amount of structure present within a material, and when exceeds the G" indicates a mainly elastic and solid material. G" represents the viscous component of a material, indicating the amount of energy dissipated by the material during the rheological measurements. Together the values obtained for these functions allow properties such as rigidity, elasticity and viscosity to be discerned. Two experiment types were conducted on the TSAM materials; oscillatory shear strain sweeps (frequency was constant, amplitude was varied) and oscillatory frequency sweeps (frequency was varied, amplitude was constant). In each of these experiments, the TSAM was exposed to one full sweep, followed by a two-minute rest period. This procedure was conducted for a total of 5 consecutive sweeps on each TSAM, with three TSAMs in total tested in each experiment. Owing to the unfolding and refolding kinetics intrinsic to R1-R3 contained within pGEL001, we predicted viscoelastic properties would be retained upon repeated exposure to shear strain.

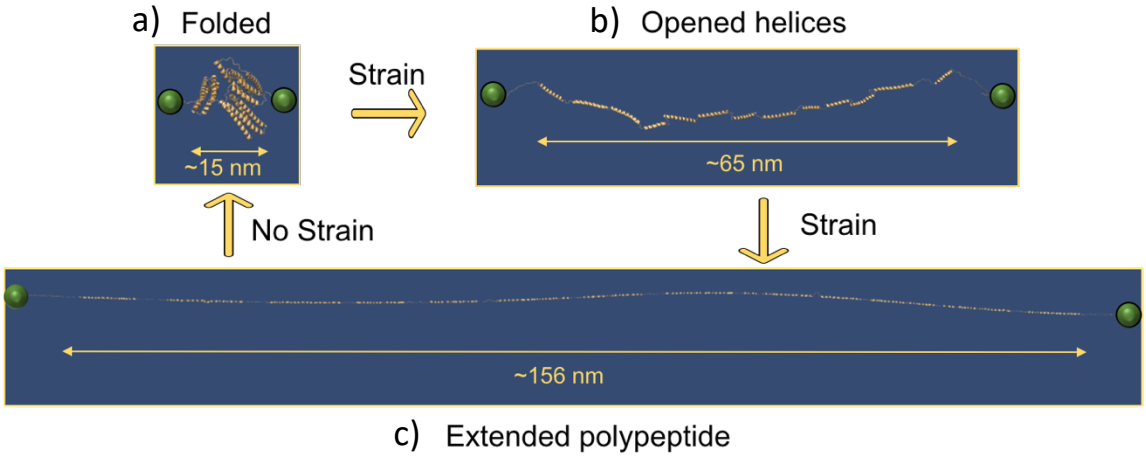

Figure 4.8: Schematic of pGEL001 (AlphaFold predicted structure) unfolding in response to force. a) pGEL001 in folded state. b) when exposed to strain pGEL001 unfolds into open helices form. c) pGEL001 further unfolded into the extended polypeptide form. Upon removal of force, pGEL001 in b) or c) can refold back to structure shown in a).

4.4.2.1 Oscillatory shear strain sweeps

Firstly, shear oscillatory amplitude sweeps were conducted on three TSAMs. The average values for shear strain, shear stress, G', G" and phase angle were calculated and plotted (Figures 4.9-4.11). The error bars display the standard error of the mean across the three TSAM samples. Oscillatory shear strain sweeps are traditionally used to determine the linear viscoelastic region (LVER) of the material; the region where the material acts elastically (shear stress changes linearly with deformation) (Öhrlund, 2018). However, due to the determination of protein unfolding being the key focus of these rheological investigations, monitoring of the materials behaviour over a range of shear strains was likely to yield the most informative data for elucidation of this question. Specifically, when unfolded, the R1-R3 talin component of pGEL001 can extended from 15 nm in length in its folded state, up to 156 nm in length in the extended polypeptide form (Figure 4.8). Thus, if pGEL001 unfolding occurred within TSAMs in response to shear strain, large amounts of slack would be introduced into the material, registering as viscous like behaviour as a result of a delay between the applied shear strain and resultant shear stress.

For the first applied oscillatory shear strain sweep on the TSAM, G' and G", as a product of shear strain presented a LVER that extended across the full range of shear strain tested (Figure 4.9a-b). A long LVER is indicative of a stable material presenting high levels of extensibility, matching the observations of TSAMs from Figure 4.7. The TSAMs presented G' > G" for all five sweeps, confirming viscoelastic behaviour during the entirety of the five consecutive oscillatory shear strain sweeps. The complex modulus (G*) (sum of G' and G") was shown to increase concomitantly with accumulated sweeps. G*s magnitude is a measure of a materials rigidity, therefore indicating here that TSAMs presented an increased resistance to deformation upon repeated exposure to shear strain (Kulkarni and Shaw, 2016). This G* increase can be explained by strain stiffening as a consequence of fibre reorganisation, a well-documented phenomenon that occurs in hydrogels formed from biopolymers (Wen and Janmey, 2011). Strain stiffening was further observed within each sweep as the increasing elastic modulus occurring with increasing shear strain, observed as the positive gradient in sweeps 3-5 with a peak reached between 0.1-10.0% strain (Figure 4.9a). A singular graph with the five sweeps G' values against shear strain is shown in Figure 4.9a, while each individuals G' and G" against shear strain is shown in Figure 4.9b-f. For sweeps 2-5 the peak maxima for G' and G" was reached between 1-5%, with each sweep's maxima shifting to the right and increasing in amplitude. Following the peak maxima, both G', G" and G* began to decrease with increasing shear strain, suggesting TSAMs started to become less rigid with increasing shear strain. This pattern occurred for strains 2-5, with the decline in G', G" and G* amplified further in each subsequent sweep. Such observations could only be explained by sudden induction of pGEL001 chain unfolding within the material, with this resulting in a decreased rigidity due to the introduction of slack within the system. Unfolding was likely induced in sweeps 2-5 due to the increased rigidity of the material from fibre reorganisation, allowing strain to become imparted onto the fibres themselves. When this strain exceeded >5 pN pGEL001 rod domains would begin to unfold until the force across the fibres within the system fell back below the threshold, at which point unfolded domains could refold.

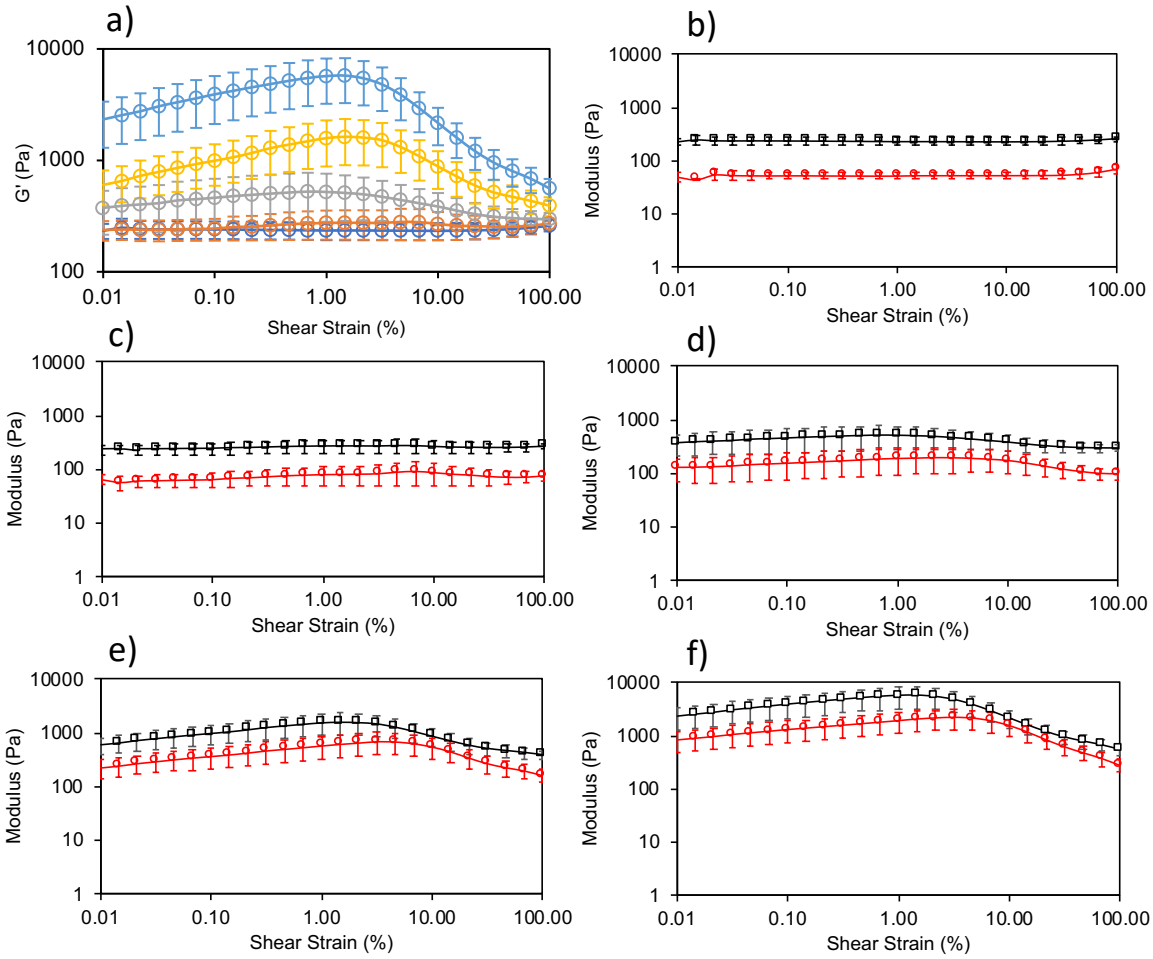

Figure 4.9: Oscillatory shear strain sweeps on TSAM. (n=3, error bars = standard error of the mean). a) G' against shear strain for all 5 sweeps. Sweep 1= dark blue, sweep 2 = orange, sweep 3 = grey, sweep 4 = yellow, sweep 5 = light blue. b) G' and G" for sweep 1. c) G' and G" for sweep 2. d) G' and G" for sweep 3. e) G' and G" for sweep 4. f) G' and G" for sweep 5. For b)-f) G' = black squares, G" = red circles.

Examination of the phase angle data from the oscillatory shear strain sweeps 1-5 revealed a bell-shaped curve for sweeps 2-5, showing a sudden increase in phase angle between 1-5% shear strain (Figure 4.10). This bell curve was shifted to the right compared to the G' against shear strain bell curve, with the positive slope of the phase angle graph corresponding to the negative gradient of the G' against shear strain graph shown in Figure 4.9a-f. Thus, an increase in phase angle was observed simultaneously with the decrease in rigidity. This data further supports pGEL001 unfolding as the cause of the decreased rigidity at shear strains above 1-5% observed in sweeps 2-5 shown in Figure 4.9a. Following the sudden introduction of slack from pGEL001 unfolding, in addition to a decrease in rigidity, a lag between the controlled

shear strain and measured shear stress sine waves would occur from the increased flow of the material. This would present as an increase in phase angle, matching the experimental observations obtained. Furthermore, the phase angle was also shown to subsequently decrease as shear strain increased above ~10%, indicating a gradual reduction in flow occurring. This can be explained by the increased shear strain pulling the slack out of the pGEL001 monomers, resulting in a reduced lag between the induced shear strain and measured shear stress, further supporting pGEL001 unfolding as the cause of these observations.

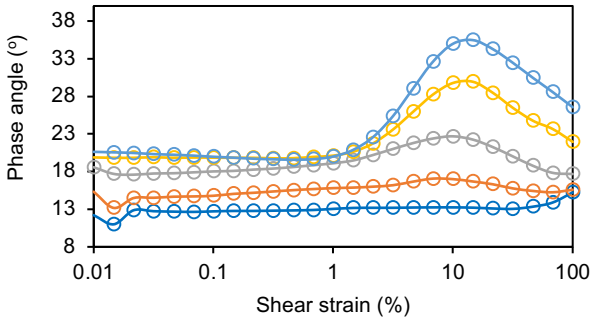

Figure 4.10: Phase angle as a product of shear strain for TSAM. (n=3). Sweep 1= dark blue, sweep 2 = orange, sweep 3 = grey, sweep 4 = yellow, sweep 5 = light blue.

When shear stress was plotted against shear strain (Figure 4.11), an exponential increase in shear modulus (G) (the gradient of the linear portion of each of the graphs) with accumulated sweeps was observed. G is another measure of rigidity, and therefore further illustrated the strain stiffening that occurred within TSAMs. Figure 4.10 also revealed that sweeps 3-5 reached shear yield points at 1-5% shear strain, beginning to move into viscous stress as seen by the induction of a slope, subsequently transitioning back into a linear gradient at >~10% shear strain (the peak maxima of phase angle bell curves) indicative of elastic behaviour reoccurring. Shear stress vs shear strain therefore provided a simple visual to determine the presence of pGEL001 unfolding events through the presence of a shear yield point.

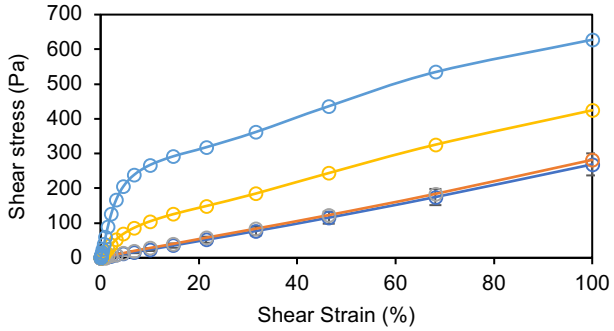

Figure 4.11: Shear stress as a product of shear strain for TSAM. (n=3). Sweep 1= dark blue, sweep 2 = orange, sweep 3 = grey, sweep 4 = yellow, sweep 5 = light blue.

4.4.2.2 Oscillatory frequency sweeps

Following the oscillatory shear strain sweeps, oscillatory frequency sweeps were conducted at a fixed shear strain of 1%, using the same protocol of 5 sweeps separated by two-minute relaxation times. A 1% shear strain was selected due to its position at the centre of the LVER on the oscillatory shear strain sweep 1. Here, the results of G' and G" as a product of angular frequency in rad/s shown in Figure 4.12a-e, presented a frequency independent trend, with G' > G", once again confirming the viscoelastic properties of TSAM. Accumulated sweeps also induced an upwards shift in both G' and G", this time as a linear slope as opposed to a bell-curve. Due to a constant low shear strain within the oscillatory frequency sweeps, tension within the fibres was likely low at all time points. Therefore, the increased rigidity witnessed was most likely due to fibre reorganisation. These results further highlight the presence of fibre reorganisation inducing increased material rigidity, but added no further insight into the unfolding of pGEL001 monomers within the TSAMs.

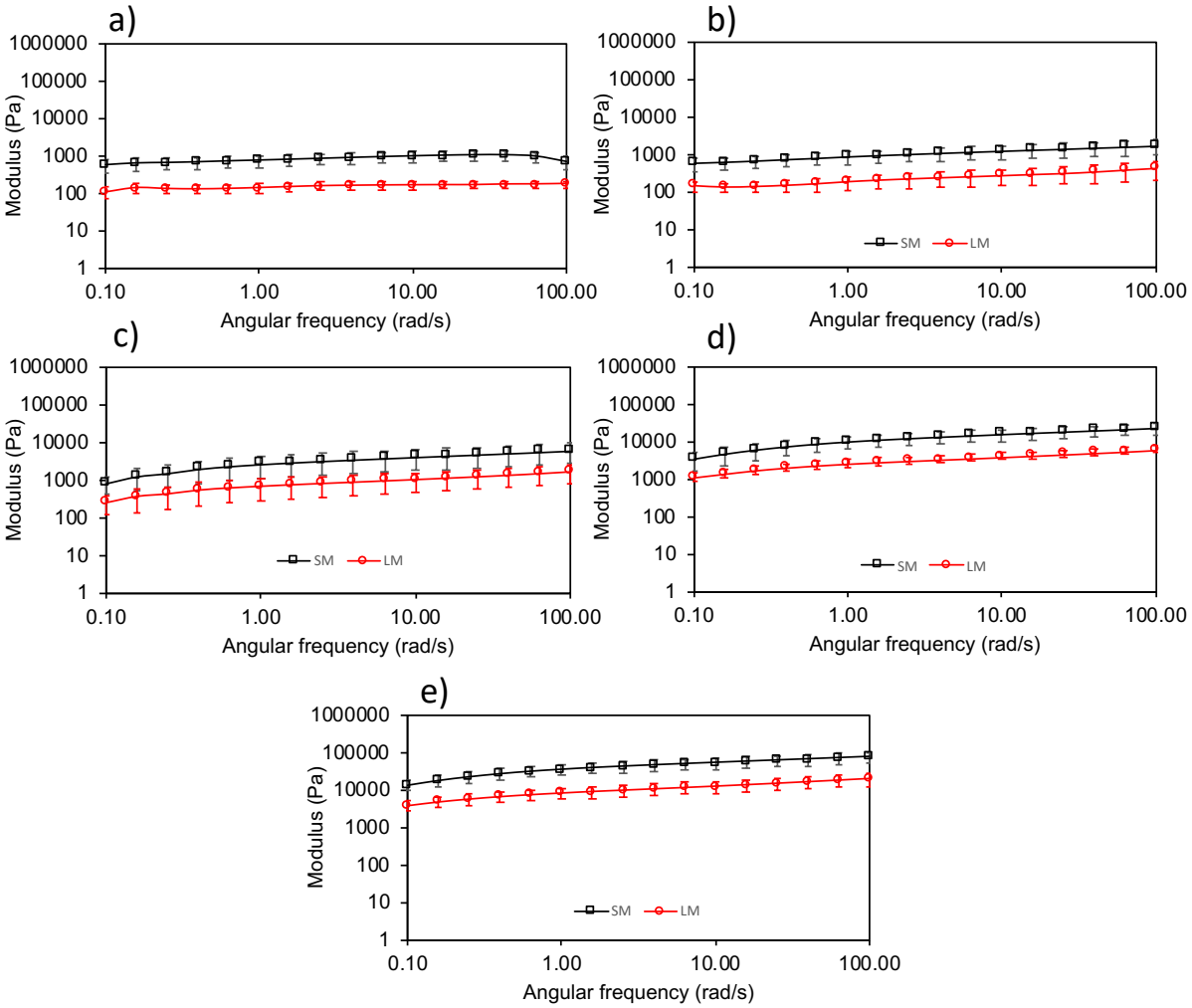

Figure 4.12: Oscillatory frequency sweeps on TSAM. (n=3, error bars = standard error of the mean). a) G' and G" against shear strain for sweep 1. b) G' and G" for sweep 2. c) G' and G" for sweep 3. d) G' and G" for sweep 4. e) G' and G" for sweep 5. G' = black squares, G" = red circles

4.4.3 Using GFP-VD1 to confirm pGEL001 unfolding was responsible for rheological observations

As discussed in Section 3.2.3, pGEL001 can bind multiple GFP-VD1 proteins, which when bound, lock pGEL001 in the unfolded conformation. To confirm the patterns attained from rheological measurements of TSAMs, described in Section 4.4.2, were due to pGEL001 unfolding in response to shear strain, GFP-VD1 was employed. Specifically, a TSAM material was swelled in a 2 mg/mL GFP-VD1 solution overnight and placed on the rheometer for oscillatory shear strain sweeps. The same protocol as the oscillatory shear strain sweeps in Section 4.4.2 was utilised; a two-minute rest

period, followed by an oscillatory shear strain sweep from 0.01%-100% shear strain, performed for a total of five sweeps. The resulting shear stress as a property of shear strain is shown in Figure 4.13a-e. For each of the five sweeps, the GFP-VD1 treated TSAM initially presented viscoelastic properties, observed as the linear region in Figure 4.13a. However, at a shear strain of 46-68%, the GFP-VD1 treated TSAM reached its shear yield point, remaining a curve up to 100% shear strain for each of the five sweeps. As stated in Section 4.4.2, the induction of a shear yield point in Figure 4.11 was thought to indicate pGEL001 unfolding, further validated here due to its occurrence in the shear stress vs shear strain graph obtained from a TSAM with induced unfolding from GFP-VD1. To confirm this observation was not induced as a consequence of the introduction of an additional protein into TSAMs, or from the now swelled state of the TSAM, several control experiments were performed. Two further TSAM materials were swelled overnight with either buffer alone or a 2 mg/mL solution of GFP. The following day the two TSAMs were exposed to oscillatory shear strain sweeps, with the experiment performed identically to the GFP-VD1 treated TSAM. Here, both the buffer swelled and GFP swelled TSAMs presented a linear relationship between shear stress and shear strain for the entire oscillatory shear strain sweep (Figure 4.13a). This same pattern was observed across all five sweeps (Figure 4.13a-e). Therefore, the control experiments confirmed that the shear yield point was not reached due the swelled state of the TSAM from buffer, nor from the presence of a non-binding protein introduced into the TSAM. Together, these results provided further strong evidence for pGEL001 unfolding being responsible for the induction of a shear yield point in TSAMs. Interestingly, oppositely to the non-treated TSAM materials discussed in 4.4.2, in all three of the TSAM treated conditions no increases in rigidity between the five strains were observed. As this observation was present across all three treated conditions (buffer, GFP, GFP-VD1), the only commonality was the swelled state of the TSAM resulting from the exposure to a buffer solution overnight. Therefore, it was likely the swelled state of the hydrogels decreased the density of the fibrous structure, minimising interactions between the fibres, which in turn was responsible for the increased rigidity seen in the non-swelled state. Overall, these investigations support the observations that indicated pGEL001 unfolding discussed in Section 4.4.2.

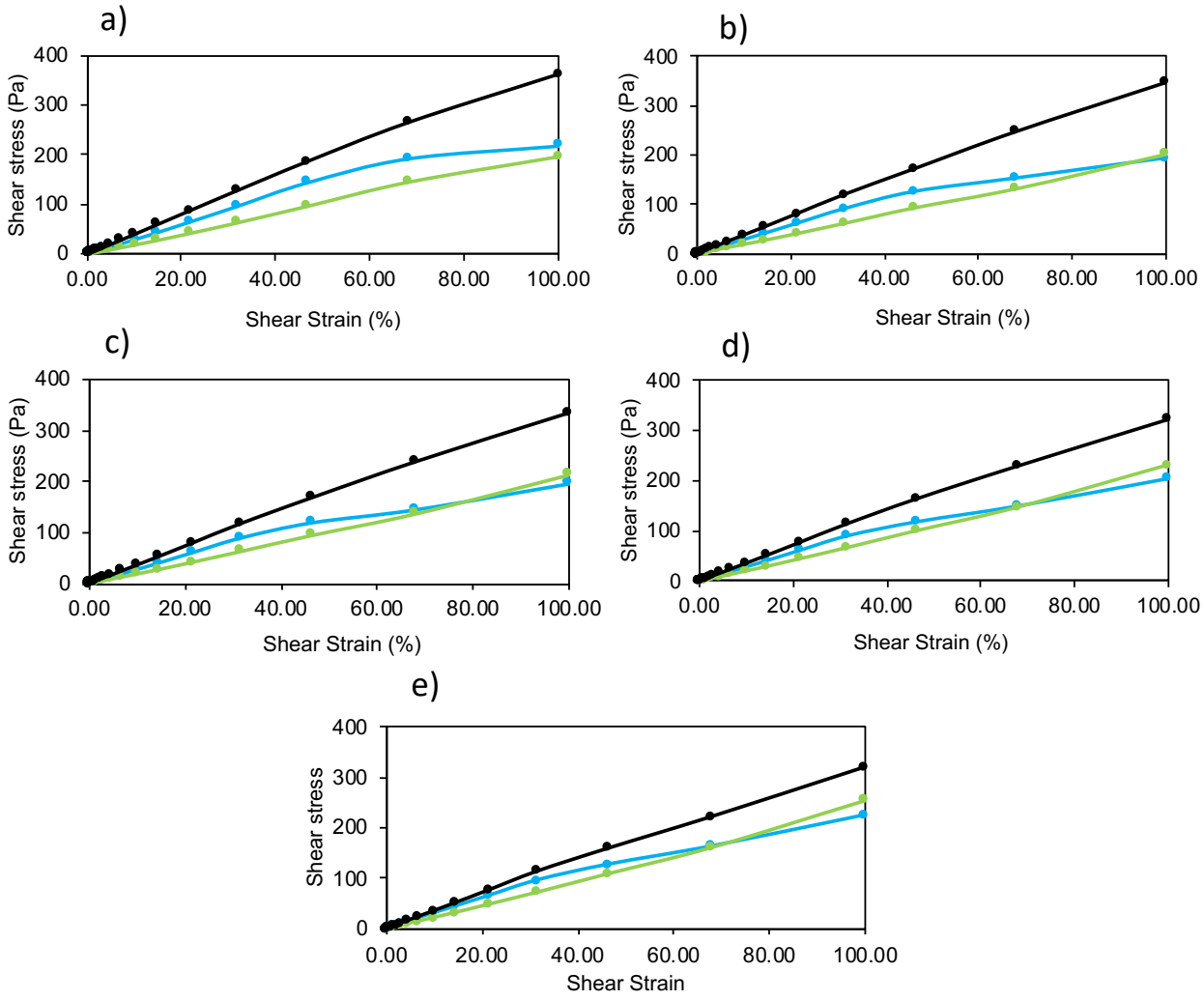

Figure 4.13: Oscillatory shear strain sweeps on TSAMs swelled with GFP-VD1, GFP or phosphate buffer. Black = phosphate buffer condition, Blue = GFP-VD1 condition, Green = GFP condition. a) Shear stress against shear strain for sweep 1. b) Shear stress against shear strain for sweep 2. c) Shear stress against shear strain for sweep 3. d) Shear stress against shear strain for sweep 4. e) Shear stress against shear strain for sweep 5.

4.4.4 Fluorescence microscopy confirmed GFP-VD1 binding to TSAM fibres

Finally, fluorescence microscopy was conducted to determine localisation of the GFP-VD1 and GFP to the TSAM fibres following rheological measurements. After the five sweeps were conducted on the GFP-VD1 and GFP treated TSAMs, the TSAMs were washed in a solution of buffer overnight to decrease background florescence during imaging, removing some of the unbound protein. Using maximum projection wide field fluorescence microscopy, transmitted light images of the fibres within the TSAM material were collected. Subsequent fluorescence images were then taken of the

same area of TSAM to compare the positioning of the GFP proteins in respect to the TSAM fibres.

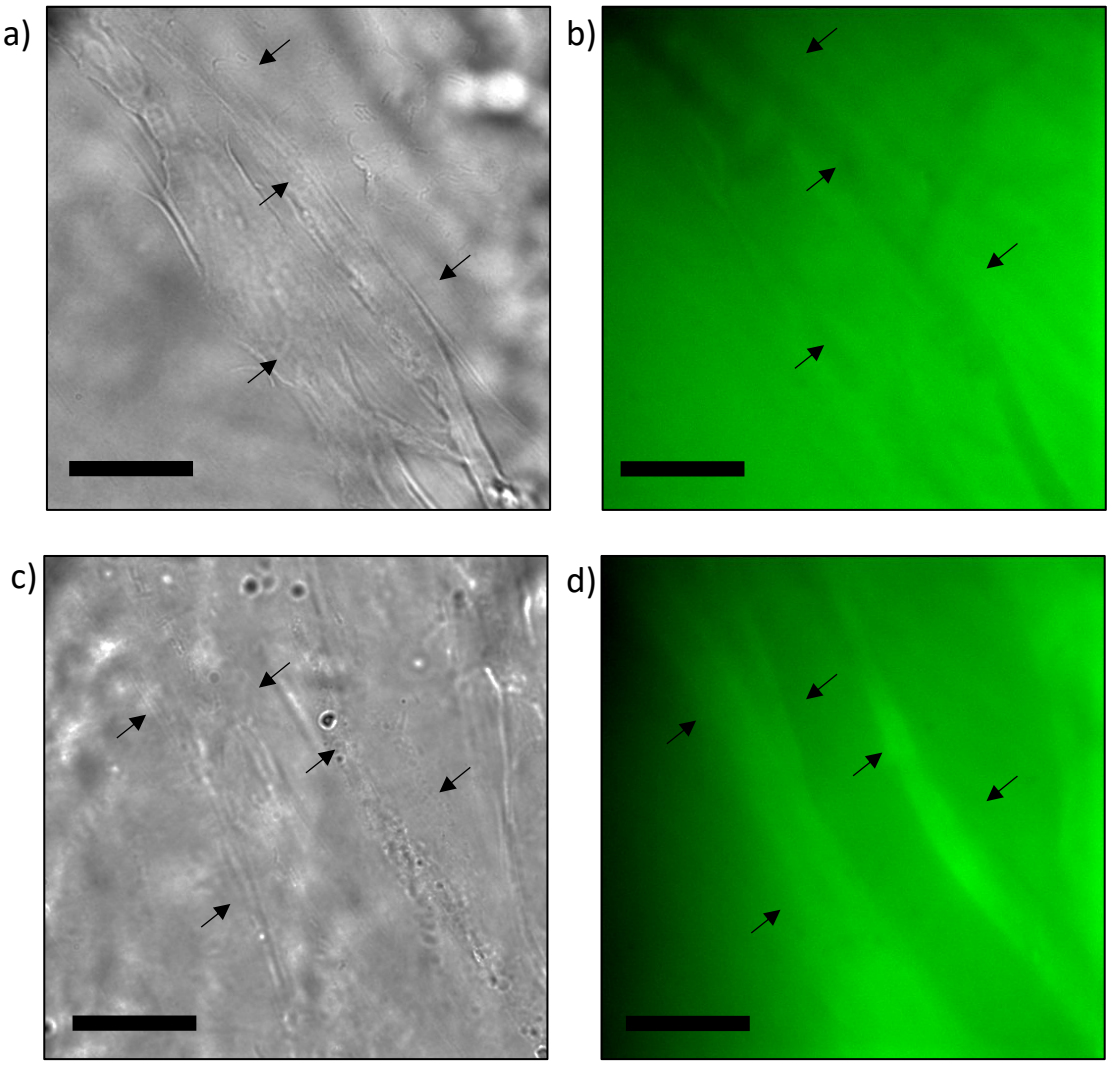

Figure 4.14: Maximum projection widefield fluorescent microscopy images of GFP-VD1 and GFP swelled TSAMS following rheology. (Scale bar = 20 μm) Observed fibres indicated with arrows. a) Transmitted light image of GFP swelled TSAM. b) GFP fluorescence image of GFP swelled TSAM. c) Transmitted light image of GFP-VD1 swelled TSAM. d) GFP fluorescence image of GFP-VD1 swelled TSAM.

The GFP swelled TSAM fluorescence images (Figure 4.14a-b) revealed high levels of fluorescence in the void spaces surrounding the fibres (observed in the transmitted light images). Furthermore, these fibre structures appeared dark in the fluorescence images, suggesting no binding of the GFP protein to the fibres had occurred. Conversely, in the GFP-VD1 swelled TSAM, the observed fibres in the transmitted light images (Figure 4.14c) presented high levels of fluorescence (Figure 4.14d), with

the void spaces much darker. Thus it was evident GFP-VD1 localised to the TSAM fibres (confirmed to consist of pGEL001 from scanning electron microscopy energy dispersive X-ray analysis), providing a strong argument for GFP-VD1 binding to pGEL001 and therefore confirming pGEL001 unfolding occurred in the GFP-VD1 swelled TSAMs.

4.5 TSAMs capable of withstanding supersonic impacts

With the rheological measurements discussed in Section 4.4 providing a strong argument for successful incorporation of pGEL001s energy dissipating mechanism within the TSAM when exposed to shear strain, the next series of experimental investigations sought to probe TSAMs effectiveness in withstanding high velocity impacts. For this purpose, a custom experiment was designed utilising a light gas gun to fire projectiles at TSAMs set in the blast tank exit aperture (BTEA) (Figure 4.15). A detailed description of the light gas gun and the experimental methodology can be found in Section 2.8.8. For these experiments basalt particles of 20-70 μm in diameter were chosen as the projectiles. The basalt was loaded into a sabot as a buck shot and accelerated towards the target at 1.5 km/s (Figure 4.15).

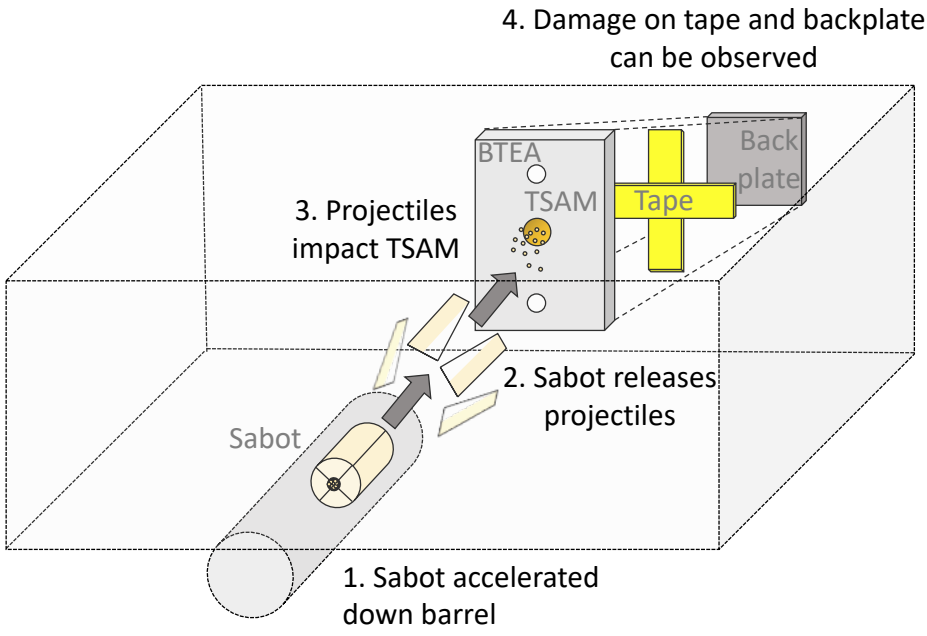

Figure 4.15: Light Gas gun experiment schematic. A sabot loaded with basalt particle projectiles is accelerated down the barrel, releasing its projectiles towards the TSAM loaded within the BTEA (stainless 304). The tape and aluminium (Al 5083) back plate can be assessed for damage following projectile impact with the TSAM.

4.5.1 TSAM survived impact at 1.5 km/s stopping all basalt particles.

Initial investigations aimed to elucidate the state of a 500 µL TSAM following impact at 1.5 km/s. Aerogels are the industry standard materials for capture and preservation of projectiles from hypervelocity experiments (Discussed in Section 1.1.2), therefore our goal was to assess whether TSAMs have similar capabilities. Specifically; 1. To stop all particles from passing completely through the material and 2. To capture basalt particles in a preserved state. For the first iteration of the light gas gun experiment, TSAM materials were shot at 1.5 km/s. Here only a piece of parafilm was present behind the TSAM on the BTEA. Following the firing of the basalt particle buck shot at the 500 µL TSAM, when observed from behind, no piercing of the parafilm had occurred (Figure 4.16a), confirming the TSAM had completely stopped all basalt particles. Furthermore, upon dehydration of the TSAM and subsequent imaging using scanning electron microscopy, a preserved basalt particle of the correct dimensions was observed (Figure 4.16b), confirmed as basalt using energy dispersive X-ray analysis, due to the presence of silicon (Figure 4.16c).

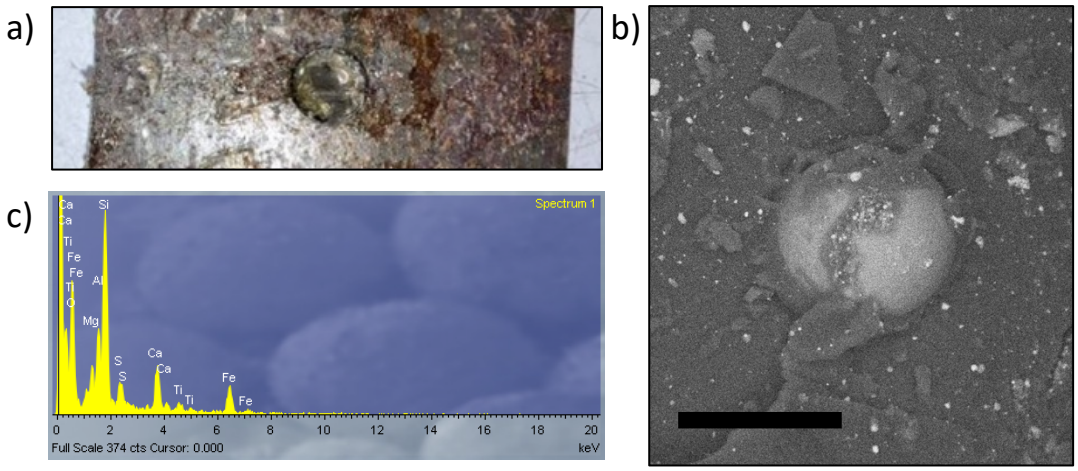

Figure 4.16: Results from first light gas gun experiment on a TSAM impacted with basalt particles fired at 1.5 km/s. a) Intact TSAM imaged from the back of the BTEA following impact at 1.5 km/s showing no penetration. b) Scanning electron microscopy image of intact basalt particle caught and preserved in a TSAM following impact (scale bar = 50 µm). c) Energy dispersive X-ray analysis confirming spherical object in b) as a basalt particle.

4.5.2 Comparison of TSAMs against a polyvinylpyrrolidone (PVP) hydrogel in supersonic impact experiments.

Following confirmation of TSAMs ability to stop basalt particles upon impact at 1.5 km/s, a second iteration of experiments was conducted, comparing a 500 µL TSAM to a 500 µL control PVP hydrogel exposed to the same impacts. Once again basalt particles were accelerated to 1.5 km/s towards the target contained in the BTEA. For these experiments both thin yellow tape and a 3 mm thick aluminium (5083) back plate were placed behind the target material (Figure 4.15); either PVP hydrogel or TSAM.

Firstly, the effects of the basalt particle impacts at 1.5 km/s against 500 µL of PVP hydrogel were determined. Following impact, removal of the BTEA presented no observable PVP hydrogel (Figure 4.17a). Therefore, it was confirmed that the entirety of the PVP hydrogel was expelled or destroyed from the BTEA by the impact force of the basalt particles. Removal of the backing tape revealed the basalt particles had penetrated through the tape (Figure 4.17b) and subsequently impacted the aluminium back plate. Inspection of the aluminium back plate revealed a crater formed on its surface directly behind the position of the PVP hydrogel (Figure 4.17c), providing a visual guide to the amount of energy transferred from the basalt particles to the impacted material. When imaged under a light microscope, the crater dimensions were determined as 1.33 mm by 0.90 mm (Figure 4.17d) with a depth of approximately 0.5 mm.

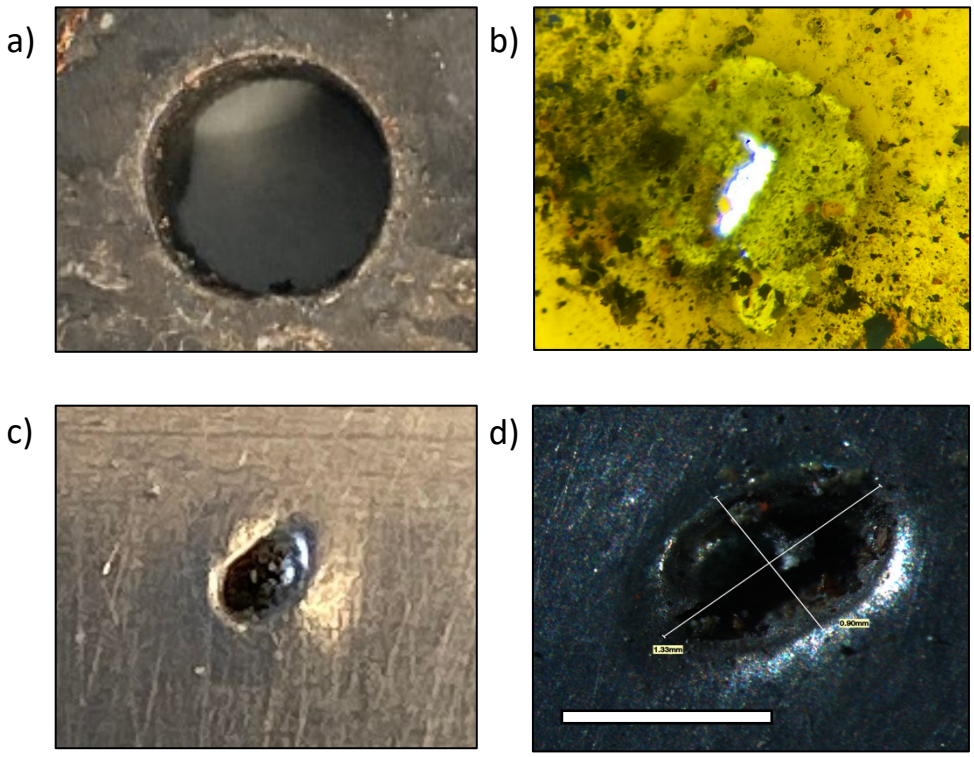

Figure: 4.17: PVP control gel results from light gas gun experiment when impacted at 1.5 km/s. a) Destroyed control gel after basalt impact at 1.5 km/s. b) Hole formed in tape from basalt projectile. c) Crater formed in aluminium back plate. d) Crater imaged under light microscope to determine crater dimensions (Scale bar = 1 mm).

Next, the same experiment was performed with a 500 µL TSAM as the target. Following impact, removal of the BTEA presented a mostly intact TSAM from the frontal view, with partial desiccation having occurred, demonstrated by the slightly solidified cover of TSAM. The resultant hole seen in Figure 4.18a likely occurred due to impact from aluminium burst disc shrapnel, not from the basalt particles themselves. Removal of the backing tape revealed intact TSAM, with light microscopy imaging (Figure 4.18b) of this TSAM indicating the presence of basalt particles embedded in the TSAMs structure. Inspection of the aluminium back plate revealed no indentations or markings of any kind resulting from the impact. It could therefore be concluded that the TSAM successfully absorbed the full impact energy of the basalt particles, further validating the results from Section 4.5.1, whilst the same volume of the control PVP hydrogel was not sufficient to absorb the impact energy.

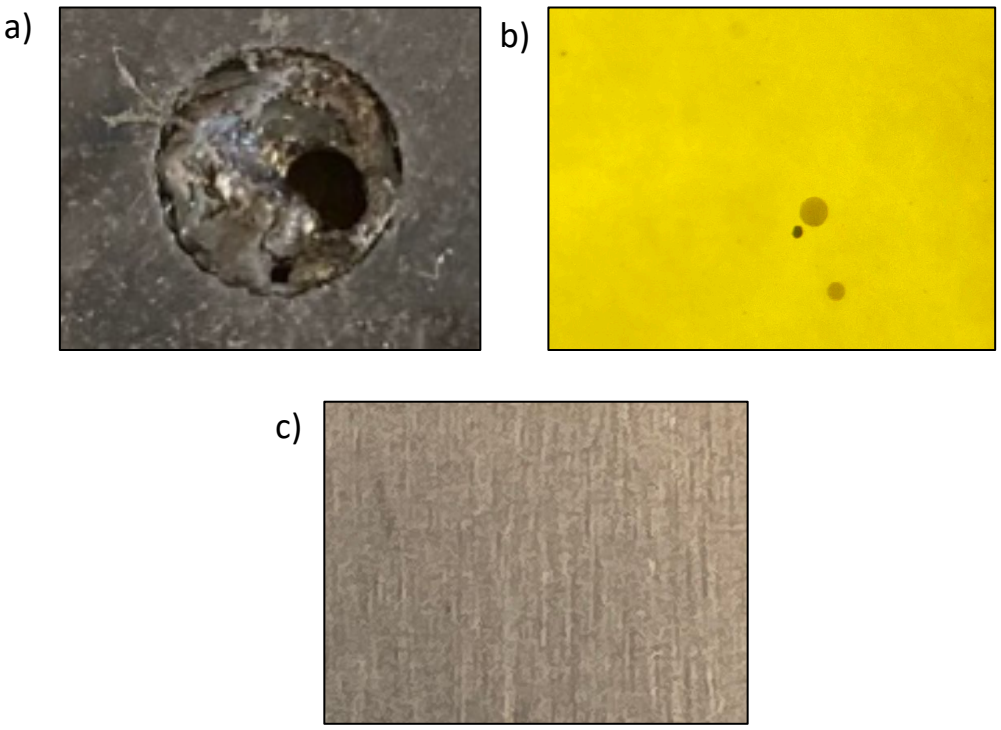

Figure 4.18: TSAM results from light gas gun experiment when impacted at 1.5 km/s. a) Mostly intact TSAM after basalt impact. b) Tape with no hole or damage, containing several caught basalt particles in the transparent TSAM attached to its surface. c) Undamaged aluminium back plate.

Upon confirming complete impact absorption, the state of the basalt particles within the TSAM was investigated. Scanning electron microscopy was employed for this purpose. The impacted TSAM was allowed to desiccate at room temperature to create a xerogel suitable for scanning electron microscopy imaging. Within this experiment, non-fired basalt particles were also imaged (Figure 4.19a) to provide the native structure of the basalt particles, and a complete elemental fingerprint from energy dispersive X-ray analysis (Figure 4.19a). These results allowed for direct comparisons to be drawn between the non-fired particles and the basalt particles integrated into TSAM following impact, further validating the obtained results. Scanning electron microscopy Imaging of the TSAM xerogel revealed multiple basalt fragments within the TSAM appearing spherical in shape (Figure 4.19b-c). When energy dispersive X-ray analysis was performed on the spherical structures (Figure 4.19b-c), the elemental profiles matched the non-fired basalt particle fingerprint spectra (Figure 4.19a). Therefore, as with the experiment in Section 4.5.1, intact preserved basalt particles were found within the impacted TSAM.

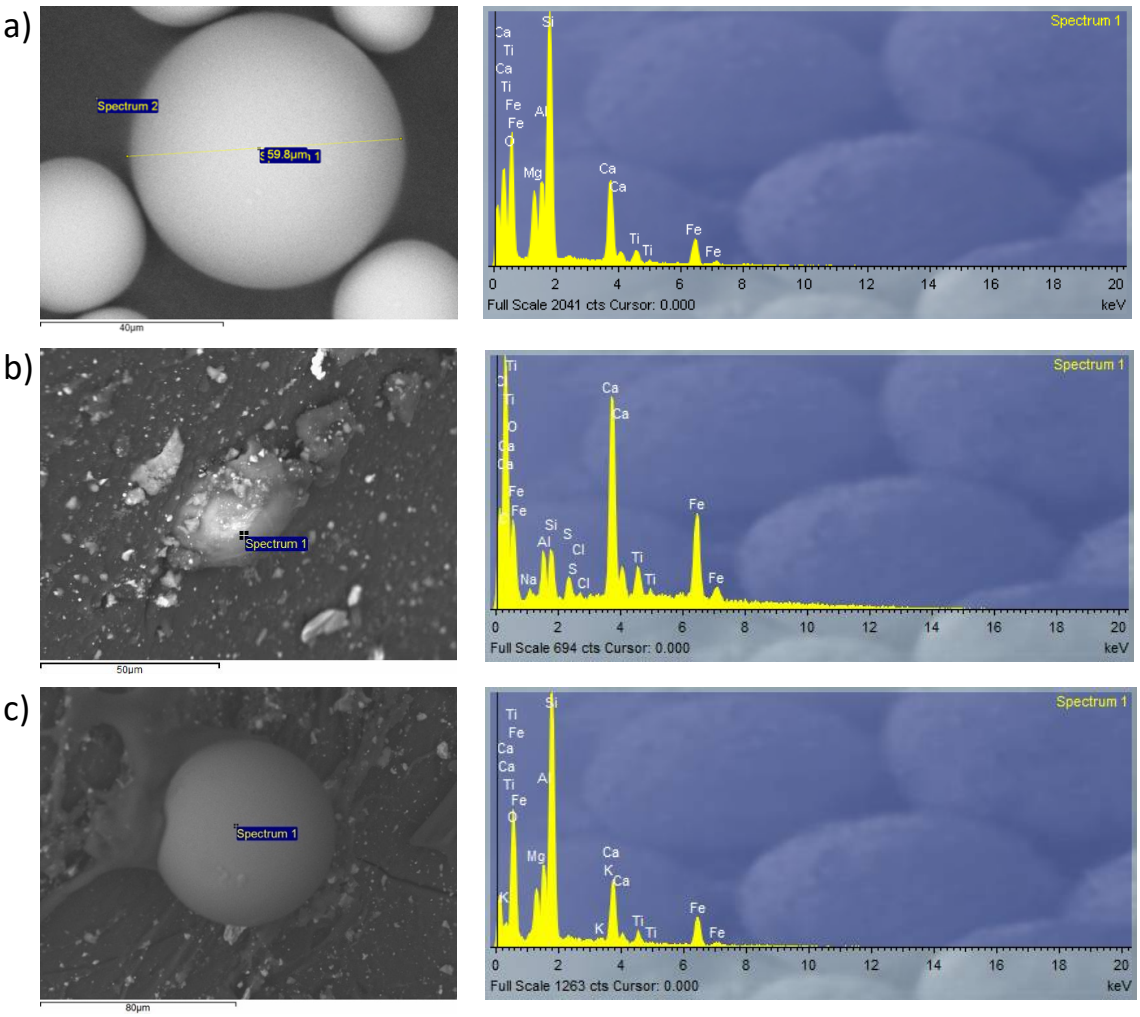

Figure 4.19: Scanning electron microscopy images and energy dispersive X-ray analysis of basalt particles from light gas gun experiment. a) Non-fired basalt particles (left) and corresponding energy dispersive X-ray spectrum (right). b) Basalt particle caught in TSAM following light gas gun experiment (left) and energy dispersive X-ray spectrum confirming particle as basalt (right). c) Basalt particle caught in TSAM following light gas gun experiment and its energy dispersive X-ray spectrum confirming particle as basalt.

4.5.3 TSAM captured and absorbed impact from aluminium shrapnel

As previously mentioned, during one of the TSAM impact experiments a fragment of aluminium burst disc impacted the 500 µL TSAM material causing the hole seen in Figure 4.18a. Imaging of the impacted TSAM revealed a fragment of aluminium between 100-200 µm in length and ~100 µm in width (Figure 4.20a). Scanning electron microscopy was used to confirm that this was an aluminium fragment and energy dispersive X-ray analysis at multiple sites across the fragment confirmed the

presence of aluminium within its composition (Figure 4.20b). As the burst disc was the only element containing aluminium that could have plausibly ended up integrating into the TSAM material, this finding confirmed that the burst disc was responsible for the impact hole observed in Figure 4.18a.

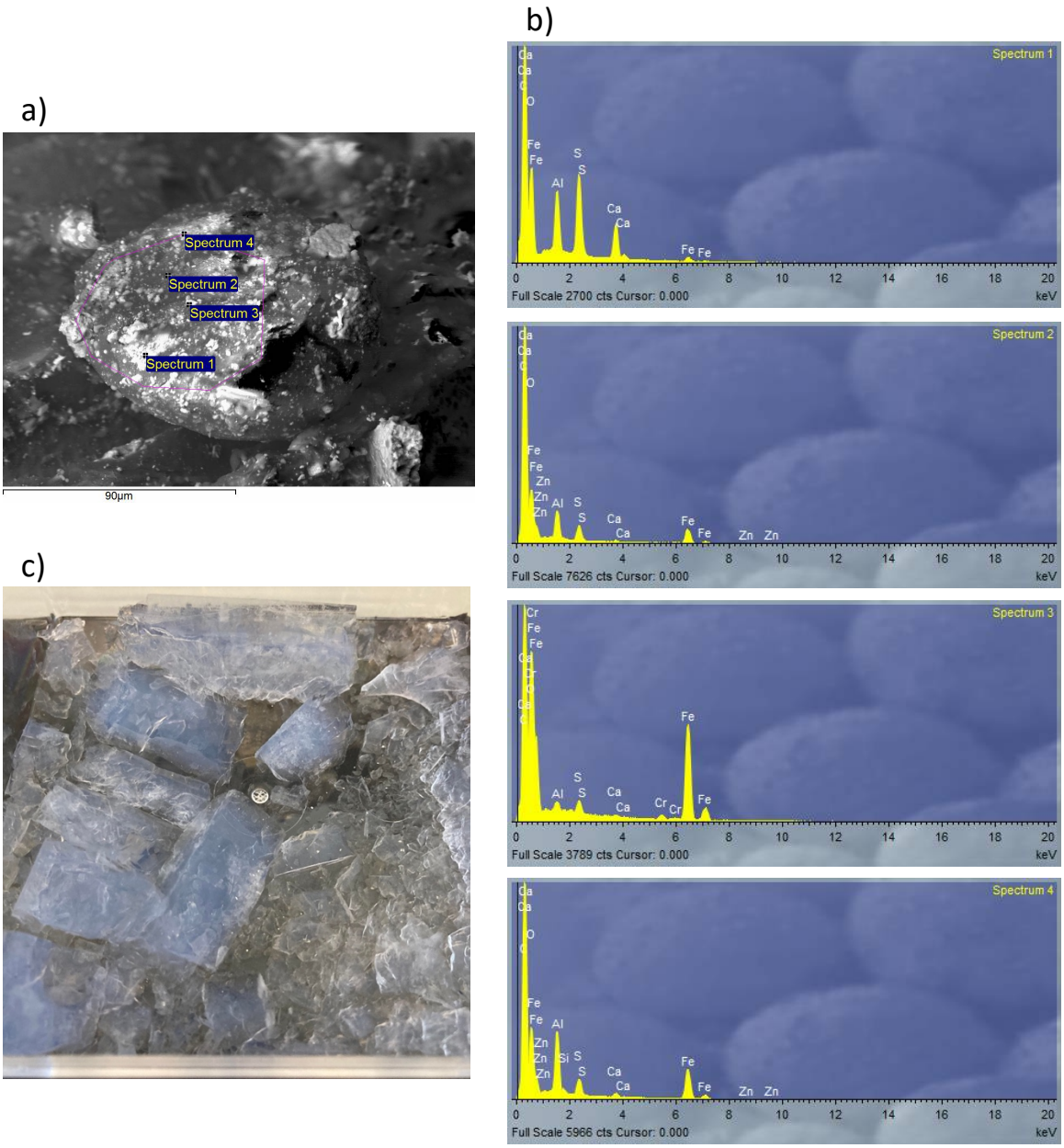

Figure 4.20: Scanning electron microscopy images and energy dispersive X-ray analysis of aluminium burst disc fragment from light gas gun experiment. a) Scanning electron microscopy image of the burst disc fragment within the TSAM. b) Energy dispersive X-ray analysis at different sites of the aluminium fragment. c) Aerogel impacted by aluminium burst disc during 3 km/s projectile experiment.

Previous experiments utilising the industry standard aerogel material for projectile capture and preservation, whereby burst disc fragments impacted the aerogel, resulted in its complete destruction. One such example of a destroyed aerogel resulting from burst disc impact is shown in Figure 4.20c. Destruction under these conditions occurred due to the brittleness of the aerogel, a property not exhibited by TSAMs. Therefore, in this respect TSAMs outperformed the current industry standard, and demonstrated the ability to withstand high velocity shrapnel impacts.

4.6 Discussion

This chapter provided a complete characterisation of the TSAMs structure, macroscale properties and shock absorbing performance upon supersonic impacts, achieving the second aim outlined in Section 1.5. Furthermore, confirmation of the energy dissipating mechanism of talin rod domain unfolding within the TSAM was confirmed, and a potential non-biomedical industrial application revealed.

Investigations into TSAMs hydrogel structure using a combination of transmission electron microscopy and scanning electron microscopy revealed the differential characteristics of the network on the nanometre and micrometre scales. Specifically, at the nanometre scale the predicted lattice structure resulting from crosslinking via tri-substituted forms of crosslinker **3** was confirmed. However, when imaged at the micrometre scale, long fibrous structures existed, forming a porous network. Combining these findings indicated that the lattice structure observed on the nanometre scale assembled into long fibrous structures on the micrometre scale, enabling the encapsulation of water and formation of a TSAM hydrogel.

Following these microscopy experiments, a previously described plate reader method for monitoring gel fibre formation was adapted for TSAMs. This novel adaptation of the plate reader methodology was shown to differentiate between solutions of crosslinked pGEL001 at concentrations below the MGC, and the gelated TSAM, by measuring deviations in OD readings compared to established patterns obtained with control solutions. This new methodology offers the benefits of small

sample volumes and retention of the aqueous state of the studied hydrogels, removing the limitation of desiccation required for transmission electron microscopy and scanning electron microscopy. Due to the retention of the aqueous state, the TSAMs from this experiment could be reused for further experimentation, saving large quantities of pGEL001 and the time and resources used in its production. This plate reader methodology can be utilised in future iterations of TSAMs to minimise material waste during characterisation. Furthermore, this methodology determined gel fibre formation within transparent hydrogels, whereby much smaller OD contributions from gel fibres would be expected compared to opaque hydrogels, exemplifying the sensitivity of the method. Therefore, this adapted form of the plate reader methodology may prove effective in future investigations on other transparent hydrogels, complementing the methodology developed by (White *et al*., 2020).

Next, key macroscale properties of TSAMs were highlighted, including extensibility, adhesivity and mouldability, each of which open TSAMs up to exploitation in a wide variety of applications. For example, one potential future application for TSAMs is artificial skin, with products used for this purpose requiring high levels of extensibility to mimic natural skin (MacNeil, 2008), mouldability for thickness and shape control, while adhesivity removes the need for invasive attachment methods such as stitching. Following the outlining of these material properties, focus moved towards confirming the retention of R1-R3 unfolding in pGEL001 when contained within TSAMs. As described in Section 4.4, few techniques are available for investigating protein unfolding in the solid state under dynamic conditions (i.e. force). Here, oscillatory shear strain sweeps were performed using a rheometer, theoretically capable of determining pGEL001 unfolding due to the large extensions in length of pGEL001 monomers in the unfolded state, inducing significant changes in the flow of the material. Experiments were conducted to obtain measurements of TSAMs with induced unfolding of pGEL001 and hindered refolding using GFP-VD1, in comparison to TSAMs containing GFP and buffer whereby no impact on mechanical properties would occur. These experiments allowed isolation of patterns in the data occurring directly due to unfolding of the pGEL001 monomers, with the presence of a shear

yield point found to occur only in the TSAM swelled with GFP-VD1. Binding of pGEL001 by GFP-VD1 was confirmed with maximum projection wide field fluorescent microscopy, whereby the GFP-VD1 was found to localise to TSAM fibres while the GFP control sample presented no selective localisation to the fibres. As GFP-VD1 can only bind to the unfolded confirmation of pGEL001, this observation confirmed induced pGEL001 unfolding in the GFP-VD1 swelled TSAM. Therefore, these results provided strong evidence for the presence of a shear yield point directly indicating pGEL001 unfolding within TSAMs. As a result of this finding, it was possible to confirm observations of decreased rigidity, increased phase angle and induction of shear yield points seen in non-swelled TSAM samples to indicate pGEL001 unfolding in response to force. The rheological investigations conducted also revealed an additional interesting property of increasing rigidity upon repeated exposure to force within TSAMs. Future studies should investigate the differential performance of TSAMs in the light gas gun experiments when used at different induced rigidity states. Importantly, the results from this set of experiments provided a proof of principle for rheology as a useable methodology for monitoring protein unfolding within a protein-based material in response to force, the first example of this within the literature to the authors best knowledge. With further data to support these findings in other materials, the rheological methodology established could fill the current void of technologies capable of dynamic protein folding characterisation in materials, facilitating future developments of protein-based materials for a diverse array of applications. In summary, the energy dissipating mechanism of pGEL001 unfolding was shown to be retained in TSAMs and triggered when exposed to force.

Finally, TSAMs ability to survive supersonic impacts was investigated. Utilising the light gas gun apparatus, 500 µL TSAMs were shown to completely absorb the impact from basalt particles shot at 1.5 km/s. Moreover, these particles were captured and preserved in their native state, indicating TSAMs as highly efficient shock absorbers capable of maintaining the force experienced by the projectiles below that of their break force. During the final impact experiment, an aluminium fragment from the burst disc was also found to impact the TSAM. This serendipitous mis-fire clearly demonstrated that the TSAM could also absorb the impact energy from this

aluminium fragment, evidenced by the undamaged aluminium backplate and tape. The industry standard silica aerogel materials used for this purpose are usually destroyed when exposed to similar burst disc impacts, as a result of the aerogel materials brittleness. Therefore, TSAMs outperformed the industry standard material in this respect. Future work will seek to investigate this result further, with a more deliberate design to achieve shrapnel impact using a range of materials and velocities. Furthermore, TSAMs utilise the endothermic energy dissipating mechanism of protein unfolding, theoretically removing the heating of projectiles that is observed when the insulating aerogel materials capture high velocity projectiles (Alwin and Shajan, 2020). Removal of projectile heating observed with aerogels, which can result in altered chemical and structural composition of the projectile (Jones *et al*., 2013) (Bheekhun *et al*., 2013), is an important added benefit of TSAMs, overcoming the primary limitation of the current industry standard material utilised in these impact studies. In addition, TSAMs display extensibility, adhesivity and theoretical refolding upon removal of force repairing the shock-absorbing mechanism, all of which are absent in aerogel materials. These high velocity impact experiments are widely employed in the aerospace sector and seek to maintain the projectile in an unaltered state for further experimentation. Therefore, a potential industrial application of TSAMs was elucidated within this investigation, with indications of superior performance compared to the current industry standard material employed for these forms of experiment. Further experimentation should seek to define the upper velocity limit TSAMs can withstand whilst still preserving the state of a variety of projectiles.

In summary, the objectives outlined within the second aim described in Section 1.5.1 were achieved within this chapter. In addition, multiple future avenues for further investigation were elucidated during the characterisation of the TSAM, including the identification and development of two assays that have the potential to greatly improve future protein-based material characterisation. Future work required to build on these findings is discussed in detail within Chapter 6.

Chapter 5: Future directions for TSAMs

5.1 Overview

This chapter focuses on preliminary data that will be used to inform the future directions of the TSAM project. First, scaling up the expression of pGEL001, required for ballistics-based impact testing of TSAMs, was investigated using multiple expression systems. Next, experimentation on characterising the unfolding force profile of the mutated pGEL001 R1-R3 domains was conducted, with the aim of establishing a protocol to enable single molecule biophysical characterisation of future TSAM monomers. Finally, two new TSAM monomers with different mechanical properties were designed, expressed and purified. A preliminary gelation investigation was conducted and the new TSAMs rheological performance tested.

5.2 Scaling up expression levels of pGEL001 for future impact experiments.

With early data showing TSAMs capable of withstanding supersonic impacts, demonstrating a real-world application in supersonic impact capture and preservation, future work will aim to establish a role for TSAMs in additional impact-based applications. Specifically, investigating TSAMs performance as a shock absorber in a variety of explosive and firearm projectile experiments will be conducted (The industry standard ceramic armour is discussed in Section 1.1.2). To enable these investigations, optimising the yield of pGEL001 was vital, due to the large quantities of protein required to cast even a small volume of TSAM. Specifically, up to 40% loss of pGEL001 can occur during TSAM preparation, therefore due to the MGC of 200 mg/mL, to produce 100 mL of TSAM up to 33 g of pGEL001 would be required. To optimise expression, two expression methods were compared to the traditional shake flask expression method; a patent protected vesicle nucleating peptide (VNp) expression system and bioreactor expression of pGEL001 both utilising BL21 DE3 *E. coli*. Direct comparisons between the yields obtained from each method were made, including the applicable limitations of each method based on laboratory resources.

5.2.1 Testing the VNp vesicular export expression system

Research conducted within the Mulvihill laboratory discovered a novel expression system capable of exporting recombinant proteins expressed in *E. coli* into the growth media (Patent application number: GB2118435.3) (Eastwood *et al*., 2022). Specifically, by introducing an α-synuclein derived VNp sequence (an alpha helical structure consisting of the terminal residues of α-synuclein) onto the N-terminal of a recombinant protein, the protein was shown to be packaging into membrane derived vesicles and exported. Previous work by the Mulvihill laboratory showed this system to facilitate expression of toxic proteins, whilst also enhancing the yields of several proteins in comparison to traditional expression methodologies. Therefore, pGEL001 was tested with two derivative VNp sequences, whereby an N-terminal VNp6 or VNp15 sequence was introduced onto the pGEL001 construct (Figure 5.1). Two derivatives of VNp were tested to determine the optimum sequence for improved expression. The two VNp sequences selected differed in the number and sequence of amino acids, with both sequences previously shown to achieve efficient exportation of its conjoined protein. Both of the VNp-pGEL001 constructs contained an N-terminal VNp sequence and a C-terminal flexible linker terminating with a His-tag, shown in Figure 5.1. PCR amplification utilising custom primers and traditional cloning methods (Described in Section 2.4) were employed to synthesise the two resulting constructs, VNp6-pGEL001 and VNp15-pGEL001, confirmed successful through sequencing.

Figure 5.1: Key sections of the recombinant VNp-pGEL001 proteins. The block labelled VNp was either VNp6 or VNp15 depending on the construct.

Following successful production of VNp6-pGEL001 and VNp15-pGEL001, expression trials were performed to confirm exportation of the proteins into the media and quantitate the resulting yield. Quantification of the yield was achieved using BSA standards of 0.075, 0.100 and 0.500 mg/mL. These standards, in addition to samples of the two VNp-pGEL001 proteins pre-induction, post-induction pellet and post-

induction supernatant were run using SDS-PAGE. Using ImageJ analysis software, the intensities of the Coomassie stained bands were determined and compared to those of the BSA standards, allowing a concentration in mg/mL to be estimated. Initially the expression trials were conducted by inoculating 25 mL of TB media in 0.5 L non-baffled flasks with the two VNp-pGEL001 constructs transformed into BL21 DE3 *E. coli*. These were the standard conditions used in the Mulvihill lab when testing this system and were therefore investigated before scaling up to larger volumes.

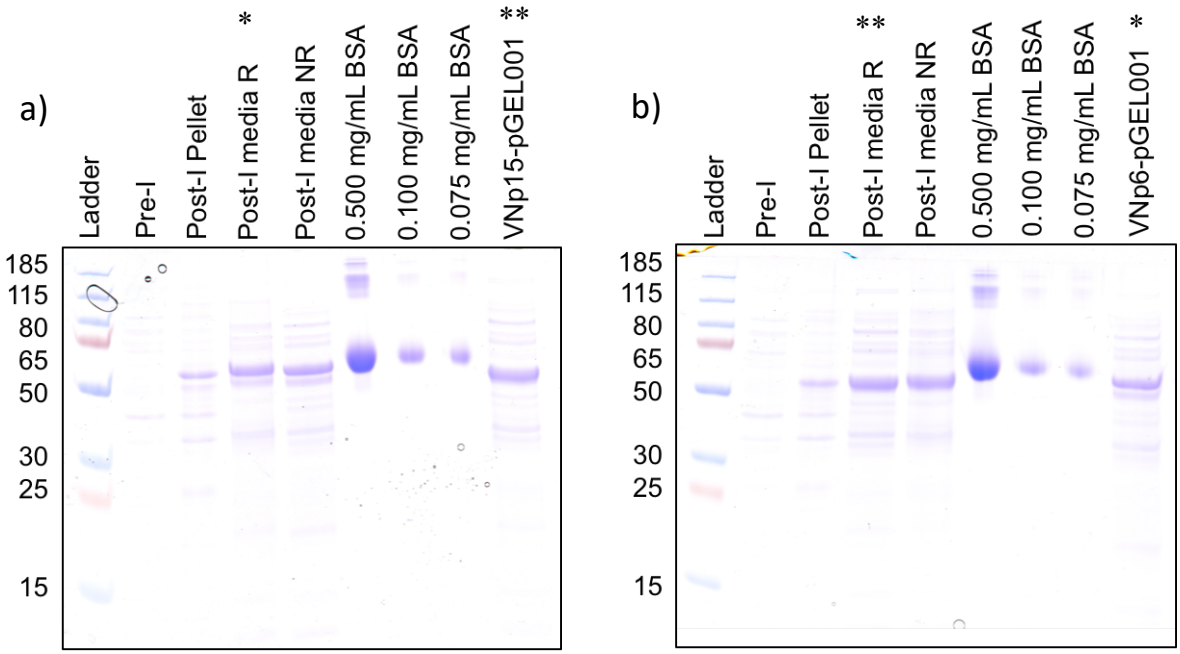

Figure 5.2: SDS-PAGE from the small-scale expression trial of VNp6-pGEL001 and VNp15-pGEL001. a) VNp6-pGEL001. b) VNp15-pGEL001. The pre-induction (Pre-I) and post-induction (Post-I) pellet and media samples (R = reduced, NR = non-reduced) of each Vnp-pGEL001 were loaded. BSA samples of 0.500 mg/mL, 0.100 mg/mL and 0.075 mg/mL were also loaded, in addition to the reduced media sample of the opposing VNp system to compare reproducibility in the estimated yields between the two gels. Lanes marked with * or ** are from the same sample. All samples were diluted to the same OD_{600} value.

Table 5.1: Calculated yields of VNp6-pGEL001 and VNp15-pGEL001 from the BSA control samples. The values marked with * and ** were controls used to validate the accuracy of the two SDS-PAGE Coomassie stained gels, whereby the same samples were loaded into each of the two gels, confirmed accurate from the almost identical mg/mL calculated in each of the two gels.

	VNp6-pGEL001 (mg/mL)				VNp15-pGEL001 (mg/mL)			
BSA standard (mg/mL)	Pellet	Media (R)	Media (NR)	VNp15 media (R)	Pellet	Media (R)	Media (NR)	VNp6 media (R)
0.500	0.06	0.19	0.20	0.24	0.06	0.23	0.26	0.13
0.100	0.04	0.11	0.11	0.14	0.04	0.16	0.18	0.09
0.075	0.02	0.06	0.08	0.15	0.04	0.17	0.19	0.10
Average	0.04	0.12*	0.13	0.18**	0.05	0.18**	0.21	0.11*

The results from the small-scale expression trial of VNp6-pGEL001 and VNp15-pGEL001 are displayed in Figure 5.2a-b. Yields for the two VNp systems from Figure 5.2a-b were calculated by taking the estimated mg/mL, quantified by comparing the intensity of the VNp-pGEL001 samples against the intensities of the 0.500 mg/mL, 0.100 mg/mL and 0.075 mg/mL BSA samples, and then averaging the three calculated values. The resulting calculated yields based off the intensity of the BSA standard samples are shown in Table 5.1. To confirm comparisons could be drawn between the two SDS-PAGE Coomassie-stained gels (Figure 5.2a and Figure 5.2b) the same sample from each of the VNp systems reduced media was loaded onto each of the two gels (VNp15 = * and VNp 6 = ** in Table 5.1). The yields of the VNp6-pGEL001 media sample were calculated as 0.12 and 0.11 mg/mL from the two gels, while the VNp15-pGEL001 yields were calculated as 0.18 mg/mL from both gels. Therefore, the yields calculated were at least 92% similar between the two gels, confirming reliable comparisons could be drawn. In Figure 5.2a showing the VNp6 samples, approximately 25% of the expressed VNp6-pGEL001 was found to remain in the cells, appearing in the pellet fraction following centrifugation of the media. Additionally, almost identical yields were obtained from the reduced and non-reduced samples in Figure 5.2a, with the SDS-PAGE results clearly showing little disulphide bonding occurring, with no change in the presence of higher order species between the two samples. For VNp15, approximately 22% of VNp15-pGEL001 was found to remain in the cells, a 3% reduction compared to that of VNp6-pGEL001 (25%). Once again, no

significant disulphide bonding was observed, with no difference in the quantity or intensity of the higher order species within the two samples, and similar calculated yields for both the reduced and non-reduced samples. Finally, comparing between the two systems revealed VNp15-pGEL001 to present higher expression levels, with a yield of 0.18 mg/mL, compared to VNp6-pGEL001 with a yield of 0.12 mg/mL.

Next, scaling up the expression from the previous 25 mL in 0.5 L flasks was investigated. Here volumes of 150 mL in 2.0 L non-baffled flasks were employed. Due to the grams of pGEL001 required for industrialised explosive and firearms testing, it was important to determine the most efficient expression method considering both yield and available resources within the laboratory. Important factors to consider were the limitation of incubator space and glassware demands (including autoclaving etc.). Specifically, if similar yields were obtained between the large-scale experiment (2.0 L flasks) and previously discussed small scale experiment (0.5 L flasks), six 0.5 L flasks would be required to produce the equivalent weight of pGEL001 obtained from one 2.0 L flask. Using the example of Fisher Scientific Pyrex™ borosilicate glass culture flasks, a 0.5 L flask presents a 105 mm diameter and therefore occupies an area of 8,659.01 mm^2, whilst a 2.0 L flask presents a 166 mm diameter and therefore occupies an area of 21,642.43 mm^2. Importantly, this means to achieve the same final weight of pGEL001 obtained from a 2 L flask, the equivalent weight of pGEL001 from 0.5 L flasks would require a minimum of 2.4x the incubator space, and substantially more glassware. The importance of these space considerations is further exemplified when considering the tens of grams that will be required, whereby at 0.18 mg/mL continuous growth of cultures in 2.0 L flasks over a 50-day period would be required, which would extend to 120 days if 500 mL flasks were used.

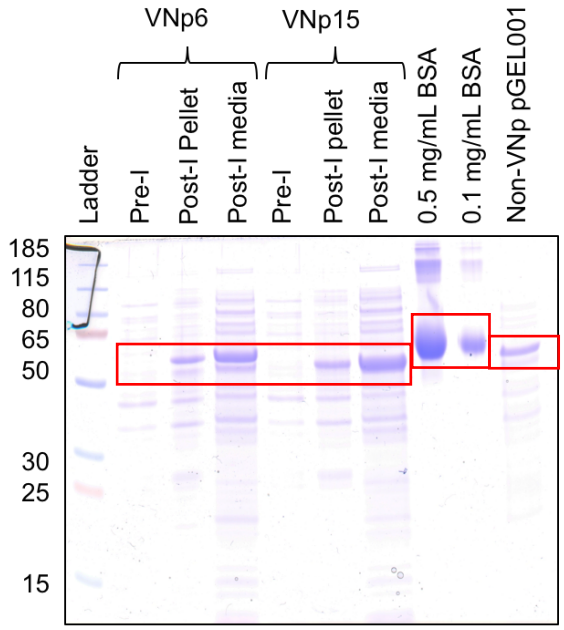

Figure 5.3: SDS-PAGE from the large-scale expression trial of VNp6-pGEL001 and VNp15-pGEL001. The pre-induction (Pre-I) and post-induction (Post-I) pellet and media samples of each VNp-pGEL001 were loaded. BSA samples of 0.5 mg/mL and 0.1 mg/mL were also loaded, in addition to the post-induction sample of pGEL001 expression through traditional means from a 750 mL culture. The bands quantitated with ImageJ are highlighted with a red box. All samples were diluted to the same OD_{600} value.

Table 5.2: Calculated yields of VNp6-pGEL001, VNp15-pGEL001 and traditionally expressed pGEL001 from the BSA control samples.

	VNp6-pGEL001 (mg/mL)		VNp15-pGEL001 (mg/mL)		
BSA standard (mg/mL)	Pellet	Media (R)	Pellet	Media (R)	pGEL001 traditional
0.500	0.04	0.12	0.04	0.20	0.05
0.100	0.02	0.07	0.02	0.12	0.03
Average	0.03	0.10	0.03	0.16	0.04

The SDS-PAGE results of samples from the large-scale expression trials using 150 mL of media inoculated with either VNp6-pGEL001 or VNp15-pGEL001 in 2.0 L flasks are shown in Figure 5.3. The yields obtained in each condition were calculated based off the intensities of 0.5 mg/mL and 0.1 mg/mL BSA samples using ImageJ analysis software, with the calculated values shown in Table 5.2. Here, 23% of VNp6-pGEL001 was shown to remain in the cells, an almost identical percentage to that obtained in

the small-scale trial (25%). Comparatively, only 16% of VNp15-pGEL001 remined in the cells, 6% less than the 22 % found to remain in the cells in the small-scale expression trial. Both VNp6-pGEL001 and VNp15-pGEL001 presented slightly smaller yields than those obtained in the small-scale trials, at 0.10 mg/mL and 0.16 mg/mL respectively, a 0.02 mg/mL decrease compared to the yield from the respective small-scale trial for both. A sample of traditionally expressed pGEL001 was also quantitated, revealing a yield of 0.04 mg/mL. Therefore, increases in yield compared to the traditional expression system were shown to be 300% for small scale and 250% for large scale VNp6-pGEL001, and 450% for small scale and 400% for large scale VNp15-pGEL001.

Overall, VNp15-pGEL001 presented the largest increase in yield compared to traditional pGEL001 expression in both the small scale and large-scale conditions. Additionally, due to there only being an 11% drop in yield between the small-scale and large-scale expression volumes, a clear benefit in using the large-scale expression conditions was apparent. Specifically, an approximate 60% drop in expression would have to have occurred for small scale expression to become equally efficient when considering the laboratory-based resource limitations. Based on the obtained yields from this large-scale expression experiment and utilising the single incubator available in the laboratory over a one-week period, VNp15-pGEL001 expression would produce a volume of 5.85 L of media requiring purification, containing 936 mg of VNp15-pGEL001. However, even though an improved expression was observed with VNp15-pGEL001 compared to traditional expression methods, due to the small volumes of 150 mL in 2.0 L flasks, pGEL001 through traditional expression methods with the same resource limitations would produce a higher yield of 1170 mg in the smaller volume 0.73 L. Therefore further volume increases need testing for VNp15-pGEL001 to display a benefit over traditional pGEL001 expression techniques.

Following the expression trials, an attempt at purifying the resultant VNp15-pGEL001 was conducted. The batch method was employed due to the large volumes of media requiring purification, with HisTrap HP columns limited by their maximum flow rate,

at larger volumes the batch method can become more time and resource efficient. The results from this purification are shown in Figure 5.4.

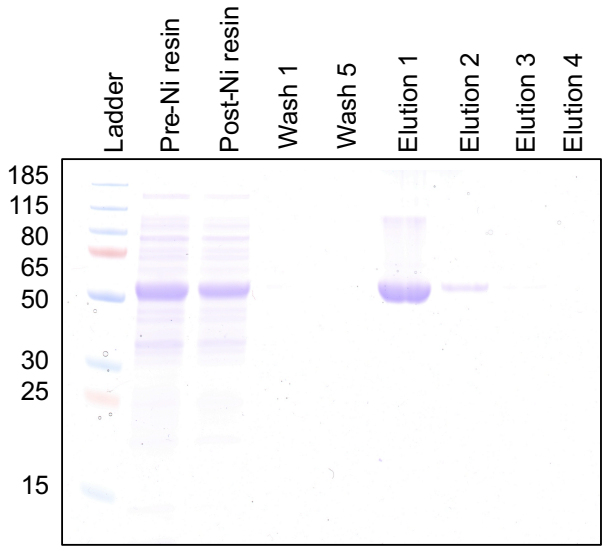

Figure 5.4: SDS-PAGE from batch His-tag purification of 150 mL of VNp15-pGEL001. Samples of the supernatant before applied to the resin (Pre-Ni resin), of the supernatant following 40-minute incubation and subsequent removal of the resin (Post-Ni resin), the flow through from washes 1 and 5 with nickel buffer A and the four 1 mL elution's with nickel buffer B are shown.

From the preliminary attempt at purifying VNp15-pGEL001 using the batch method, the affinity of VNp15-pGEL001 for the nickel resin appeared to be low. A sufficient amount of nickel resin was applied to ensure at 100% binding of the expressed VNp15-pGEL001 to the resin, saturation of the resin would not occur. When looking at the pre-Ni resin and post-Ni resin lanes in Figure 5.4 it is clear that a large quantity of the VNp15-pGEL001 remained in the supernatant following removal of the beads. This result was verified with a second attempt at purifying a different batch of VNp15-pGEL001. Furthermore, the elution's in Figure 5.4 also showed a low yield of VNp15-pGEL001, further confirming a low affinity of VNp15-pGEL001 to the resin in these experiments. As a result, a comparative purification utilising the HisTrap HP column should be conducted to determine whether the issue was due to low release of VNp15-pGEL001 from vesicles via sonication, low binding to the specific resin used, or with VNp15-pGEL001s affinity for His-tag based purification methods. The C-terminal His-tag used within this construct compared to the N-terminal His-tag used

in the previous pGEL001 constructs may be an additional potential explanation for the low binding affinity to the nickel resin.

5.2.2 Bioreactor expression of pGEL001

Bioreactor systems are often employed for large scale production of proteins, widely utilised in the biopharmaceutical industry (Tripathi and Shrivastava, 2019). Bioreactors are categorised as batch, fed-batch or continuous culture systems each allowing for continued expression of protein over a prolonged period of time (Kopp *et al*., 2020). Here, multifors (Infors) fed-batch bioreactors were employed. This fed-batch form of bioreactor allows for optimisation of the feeding profile required by the culture, allowing for addition of carbon sources (ensuring sufficient bacterial cyclic adenosine monophosphate concentrations for enzyme biosynthesis) and other nutrient forms over time to replenish the depleted resources resulting from the continued growth of the bacteria (Srivastava and Gupta, 2011). Bioreactors achieve high expression levels of proteins due to the much higher cell densities reached compared to that of traditional expression methods. Therefore, investigations into the maximum achievable yields using the fed-batch bioreactor system were conducted.

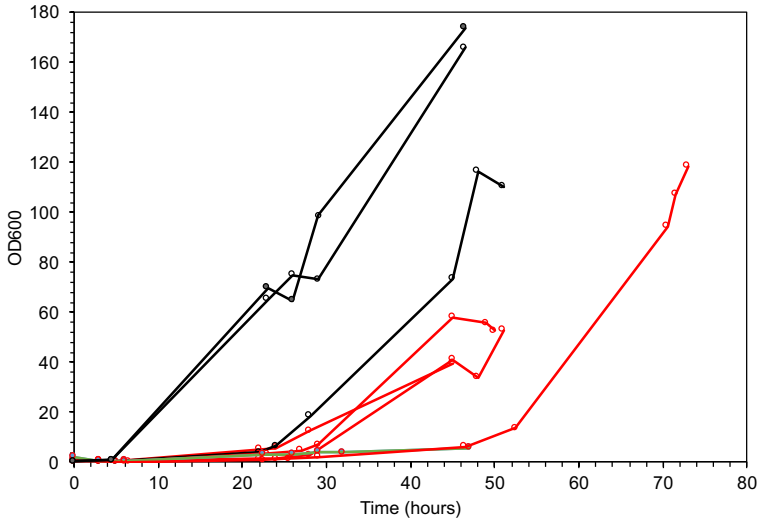

Figure 5.5: Growth profiles of the bioreactor runs attempted for pGEL001 in BL21 DE3 *E. coli*. Black = expression of pGEL001, Red = No expression of pGEL001.

In total, eight bioreactor runs were performed, with the growth profiles displayed in Figure 5.5. Of the eight runs, three displayed expression of pGEL001, confirmed through both Coomassie staining of the resultant SDS-PAGE gels and N-terminal anti-His-tag western blots shown in Figure 5.6a-b. The 5 unsuccessful runs failed due to issues of contamination or slow growth resulting in low or no expression of pGEL001. The successful bioreactor runs all reached OD_{600} values exceeding 100, indicating cell densities over 25-fold those obtained in traditional expression methodologies.

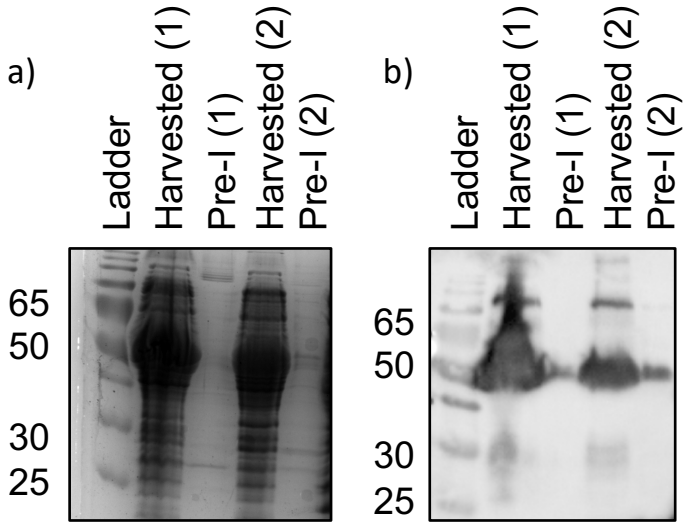

Figure 5.6: SDS-PAGE results from a successful bioreactor run. a) Coomassie stained gel of pre-induction and post-induction samples from one bioreactor run. b) Anti-His western blot of the same samples in a).

To obtain an approximate yield of pGEL001 from the successful bioreactor runs, HisTrap HP column purifications were performed on the harvested cells, utilising the same purification protocol applied for all previous pGEL001 purifications performed in Chapters 3-4. Due to the high cell densities achieved, the harvested pellets from the bioreactor cultures reached weights of up to 160 g. Resuspension was performed with nickel buffer A using the standard of 10 mL per 1 g of pellet. Therefore, a single bioreactor produced up to 1.6 L of media for application to the HisTrap HP column. A total of 250 mL of media was loaded onto a single HisTrap HP column, with seven sets of purifications required per bioreactor run. An example set of elution's following purification from 250 mL of a successful bioreactor growth is shown in Figure 5.7.

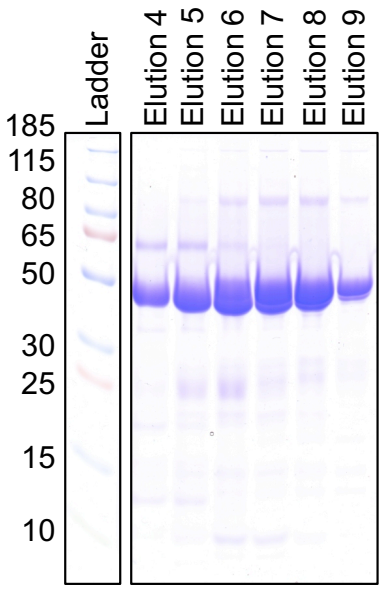

Figure 5.7: Example Coomassie stained SDS-PAGE gel of elution's from HisTrap HP purification of a successful bioreactor run.

Following the complete purification of two separate successful bioreactor growths of pGEL001, total purified yields were calculated at 1.1 g/L and 1.2 g/L for each of the bioreactor runs respectively. Although the yields were substantially higher than both traditional and VNp based expression systems (determined in Section 5.2.1), with these values also representing the purified yield as opposed to the crude pGEL001 concentration in the media, only 400 mL of culture is produced from a single bioreactor. Therefore, one successful bioreactor run taking a full week to perform would produce approximately 1.6 L of media requiring purification, resulting in 480 mg of pGEL001. Up to three bioreactor runs could be performed over a one-week period, therefore producing up to 1440 mg of pGEL001 in 5.5 L of media. Although this yield was higher than both VNp15-pGEL001 and traditional pGEL001 expression, many of the bioreactor runs failed, therefore presenting low consistency. Further investigation into how to decrease the number of failed bioreactor runs would be required before this method can be relied on for high-throughput production of pEL001.

5.3 Biophysical characterisation of pGEL001 utilising the C-trap® apparatus

Measurements of pGEL001s unfolding force and extension profile were attempted using a newly acquired C-trap® apparatus from Lumicks. As discussed in aim three of Section 1.5, results from single molecule unfolding measurements could facilitate future TSAM hydrogel design, exemplified by the works of Fang *et al*. (Fang *et al*., 2013) and lv *et al*. (Lv *et al*., 2010). The C-trap® apparatus combines high resolution optical tweezers with fluorescence microscopy to allow for dynamic single-molecule measurements. By labelling pGEL001 at its termini with 5'digoxigenin or 5' biotin modified DNA handles, the resulting labelled protein could be tethered to anti-digoxigenin and streptavidin beads. Optical tweezers employ focused light to trap these beads, allowing precise forces to be applied to pGEL001 and subsequent changes in length to be measured through manipulation of the beads (Mondal *et al*., 2022). Furthermore, binding of fluorescently tagged proteins to pGEL001 could also theoretically be monitored through the attached fluorescence microscope. This described series of events is summarised in Figure 5.8. An in-depth description of the experimental produce can be found in Section 2.7.4. C-trap® biophysical measurements were performed on pGEL001 with the aims of 1) Characterising the effects on the unfolding force of R1-R3 resulting from the cysteine to serine mutations, and 2) Establish a new methodology for inhouse biophysical characterisation of protein unfolding. The latter aim would allow characterisation of future hydrogel monomers unfolding forces, in addition to facilitating fundamental biophysical research conducted within the Goult laboratory.

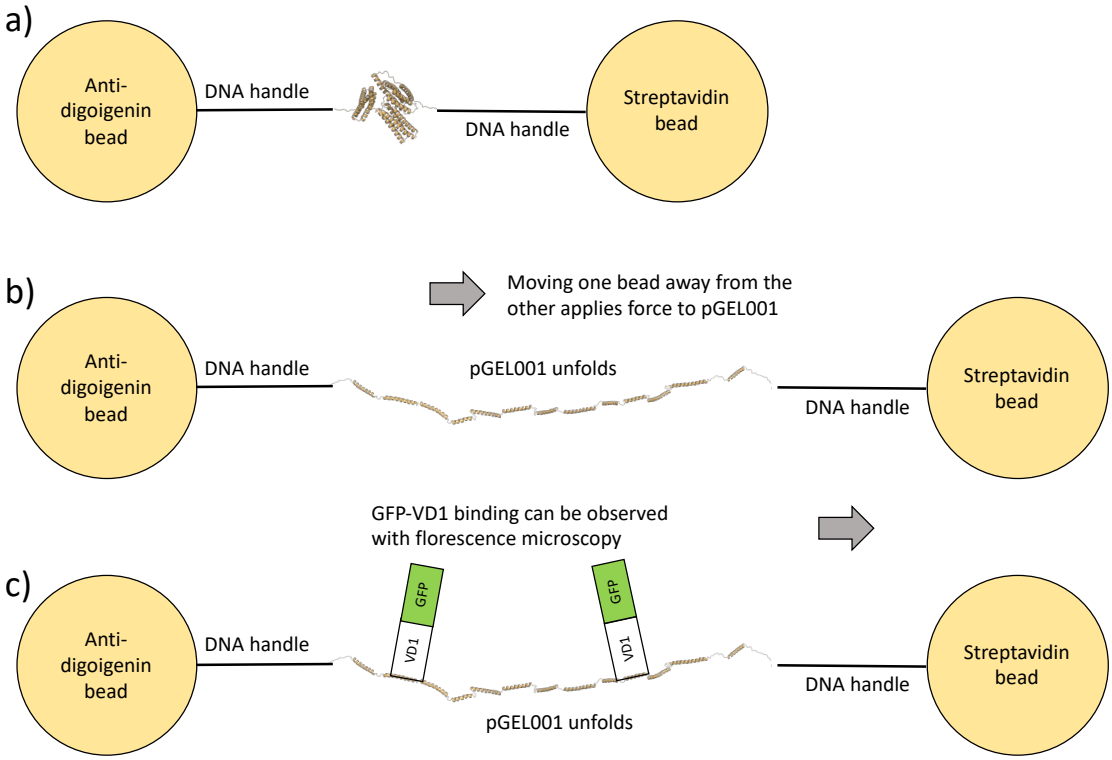

Figure 5.8: Theoretical C-Trap® biophysical characterisation of pGEL001. a) pGEL001 tethered between two beads via terminal DNA handles. b) Moving one bead away from the other applies force to the tethered pGEL001, causing unfolding of its mutated R1-R3 domains. c) Binding of GFP-VD1 to the unfolded pGEL001 could be visualised through the fluorescence microscope.

Labelling of pGEL001 was conducted using maleimide modified oligos from Lumicks. These oligos reacted with the N- and C-terminal cysteines of pGEL001, providing labelling of pGEL001 at its terminals. The resulting labelled pGEL001 was subsequently diluted to a DNA concentration of 20 ng/μL. Immediately before application to the C-trap®, long DNA handles were hybridised to the short oligos attached to pGEL001, followed by coupling of the 5' digoxigenin modified long DNA handles to the anti-digoxigenin beads (bead 1). The bead 1 tethered to pGEL001 was then injected into the microfluidic channel 1 of the flow cell, with buffer injected into microfluidic channel 2 and streptavidin beads (bead 2) injected into microfluidic channel 3. Using the optical tweezers, a single bead 1 tethered to pGEL001 and a bead 2 (untethered) were trapped and moved into the microfluidic channel 2 (containing only buffer) for force and distance measurements. When in microfluidic channel 2, bead 2 was moved within close proximity to bead 1, allowing the

remaining untethered long DNA handle to react with bead 2, forming a complete tether between the two beads. Complete tethers were confirmed through observations of the two beads moving in tandem when only bead 2 was moved via the optical tweezer controls. Following confirmation of the complete tether, continuous movement of bead 2 away from the stationary bead 1 was performed at a constant velocity, with the resultant force required for this movement measured. New beads were trapped when tether breakage occurred (no more complimentary movement of bead 1 when bead 2 moved). An optimised methodology obtaining frequent tethers whilst reducing multiple tethers between two beads was elucidated through varying the sizes of beads 1 and 2.

Experiments looking at pGEL001 in the absence of GFP-VD1 revealed no clear three step unfolding events expected from R1-R3 at ~5, ~15 and ~20 pN. However, on two occasions promising results possibly indicating an unfolding event were observed. The resulting distance as a product of time, and force as a product of time graphs of these two tethers are displayed in Figure 5.9a-d. Specifically, the data from the first tether of interest is shown In Figure 5.9a-b. Here, in Figure 5.9a steps were observed at time points 31.86 seconds and 35.22 seconds, corresponding to sudden increases in distance of approximately 30 nm and 100 nm respectively. The time points for these changes in length also corresponded with the sudden changes in force shown in Figure 5.9b. Here, the ~30 nm increase in length was accompanied by a drop in force from 26.56 pN to 15.41 pN, which was equal to 21.48 and 10.33 pN when the baseline 5.08 pN force was subtracted. Therefore this ~30 nm unfolding event reduced the force experienced by pGEL001 by 11.15 pN. Interestingly, the unfolding force observed at 21.48 nm corresponds to that of the previously shown unfolding force of R1 (~20 pN) and close to that of R2 (~15 pN) (Yao *et al*., 2014), with the 30 nm increase in length matching the expected range of extension from two four helix bundles unfolding (one helix = 5 nm, (Barnett and Goult, 2022)). The second spike observed corresponded to a complete snap of the tether, confirmed due to the large 100 nm extension and 38.66 pN drop in force, with no increase in force occurring from the movement of bead 2 away from bead 1. The second tether that indicated potential unfolding is displayed in Figures 5.9c-d. Here, steps in the distance time

graph shown in Figure 5.9c occurred at time points 73.55 seconds and 75.29 seconds corresponding to extensions of 30 nm and 50 nm respectively. These spikes in extension also corresponded to sudden drops in the force experienced by the molecule. Specifically, at the same time point as the 30 nm extension, the force dropped from 14.31 pN to 8.05 pN, equal to 13.57 pN and 7.31 pN when the baseline force of 0.74 pN was subtracted. Therefore the 30 nm extension reduced the force experienced by the molecule by 6.26 pN. This unfolding force of 13.57 pN matches that of the previously attained unfolding force of R2 (~15 pN) and close to the unfolding force of R1 (~20 pN), with the 30 nm extension closely matching the expected increase from one four helix and one five helix bundle unfolding.

Overall, promising preliminary data supporting the application of the C-trap® apparatus for pGEL unfolding measurements was obtained over the course of these experiments, presenting indications that the mutated R2 could be undergoing cooperative unfolding with the mutated R1. Due to the snapping of the tethers observed at forces as low as 20 pN, reproducing cycles of folding and unfolding on a single tether proved unsuccessful during these two experiments, with snapping occurring before the cycle was repeated. Future investigations will need to ensure forces do not exceed 20 pN to eliminate tether snapping, allowing verification of these unfolding events via repeated folding/unfolding cycles on the same tether. Two further preliminary experiments were attempted with pGEL001 on the C-trap® using RED-tris-NTA dye and GFP-VD1 and are discussed herein.

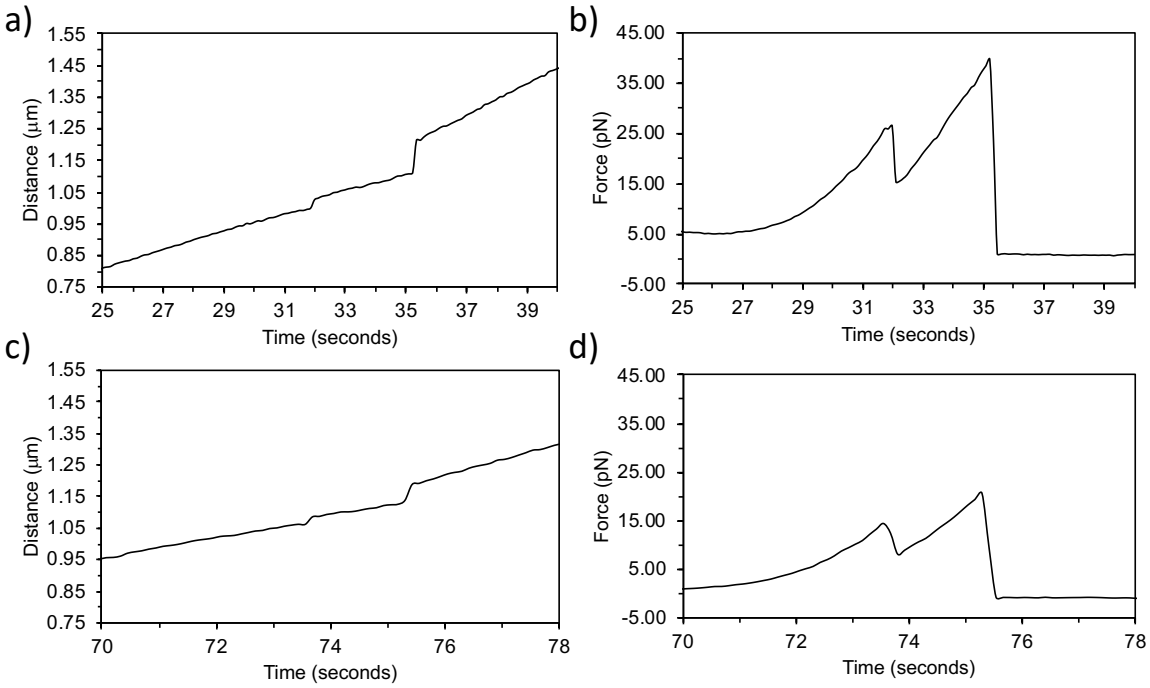

Figure 5.9: Distance and force measurements of pGEL001 during C-trap® experiments. a) Distance moved by bead 2 over time in tether 1. b) Force required to move bead 2 over time in tether 1. c) Distance moved by bead 2 over time in tether 2. d) Force required to move bead 2 over time in tether 2.

Firstly, in order to confirm pGEL001 molecules were present in the complete tethers, pGEL001 was labelled via its His-tag using RED-tris-NTA dye (NanoTemper). Using the fluorescent microscope available on the C-trap®, the presence of red fluorescence was monitored upon complete tether formation between beads 1 and 2. This experiment was performed with the goal of verifying the potential unfolding events observed in Figures 5.9b and 5.9d occurred when only a single pGEL001 was present. However, no fluorescence was observed throughout the course of these experiments, suggesting optimisation of the RED-tris-NTA dye labelling to the pGEL001 was required. No fluorescence was observed in microfluidic channel 1 where pGEL001 was present, confirming the issue was likely with the RED-tris-NTA dye labelling rather than the absence of pGEL001 itself, which had already been confirmed to be present during the coupling of the oligos.

The second and final preliminary investigation was to monitor GFP-VD1 binding to pGEL001 within the C-trap®. Here, observations of the localisation of GFP-VD1 to

unfolded pGEL001 molecules was thought to be possible through fluorescence microscopy, whilst the locking of pGEL001 would abolish the unfolding events witnessed in the experiments shown in Figures 5.9b and 5.9d. Together these two results would act as controls to verify both the presence of pGEL001 and the changes in force and length observed in experiments such as those shown in Figure 5.9a-d were as a result of pGEL001 unfolding. During these experiments high levels of non-specific binding of GFP-VD1 occurred on both beads 1 and 2, which when combined with the small size of the tether between the beads, made any observations of GFP-VD1 binding to pGEL001 impossible. Furthermore, during these experiments no tethers were captured that appeared to show potential pGEL001 unfolding events. Therefore, future experimentation is needed to determine whether smaller beads can be utilised to create a larger gap between the two beads, allowing for clearer observations of GFP-VD1 binding to pGEL001.

5.4 Investigating the expression, purification and gelation of next generation TSAM monomers

Following the successful formation of the pGEL001 TSAM, investigations into the potential tuneability of the macroscale material properties of TSAMs became an avenue of interest. Due to the different unfolding forces of the rod domains within talin, extending from 5 pN up to >20 pN, tunability in TSAMs shock absorbing properties should be possible via incorporation of monomers displaying differing unfolding forces. Here, the groundwork to facilitate these future investigations was conducted. Specifically two new monomer units were designed; pGEL002 and pGEL003, with their solubility confirmed and subsequent purification performed, followed by preliminary gelation investigations.

5.4.1 Design of pGEL002 and pGEL003

Each of the new TSAM monomers were designed to present identical components to pGEL001, only differing in the rod domains of talin incorporated. The design of these recombinant proteins is shown in Figure 5.10a-b. For pGEL002 (Figure 5.10a) three consecutive R9 domains were introduced in the place of the R1-R3 domains that were present in pGEL001. Each R9 domain has an unfolding force of ~20 pN, therefore pGEL002 would present a higher threshold unfolding force than pGEL001. The aim was to build materials with different rheological profiles, either displaying unfolding at a much higher material stiffness or displaying no unfolding due to TSAM breakage occurring before the monomers experienced their threshold unfolding force. A flexible linker consisting of GGGGSGGGGS was placed between each of the R9 domains to allow for proper folding of the domains (Sabourin *et al.*, 2007). Additionally, two cysteine to serine mutations (C1661S and C1671S) were introduced into each of the R9 domains to ensure tethering of pGEL002 at the two terminal cysteines. The structure of pGEL003 (Figure 5.10b) consisted of three consecutive R3 domains replacing the R1-R3 domain present in pGEL001. Each of these R3 domains has an unfolding force of ~5 pN, and would therefore result in the entire monomer unfolding at a lower force than pGEL001. Flexible linkers consisting of GGGGSGGGGS were placed between each of the R3 domains to promote wild-type folding. No mutations were introduced into the structure of R3 due to the absence of cysteines.

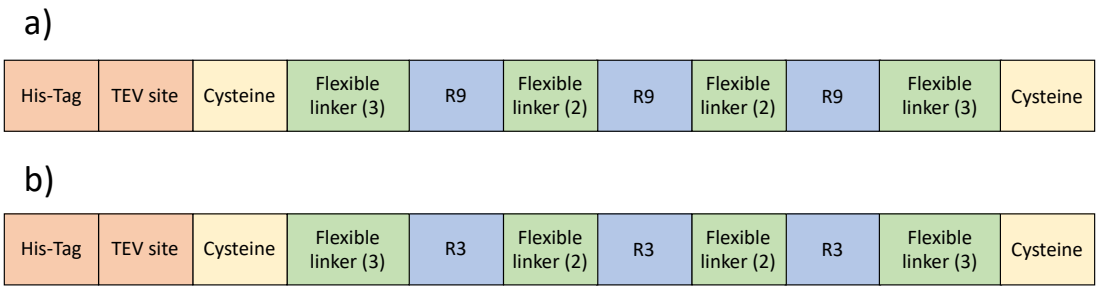

Figure 5.10: Key sections of the recombinant pGEL002 and pGEL003 proteins. a) The key sections of pGEL002. b) The key sections of pGEL003. Flexible linker (2) or (3) refers to the number of GGGGS repeats constituting the linker.

5.4.2 Expression and purification of pGEL002 and pGEL003.

Preliminary expression trials of each pGEL monomer were conducted using the traditional shake flask expression method (see Section 2.5.4.1) used for pGEL001. Here, expression was conducted at 20°C overnight followed by harvesting the following morning. Samples were taken from the two cultures of each construct and analysed with SDS-PAGE, with each sample diluted to identical OD_{600} values. Pre-induction and post-induction samples from each culture were run in neighbouring lanes to allow for direct comparisons of protein content. The resulting SDS-PAGE displayed in Figure 5.11 confirmed the expression of both pGEL002 and pGEL003, observed as the overexpressed band in the post-induction samples, absent in the pre-induction samples (highlighted with red boxes).

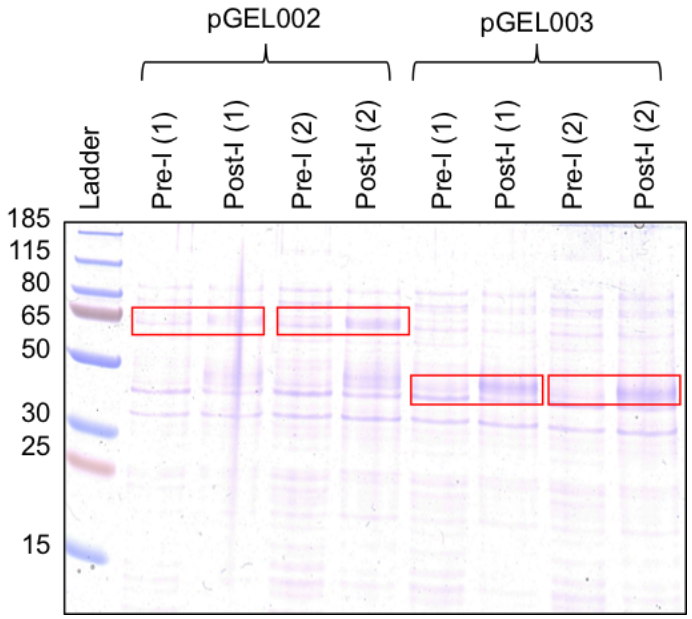

Figure 5.11: SDS-PAGE from expression trials of pGEL002 and pGEL003. Bands corresponding to th e expressed protein in the post-induction (Post-I) samples are highlighted in red, with the pre-induction (Pre-I) sample from the same culture also highlighted, showing the absence of the over expressed band.

Next, His-tag purifications were performed on 6 L of pGEL002 or pGEL003 harvested cultures. Purifications were performed using HisTrap HP columns connected to an AKTA start system. Following the His-purification, combining of the elution's containing the desired protein was performed, followed by dialysis into Q buffer A and ion exchange chromatography to remove remaining impurities. Dialysis into phosphate buffer (pH 7.4) was then conducted, rendering the protein ready for

gelation trials. Yields of 205 mg of pGEL002 and 300 mg of pGEL003 were obtained from the 6 L of culture for each construct (within similar range to pGEL001 expression). Therefore, it appeared pGEL003 presented higher expression levels under these conditions, producing 50 mg/L. Attempts at forming TSAM hydrogels were conducted in an identical manor to TSAM hydrogels formed from pGEL001. Only the concentration of 200 mg/mL was tested for these preliminary investigations to allow for direct comparisons between the two new pGEL TSAM hydrogels and the original pGEL001 TSAM hydrogel. Following completion of the TSAM development procedure, no hydrogel formation was observed with pGEL002 at 200 mg/mL, whilst a TSAM hydrogel was observed at 200 mg/mL of pGEL003. The resulting gel, appeared to be highly extensible similar to pGEL001, in addition to showing high levels of adhesivity both of which are exemplified in Figure 5.12a-b.

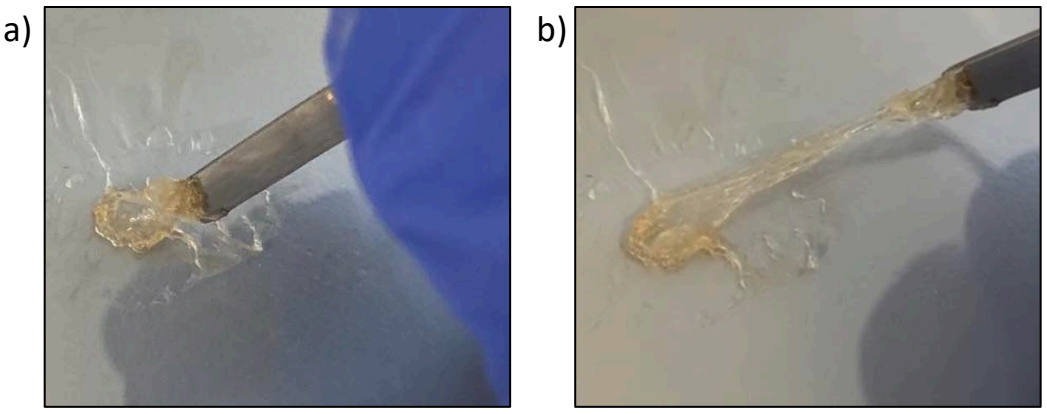

Figure 5.12: Images demonstrating the extensibility and adhesivity of the pGEL003 TSAM. a) pGEL003 TSAM before being stretched. b) pGEL003 TSAM stretched.

Following the formation of a pGEL003 TSAM, a preliminary rheology experiment was conducted. Here, five oscillatory shear strain sweeps were conducted on the pGEL003 TSAM with a two-minute rest period between each sweep. This procedure was performed identically to the pGEL001 TSAM oscillatory shear strain sweeps. However, only a single pGEL003 TSAM was produced, therefore the rheology data shown in Figure 5.13a-c is of a single pGEL003 TSAM. Looking at Figure 5.13a displaying the G’ and G” values against shear strain, a similar level of rigidity (indicated by the magnitude of G’ and G*) was observed compared to the first two sweeps of the non-swelled pGEL001 TSAMs in Section 4.4.2.1. Unlike pGEL001

TSAMs, no significant increases in rigidity were observed between sweeps 1-4, with a slight increase in rigidity observed in sweep 5. Moreover, decreases in the G' and G* occurred from 10 % shear strain onwards. These decreases may have indicated the new pGEL003 monomer containing the R3 domains (therefore presenting a lower unfolding force) experienced sufficient force at this percentage shear strain to induce unfolding. Indications of unfolding are further exemplified in the shear stress vs shear strain graph in Figure 5.13b and the phase angle graph shown in Figure 5.13c. Specifically, a shear yield point was present in sweeps 1-3 of the shear stress vs shear strain graphs in Figure 5.13b, whilst a clear transition to a higher phase angle was observed in Figure 5.13c at the higher shear strains, suggesting sudden increases in flow. An increase in flow would occur due to the sudden extension of the unfolded R3 domains, introducing slack into the system.

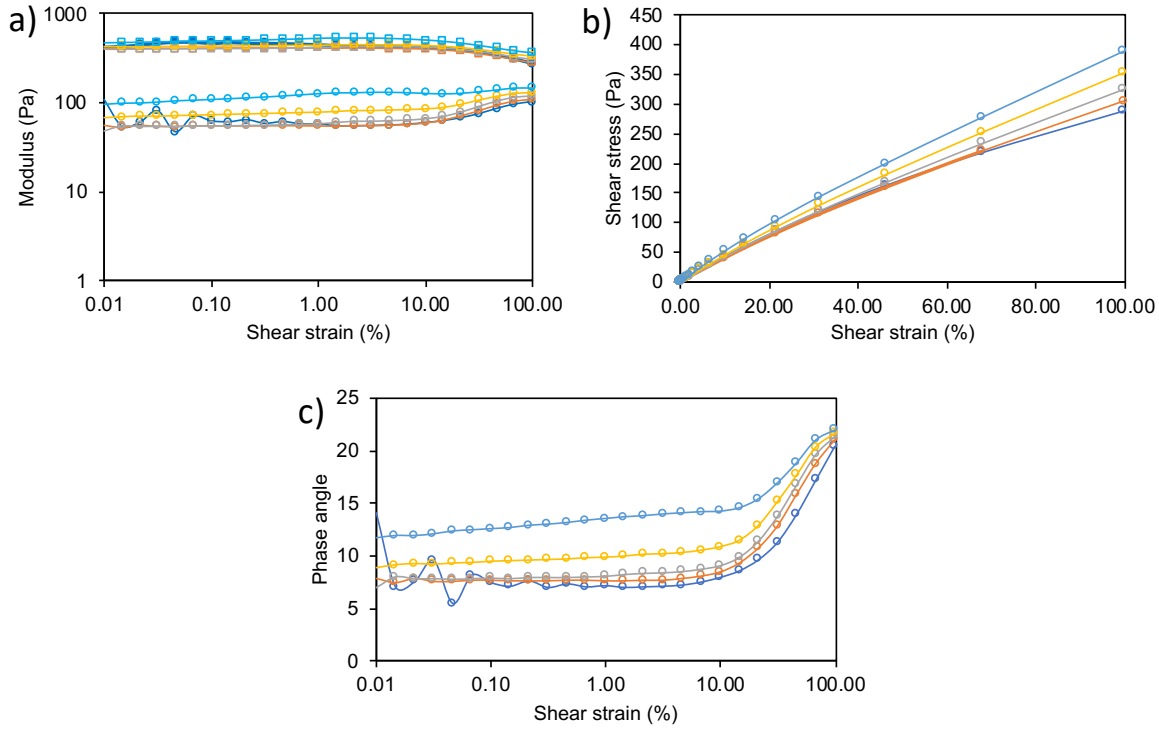

Figure 5.13: Rheology measurements from five oscillatory shear amplitude sweeps on the pGEL003 TSAM. a) G' and G" as a product of shear strain. b) Shear stress as a product of shear strain. c) Phase angle as a product of shear strain. Sweep 1= dark blue, sweep 2 = orange, sweep 3 = grey, sweep 4 = yellow, sweep 5 = light blue.

5.5 Discussion

Within this chapter, preliminary data for the scaled-up expression of pGEL001 was obtained, with the merits and limitations of each methodology highlighted and

addressed. This work was vital to elucidate the specific areas requiring addressal for more in depth optimisation of each expression system. Furthermore, promising results from the C-trap® apparatus revealed indications of pGEL001 unfolding in response to force, in addition to elucidating the key parameters needing further investigation to obtain more detailed and reliable biophysical data. Finally, the expression, purification and gelation data obtained for pGEL002 and pGEL003 provided information on the yields of these proteins from traditional expression methods in addition to revealing the successful formation of a second TSAM material. The rheological results from the pGEL003 provided early indications of potential macroscale tailoriability, indicating that tuning of the TSAMs shock absorbing properties may be possible through varying the rod domains within the monomer unit. For clarity the discussion has been split into three subsections, one for each of the key objectives addressed within this chapter

Discussion for Section 5.2 – Scaling up expression of pGEL001

During the expression optimisation trials three techniques were compared. From these techniques the achievable yields over a one-week period were calculated, allowing direct comparisons between the methods. The traditional expression system used for pGEL001 was calculated to produce a yield of 1170 mg contained within 0.73 L of media, the VNp15 system was calculated to produce a yield of 936 in 5.85 L of media, whilst the bioreactor was calculated to produce a yield of 1440 mg contained within 5.50 L of media. Although from these calculations the bioreactors produced the highest overall yield of pGEL001, a large increase in volume of 4.77 L requiring purification was incurred compared to the traditional shake flask expression system used. This is an important issue due to the increase in volume increasing the time of the subsequent purification procedure. Therefore, although more pGEL001 would be produced in one week using the bioreactors, the purification using HisTrap HP columns would take over one week longer than that of the traditional shake flask expression system used, which only produces 270 mg less of pGEL001. Furthermore, the bioreactor cultures were prone to failure, whereby only 37.5% of the bioreactor growths were successful. A similar issue of increased volume was also seen with the VNp15 system, producing an extra 5.12 L volume for a similar

yield of protein to that of the traditional expression system. Overall, based off the expression systems tested within this study, the traditional shake flask expression system proved the optimal method when considering the limitations of laboratory resources. However, within the scope of this investigation the VNp15 system was only tested up to 150 mL cultures in 2.0 L flasks; if larger volumes of culture can be grown in 2.0 L flasks and achieve similar yields to those obtained within this study, the VNp15 system has the potential to dramatically increase the pGEL001 yields compared to the traditional shake flask expression system. Investigations into the ability to remove the vesicle packaged protein from the media, followed by vesicle resuspension in smaller volumes of media, would also significantly reduce the volume requiring purification. Thus, future investigations should seek to address these points to greatly increased pGEL001 yields and reduce the volumes requiring purification. A further benefit of the VNp15 system is the reduction in contaminant proteins which may in turn enable achievement of higher purity pGEL001 from single step purifications. Finally, although the batch method His-tag purification of VNp15 tested within Section 5.2.1 proved unsuccessful in purifying the majority of VNp15-pGEL001, if further optimisation of this system proved to increase the success of the purification, the larger volumes of culture requiring purification from the VNp and bioreactor systems would become a significantly reduced issue due to the batch method allowing simultaneous purification of litres of media.

Discussion for Section 5.3 – Biophysical characterisation of pGEL001

Preliminary investigations into the biophysical characterisation of pGEL001 using the C-trap® apparatus revealed promising indications of rod domain unfolding events. Here, two tethers were achieved showing drops in force experienced at the expected unfolding forces of R1 and R2, with the corresponding extensions measured closely matching that expected from the four and five helix bundles unfolding. However, during these experiments the tethers snapped before a repeat measurement could be performed, inhibiting rulings on whether these measurements definitively corresponded to unfolding events. Furthermore, experiments monitoring fluorescence of either RED-tris-NTA dye tagged pGEL001 or pGEL001 in the presence of GFP-VD1 failed to produce data confirming the presence of pGEL001 in a teather.

Specifically, no fluorescence was observed in any microfluidic channel when pGEL001 was tagged with RED-tris-NTA dye, suggesting labelling of pGEL001 with this dye was unsuccessful. In addition, no clear binding of GFP-VD1 was observed in a separate C-trap® investigation on pGEL001, likely due to the high levels of background fluorescence resulting from non-specific binding of GFP-VD1 to beads 1 and 2. Here, the large beads combined with the comparatively small gap between the beads where the tether was located also meant any instance where binding may have occurred could not be distinguished from non-specific binding of GFP-VD1 to the beads. Therefore, further investigation into the use of smaller beads is required. Furthermore, ligation of the DNA handles to the oligos on pGEL001 may increase the snapping force of the captured tethers, allowing for increased opportunity for repeated cycling of measurements on a single tether before snapping occurs.

Discussion for Section 5.4 – Next generation TSAM monomers

Finally, the two new TSAM monomers design strategy was discussed, with the key structural elements identified. The solubility and subsequent purification of both pGEL002 and pGEL003 was confirmed with the yields from 6 L of media calculated. This information was vital to ensure these two monomers could be moved forward towards MGC trials to develop two new iterations of TSAMs. The gelation of both monomers at 200 mg/mL was tested, revealing only pGEL003 formed a hydrogel at this concentration. Therefore, future investigations into pGEL002s MGC should seek to test concentrations above 200 mg/mL. Following the creation of the pGEL003 TSAM, five oscillatory shear strain sweeps were conducted to allow preliminary comparisons to be drawn to the pGEL001 TSAM. Here, the new pGEL003 TSAM presented a similar rigidity to that of the pGEL001 TSAM, however a significant reduction in the strain induced stiffening of the material was observed in the pGEL003 TSAM compared to that of the pGEL001 TSAM. Observations previously deduced to indicate rod domain unfolding in Section 4.4.2 were seen in all five pGEL003 TSAM sweeps, suggesting that the new reduced threshold unfolding force of the entire protein monomer caused the TSAM to unfold at a much lower shear strain. Therefore, the obtained data indicates TSAMs shock absorbing characteristics (i.e. forces at which monomers unfold at and therefore energy dissipated from the

increased number of unfolding events) can be tuned through changing the monomer rod domains. Furthermore, reducing the threshold unfolding force may act to increase the performance of TSAMs in impact-based experiments, as energy can be dissipated faster from the larger number of rod domains unfolding over a set time due to the force required for inducing unfolding being met sooner.

In summary, although the work within this chapter is not complete, multiple avenues for investigation have been highlighted. All of the objectives for aim three outlined in Section 1.5 were investigated, with preliminary results obtained for each. Results within this chapter will be used to inform the future development of both pGEL001 TSAMs and the new iterations of TSAMs made from pGEL002 and pGEL003.

Chapter 6: Conclusions

6.1 Summary

From the literature discussed in Chapter 1, it is apparent that the current industry standard shock absorbing materials display multiple inherent limitations. Specifically, ceramic armour presents low durability, whilst aerogels alter the chemical composition of captured projectiles due to their insulating properties. Protein-based materials revealed themselves as promising candidates to address the limitations seen with both ceramic armour and aerogels. However, research to date has focused on protein-based materials for biomedical applications only. Here, the mechanosensory protein talin was employed to develop a next generation protein-based shock absorbing material, with the goal of establishing the materials performance during high velocity impacts and reveal a future industrial application outside of the biomedical sector.

The initial aim of this project was to produce the first iteration of a TSAM. For this purpose, the recombinant protein pGEL001 was designed, containing modified R1-R3 domains of talin. Biochemical characterisation of pGEL001 was performed and confirmed the cysteine to serine mutations introduced within pGEL001s R1-R3 domains did not abolish wild-type folding or binding with GFP-VD1. The physiochemical properties of the maleimide-based crosslinkers were characterised, with the resulting solubility and hydrolysis data used to inform the final TSAM gelation protocol. During LCMS studies used to confirm the functionality of the crosslinkers maleimide groups, the reducing agent TCEP was found to react with the crosslinkers themselves. Due to this likely resulting in either heterogenous hydrogel formation or eliminating the formation of a hydrogel completely, investigation was conducted to remove TCEP from the pGEL001 mixture prior to crosslinker addition. Finally, MGC trials were performed and revealed the formation of the first TSAM material at 200 mg/mL following addition of crosslinker **3**. Calculations to determine the theoretical maximum energy dissipation of the resultant TSAM found that the

value exceeded that of Kevlar and a carbon-nanotube material capable of surviving supersonic impacts, revealing TSAMs potential as shock absorbing materials.

Following the successful development of a TSAM material, the second aim sought to characterise TSAMs structure, properties and determine its shock absorbing performance. Transmission and scanning electron microscopy revealed the underlying structure to consist of a lattice on the nanometre scale, resulting in fibrous structures on the micrometre scale. A novel plate reader methodology was subsequently elucidated to facilitate characterisation of future iterations of TSAMs, providing the distinct benefit of retaining the aqueous environment of the material. Employing GFP-VD1 to induce pGEL001 unfolding, rheology in combination with fluorescence microscopy was used to confirm pGEL001s unfolding in response to force. With few available technologies to measure dynamic protein unfolding in the solid state, this methodology revealed itself as a unique assay with great potential for future use in the growing protein-based materials field. Following the successful incorporation of the energy dissipating mechanism of talin into TSAMs, impact-based studies were conducted using a light gas gun. Here, TSAMs were shown to capture and preserve basalt particle impacting at 1.5 km/s. Furthermore, aluminium shrapnel was caught by the TSAM, an event that usually destroys the industry standard aerogel materials due to their brittleness. With TSAMs confirmed to present the endothermic energy dissipating mechanism of protein unfolding, whilst also presenting high extensibility in place of brittleness, TSAMs revealed themselves as a viable alternative to the industry standard aerogel materials, displaying enhanced properties directly overcoming the limitations of aerogels.

Finally, the third aim of this project focused on optimising the expression of pGEL001 and laying the groundwork for future iterations of TSAMs. For this purpose, three expression systems were compared; traditional shake flask expression, VNp expression technology and fed-batch bioreactors. Although neither the VNp system, nor the bioreactor systems proved more efficient than the traditional shake flask expression due to laboratory equipment limitations, both systems indicated great potential should optimisation on the downstream harvesting and purification be

performed. Inspired by the works of Lv *et al.* (Lv *et al*., 2010) and Wu *et al.* (Wu *et al*., 2018), each of whom exemplified the importance of single molecule unfolding forces on the resultant protein-based material properties, work was conducted on characterising pGEL001 using the C-trap® apparatus. Here, preliminary investigations revealed potential cooperative unfolding of the R1 and R2 domains occurring within pGEL001. In addition, the experimental limitations requiring addressal to produce more conclusive results in future C-trap® experiments were identified. Finally, two new pGEL monomers were designed: pGEL002 containing three R9 domains and pGEL003 containing three R3 domains. These two monomers were designed to present the upper and lower limits of talin unfolding forces, used to determine whether the macroscale material properties of TSAMs could be tuned by the monomer unfolding force. Hydrogel formation was attempted at 200 mg/mL with crosslinker **3**, revealing only pGEL003 to form a TSAM at this concentration. Rheological measurements on the resultant pGEL003 TSAM suggested the material was unfolding at lower shear strains than the pGEL001 TSAM. Therefore, this result indicated that TSAMs macroscale properties are defined by the mechanical properties of the monomer, with the TSAMs macroscale properties tailorable through alteration of the talin domains incorporated into the pGEL monomer.

In summary, all three aims identified for this project were achieved, and an industrial application for TSAMs was established. In addition, this work revealed a novel application for protein-based shock absorbing materials. We hope this work inspires future research to expand the use of protein-based materials into a host of other non-biomedical applications, whereby we can begin to utilise the highly evolved proteins developed by nature to solve current technological limitations.

6.2 Limitations of the research

Whilst extensive research was conducted to ensure valid characterisation of every element of TSAMs during their development, several limitations still presented within this project. Firstly, during rheology experiments it was observed TSAMs in the non-swelled state increased in rigidity with increasing oscillatory shear strain sweeps.

However, due to the large protein requirements for the production of a TSAM and the limitations on time during the initial investigations, this data was only collected up to sweep 5 on each TSAM repeat. As a result, it is currently unknown whether further sweeps would have caused rigidity to increase up to a maximum and then remain at that value, or, if rigidity would have continuously increased until sufficient rigidity was acquired to remove the elastic and energy dissipating nature of the material, resulting in its breakage during the experiment.

Another limitation of the investigation, once again due to the large protein demands in producing TSAMs, was the single projectile velocity of 1.5 km/s tested during the light gas gun experiments. Although this data is sufficient to confirm TSAMs display significant energy dissipation and establish their applicability as materials for use in projectile capture and preservation experiments at and below 1.5 km/s, an upper limit of performance was not determined. Therefore, the complete range of velocities TSAMs can capture and preserve projectiles at was not established during the course of this investigation.

Finally, although the TSAM was shown to absorb the impact of aluminium shrapnel during the final light gas gun experiment, due to this impact occurring by accident, the exact conditions of the impact including the shrapnel's velocity and pre-impact size are unknown. Consequently, only limited conclusions can be drawn concerning the energy absorbed by the material resulting from this shrapnel impact. Despite this, the result still presented promising implications for future uses of TSAMs and indicated a potential interesting secondary application for the material within military applications such as body armour.

6.3 Future work

To build upon the foundations laid within this project, multiple avenues for future investigation are apparent. These can be divided into three categories:

1. Facilitating the design and development of future TSAMs.

2. Optimising the performance of TSAMs in supersonic projectile capture and preservation.
3. Investigating further industrial applications for TSAMs.

6.3.1 Facilitating the design and development of future TSAMs

Firstly, in order to test TSAMs for larger volume applications such as personal body armour, work should be completed on optimising the yield of pGEL001 obtained from expression and purification. As stated in Section 5.2, although the bioreactor and VNp system obtained larger yields of pGEL001 per litre than the traditional expression system, due to the limitations of laboratory equipment and current harvesting and purification procedures, the increased volume of media requiring purification rendered each of these technologies less efficient than the traditional shake flask expression. Therefore, future work on the VNp system should be conducted attempting to isolate the pGEL001 containing vesicles and concentrate these within a smaller volume of media. This will result in a greatly reduced volume requiring purification which can be purified utilising the AKTA start HisTrap HP column purification method. In addition, early work was conducted to determine the effectiveness of the batch method of purification on the VNp15-pGEL001 protein expressed. Success with this system would have reduced the issue of the larger volumes of media requiring purification produced by the VNp system, removing the need for vesicle concentration. However, during the work performed in Section 5.2.1, this method of purification provided inadequate yields of the VNp15-pGEL001 protein. Work should be conducted to optimise the yields attainable from this method and determine the cause of the low yields obtained within the scope of this investigation. The most likely explanation for the poor performance from the purification was insufficient release of the VNp15-pGEL001 during sonication, therefore work should look to establish this as the cause and determine an optimal lysis method of the vesicles. Specifically, investigation into longer sonication times, the use of lysozyme or alternative lysis methods including use of a cell disrupter should be performed. Similarly, to the VNp system, the issues of the larger volumes requiring purification from the bioreactor system could also be mitigated by utilising the batch method of purification. Consequently, work should also be conducted to

investigate the yields obtained from batch method purification of the harvested bioreactor pellets. A secondary issue with the bioreactor systems was the low success rate in obtaining repeatable yields of pGEL001, with work into establishing a more consistent performance with this system required before it can be considered as a viable alternative to shake flask expression.

Within the C-trap® experiments, issues with tether snapping at low forces caused a significant problem with accurately determining successful capture of tethers containing a single pGEL001. In addition, repeated cycles of unfolding and refolding could not be performed to validate results due to the tether snapping almost immediately after suspected unfolding events were witnessed. Future work should be conducted on ligating the annealed DNA handles used to obtain the tethers, therefore increasing their breakage force. This would allow repeated cycles of unfolding and refolding to be observed on a single tether and a more accurate distinction between protein unfolding events and tether snapping events. Work should also be re-attempted to observe VD1 binding to the pGEL001 molecules. Due to the primary issues within this investigation being the low fluorescence of the GFP attached to the VD1 used, as well as the high levels of non-specific binding to the beads, two clear avenues forward are present. Firstly, smaller beads should be used to reduce the background fluorescence occurring from the non-specific binding. Secondly, an alternate fluorophore should be utilised displaying brighter fluorescence than GFP, increasing the likelihood of observing the binding of a single VD1 protein with the fluorescence microscope.

Finally, two new protein monomers, pGEL002 and pGEL003 were developed. As pGEL002 did not form a hydrogel with crosslinker **3** at 200 mg/mL, a MGC trial should be conducted at concentrations above this value. Careful investigation into crosslinker **3**'s solubility at these higher concentrations should also be elucidated. Furthermore, CD or NMR experiments should be performed on the R9 domains incorporated within pGEL002 to ensure the two cysteine to serine mutations introduced within each R9 domain did not significantly alter folding compared to the wild-type domains. In addition, pGEL003 was shown to form a hydrogel at 200 mg/mL

and an initial rheology experiment was performed. To validate the data collected, two further repeat oscillatory shear strain experiments should be conducted on two new pGEL003 TSAMs. This will enable the tunability of TSAMs based on the protein monomer unfolding force to be conclusively confirmed.

6.3.2 Optimising the performance of TSAMs in supersonic projectile capture and preservation

With TSAMs being shown to successfully capture and preserve basalt particles impacting at 1.5 km/s, future work should seek to find the maximum velocity at which TSAMs can achieve this result. This data would provide the full spectrum of velocities TSAMs can be used for when looking at projectiles of similar dimensions to the basalt particles and allow direct comparisons of TSAMs upper limit of performance to the industry standard aerogel materials. In addition, projectiles of varying material type and size should also be investigated, further determining the applicability of TSAMs across a broader range of experiment types. In particular, effort should be made to replicate the aluminium shrapnel impact observed in Section 4.5.3, in a more controlled experiment, allowing estimates of the energy dissipated in the impact to be conducted. Finally, with the observation of increased rigidity seen with pGEL001 when applied to multiple sweeps of shear strain, investigations into whether a TSAM with increased rigidity performs better in supersonic impact experiments should be conducted.

6.3.3 Investigating further industrial applications for TSAMs.

With the successful capture of aluminium shrapnel during the light gas gun experiment, in addition to the significant energy dissipation shown in the capture and preservation of impacting basalt particles, TSAMs could present as a promising material for armour-based applications. As discussed in Section 1.2, ceramic armours commonly employ a dual system, utilising a deformable backing material to dissipate the remainder of the projectiles energy following its impact with the ceramic plate. Here, TSAMs could present as a viable material to replace the deformable backing commonly used in these ceramic armour dual systems. TSAMs are hydrogels and

therefore present low densities, as well as employing a mechanism of energy dissipation that can undergo repeated force cycles and still reform. As a result, TSAMs could display durability far superior to the currently employed backing material and reveal themselves as suitable for multiple uses. This could reduce the costs compared to the traditional single use systems. Furthermore, TSAMs may also reveal themselves as more efficient energy dissipaters, alleviating the behind armour blunt trauma witnessed with current armour systems. Future work should seek to test TSAMs as a backing material to ceramic plates during a variety of impacts, ranging from low calibre bullet impacts to shrapnel stoppage from explosives.

Through completion of this future work, the limitations outlined in Section 6.2 will have been addressed, solidifying TSAMs use for high velocity impact capture and preservation applications. Furthermore, a secondary industrial application within ceramic armour systems may also be elucidated, exemplifying the future potential of protein-based materials as next-generation materials addressing the limitations seen with many of our current industry standards. As it stands, TSAMs have been shown to display extensibility, adhesively, mouldability, an endothermic mechanism of energy dissipation and durability resulting from the unfolding/refolding kinetics of talin. When combined, these attributes reveal TSAMs to display properties superior to the industry standard aerogel materials employed within high velocity impact experiments, presenting a strong argument for TSAMs eventual overtaking of aerogels used for this purpose following the complete characterisation of the materials impact velocity limits.

Chapter 7: References

ABASCAL, N. C. & REGAN, L. (2018). The past, present and future of protein-based materials. *Open Biology,* 8, 180113.

AHMED, E. M. (2015). Hydrogel: Preparation, characterization, and applications: A review. *Journal of Advanced Research,* 6, 105-121.

AKHTAR, M. F., HANIF, M. & RANJHA, N. M. (2016). Methods of synthesis of hydrogels ... A review. *Saudi Pharmaceutical Journal,* 24, 554-559.

ALBERTS , B. J., ALEXANDER. LEWIS , JULIAN. RAFF , MARTIN. ROBERTS , KEITH. WALTER , PETER. (2002). *Molecular Biology of the Cell,* New York, Garland Science.

ALWIN, S. & SHAJAN, X. S. (2020). Aerogels: promising nanostructured materials for energy conversion and storage applications. *Materials for Renewable and Sustainable Energy,* 9, 7.

ANCHORDOQUY, T. J. & CARPENTER, J. F. (1996). Polymers protect lactate dehydrogenase during freeze-drying by inhibiting dissociation in the frozen state. *Archives of Biochemistry and Biophysics,* 332, 231-238.

ATHERTON, P., LAUSECKER, F., CARISEY, A., GILMORE, A., CRITCHLEY, D., BARSUKOV, I. & BALLESTREM, C. (2020). Relief of talin autoinhibition triggers a force-independent association with vinculin. *Journal of Cell Biology,* 219, e201903134.

AUGOFF, K., HRYNIEWICZ-JANKOWSKA, A. & TABOLA, R. (2020). Invadopodia: clearing the way for cancer cell invasion. *Annals of Translational Medicine,* 8, 902.

BALU, R., DUTTA, N. K., DUTTA, A. K. & CHOUDHURY, N. R. (2021). Resilin-mimetics as a smart biomaterial platform for biomedical applications. *Nature Communications,* 12, 149.

BANNO, A., GOULT, B. T., LEE, H., BATE, N., CRITCHLEY, D. R. & GINSBERG, M. H. (2012). Subcellular Localization of Talin Is Regulated by Inter-domain Interactions. *Journal of Biological Chemistry,* 287, 13799-13812.

BARNETT, S. F. H. & GOULT, B. T. (2022). The MeshCODE to scale – Visualising synaptic binary information. *bioRxiv*, 2022.06.16.496395.

BARTHELAT, F., TANG, H., ZAVATTIERI, P. D., LI, C. M. & ESPINOSA, H. D. (2007). On the mechanics of mother-of-pearl: A key feature in the material hierarchical structure. *Journal of the Mechanics and Physics of Solids,* 55, 306-337.

BATE, N., GINGRAS, A. R., BACHIR, A., HORWITZ, R., YE, F., PATEL, B., GOULT, B. T. & CRITCHLEY, D. R. (2012). Talin Contains A C-Terminal Calpain2 Cleavage Site Important In Focal Adhesion Dynamics. *Plos One,* 7, e34461.

BHATNAGAR, B. S., BOGNER, R. H. & PIKAL, M. J. (2007). Protein stability during freezing: Separation of stresses and mechanisms of protein stabilization. *Pharmaceutical Development and Technology,* 12, 505-523.

BHEEKHUN, N., ABU TALIB, A. & HASSAN, M. R. (2013). Aerogels in Aerospace: An Overview. *Advances in Materials Science and Engineering,* 2013, 406065.

BIGGAR, K. K., DAWSON, N. J. & STOREY, K. B. (2012). Real-time protein unfolding: a method for determining the kinetics of native protein denaturation using a quantitative real-time thermocycler. *Biotechniques,* 53, 231-238.

BORGON, R. A., VONRHEIN, C., BRICOGNE, G., BOIS, P. R. J. & IZARD, T. (2004). Crystal structure of human vinculin. *Structure,* 12, 1189-1197.

BOUCHET, B. P., GOUGH, R. E., AMMON, Y. C., VAN DE WILLIGE, D., POST, H., JACQUEMET, G., ALTELAAR, A. F. M., HECK, A. J. R., GOULT, B. T. & AKHMANOVA, A. (2016). Talin-KANK1 interaction controls the recruitment of cortical microtubule stabilizing complexes to focal adhesions. *Elife,* 5, e18124.

BOUJEMAA-PATERSKI, R., MARTINS, B., EIBAUER, M., BEALES, C. T., GEIGER, B. & MEDALIA, O. (2020). Talin-activated vinculin interacts with branched actin networks to initiate bundles. *Elife,* 9, e53990.

BURCHELL, M. J., COLE, M. J., MCDONNELL, J. A. M. & ZARNECKI, J. C. (1999). Hypervelocity impact studies using the 2 MV Van de Graaff accelerator and two-stage light gas gun of the University of Kent at Canterbury. *Measurement Science and Technology,* 10, 41-50.

BURRIDGE, K. & CONNELL, L. (1983). A NEW PROTEIN OF ADHESION PLAQUES AND RUFFLING MEMBRANES. *Journal of Cell Biology,* 97, 359-367.

CAI, J. Z., GRIESBACH, C. & THEVAMARAN, R. (2021). Extreme Dynamic Performance of Nanofiber Mats under Supersonic Impacts Mediated by Interfacial Hydrogen Bonds. *Acs Nano,* 15, 19945-19955.

CALO, E. & KHUTORYANSKIY, V. V. (2015). Biomedical applications of hydrogels: A review of patents and commercial products. *European Polymer Journal,* 65, 252-267.

CARVALHO, E. M. & KUMAR, S. (2022). Lose the stress: Viscoelastic materials for cell engineering. *Acta biomaterialia* [Online]. Available from: 10.1016/j.actbio.2022.03.058. [Accessed 08 November 2022].

CATALANO, C., AL MUGHRAM, M. H., GUO, Y. Z. & KELLOGG, G. E. (2021). 3D interaction homology: Hydropathic interaction environments of serine and cysteine are strikingly different and their roles adapt in membrane proteins. *Current Research in Structural Biology,* 3, 239-256.

CHAI, Q. Y., JIAO, Y. & YU, X. J. (2017). Hydrogels for Biomedical Applications: Their Characteristics and the Mechanisms behind Them. *Gels,* 3, 6.

CHASTNEY, M. R., CONWAY, J. R. W. & IVASKA, J. (2021). Integrin adhesion complexes. *Current Biology,* 31, R536-R542.

CHEN, H. B., WANG, J. J., CHENG, Y. H., WANG, C. S., LIU, H. C., BIAN, H. G., PAN, Y. R., SUN, J. Y. & HAN, W. W. (2019). Application of Protein-Based Films and Coatings for Food Packaging: A Review. *Polymers,* 11, 584-671.

CHEN, Q. Z., LIANG, S. L. & THOUAS, G. A. (2013). Elastomeric biomaterials for tissue engineering. *Progress in Polymer Science,* 38, 584-671.

COHEN, D. M., CHEN, H., JOHNSON, R. P., CHOUDHURY, B. & CRAIG, S. W. (2005). Two distinct head-tail interfaces cooperate to suppress activation of vinculin by talin. *Journal of Biological Chemistry,* 280, 17109-17117.

CRIADO-GONZALEZ, M., WAGNER, D., FORES, J. R., BLANCK, C., SCHMUTZ, M., CHAUMONT, A., RABINEAU, M., SCHLENOFF, J. B., FLEITH, G., COMBET, J., SCHAAF, P., JIERRY, L. & BOULMEDAIS, F. (2020). Supramolecular Hydrogel Induced by Electrostatic Interactions between Polycation and Phosphorylated-Fmoc-Tripeptide. *Chemistry of Materials,* 32, 1946-1956.

DAS, M., ITHYCHANDA, S. S., QIN, J. & PLOW, E. F. (2014). Mechanisms of talin-dependent integrin signaling and crosstalk. *Biochimica Et Biophysica Acta-Biomembranes,* 1838, 579-588.

DAVARI, N., BAKHTIARY, N., KHAJEHMOHAMMADI, M., SARKARI, S., TOLABI, H., GHORBANI, F. & GHALANDARI, B. (2022). Protein-Based Hydrogels: Promising Materials for Tissue Engineering. *Polymers,* 14, 986.

DESAI, M. S. & LEE, S. W. (2015). Protein-based functional nanomaterial design for bioengineering applications. *Wiley Interdisciplinary Reviews-Nanomedicine and Nanobiotechnology,* 7, 69-97.

DOI, M. (1995). *Introduction to Polymer Physics,* Oxford, Oxford University Press.

EASTWOOD, T. A., BAKER, K., STREATHER, B. R., ALLEN, N., WANG, L., BOTCHWAY, S. W., BROWN, I. R., HISCOCK, J. R., LENNON, C. & MULVIHILL, D. P. (2022). Exceptional yield vesicle packaged recombinant protein production from E. coli. *bioRxiv*, 2022.04.22.489142.

ELLIOTT, P. R., GOULT, B. T., KOPP, P. M., BATE, N., GROSSMANN, J. G., ROBERTS, G. C. K., CRITCHLEY, D. R. & BARSUKOV, I. L. (2010). The Structure of the Talin Head Reveals a Novel Extended Conformation of the FERM Domain. *Structure,* 18, 1289-1299.

ELOH, K., DEMURTAS, M., MURA, M. G., DEPLANO, A., ONNIS, V., SASANELLI, N., MAXIA, A. & CABONI, P. (2016). Potent Nematicidal Activity of Maleimide Derivatives on Meloidogyne incognita. *Journal of Agricultural and Food Chemistry,* 64, 4876-4881.

ELVIN, C. M., BROWNLEE, A. G., HUSON, M. G., TEBB, T. A., KIM, M., LYONS, R. E., VUOCOLO, T., LIYOU, N. E., HUGHES, T. C., RAMSHAW, J. A. M. & WERKMEISTER, J. A. (2009). The development of photochemically crosslinked native fibrinogen as a rapidly formed and mechanically strong surgical tissue sealant. *Biomaterials,* 30, 2059-2065.

ELVIN, C. M., VUOCOLO, T., BROWNLEE, A. G., SANDO, L., HUSON, M. G., LIYOU, N. E., STOCKWELL, P. R., LYONS, R. E., KIM, M., EDWARDS, G. A., JOHNSON, G., MCFARLAND, G. A., RAMSHAW, J. A. M. & WERKMEISTER, J. A. (2010). A highly elastic tissue sealant based on photopolymerised gelatin. *Biomaterials,* 31, 8323-8331.

FANG, J., MEHLICH, A., KOGA, N., HUANG, J. Q., KOGA, R., GAO, X. Y., HU, C. G., JIN, C., RIEF, M., KAST, J., BAKER, D. & LI, H. B. (2013). Forced protein unfolding leads to highly elastic and tough protein hydrogels. *Nature Communications,* 4, 2974.

FEJDYS, M., KOSLA, K., KUCHARSKA-JASTRZABEK, A. & LANDWIJT, M. (2021). Influence of ceramic properties on the ballistic performance of the hybrid ceramic-multi-layered UHMWPE composite armour. *Journal of the Australian Ceramic Society,* 57, 149-161.

FENG, S. B., CHEN, J. K., YU, H. T., SIMON, J. A. & SCHREIBER, S. L. (1994). 2 BINDING ORIENTATIONS FOR PEPTIDES TO THE SRC SH3 DOMAIN - DEVELOPMENT OF A GENERAL-MODEL FOR SH3-LIGAND INTERACTIONS. *Science,* 266, 1241-1247.

FILLINGHAM, I., GINGRAS, A. R., PAPAGRIGORIOU, E., PATEL, B., EMSLEY, J., CRITCHLEY, D. R., ROBERTS, G. C. K. & BARSUKOV, I. L. (2005). A vinculin binding domain from the talin rod unfolds to form a complex with the vinculin head. *Structure,* 13, 65-74.

FRANKE, I. & PINGOUD, A. (1999). Synthesis and biochemical characterization of obligatory dimers of the sugar non-specific nuclease from Serratia marcescens using specifically designed bismaleimidoalkanes as SH-specific crosslinking reagents. *Journal of Protein Chemistry,* 18, 137-146.

FRENZEL, T., FINDEISEN, C., KADIC, M., GUMBSCH, P. & WEGENER, M. (2016). Tailored Buckling Microlattices as Reusable Light-Weight Shock Absorbers. *Advanced Materials,* 28, 5865-5870.

FREUNDT, J. K. & LINKE, W. A. (2019). Titin as a force-generating muscle protein under regulatory control. *Journal of Applied Physiology,* 126, 1474-1482.

GADZALA, M., DULAK, D., KALINOWSKA, B., BASTER, Z., BRYLINSKI, M., KONIECZNY, L., BANACH, M. & ROTERMAN, I. (2019). The aqueous environment as an active participant in the protein folding process. *Journal of Molecular Graphics & Modelling,* 87, 227-239.

GAO, X. Y., FANG, J., XUE, B., FU, L. L. & LI, H. B. (2016). Engineering Protein Hydrogels Using SpyCatcher-SpyTag Chemistry. *Biomacromolecules,* 17, 2812-2819.

GINGRAS, A. R., ZIEGLER, W. H., BOBKOV, A. A., JOYCE, M. G., FASCI, D., HIMMEL, M., ROTHEMUND, S., RITTER, A., GROSSMANN, J. G., PATEL, B., BATE, N., GOULT, B. T., EMSLEY, J., BARSUKOV, I. L., ROBERTS, G. C. K., LIDDINGTON, R. C., GINSBERG, M. H. & CRITCHLEY, D. R. (2009). Structural Determinants of Integrin Binding to the Talin Rod. *Journal of Biological Chemistry,* 284, 8857-8867.

GINGRAS, A. R., ZIEGLER, W. H., FRANK, R., BARSUKOV, I. L., ROBERTS, G. C. K., CRITCHLEY, D. R. & EMSLEY, J. (2005). Mapping and consensus sequence identification for multiple vinculin binding sites within the Talin rod. *Journal of Biological Chemistry,* 280, 37217-37224.

GOMBERT, Y., RONCORONI, F., SANCHEZ-FERRER, A. & SPENCER, N. D. (2020). The hierarchical bulk molecular structure of poly(acrylamide) hydrogels: beyond the fishing net. *Soft Matter,* 16, 9789-9798.

GOSLINE, J., LILLIE, M., CARRINGTON, E., GUERETTE, P., ORTLEPP, C. & SAVAGE, K. (2002). Elastic proteins: biological roles and mechanical properties. *Philosophical Transactions of the Royal Society B-Biological Sciences,* 357, 121-132.

GOUGH, R. E. & GOULT, B. T. (2018). The tale of two talins - two isoforms to fine-tune integrin signalling. *Febs Letters,* 592, 2108-2125.

GOUGH, R. E., JONES, M. C., ZACHARCHENKO, T., LE, S., YU, M., JACQUEMET, G., MUENCH, S., YAN, J., HUMPHRIES, J. D., JORGENSEN, C., HUMPHRIES, M. J. & GOULT, B. T. (2021). Talin mechanosensitivity is modulated by a direct interaction with cyclin-dependent kinase-1. *Journal of Biological Chemistry,* 297, 100837.

GOULT, B. T., BOUAOUINA, M., ELLIOTT, P. R., BATE, N., PATEL, B., GINGRAS, A. R., GROSSMANN, J. G., ROBERTS, G. C. K., CALDERWOOD, D. A., CRITCHLEY, D. R. & BARSUKOV, I. L. (2010). Structure of a double ubiquitin-like domain in the talin head: a role in integrin activation. *Embo Journal,* 29, 1069-1080.

GOULT, B. T., XU, X. P., GINGRAS, A. R., SWIFT, M., PATEL, B., BATE, N., KOPP, P. M., BARSUKOV, I. L., CRITCHLEY, D. R., VOLKMANN, N. & HANEIN, D. (2013). Structural studies on full-length talin1 reveal a compact auto-inhibited dimer: Implications for talin activation. *Journal of Structural Biology,* 184, 21-32.

GOULT, B. T., YAN, J. & SCHWARTZ, M. A. (2018). Talin as a mechanosensitive signaling hub. *Journal of Cell Biology,* 217, 3776-3784.

GOULT, B. T., ZACHARCHENKO, T., BATE, N., TSANG, R., HEY, F., GINGRAS, A. R., ELLIOTT, P. R., ROBERTS, G. C. K., BALLESTREM, C., CRITCHLEY, D. R. & BARSUKOV, I. L. (2013). RIAM and Vinculin Binding to Talin Are Mutually Exclusive and Regulate Adhesion Assembly and Turnover. *Journal of Biological Chemistry,* 288, 8238-8249.

GRAHAM, L. & ORENSTEIN, J. M. (2007). Processing tissue and cells for transmission electron microscopy in diagnostic pathology and research. *Nature Protocols,* 2, 2439-2450.

GREENFIELD, N. J. (2006). Using circular dichroism spectra to estimate protein secondary structure. *Nature Protocols,* 1, 2876-2890.

HAAS, S., KORNER, S., ZINTEL, L. & HUBBUCH, J. (2022). Changing mechanical properties of photopolymerized, dityrosine-crosslinked protein-based hydrogels. *Frontiers in Bioengineering and Biotechnology,* 10, 1006438.

HAN, J. C. & HAN, G. Y. (1994). A PROCEDURE FOR QUANTITATIVE-DETERMINATION OF TRIS(2-CARBOXYETHYL)PHOSPHINE, AN ODORLESS REDUCING AGENT MORE STABLE AND EFFECTIVE THAN DITHIOTHREITOL. *Analytical Biochemistry,* 220, 5-10.

HANLON, A. M., MARTIN, I., BRIGHT, E. R., CHOUINARD, J., RODRIGUEZ, K. J., PATENOTTEA, G. E. & BERDA, E. B. (2017). Exploring structural effects in single-chain "folding" mediated by intramolecular thermal Diels-Alder chemistry. *Polymer Chemistry,* 8, 5120-5128.

HAZRA, C., SAMANTA, T. & MAHALINGAM, V. (2014). A resonance energy transfer approach for the selective detection of aromatic amino acids. *Journal of Materials Chemistry C,* 2, 10157-10163.

HELMES, M., TROMBITAS, K., CENTNER, T., KELLERMAYER, M., LABEIT, S., LINKE, W. A. & GRANZIER, H. (1999). Mechanically driven contour-length adjustment in rat cardiac titin's unique N2B sequence - Titin is an adjustable spring. *Circulation Research,* 84, 1339-1352.

HEMMINGS, L., REES, D. J. G., OHANIAN, V., BOLTON, S. J., GILMORE, A. P., PATEL, B., PRIDDLE, H., TREVITHICK, J. E., HYNES, R. O. & CRITCHLEY, D. R. (1996). Talin contains three actin-binding sites each of which is adjacent to a vinculin-binding site. *Journal of Cell Science,* 109, 2715-2726.

HIBBERT, R., COLE, M. J., PRICE, M. C. & BURCHELL, M. J. (2017). The Hypervelocity Impact Facility at the University of Kent: Recent Upgrades and Specialized Capabilities. *14th Hypervelocity Impact Symposium (Hvis 2017),* 204, 208-214.

HOFFMAN, A. S. (2002). Hydrogels for biomedical applications. *Advanced Drug Delivery Reviews,* 54, 3-12.

HONG, P., KOZA, S. & BOUVIER, E. S. P. (2012). A REVIEW SIZE-EXCLUSION CHROMATOGRAPHY FOR THE ANALYSIS OF PROTEIN BIOTHERAPEUTICS AND THEIR AGGREGATES. *Journal of Liquid Chromatography & Related Technologies,* 35, 2923-2950.

HU, X., CEBE, P., WEISS, A. S., OMENETTO, F. & KAPLAN, D. L. (2012). Protein-based composite materials. *Materials Today,* 15, 208-215.

HUANG, P. S., BOYKEN, S. E. & BAKER, D. (2016). The coming of age of de novo protein design. *Nature,* 537, 320-327.

HUERTA-LOPEZ, C. & ALEGRE-CEBOLLADA, J. (2021). Protein Hydrogels: The Swiss Army Knife for Enhanced Mechanical and Bioactive Properties of Biomaterials. *Nanomaterials,* 11, 1656.

HUNTLEY, M. B. (2016). Fatigue and Modulus Characteristics of Wire-Lay Nylon Rope. In: *Oceans 2016 Mts/Ieee Monterey,* 19-23 September, 2016. Monterey: IEEE, pp 1-6.

JIAO, J., REBANE, A. A., MA, L. & ZHANG, Y. (2017). Single-Molecule Protein Folding Experiments Using High-Precision Optical Tweezers. *Optical Tweezers: Methods and Protocols,* 1486, 357-390.

JONES, J. C. R. (2016). Pre- and Post-embedding Immunogold Labeling of Tissue Sections. *High-Resolution Imaging of Cellular Proteins: Methods and Protocols,* 1474, 291-307.

JONES, S. M., ANDERSON, M. S., DOMINGUEZ, G. & TSAPIN, A. (2013). Thermal calibrations of hypervelocity capture in aerogel using magnetic iron oxide particles. *Icarus,* 226, 1-9.

KAN, A. & JOSHI, N. S. (2019). Towards the directed evolution of protein materials. *Mrs Communications,* 9, 441-455.

KANTNER, T. & WATTS, A. G. (2016). Characterization of Reactions between Water-Soluble Trialkylphosphines and Thiol Alkylating Reagents: Implications for Protein-Conjugation Reactions. *Bioconjugate Chemistry,* 27, 2400-2406.

KAROYO, A. H. & WILSON, L. D. (2017). Physicochemical Properties and the Gelation Process of Supramolecular Hydrogels: A Review. *Gels,* 3, 1.

KEARSLEY, A. T. (2017). How laboratory hypervelocity impact experiments have helped us to understand comet dust samples: a brief review. *14th Hypervelocity Impact Symposium (Hvis 2017),* 204, 43-50.

KIM, Y. G., HO, S. O., GASSMAN, N. R., KORLANN, Y., LANDORF, E. V., COLLART, F. R. & WEISS, S. (2008). Efficient site-specific Labeling of proteins via cysteines. *Bioconjugate Chemistry,* 19, 786-791.

KIRCHHOF, S., STRASSER, A., WITTMANN, H. J., MESSMANN, V., HAMMER, N., GOEPFERICH, A. M. & BRANDL, F. P. (2015). New insights into the cross-linking

and degradation mechanism of Diels-Alder hydrogels. *Journal of Materials Chemistry B,* 3, 449-457.

KIRTANIA, M. D., KAHALI, N. & MAITY, A. (2021). Chapter 8 - Inulin-based hydrogel. In: GIRI, T. K. & GHOSH, B. (eds.) *Plant and Algal Hydrogels for Drug Delivery and Regenerative Medicine.* Woodhead Publishing, pp 261-292.

KISELEVA, A. P., KRIVOSHAPKIN, P. V. & KRIVOSHAPKINA, E. F. (2020). Recent Advances in Development of Functional Spider Silk-Based Hybrid Materials. *Frontiers in Chemistry,* 8, 554.

KLAPHOLZ, B. & BROWN, N. H. (2017). Talin - the master of integrin adhesions. *Journal of Cell Science,* 130, 2435-2446.

KOGA, N., TATSUMI-KOGA, R., LIU, G. H., XIAO, R., ACTON, T. B., MONTELIONE, G. T. & BAKER, D. (2012). Principles for designing ideal protein structures. *Nature,* 491, 222-227.

KOPP, J., KITTLER, S., SLOUKA, C., HERWIG, C., SPADIUT, O. & WURM, D. J. (2020). Repetitive Fed-Batch: A Promising Process Mode for Biomanufacturing With E. coli. *Frontiers in Bioengineering and Biotechnology,* 8, 573607.

KULKARNI, V. S. & SHAW, C. (2016). Chapter 9 - Rheological Studies. *In:* KULKARNI, V. S. & SHAW, C. (eds.) *Essential Chemistry for Formulators of Semisolid and Liquid Dosages.* Boston: Academic Press, pp 145-182.

KUSZEWSKI, J., GRONENBORN, A. M. & CLORE, G. M. (1999). Improving the packing and accuracy of NMR structures with a pseudopotential for the radius of gyration. *Journal of the American Chemical Society,* 121, 2337-2338.

LAPIDUS, L. J. (2017). Protein unfolding mechanisms and their effects on folding experiments. *F1000Research,* 6, 1723.

LEE, S., TONG, X. M. & YANG, F. (2016). Effects of the poly(ethylene glycol) hydrogel crosslinking mechanism on protein release. *Biomaterials Science,* 4, 405-411.

LIN, L. H., KOLLIPARA, P. S. & ZHENG, Y. B. (2019). Digital manufacturing of advanced materials: Challenges and perspective. *Materials Today,* 28, 49-62.

LINKE, W. A., POPOV, V. I. & POLLACK, G. H. (1994). PASSIVE AND ACTIVE TENSION IN SINGLE CARDIAC MYOFIBRILS. *Biophysical Journal,* 67, 782-792.

LIU, J. R., WANG, Y. L., GOH, W. I., GOH, H., BAIRD, M. A., RUEHLAND, S., TEO, S., BATE, N., CRITCHLEY, D. R., DAVIDSON, M. W. & KANCHANAWONG, P. (2015). Talin determines the nanoscale architecture of focal adhesions. *Proceedings of the National Academy of Sciences of the United States of America,* 112, E4864-E4873.

LIU, Y. & HSU, S. H. (2018). Synthesis and Biomedical Applications of Self-healing Hydrogels. *Frontiers in Chemistry,* 6, 449.

LJUBETIC, A., GRADISAR, H. & JERALA, R. (2017). Advances in design of protein folds and assemblies. *Current Opinion in Chemical Biology,* 40, 65-71.

LONG, T. J., LI, Y. X., FANG, X. & SUN, J. Q. (2018). Salt-Mediated Polyampholyte Hydrogels with High Mechanical Strength, Excellent Self-Healing Property, and Satisfactory Electrical Conductivity. *Advanced Functional Materials,* 28, 1804416.

LV, S., DUDEK, D. M., CAO, Y., BALAMURALI, M. M., GOSLINE, J. & LI, H. B. (2010). Designed biomaterials to mimic the mechanical properties of muscles. *Nature,* 465, 69-73.

LYNCH, N. J. (1999). Constant kinetic energy impacts of scale size KE projectiles at ordnance and hypervelocity. *International Journal of Impact Engineering,* 23, 573-584.

MACNEIL, S. (2008). Biomaterials for tissue engineering of skin. *Materials Today,* 11, 26-35.

MAGAZ, A., ROBERTS, A. D., FARAJI, S., NASCIMENTO, T. R. L., MEDEIROS, E. S., ZHANG, W. Z., GREENHALGH, R. D., MAUTNER, A., LI, X. & BLAKER, J. J. (2018). Porous, Aligned, and Biomimetic Fibers of Regenerated Silk Fibroin Produced by Solution Blow Spinning. *Biomacromolecules,* 19, 4542-4553.

MAITRA, J. & SHUKLA, V. K. (2014). Cross-linking in hydrogels - a review. *American Journal of Polymer Science*, 4, 25-31.

MALAKOOTI, S., VIVOD, S. L., PEREIRA, M., RUGGERI, C. R., REVILOCK, D. M., ZHANG, R. Y., GUO, H. Q., SCHEIMAN, D. A., MCCORKLE, L. S. & LU, H. B. (2022). Polyimide aerogels for ballistic impact protection. *Scientific Reports,* 12, 13933.

MANNING, M. C. (2005). Use of infrared spectroscopy to monitor protein structure and stability. *Expert Review of Proteomics,* 2, 731-743.

MARGADANT, F., CHEW, L. L., HU, X., YU, H., BATE, N., ZHANG, X. & SHEETZ, M. (2011). Mechanotransduction In Vivo by Repeated Talin Stretch-Relaxation Events Depends upon Vinculin. *Plos Biology,* 9, 1001223.

MATSUI, S. & AIDA, H. (1978). HYDROLYSIS OF SOME N-ALKYLMALEIMIDES. *Journal of the Chemical Society-Perkin Transactions 2*, 1277-1280.

MAYERHOFER, T. G. & POPP, J. (2019). Beer's Law - Why Absorbance Depends (Almost) Linearly on Concentration. *Chemphyschem,* 20, 511-515.

MEJIA, G., WANG, Y. Q., HUANG, Z. H., SHI, Q. N. & ZHANG, Z. (2021). Maleimide Chemistry: Enabling the Precision Polymer Synthesis. *Chinese Journal of Chemistry,* 39, 3177-3187.

MENG, J. M. & MCKNIGHT, C. J. (2008). Crystal structure of a pH-stabilized mutant of villin headpiece. *Biochemistry,* 47, 4644-4650.

MONDAL, P. P., BARO, N., SINGH, A., JOSHI, P. & BASUMATARY, J. 2022. Lightsheet optical tweezer (LOT) for optical manipulation of microscopic particles and live cells. *Scientific Reports,* 12, 10229.

MONKLEY, S. J., ZHOU, X. H., KINSTON, S. J., GIBLETT, S. M., HEMMINGS, L., PRIDDLE, H., BROWN, J. E., PRITCHARD, C. A., CRITCHLEY, D. R. & FASSLER, R. (2000). Disruption of the talin gene arrests mouse development at the gastrulation stage. *Developmental Dynamics,* 219, 560-574.

NAIR, A. N., SUNDHARESAN, S. & AL TUBI, I. S. M. (2020). Kevlar-based Composite Material and its Applications in Body Armour: A Short Literature Review. *IOP Conference Series: Materials Science and Engineering,* 987, 012003.

OMIDI, M., FATEHINYA, A., FARAHANI, M., AKBARI, Z., SHAHMORADI, S., YAZDIAN, F., TAHRIRI, M., MOHARAMZADEH, K., TAYEBI, L. & VASHAEE, D. 2017. 7 - Characterization of biomaterials. In: TAYEBI, L. & MOHARAMZADEH, K. (eds.) *Biomaterials for Oral and Dental Tissue Engineering.* Woodhead Publishing, pp 97-115.

OWEN, L. M., BAX, N. A., WEIS, W. I. & DUNN, A. R. (2022). The C-terminal actin-binding domain of talin forms an asymmetric catch bond with F-actin. *Proceedings of the National Academy of Sciences of the United States of America,* 119, e2109329119.

PACE, C. N., TREVINO, S., PRABHAKARAN, E. & SCHOLTZ, J. M. (2004). Protein structure, stability and solubility in water and other solvents. *Philosophical Transactions of the Royal Society of London Series B-Biological Sciences,* 359, 1225-1234.

PAPAGRIGORIOU, E., GINGRAS, A. R., BARSUKOV, I. L., BATE, N., FILLINGHAM, I. J., PATEL, B., FRANK, R., ZIEGLER, W. H., ROBERTS, G. C. K., CRITCHLEY, D. R. & EMSLEY, J. (2004). Activation of a vinculin-binding site in the talin rod involves rearrangement of a five-helix bundle. *Embo Journal,* 23, 2942-2951.

PARHI, R. (2017). Cross-Linked Hydrogel for Pharmaceutical Applications: A Review. *Advanced Pharmaceutical Bulletin,* 7, 515-530.

PARK, J. L., CHI, Y. S., HAHN, M. H. & KANG, T. J. (2012). Kinetic Dissipation in Ballistic Tests of Soft Body Armors. *Experimental Mechanics,* 52, 1239-1250.

PEARSON, M. A., RECZEK, D., BRETSCHER, A. & KARPLUS, P. A. (2000). Structure of the ERM protein moesin reveals the FERM domain fold masked by an extended actin binding tail domain. *Cell,* 101, 259-270.

QIAN, J., CAI, H. P., MA, W. W. & HAO, Z. W. (2015). Shock Analysis on a Packaged Washing Machine from Damage Boundary: Shock Response Spectrum to Component Failure. *Shock and Vibration,* 2015, 462492.

QIAO, P. Z., YANG, M. J. & BOBARU, F. (2008). Impact mechanics and high-energy absorbing materials: Review. *Journal of Aerospace Engineering,* 21, 235-248.

RANGANATHAN, N. J. B., R. ABDUL KADER, M. NAYAK, S.K. (2018). Synthesis and Properties of Hydrogels Prepared by Various Polymerization Reaction Systems. In: Mondal, M. (eds). *Cellulose-Based Superabsorbent Hydrogels*. *Polymers and and polymeric Composites: A Reference Series.* Springer, Cham. pp 1-25.

RAPHEL, G., JACOB, M. M. & VISWANATHAN, S. (2019). Bioinspired designs for shock absorption, based upon nacre and Bouligand structures. *Sn Applied Sciences,* 1, 1022.

REIS, R. H. M., NUNES, L. F., DA LUZ, F. S., CANDIDO, V. S., DA SILVA, A. C. R. & MONTEIRO, S. N. (2021). Ballistic Performance of Guaruman Fiber Composites in Multilayered Armor System and as Single Target. *Polymers,* 13, 1203.

ROBERTS, G. C. K. & CRITCHLEY, D. R. (2009). Structural and biophysical properties of the integrin-associated cytoskeletal protein talin. *Biophysical reviews,* 1, 61-69.

ROMER, L. & SCHEIBEL, T. (2008). The elaborate structure of spider silk Structure and function of a natural high performance fiber. *Prion,* 2, 154-161.

ROSENBAUM, D. M., RASMUSSEN, S. G. F. & KOBILKA, B. K. (2009). The structure and function of G-protein-coupled receptors. *Nature,* 459, 356-363.

ROSTAMABADI, H., FALSAFI, S. R. & JAFARI, S. M. (2020). Chapter Two - Transmission electron microscopy (TEM) of nanoencapsulated food ingredients. *In:* JAFARI, S. M. (ed.) *Characterization of Nanoencapsulated Food Ingredients.* Academic Press, pp 53-82.

ROUGHTON, B. C., IYER, L. K., BERTELSEN, E., TOPP, E. M. & CAMARDA, K. V. (2013). Protein aggregation and lyophilization: Protein structural descriptors as predictors of aggregation propensity. *Computers & Chemical Engineering,* 58, 369-377.

SABOURIN, M., TUZON, C. T., FISHER, T. S. & ZAKIAN, V. A. (2007). A flexible protein linker improves the function of epitope-tagged proteins in Saccharomyces cerevisiae. *Yeast,* 24, 39-45.

SAINI, K. (2016). Preparation method, properties and crosslinking of hydrogel: a review. *Pharmatutor*, 5(1), 27-36.

SCHNEIDER, C. A., RASBAND, W. S. & ELICEIRI, K. W. (2012). NIH Image to ImageJ: 25 years of image analysis. *Nature Methods,* 9, 671-675.

SCHON, A., CLARKSON, B. R., JAIME, M. & FREIRE, E. (2017). Temperature stability of proteins: Analysis of irreversible denaturation using isothermal calorimetry. *Proteins-Structure Function and Bioinformatics,* 85, 2009-2016.

SEO, J. Y., LEE, B., KANG, T. W., NOH, J. H., KIM, M. J., JI, Y. B., JU, H. J., MIN, B. H. & KIM, M. S. (2018). Electrostatically Interactive Injectable Hydrogels for Drug Delivery. *Tissue Engineering and Regenerative Medicine,* 15, 513-520.

SHEDBALE, N. & MULEY, P. (2017). Review on Viscoelastic Materials used in Viscoelastic Dampers. International Research Journal of Engineering and Technology (IRJET), 4(7), 3375-3381.

SHEN, Y., LEVIN, A., KAMADA, A., TOPRAKCIOGLU, Z., RODRIGUEZ-GARCIA, M., XU, Y. F. & KNOWLES, T. P. J. (2021). From Protein Building Blocks to Functional Materials. *Acs Nano,* 15, 5819-5837.

SHEN, Y., NYSTROM, G. & MEZZENGA, R. (2017). Amyloid Fibrils form Hybrid Colloidal Gels and Aerogels with Dispersed CaCO3 Nanoparticles. *Advanced Functional Materials,* 27, 1700897.

SONG, X. Q., YANG, J., HIRBAWI, J., YE, S., PERERA, H. D., GOKSOY, E., DWIVEDI, P., PLOW, E. F., ZHANG, R. G. & QIN, J. (2012). A novel membrane-dependent

on/off switch mechanism of talin FERM domain at sites of cell adhesion. *Cell Research,* 22, 1533-1545.

SPITERI, S. (2019). Shock Absorber Applications. *European Journal of Engineering and Technology Research,* 4, 37-41.

SPUDICH, J. A. (2001). The myosin swinging cross-bridge model. *Nature Reviews Molecular Cell Biology,* 2, 387-392.

SRIVASTAVA, A. K. & GUPTA, S. (2011). 2.38 - Fed-Batch Fermentation – Design Strategies. In: MOO-YOUNG, M. (ed.) *Comprehensive Biotechnology (Second Edition).* Burlington: Academic Press, pp 515-526.

STIE, M. B., KALOUTA, K., VETRI, V. & FODERA, V. (2022). Protein materials as sustainable non- and minimally invasive strategies for biomedical applications. *Journal of Controlled Release,* 344, 12-25.

STORASKA, A. J. & NEUBIG, R. R. (2013). Chapter Eight - NMR Methods for Detection of Small Molecule Binding to RGS4. In: CONN, P. M. (ed.) *Methods in Enzymology.* Academic Press, pp 133-152.

SZIJJ, P. A., BAHOU, C. & CHUDASAMA, V. (2018). Minireview: Adddressing the retro-Michael instability of maleimide bioconjugates. *Drug discovery today. Technologies*, 30, 27-34.

TALEBIAN, S., MEHRALI, M., TAEBNIA, N., PENNISI, C. P., KADUMUDI, F. B., FOROUGHI, J., HASANY, M., NIKKHAH, M., AKBARI, M., ORIVE, G. & DOLATSHAHI-PIROUZ, A. (2019). Self-Healing Hydrogels: The Next Paradigm Shift in Tissue Engineering? *Advanced Science,* 6, 1801664.

TANG, D. D. (2018). Chapter One - The Dynamic Actin Cytoskeleton in Smooth Muscle. In: KHALIL, R. A. (ed.) *Advances in Pharmacology.* Academic Press, pp 1-38.

TANZI, M. C., FARÈ, S. & CANDIANI, G. (2019). Chapter 2 - Mechanical Properties of Materials. *In:* TANZI, M. C., FARÈ, S. & CANDIANI, G. (eds.) *Foundations of Biomaterials Engineering.* Academic Press, pp 105-136.

TELEGDI, J., SHABAN, A. & VASTAG, G. (2018). Biocorrosion—Steel. *In:* WANDELT, K. (ed.) *Encyclopedia of Interfacial Chemistry.* Oxford: Elsevier, pp 28-42.

TENG, Z., XU, R. Y. & WANG, Q. (2015). Beta-lactoglobulin-based encapsulating systems as emerging bioavailability enhancers for nutraceuticals: a review. *Rsc Advances,* 5, 35138-35154.

TRIPATHI, N. K. & SHRIVASTAVA, A. (2019). Recent Developments in Bioprocessing of Recombinant Proteins: Expression Hosts and Process Development. *Frontiers in Bioengineering and Biotechnology,* 7, 420.

TUNCABOYLU, D. C., SARI, M., OPPERMANN, W. & OKAY, O. (2011). Tough and Self-Healing Hydrogels Formed via Hydrophobic Interactions. *Macromolecules,* 44, 4997-5005.

VARGHESE, S. A., RANGAPPA, S. M., SIENGCHIN, S. & PARAMESWARANPILLAI, J. (2020). Chapter 2 - Natural polymers and the hydrogels prepared from them. In: CHEN, Y. (ed.) *Hydrogels Based on Natural Polymers.* Elsevier, pp 17-47.

WANG, H. Y. & HEILSHORN, S. C. (2015). Adaptable Hydrogel Networks with Reversible Linkages for Tissue Engineering. *Advanced Materials,* 27, 3717-3736.

WANG, K. K., MENG, X. G. & GUO, Z. K. (2021). Elastin Structure, Synthesis, Regulatory Mechanism and Relationship With Cardiovascular Diseases. *Frontiers in Cell and Developmental Biology,* 9, 596702.

WANG, Y. N., YAO, M. X., BAKER, K. B., GOUGH, R. E., LE, S., GOULT, B. T. & YAN, J. (2021). Force-Dependent Interactions between Talin and Full-Length Vinculin. *Journal of the American Chemical Society,* 143, 14726-14737.

WAUDBY, C. A., LAUNAY, H., CABRITA, L. D. & CHRISTODOULOU, J. (2013). Protein folding on the ribosome studied using NMR spectroscopy. *Progress in Nuclear Magnetic Resonance Spectroscopy,* 74, 57-75.

WEN, L., LYU, Q., LEY, K. & GOULT, B. T. (2022). Structural Basis of β2 Integrin Inside—Out Activation. *Cells*, 11(19), 3039.

WEN, Q. & JANMEY, P. A. (2011). Polymer physics of the cytoskeleton. *Current Opinion in Solid State & Materials Science,* 15, 177-182.

WEN, Y. K., XU, C., WANG, S. & BATRA, R. C. (2015). Analysis of behind the armor ballistic trauma. *Journal of the Mechanical Behavior of Biomedical Materials,* 45, 11-21.

WHITE, L. J., WARK, C., CROUCHER, L., DRAPER, E. R. & HISCOCK, J. R. (2020). High-throughput characterisation of supramolecular gelation processes using a combination of optical density, fluorescence and UV-Vis absorption measurements. *Chemical Communications,* 56, 9557-9560.

WILSON, D. I. (2018). What is rheology? *Eye,* 32, 179-183.

WISE, S. G., BYROM, M. J., WATERHOUSE, A., BANNON, P. G., NG, M. K. C. & WEISS, A. S. (2011). A multilayered synthetic human elastin/polycaprolactone hybrid

vascular graft with tailored mechanical properties. *Acta Biomaterialia,* 7, 295-303.

WOIGNIER, T., DUFFOURS, L., COLOMBEL, P. & DURIN, C. (2013). Aerogels Materials as Space Debris Collectors. *Advances in Materials Science and Engineering,* 2013, 484133.

WU, J. H., LI, P. F., DONG, C. L., JIANG, H. T., XUE, B., GAO, X., QIN, M., WANG, W., CHEN, B. & CAO, Y. (2018). Rationally designed synthetic protein hydrogels with predictable mechanical properties. *Nature Communications,* 9, 620.

XIANG, D. F., WU, X., CAO, W., XUE, B., QIN, M., CAO, Y. & WANG, W. (2020). Hydrogels With Tunable Mechanical Properties Based on Photocleavable Proteins. *Frontiers in Chemistry,* 8, 1-9.

XIAO, P., BOLTON, D., MUNRO, R. A., BROWN, L. S. & LADIZHANSKY, V. (2019). Solid-state NMR spectroscopy based atomistic view of a membrane protein unfolding pathway. *Nature Communications,* 10, 3867.

XU, J. Y., FAN, Z. W., DUAN, L. J. & GAO, G. H. (2018). A tough, stretchable, and extensively sticky hydrogel driven by milk protein. *Polymer Chemistry,* 9, 2617-2624.

XUE, J. J., WU, T., DAI, Y. Q. & XIA, Y. N. (2019). Electrospinning and Electrospun Nanofibers: Methods, Materials, and Applications. *Chemical Reviews,* 119, 5298-5415.

YANG, K. H. (2018). Chapter 5 - Material Laws and Properties. In: YANG, K. H. (ed.) *Basic Finite Element Method as Applied to Injury Biomechanics.* Academic Press, pp 231-256.

YAO, M. X., GOULT, B. T., CHEN, H., CONG, P. W., SHEETZ, M. P. & YAN, J. (2014). Mechanical activation of vinculin binding to talin locks talin in an unfolded conformation. *Scientific Reports,* 4, 4610.

YAO, M. X., GOULT, B. T., KLAPHOLZ, B., HU, X., TOSELAND, C. P., GUO, Y. J., CONG, P. W., SHEETZ, M. P. & YAN, J. (2016). The mechanical response of talin. *Nature Communications,* 7, 19966.

YIN, Z., HANNARD, F. & BARTHELAT, F. (2019). Impact-resistant nacre-like transparent materials. *Science,* 364, 1260-1263.

YU, H., XIAO, Q. H., QI, G. L., CHEN, F. X., TU, B. Y., ZHANG, S., LI, Y. P., CHEN, Y. & DUAN, P. (2022). A Hydrogen Bonds-Crosslinked Hydrogels With Self-Healing and Adhesive Properties for Hemostatic. *Frontiers in Bioengineering and Biotechnology,* 10, 855013.

ZHANG, J. J., LU, G. X. & YOU, Z. (2020). Large deformation and energy absorption of additively manufactured auxetic materials and structures: A review. *Composites Part B-Engineering,* 201, 108340.

ZHANG, N., YANG, S. F., XIONG, L. M., HONG, Y. & CHEN, Y. P. (2016). Nanoscale toughening mechanism of nacre tablet. *Journal of the Mechanical Behavior of Biomedical Materials,* 53, 200-209.

ZHANG, P., AZIZI, L., KUKKURAINEN, S., GAO, T., BAIKOGHLI, M., JACQUIER, M.-C., SUN, Y., MAATTA, J. A. E., CHENG, R. H., WEHRLE-HALLER, B., HYTONEN, V. P. & WU, J. (2020). Crystal structure of the FERM-folded talin head reveals the determinants for integrin binding. *Proceedings of the National Academy of Sciences of the United States of America,* 117, 32402-32412.

ÖHRLUND, Å. (2018). Evaluation of Rheometry Amplitude Sweep Cross-Over Point as an Index of Flexibility for HA Fillers. Journal of Cosmetics, Dermatological Sciences and Applications, 8, 47-54.